

# Gas Sensing Using Quantum Cascade Lasers

Kenneth Gillespie Hay

University of Strathclyde

Department of Physics



**U**NIVERSITY OF  
**S**TRATHCLYDE

A Thesis presented in fulfilment of the requirements for  
the degree of Doctor of Philosophy

2010

This thesis is the result of the author's original research. It has been composed by the author and has not been previously submitted for examination which has led to the award of a degree.

© Copyright 2010.

The copyright of this thesis belongs to the author under the terms of the United Kingdom Copyright Acts, as qualified by University of Strathclyde Regulation 3.50. Due acknowledgement must always be made of the use of any material contained in, or derived from, this thesis.

University of Strathclyde Regulation 3.50:

"Where the author has not lodged with the Librarian a written objection to the copying of their thesis, the Librarian may give permission for single copies of that thesis, in whole or in part, to be made for the purposes of research or private study, or for deposit in the British Library."

## Acknowledgements

Firstly I'd like to thank my supervisors, Dr. Nigel Langford and Prof. Geoffrey Duxbury for their help and support all the way through, Paul Black for much of my "on-the-job training" at the start, and David Wilson who started as I finished, giving me a hand on the last few bits of lab work.

Over the course of my work, a lot of research has been carried out in collaboration with others away from our lab, so I would like to acknowledge help from the following: Carl Joseph, David Davies and Gary Llewellyn at ARSF, Oxford (later Gloucester); Eiko Nemitz and Daniela Famulari at CEH, Edinburgh; Professor Mike Ashfold and Jie Ma at Bristol University School of Chemistry; John Black and Mark Johnson at Rolls Royce and everyone from Scitek, Derby; Glasgow Vintage Vehicle Trust for allowing me to measure emissions from their vintage bus collection, as well as certain members for lending me their own buses. Also, thanks to my Aunt Alice and to Mary Divine for giving me a place to stay in Edinburgh while working there.

On the opposite side of collaboration, I'd like to thank Nicola Tasinato and Rajiv Boddeda for coming to work with us. Lab work is much easier if there's two of you!

I also want to thank the electronics workshop (John, Mark & Ged) and the Photonics Group Workshop (Bob, Ewan & Lisa) for various jobs and supply guru Brian for always having the vital nut or bolt I needed.

For company, ice creams and an introduction to Sushi, I want to thank all the folks who have been downstairs in the Photonics Group over my 3½ years (Wei, Kyle, Iain, Mateusz, Yann, Luke, Alessio, Griff, Stefanie, Aline, Chris, Neal, Matthieu, Umakanth, Nick, Kanupriya, Aline and Yoann).

I would never have got anywhere without the support of my family, particularly in letting me stay at home despite looking like I was going to carry on being a student for all eternity!

Finally, thanks to the EPSRC Doctoral Training Fund for my bursary which has kept my bus on the road through the last few years!

# Contents

Acknowledgements . . . . .	3
Abbreviations . . . . .	7
Abstract . . . . .	8
Chapter 1: Introduction . . . . .	9
Chapter 2: Background Theory . . . . .	15
2.1: Introduction . . . . .	15
2.2: What is a QC Laser? . . . . .	16
2.3: Inter- and Intra-Pulse Tuning . . . . .	19
2.4: Absorption Spectroscopy. . . . .	23
2.5: Rapid Passage . . . . .	30
2.6: Conclusion . . . . .	32
Chapter 3: About The Instruments . . . . .	33
3.1: Introduction . . . . .	33
3.2: Instrument Design . . . . .	34
Laser Systems . . . . .	35
Optical Setup . . . . .	35
Photodetectors. . . . .	38
Digitisers . . . . .	39
Pressure Control System . . . . .	39
3.3: The Data Analysis Process . . . . .	41
Nitrous Oxide During Field Fertilization – Calibration . . . . .	46
In-Flight Atmospheric Measurements – Fitting test . . . . .	46
Bus Exhaust Fumes – Zero measurements. . . . .	46
3.4: New Laser Drive Box – Power Supply Instability . . . . .	47
3.5: Laser Characterisation . . . . .	53

Methodology . . . . .	53
Summary of Characteristics . . . . .	54
Results. . . . .	55
Comparison of the Two 8 $\mu\text{m}$ Lasers . . . . .	63
Laser 61 Bistability . . . . .	64
Laser 64 High Voltage Behaviour . . . . .	66
3.6: Control Software . . . . .	70
Acquisition Only.vi . . . . .	70
Flight Program.vi . . . . .	72
Acquisition Only for New Digitisers.vi . . . . .	75
3.7: Data Analysis Software . . . . .	77
Datafix.vi . . . . .	77
BGfix.vi . . . . .	78
Polyfitta.vi . . . . .	79
Graphfix.vi . . . . .	79
Drawgraph.vi . . . . .	80
Basefix.vi . . . . .	80
9-point Savitky-Golay.vi . . . . .	81
Fitting Peaks . . . . .	81
3.8: The 4-Laser Miniature Spectrometer . . . . .	84
Original Design . . . . .	84
Modifications . . . . .	86
Software . . . . .	87
3.9: Conclusion . . . . .	91
Chapter 4: Experimental Results . . . . .	92
4.1: Introduction . . . . .	92
4.2: Nitrous Oxide During Field Fertilization. . . . .	94
4.3: In-Flight Atmospheric Measurements . . . . .	101
Oxford Airport Based Flights . . . . .	102
Gloucester Airport Based Flight . . . . .	113
4.4: Hot Acetylene and Methane in a CVD Reactor . . . . .	122

4.5: Jet Engine Exhaust Plume Measurements	. . .	. 134
4.6: Bus Exhaust Fumes	. . . . .	. 139
4.7: Rapid Passage	. . . . .	. 151
4.8: 2-Laser Spectroscopy	. . . . .	. 162
4.9: Conclusion	. . . . .	. 166
Chapter 5: Conclusion.	. . . . .	. 167
Chapter 6: Future Work	. . . . .	. 169
References	. . . . .	. 171
Publications	. . . . .	. 190
Papers	. . . . .	. 190
Talks	. . . . .	. 192
Posters.	. . . . .	. 193
Appendix: LabVIEW Program Diagrams	. . . . .	. 194

# Abbreviations

All abbreviations used in this thesis are detailed below:

AC	Alternating Current
ACCORD	Advanced Components Cooperation for Optoelectronics Research and Development
AEC	Associated Equipment Company
AIMMS	Aircraft Integrated Meteorological Measurement System
ARSF	Airborne Research & Survey Facility
BNC	Bayonet Neill-Concelman
BOC	British Oxygen Company
BST	British Summer Time
CDIAC	Carbon Dioxide Information Analysis Center
CEAS	Cavity Enhanced Absorption Spectroscopy
CEH	Centre for Ecology and Hydrology
COPD	Chronic Obstructive Pulmonary Disease
CRDS	Cavity Ringdown Spectroscopy
CVD	Chemical Vapour Deposition
CW	Continuous Wave
ER-2	Earth Resources - 2
ESRI	Environmental Systems Research Institute
FAAM	Facility for Airborne Atmospheric Measurements
FAGE	Fluorescence Assay by Gas Expansion
FID	Free Induction Decay
FTS	Fourier Transform Spectrometer
FWHM	Full Width at Half Maximum
GMT	Greenwich Mean Time
GPS	Global Positioning System
GRINGO	GPS RINEX Generator
HITRAN	High Resolution Transmission Database
IPCC	Intergovernmental Panel on Climate Change
LabVIEW	Laboratory Virtual Instrumentation Engineering Workbench
LIF	Laser Induced Fluorescence
MBE	Molecular Beam Epitaxy
MCT	Mercury Cadmium Telluride
MCW	Metro-Cammell Weymann
MKS	MKS
MOT	Ministry of Transport
MSE	Mean Squared Error
NASA	National Aeronautics and Space Administration
NERC	Natural Environment Research Council
NMR	Nuclear Magnetic Resonance
PCI	Peripheral Component Interconnect
QC	Quantum Cascade
QVF	QVF
RAL	Rutherford Appleton Laboratory
RINEX	Receiver Independent Exchange Format
TATP	Triacetone Triperoxide
TDLAS	Tunable Diode Laser Absorption Spectroscopy
TNT	Trinitrotoluene
UK	United Kingdom
US	United States
USB	Universal Serial Bus
VI	Virtual Instrument
VOCs	Volatile Organic Compounds

## Abstract

This work involved development and operation of a spectrometer based on quantum cascade (QC) lasers performing absorption spectroscopy. Applying a 1300 ns long current pulse to a QC laser generates a frequency downchirp covering a typical range of  $3.5 \text{ cm}^{-1}$ , allowing several spectral lines to be recorded simultaneously. This gives the instrument a high relative accuracy when comparing simultaneous measurements of different gases. Depending upon the absorption line, the detection limit of the instrument, defined as three times the standard deviation while measuring synthetic air [1], can be as low as 1.86 ppb.

Laboratory work concentrated on rapid passage effects in gases, as well as developing the system for fieldwork, several examples of which were performed.

Developing the system included realigning the gas cell to increase path length and consequently absorption, as well as debugging the in-flight instrument control software. Additional lasers operating at different wavelengths were acquired and characterised, and new detectors considerably improved the sensitivity of the instrument. A commercial 4-laser version of the spectrometer (Cascade Technologies CT2400) was also acquired and many improvements were made to its cooling and pressure control systems. Data recorded by both instruments utilised data processing software written in LabVIEW.

Field measurements carried out include flight based pollution measurements from the NERC ARSF aircraft on two separate occasions, measurements of airborne nitrous oxide levels at the field site of the Centre for Ecology and Hydrology before, during and after an artificial nitrate fertilizer was spread on the field, single-pass spectroscopy of carbon/argon/hydrogen plasmas used for chemical vapour deposition of artificial diamond in collaboration with Prof. Mike Ashfold's group in the Chemistry department at Bristol University, free-space spectroscopy through the exhaust plume of a Rolls-Royce turbojet engine in collaboration with Rolls-Royce and Scitech Consultants, and measurements of exhaust pollution from diesel vintage bus engines.



# Chapter 1: Introduction

The group at the University of Strathclyde have previously developed a compact intra-pulse approach Quantum Cascade (QC) laser spectrometer [2] and in an earlier flight from Oxford airport demonstrated its potential for making atmospheric measurement of methane and nitrous oxide.

Although the instrument used has been developed in many ways during this work, a basic description of its design is as follows.

The emission frequency of a quantum cascade laser decreases as the temperature of the device increases. When a long current pulse is applied to a QC laser, the consequential heating of the laser causes the emission frequency to decrease rapidly as a function of time. This effect is known as a frequency downchirp.

The rate of temperature rise depends upon the heat input from current flowing within the laser and upon the rate of heat extraction from the thermoelectric cooler. Over time, the temperature approaches equilibrium between the heating and cooling. As equilibrium is approached, the rate of the frequency downchirp slows. A spectrum can therefore be recorded making use of the change of frequency with time during the application of a current pulse. By passing the chirped laser output pulse through a multipass astigmatic Herriott cell [3] filled with atmospheric gas at low pressure, the long path length allows absorption by the gas to be measured with great sensitivity. On leaving the cell, the pulse is incident on a fast photodetector, whose output is fed to a fast digitiser and saved on the control computer.

As the emission frequency varies with time, each time interval within the pulse thus corresponds to a particular frequency. As absorption reduces the light intensity incident on the photodetector at a particular frequency, the resultant measurement of intensity as a function of time corresponds to an absorption spectrum, which can then be used to determine the mixing ratio of the different gases in the cell.

One of the key uses of the instrument is for measuring mixing ratios of greenhouse

gases and other pollutants in the atmosphere. Methane, carbon dioxide and nitrous oxide are some of the main gases monitored as part of a worldwide measurement programme for greenhouse gases [4]. The main organisation which reviews the contribution of greenhouse gases to global warming is the Intergovernmental Panel on Climate Change (IPCC). The average tropospheric concentrations of greenhouse gases in December 2009 have been given by Blasing, who has summarised the results from the Carbon Dioxide Information Analysis Center (CDIAC) project [5]. Measurements are usually compared to the background levels in clean sites with little exposure to industrial pollution. The closest reference site of this kind for the UK is Mace Head on the west coast of Ireland [6], and it is these values used when referring to "background levels". Many atmospheric pollutants take a long time to be removed from the atmosphere. The estimated atmospheric lifetime (*i.e.* the time to decay to  $1/e$  of the quantity added) of carbon dioxide for instance is estimated at around 100 years. Nitrous oxide has an atmospheric lifetime of 114 years, while methane is more short-lived with an atmospheric lifetime of 12 years.

This project has involved the investigation and solution of a variety of technical problems, including greatly increasing the path length of the multipass cell, installing a wider bandwidth detector, improving the electrical isolation of the instrument and characterising additional lasers operating at different wavelengths. A Cascade Technologies CT-2400 commercially available 4-laser version of the spectrometer was also acquired and a detailed investigation led to improvements to its cooling systems and pressure control. Data recorded by both instruments utilised data processing software written in LabVIEW although the 4-laser system calculated gas concentrations on-the-fly using the analysis software integrated with the control program supplied with the system.

The improved single laser system was used for a wide variety of field measurements, including flight based atmospheric measurements and field based nitrous oxide measurements. With a simple laser / detector version of the system *i.e.* without the multipass cell, measurements of hot methane and acetylene in a chemical vapour deposition (CVD) plasma reactor have been carried out as have free space

measurements of carbon monoxide, carbon dioxide and water vapour in a turbojet engine exhaust plume.

The 4-laser system has also been used for fieldwork, again measuring pollution levels while airborne in the NERC Dornier [7], as well as for a brief study on the differences in diesel engine pollution from buses of various ages from the 1930s right through to the 1990s.

As is apparent from the above, the main application of the instruments is for use in atmospheric measurements of various gases. The main advantages of our system are the speed with which a spectrum is recorded (typically 1300 ns) rendering the instrument relatively immune to vibration, such as that encountered during flight based work, and the wide (typically  $3.5 \text{ cm}^{-1}$ ) tuning range which allows several absorption lines to be measured simultaneously. This also gives the instrument a high relative accuracy for the determination of comparative mixing ratios of a range of gases, which are simultaneously measured under identical conditions.

With concerns over pollution, acid rain, and global warming, atmospheric monitoring is a very important area. Spectrometry based upon the use of QC lasers is one method which is being applied in this area.

Manne, Jäger and Tulip have carried out measurements of ammonia and ethylene using a QC laser operating at  $970 \text{ cm}^{-1}$ , in both intra-pulse mode and inter-pulse mode [8]. They concluded that the intra-pulse method gave a wider tuning range, either allowing broader lines or more lines to be probed, while the resolution was also better, and could be improved yet further by using a slower chirping laser. They then used the intra-pulse method to carry out measurements of ammonia in breath.

Nitric oxide in breath has been measured by laser absorption spectroscopy [9], in this case using lead salt lasers. Nitric oxide can be an indication of a variety of medical conditions including asthma and chronic obstructive pulmonary disease (COPD). Breath gas measurements are a useful medical diagnostic since they are non-invasive

and carry no risk to the patient. Methane in breath has long been known to be a possible indication of bowel cancer [10].

In addition to the measurements described in Chapter 4.2, nitrous oxide levels were measured by Famulari *et al* using a Tunable Diode Laser Absorption Spectroscopy (TDLAS) system using a lead salt laser [11]. This system has also been used to measure ammonia [12]. This method involves locking the laser to a selected absorption line. Although the laser used for the ammonia measurements was not a QC laser, the tuning method is essentially the inter-pulse tuning method described in Chapter 2.3, using a subthreshold current ramp. The system is computer controlled, with the recorded spectrum being examined to check for laser drift which can then be corrected to ensure the tuning remains accurate. Although the system contains two lasers [13], each can only monitor one absorption line. A key advantage of the intra-pulse QC laser system is the ability to simultaneously measure several lines.

Another TDLAS system has been used by Pihlatie *et al* to measure nitrous oxide emissions from the forest floor. As a confirmation of their results, they also used soil enclosure techniques [14] to trap nitrous oxide emissions which were later analysed by a gas chromatograph. Where measurements are not needed with high temporal resolution, this is an effective method of atmospheric analysis, and one which may be used to calibrate the QC laser spectrometer by confirming results from fieldwork.

Aircraft based measurements of  $\text{NH}_4^+$ ,  $\text{NO}_3^-$ , and  $\text{SO}_4^{2-}$  have been carried out by the Aerodyne group [15] using an aircraft based mass spectrometer. The Aerodyne group also uses QC laser systems to carry out atmospheric measurements [16]. Their spectrometers use the inter-pulse tuning method as described in Chapter 2.3, but are in all other respects very similar to the QC laser spectrometers described in this thesis. Measurements of atmospheric formaldehyde [17] have been carried out from an aircraft. A similar ground-based instrument has been used for measuring the atmospheric abundance of different isotopes of carbon dioxide [18], utilising the absorption lines around  $2310\text{ cm}^{-1}$ . By switching to a laser operating around  $1274\text{ cm}^{-1}$ , nitrous oxide and methane have also been measured [19].

QC laser spectroscopy, again using the more common inter-pulse tuning method, has also been applied to measurements of the gases present within cigarette smoke [20], with the simultaneous measurements of multiple species paving the way for a detailed investigation of cigarette burning and pyrolysis processes.

Joly *et al* have also carried out atmospheric methane and nitrous oxide measurements in this region [21], which has a number of methane, nitrous oxide and water lines to measure in a relatively narrow region of the spectrum. They used a continuous wave (CW) QC laser operating around  $1270\text{ cm}^{-1}$ , tuned by a subthreshold current ramp to record the spectra of gases in a multipass cell.

A potential method of detecting explosives [22] uses CW QC lasers, either in a stand-off setup, searching for trinitrotoluene (TNT), or in a fibre coupled open air cell for detection of triacetone triperoxide (TATP). The high sensitivity of a QC spectrometer is vital for explosive detection in applications such as airport screening.

Measurements of carbon dioxide in the exhaust emissions of a diesel engine have been carried out using a black body emitter at  $4.24\text{ }\mu\text{m}$ , with the light coupled into and out of a 120 mm long gas cell by optical fibres [23]. This sensor is effectively monochromatic but demonstrates the viability of measuring exhaust gases using infrared absorption. Nondispersive infrared absorption is used in commercial systems for measuring vehicular emissions during the annual MOT test.

Alternative techniques for atmospheric measurements involve the use of resonant cavities to enable long absorbing path lengths. The first of these is based upon the variation of the decay of the energy stored in the cavity after a laser pulse has been applied. This is known as cavity ringdown spectroscopy (CRDS), which has been used in a laboratory environment to record detailed spectra of methane [24], and has also been applied in field measurements of nitrous oxide and nitric oxide in the exhaust emissions of a diesel engine [25]. QC lasers have been used in CRDS measurements of ammonia in breath samples [26].

CRDS uses a narrow band of laser frequencies to measure absorption, allowing the absorption over a small frequency range to be measured with a single pulse. A spectrum is then recorded by slowly scanning the frequency of the laser source.

A related use of a similar cavity is the technique known as cavity enhanced absorption spectroscopy (CEAS). Early implementations of this method used a short scanning CW laser to couple to the modes. Alternatively, a broadband light source can be used. The output light from the cavity is either spectrally dispersed onto a photodetector using a grating or else the resultant interference pattern can instead be recorded, later to be Fourier transformed. Measurements of multiple gas species simultaneously have been carried out by Langridge *et al* using this technique [27]. This method has a very low detection limit, and is relatively simple to implement.

An extremely sensitive technique, laser induced fluorescence (LIF) is used by Prof. Dwayne Heard's Group at Leeds University in their Fluorescence Assay by Gas Expansion (FAGE) instrument [*e.g.* 28, 29]. Although this method is very sensitive, it relies on the fragmentation of a parent molecule and detects the radicals into which it fragments. Consequently molecules which do not fragment in an unambiguous way cannot be measured using this method. For those that can, where a fragmentation pathway is known, extremely low concentrations can be measured, equivalent to  $2 \times 10^{-5}$  ppb for the OH<sup>•</sup> radical, a fragmentation product of water.

Microwave radiometry is a well established technique for detecting pressure broadened atmospheric emission spectra. Aircraft based microwave radiometry measurements of ozone and water utilising a digital fast Fourier transform have been demonstrated [30, 31]. A field-programmable gate array is used to compute the Fourier transform by hardware. This approach considerably reduces the instrument's susceptibility to vibration and temperature fluctuations which can be a problem using conventional methods on board aircraft where vibration is inevitable and temperature fluctuations are common. The use of hardware to carry out calculations before data is stored could also be a logical improvement to the instrument described in this thesis.

# Chapter 2: Background Theory

## 2.1: Introduction

This chapter will discuss the background theory involved in gas sensing using QC lasers. The theory for both straightforward absorption spectroscopy and nonlinear rapid passage effects is discussed, as is the design and operation of QC lasers.

Chapter 2.2 describes the design of QC lasers and how their bandgap structure can be used to create a laser diode with a customised wavelength to suit specific applications.

Chapter 2.3 introduces the two main methods of tuning QC lasers, inter-pulse tuning and intra-pulse tuning, and discusses the advantages and disadvantages of each method.

Chapter 2.4 discusses absorption spectroscopy, conditions where straightforward linear absorption is and is not an acceptable approximation and the effects of pressure on lineshape.

Chapter 2.5 introduces the nonlinear behaviour of absorption at low pressure and / or high chirp rate, known as rapid passage, and describes the history of observations of this effect.

## 2.2: What is a QC Laser?

The QC laser was first proposed in 1971 by Kazarinov and Suris [32], although it was not until twenty years later that the first QC lasers were fabricated by Faist, Capasso, Sivco, *et al* [33]. In the intervening years, huge progress had been made in methods of manufacturing semiconductor devices. QC lasers are manufactured using methods originally developed for the telecommunications industry. It was the use of Molecular Beam Epitaxy (MBE) [34] which was capable of depositing sufficiently thin layers during semiconductor manufacture that enabled fabrication of a QC laser.

A QC laser is a semiconductor laser diode, the emission wavelength of which does not depend on the bandgap of the semiconductor material used. Instead, alternate layers of different semiconductor materials are used to build a set of square quantum well potentials into the conduction band, which are then offset by the application of an electric field. The resultant conduction band is shown in Figure 2.2.1.

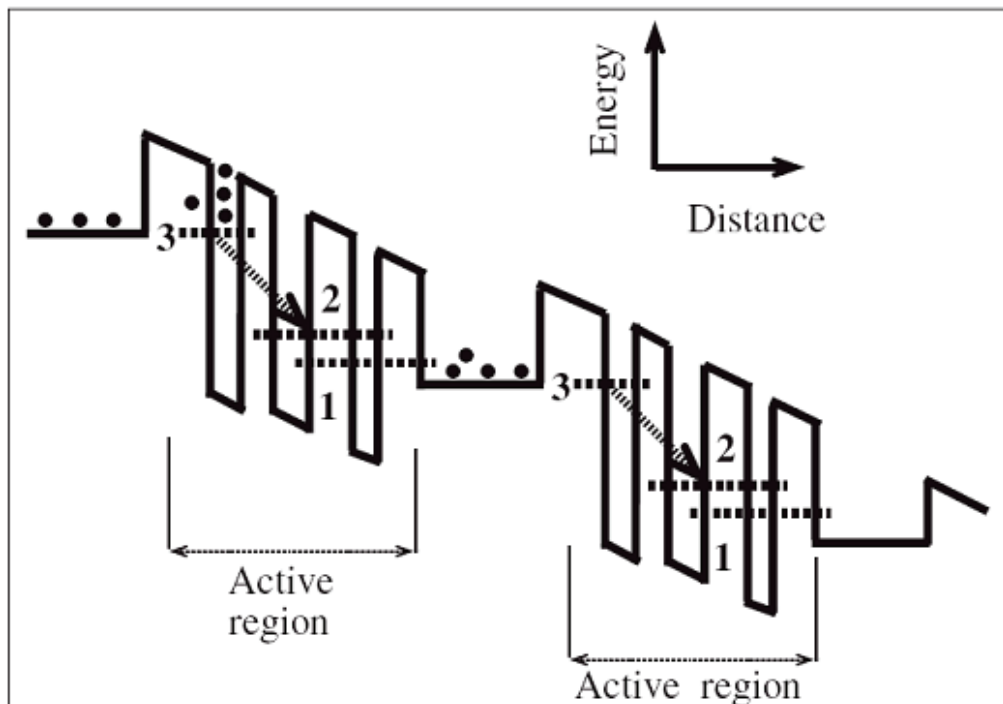


Figure 2.2.1: Energy-level diagram of the conduction band of a QC laser. Electrons are injected to the  $n=3$  level, the laser transition takes them down to  $n=2$  which is depleted by relaxation to  $n=1$ . They then transfer to the next injection region from which the cascade repeats. (After [33]).



The adjacent wells effectively give a 3-level laser system. Electrons start in an injection band, from which they are injected into level 3. Light is emitted when they make the transition from level 3 to level 2. They then rapidly relax, falling into level 1. This is coupled to the next injection band, and the cascade repeats in the next set of quantum wells.

The original QC lasers [33] were grown with up to 25 identical steps in the cascade by molecular beam epitaxy, the barrier layers between wells consisting of  $\text{Al}_{0.6}\text{In}_{0.4}\text{As}$  and the wells consisting of  $\text{Ga}_{0.38}\text{In}_{0.62}\text{As}$ . This produced a laser operating at a wavelength of  $4.26\ \mu\text{m}$  with an energy separation of 295 meV.

Since then there has been a huge increase in available wavelengths, with QC lasers now capable of operating in the terahertz region of the spectrum (over  $100\ \mu\text{m}$ ) now possible [e.g. 35]. The laser used for the majority of this work was an  $8\ \mu\text{m}$  QC laser, supplied by Alpes Laser.

One of the main uses of QC lasers has been as a "drop-in" replacement for lead salt lasers, pulsed QC lasers being capable of operating at room temperature. QC lasers have a very narrow instantaneous linewidth as their optical transitions are intersubband, not band to band as in a conventional semiconductor laser diode. This means that the two levels involved in the transition are parallel, so transitions off the band centre still have the same wavelength (see Figure 2.2.2).

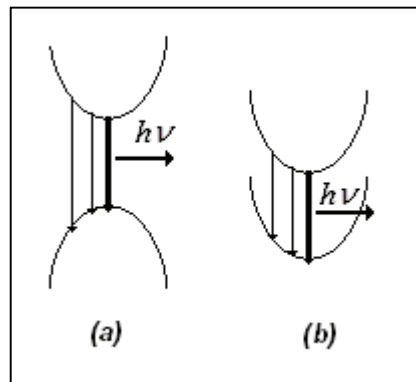


Figure 2.2.2: Lasing transitions in (a) a conventional semiconductor laser and (b) a QC laser.

QC lasers also have a higher output power than lead salt lasers, and have an

approximately symmetric gain profile. This makes it possible to carry out measurements which require high power, narrow linewidth and tuneability; including sensitive atmospheric measurements and sub-Doppler saturation spectroscopy.

Currently, room-temperature pulsed QC lasers and liquid nitrogen cooled CW QC lasers are commonplace and room temperature CW lasers are now also becoming available [36, 37, 38].

The wavelength of most QC lasers is set by a distributed feedback method, consisting of a grating etched into the laser waveguide to force the cavity standing wave to a specific wavelength. This additionally allows higher harmonics (see Chapter 3.3: Laser 61 Bistability for an example), which are eliminated by the inclusion of a  $2\lambda$  wide fringe in the grating to block harmonics.

As the laser is heated or cooled, the grating expands or contracts, changing the wavelength which it imposes on the laser. The heating can be very quick if caused by Joule heating of the device with the application of a long current pulse, or more gradual if caused by changing the temperature of the device using an external method such as a Peltier cooler. These different methods of heating the laser are compared in Chapter 2.3.

This sweeping change in wavelength is known as a frequency chirp. Experiments carried out by Faist *et al* [39] demonstrated that during the rapid sweep to lower frequency caused by the application of a long current pulse, the laser maintained the very narrow linewidth, as anticipated from the calculated behaviour of QC lasers. In early QC lasers, the application of a 100 ns current pulse was enough to heat the active region by up to 20 °C, causing a rapid change in the refractive index.

The various lasers used during this work typically produce a frequency downchirp of  $3.5 \text{ cm}^{-1}$  (around  $1 \times 10^6 \text{ MHz}$ ) when a 1300 ns current pulse is applied, with the Peltier cooler set at 0 °C. Individual lasers have widely varying chirp rates between 72.4 MHz/ns and 362.17 MHz/ns at the start of the pulse.

### 2.3: Inter- and Intra-Pulse Tuning

Most pulsed QC laser spectrometers are operated using the inter-pulse method pioneered by Namjou *et al* [40]. Essentially, a subthreshold current ramp is superimposed on the pulsed waveform which drives the pulsed operation of the laser. The subthreshold ramp heats the laser, so each pulse is at a different wavelength from the one before. Namjou *et al* used 11 ns pulses to reduce the frequency chirp as far as possible, and used the subthreshold current ramp to increase the wavenumber by approximately  $1 \text{ cm}^{-1}$  between pulses.

Kosterev *et al* [41] used a variation on the inter-pulse technique which they referred to as the "slow scan" method, adjusting the laser temperature rather than the current to create the tuning. This allows wider spectral coverage than the use of a subthreshold current ramp, however owing to the bulk of the laser and heatsink, rapid temperature tuning is not possible and this technique takes 25.5 ms to record a spectrum, consisting of 510 scans averaged together. This is comparable to the performance which can now be achieved by averaging 500 pulses using the intra-pulse tuning method. The systems used throughout most of this work required considerably more averaging, in the region of 10,000 averages.

An alternative method, which forms the basis of our spectrometer system, is the intra-pulse method, pioneered by Normand *et al* [42]. A longer pulse (1300 ns for most of the work described in this thesis) is applied to the laser, and there is no subthreshold ramp. The long pulse results in the laser being heated during its lasing. This causes a frequency downchirp as discussed before, which scans the laser frequency. To successfully resolve the absorption lines, a fast, high bandwidth detector and amplifier are required. The digitiser used to feed the signal to computer must be capable of running at the speed of the fast detector.

The inter-pulse method has the disadvantage that shot-to-shot noise in the laser pulses will affect subsequent points in a spectrum while the intra-pulse method has the ability to record a wide spectrum with a single pulse. With both methods it is

necessary to average several spectra to reduce the full-spectrum noise.

The intra-pulse tuning method gives a wider tuneable range than that achievable using the inter-pulse tuning method. The detector system resolution is set by the time-bandwidth product of the detected signal [43], and the chirp rate of the laser, hence the slowing of the chirp causes variable resolution across the pulse. This results in absorption features near the start of the pulse being poorly resolved compared to these at the end, which can be a minor disadvantage of this method.

An intermediate method using medium length (50 ns – 100 ns) pulses combined with temperature tuning has recently been developed by Grouiez *et al* [44]. This effectively uses medium pulses to record spectra by the intra-pulse tuning method, while also shifting the lasing frequency by temperature tuning. Applying a 12 °C temperature ramp allows the laser to scan through 0.5 cm<sup>-1</sup>, while each pulse also exhibits a frequency downchirp such that different spectra can be viewed by looking at different points in the pulse across the whole temperature scan. This method does not remove the variable resolution between the start and the end of pulses, moreover the temperature tuning makes it inherently slow.

Our use of the intra-pulse method allows us to obtain one spectrum in 1300 ns, covering between 1.6 cm<sup>-1</sup> and 5 cm<sup>-1</sup>, depending on the laser used. To reduce the noise, many of these spectra are then averaged together. Running at typical pulse repetition rate of 10 kHz and averaging 10,000 spectra allows us to obtain very high quality averaged spectra at a rate of one per second. For faster recording, frequencies up to 20 kHz have been used. Recording fewer averages also speeds up the acquisition rate, although the spectra are obviously noisier. The number of averages used is therefore picked as a compromise between fast acquisition and high signal-to-noise ratio. The fast acquisition rate is the most important feature of our laser spectrometer when used in-flight where rapid changes in atmospheric gas mixing ratios are likely.

The resolution of a QC laser based spectrometer is similar, regardless of whether the

inter-pulse method or the intra-pulse method is used [45]. Using the inter-pulse tuning method, the resolution limit is set by the transform limit (time-bandwidth product) of the pulse. Kosterev *et al* [41] have shown that the majority (75%) of their laser energy lies within the transform limit. Analysis of the spectral line shapes observed revealed that it is possible to obtain a resolution (full-width-at-half-maximum, FWHM) of  $9.5 \times 10^{-3} \text{ cm}^{-1}$ .

With the intra-pulse method, the detector system resolution is set by the time-bandwidth product of the detected signal [43], and the chirp rate of the laser, hence the variable resolution across the pulse.

In both methods, the time-bandwidth product has been demonstrated for a Gaussian time window [46] to have a minimum value:

$$\Delta t \Delta \nu \geq C = 0.441 \quad (2.3.1)$$

where  $\Delta t$  is time,  $\Delta \nu$  is bandwidth and for a rectangular window,  $C = 0.886$ . This is a restatement of the Heisenberg Uncertainty Principle [47] in terms of time and frequency. Kosterev *et al* [41] have demonstrated that their  $9.5 \times 10^{-3} \text{ cm}^{-1}$  (285 MHz) resolution cannot be improved upon by changing the pulse length.

Similarly, McCulloch *et al* [43] have shown that the chirp rate resolution limit is given by

$$\Delta \nu = \sqrt{C \frac{d\nu}{dt}} \quad (2.3.2)$$

where  $\frac{d\nu}{dt}$  is the laser chirp rate. Using a chirp rate of 200 MHz/ns, which is a fairly typical chirp rate for the start of the pulse for the lasers used, the resolution would be  $0.015 \text{ cm}^{-1}$  (450 MHz). Over the course of a laser pulse, the chirp rate slows, and hence the resolution improves. At the end of the pulse, the slowest chirping lasers can reach chirp rates slightly less than 20 MHz/ns, which corresponds to a resolution of  $0.0044 \text{ cm}^{-1}$  (132 MHz), which is on a par with many Fourier Transform Spectrometers.

Figure 2.3.1 illustrates a spectrum of  $\text{CH}_3\text{CF}_3$ , recorded by a previous student using a Bruker Fourier Transform Spectrometer (FTS) at Rutherford Appleton Laboratory (RAL), compared to that recorded using the original  $8\ \mu\text{m}$  QC laser which reached a chirp rate of  $33\ \text{MHz/ns}$  at the end of the pulse (the low wavenumber end of the spectrum). This gives a resolution of  $0.006\ \text{cm}^{-1}$  ( $180\ \text{MHz}$ ).

The series of lines which make 1,1,1-trifluoroethane act as a "molecular ruler" can be resolved by the QC laser spectrometer nearly as well as the FTS.

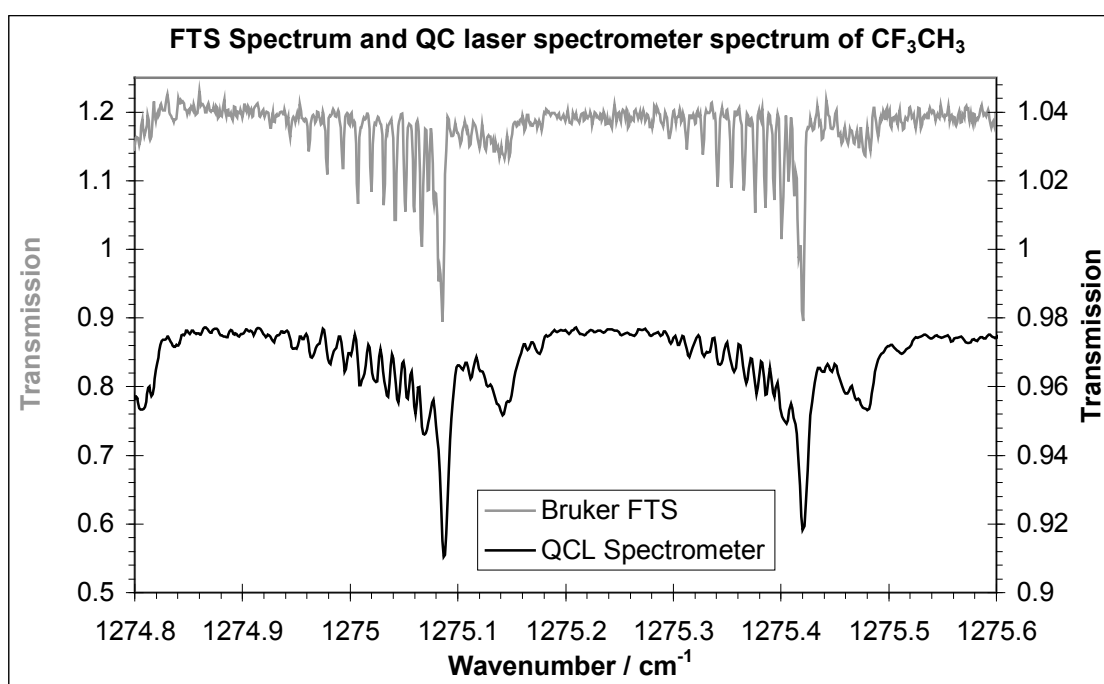


Figure 2.3.1: FTS and QC laser spectrometer spectra of 1,1,1-trifluoroethane. The QC laser spectrometer has a resolution of  $0.006\ \text{cm}^{-1}$  at the end of the pulse, which is the low frequency end of the spectrum. The Bruker FTS had a resolution of  $0.0018\ \text{cm}^{-1}$ .

The possibility of using such good resolution, coupled with the ability to record spectra in short timescales and the simplicity of the system gave us strong grounds for using the intra-pulse tuning method which has fewer disadvantages than the inter-pulse alternative.

## 2.4: Absorption Spectroscopy

The quantum mechanical description of a molecule is given by its eigenfunction  $\psi$ . Each eigenfunction describes a permitted energy level for the molecule to occupy. As only certain energies are permitted levels, transitions between permitted levels have fixed energy differences, corresponding to absorption of light at specific wavelengths. This is the basis of absorption spectroscopy.

For a linear molecule, the total eigenfunction is given by the product of the eigenfunctions for that molecule's electronic, vibrational and rotational eigenfunctions, that is

$$\Psi = \psi_e \psi_v \psi_r \quad (2.4.1)$$

Each rotational J level can be described as symmetry negative or positive, depending upon whether reflection of all particles within the molecule changes the sign of  $\psi$  or leaves it unaltered.

For all known linear molecule ground states,  $\psi_e$  and  $\psi_v$  are unaltered by reflection and hence the symmetry behaviour of the molecule only depends upon the symmetry behaviour of  $\psi_r$ . Where the molecule has a centre of symmetry, such as  $C_2H_2$ , in addition to the symmetry positive/negative behaviour described above, the rotational levels can be described as symmetric or antisymmetric if the sign of  $\psi$  remains constant or changes when the nuclei on one side of the centre of symmetry are exchanged with the nuclei on the other side.

As illustrated in Figure 2.4.1, either the positive levels are symmetric and the negative antisymmetric, or vice versa.

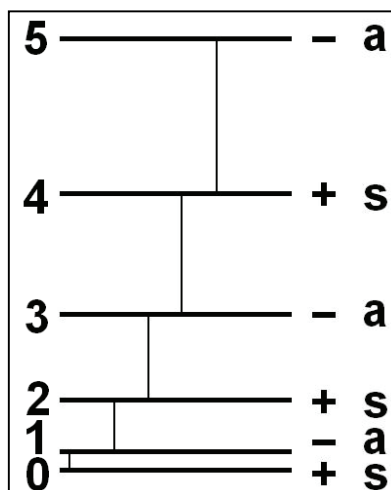


Figure 2.4.1: Rotational energy level diagram for a typical linear molecule, illustrating positive symmetric and negative antisymmetric states for alternate J values. After [48].

Where a molecule has a centre of symmetry, in addition to alternate energy levels having different positive/negative symmetry, they also have alternating statistical weights caused by the effect of nuclear spin.

The population,  $N_J$ , of the rotational energy levels is given by:

$$N_J \approx g_J e^{-\left(\frac{E_r}{kT}\right)} \quad (2.4.2)$$

where  $g_J$  is the statistical weight;  $E_r$  is the rotational energy in erg;  $k$  is Boltzmann's constant and  $T$  is the absolute temperature in Kelvin.

A transition between levels due to dipole radiation can only occur if the molecule has a permanent dipole moment. Transitions can only take place between levels with opposite sign symmetry, and the change in rotational energy must be  $\Delta J = \pm 1$ . This is illustrated in Figure 2.4.2, which shows the permitted transitions in a linear molecule between two vibrational states, each with associated rotational levels.



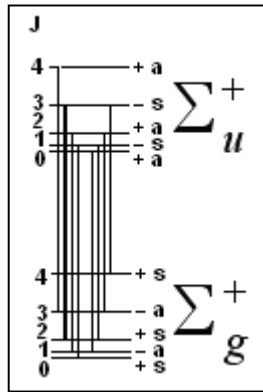


Figure 2.4.2: Schematic diagram of the permitted transitions between rotational levels of successive vibrational states of a linear molecule such as  $N_2O$ . The  $J=3$  to  $J=2$  transition shown in bold is used as an example of a 2-level system.

The levels a transition takes place between can be assumed to make up a 2-level system, independently of the rest of the molecule. This assumption neglects the effects of collisional coupling of molecules between different vibration-rotation energy levels. In Figure 2.4.2, treating the  $J=2$  to  $J=3$  transition between the  $\Sigma_g^+$  and  $\Sigma_u^+$  levels as a two level system, only the  $\Sigma_u^+ J=3$  and  $\Sigma_g^+ J=2$  levels would be considered.

When a laser of linear polarisation is in interaction with a gas, assuming that the laser is of sufficiently low intensity that it does not perturb the gas being studied, two processes occur:

Treating the transition as a 2-level system, absorption of photons excites molecules to the upper state, tending to equalize the upper and lower state populations. The upper state has a lifetime  $T_1$ , known as the transverse relaxation time. This is the time taken for the population of an upper state molecule to deexcite. Absorption depends upon the population difference between the two levels, so the populations can be equalized at best.

As QC lasers are linearly polarised, selective pumping of the differently polarized  $M_J$  components leads to the gas becoming polarized. The transition dipole moment is dephased in the longitudinal relaxation time  $T_2$ , destroying the polarization of the

gas.

Under normal circumstances where the reaction time of the molecule to the light is greater than both transverse and longitudinal relaxation times and provided saturation does not occur, absorption is described by the Beer-Lambert Law:

$$I = I_0 e^{-\alpha l} \quad (2.4.3)$$

where  $I$  is the intensity of the laser following absorption;  $I_0$  is the initial intensity of the laser;  $P$  is the partial pressure of the gas being studied;  $l$  is the optical path length and  $\alpha$  is given by:

$$\alpha = NSg(\nu - \nu_0) \quad (2.4.4)$$

where  $N$  is the number of absorbing molecules per atmosphere, measured in  $\text{cm}^{-3}\text{atm}^{-1}$ ;  $S$  is the line intensity, measured in  $\text{mol}^{-1}\text{cm}$  and  $g(\nu - \nu_0)$  is the lineshape function, with  $\nu_0$  the line centre. For a transition between levels  $i$  and  $j$ , assuming the transition is a 2-level system,  $S$  is  $s_{ij}$  in HITRAN, the **high resolution transmission** database of absorption lines, maintained by Rothman *et al* [49].

At high pressure, or with strong lines, saturation can occur which renders the Beer-Lambert law invalid. As a line nears 100% absorption, the number of absorbing molecules becomes greater than the number of photons available. Consequently all incident photons are absorbed, while there are still molecules in the lower state. This makes the linear relation between absorption and concentration invalid, described as absorption saturation.

At low pressures, or high chirp rates, absorption lines become asymmetric and develop an emission spike following the absorption. This effect, known as rapid passage, is described in more detail in Chapter 2.5. Under these circumstances, the linear assumption is also invalid.

Within the linear regime, the lineshape will be one of 3 possible cases. Under low pressure (but not so low as to induce rapid passage effects), the dominant source of broadening is Doppler broadening. This arises from the fact that different molecules

within the gas have different velocities relative to the laser beam. The Doppler lineshape is a Gaussian of the form:

$$g(\nu - \nu_0) = \frac{1}{\delta\sqrt{\pi}} e^{-\left(\frac{\nu - \nu_0}{\delta}\right)^2} \quad (2.4.5)$$

where

$$\delta = \frac{\nu_0}{c} \sqrt{\frac{2kT}{M}} \quad (2.4.6)$$

where  $\nu_0$  is the line centre;  $c$  is the speed of light;  $k$  is Boltzmann's constant;  $T$  is the absolute temperature in Kelvin and  $M$  is the mass of the absorbing molecule. This Gaussian has a full width at half maximum (FWHM) of  $2\delta\sqrt{\ln 2}$ .

The different velocity components can be modelled as illustrated in Figure 2.4.3. A series of Lorentzian lines are used, with the Doppler broadening being created by the Gaussian "envelope" enclosing them.

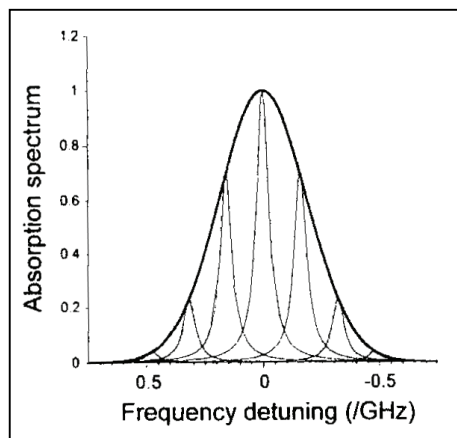


Figure 2.4.3: Schematic diagram of the modelling of the different velocity molecules within a gas. The Lorentzian lines represent different velocity components. In the interests of clarity, only seven are shown

As the laser chirps through the line, each individual component is interrogated in turn, with the observed lineshape being the sum of the lineshape from each Doppler component.

At higher pressure, whether the increase in pressure is a result of adding the gas under discussion, or some foreign gas, the pressure broadening dominates. This leads

to a Lorentzian lineshape of the form:

$$g(\nu - \nu_0) = \frac{1/\gamma_L}{(\nu - \nu_0)^2 + \gamma_L^2} \quad (2.4.7)$$

where the FWHM is given by:

$$\gamma_L = (\gamma_s P_s + \gamma_f P_f) \sqrt{\frac{T_0}{T}} \quad (2.4.8)$$

where  $\gamma_s$  and  $\gamma_f$  are the self-broadening and foreign gas broadening coefficients respectively;  $P_s$  and  $P_f$  are the partial pressures of the gas being studied and the foreign gas respectively;  $T$  is the temperature and  $T_0$  is a reference temperature for an unbroadened line. In HITRAN [49], the reference temperature is 296 K.

At intermediate pressures, both the Doppler broadening and pressure broadening contribute to the lineshape which is therefore a convolution of a Gaussian and a Lorentzian. This is known as the Voigt profile, and has the form

$$g(\nu - \nu_0) = \frac{Bx}{\pi} \int_{-\infty}^{\infty} \frac{e^{-y^2}}{x^2 + (z - y)^2} dy \quad (2.4.9)$$

where

$$B = \frac{1}{\gamma_G} \sqrt{\frac{\ln 2}{\pi}} \quad (2.4.10)$$

$$x = \frac{\gamma_L}{\gamma_G} \sqrt{\ln 2} \quad (2.4.11)$$

$$z = \frac{\nu - \nu_0}{\gamma_G} \sqrt{\ln 2} \quad (2.4.12)$$

where  $\gamma_G$  and  $\gamma_L$  are the Gaussian and Lorentzian FWHMs.

In practice, for most of this work, the pressure has been deliberately selected to remain within the pressure broadened regime so that a Lorentzian approximation can be used since the Voigt profile is more complicated to fit in LabVIEW. The only low-pressure atmospheric work attempted so far has been the work at Penicuiik measuring nitrous oxide (See Chapter 4.2), where the lines were fitted with a Gaussian lineshape.

Using the intra-pulse method, where the chirp rate is sufficiently high and the gas pressure is sufficiently low, absorption lines exhibit behaviour known as rapid passage [50], initially visible as an asymmetric lineshape, or in more extreme cases, an emission spike following the absorption can be observed. Investigations into rapid passage have been carried out where the absorption is nonlinear. The theory behind rapid passage is discussed in Chapter 2.5.

## 2.5: Rapid Passage

Rapid passage effects and free induction decay (FID) were first seen in magnetic resonance experiments, which have been described in great detail by Ernst [51]. Their optical equivalents in infrared absorption spectroscopy were first observed in the period from 1960 to 1980, mainly making use of high power line-tuneable carbon dioxide lasers [52, 53]. Given the very narrow tuning range of these lasers, tuning the molecule was instead accomplished by electric field tuning of the  $M_J$  components of a vibration-rotation transition. This was used to achieve resonance with a particular laser line.

These early experiments were followed by experiments which made use of near-infrared diode lasers whose frequency may be swept very rapidly using fast sweep modulation of the laser current. These experiments were either targeted at studies of transient effects in the spectra of laser-cooled or trapped atoms [54, 55], or FID observed in the gas-phase spectra of atoms or molecules [56, 57], and in the solid state spectra of ions [58]. In 1998 Pietiläinen and his colleagues [55] noted that "because increasingly finer details are observed in the optical spectra of atomic samples, coherent transients are nearly unavoidable in frequency sweep experiments".

The typical approach to this process is based on the Maxwell-Bloch Equations [59], which are derived from the Bloch vector approach to NMR.

When light of the correct frequency passes through resonance with an absorption line, the light is absorbed, moving molecules into an excited state. The dipole moment of the transition then dephases with a characteristic time, known as the longitudinal relaxation time. Similarly, the electrons within the excited state decay to a lower state by collisional deexcitation within a characteristic time known as the transverse relaxation time.

If the interaction time between the laser and the molecule is less than both the

transverse and longitudinal relaxation times, there is therefore no collisional deexcitation or dephasing and rapid passage can occur. This occurs either with a very fast scan through the absorption wavelength, or at low pressure where collisions are less frequent.

In this case, there is coherent transfer of population between the levels, with the system oscillating at the Rabi frequency. This effectively aligns the gas molecules with the polarisation of the laser light. Once the gas has finished absorbing, it emits light as the molecules de-excite, leading to the spike following the main absorption, illustrated in Figure 2.5.1.

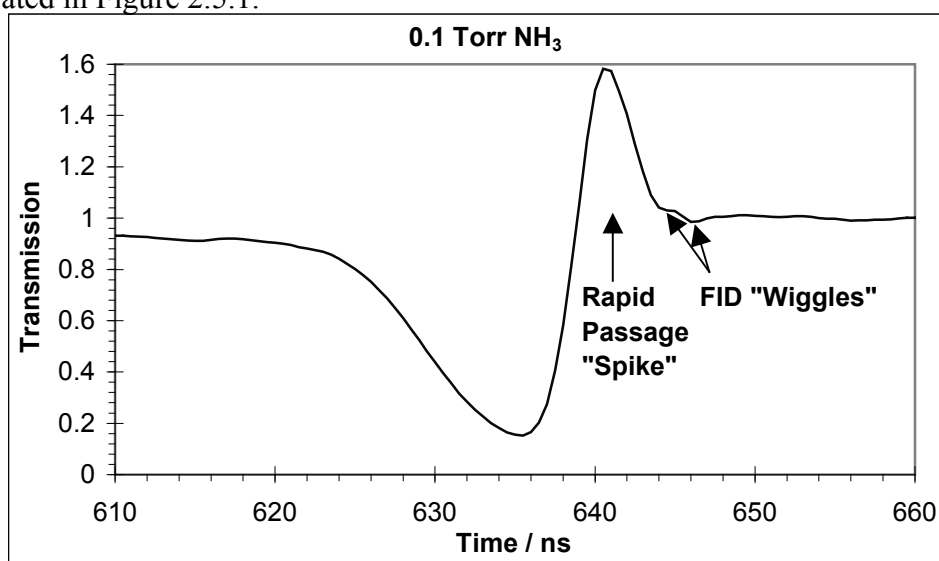


Figure 2.5.1: The characteristic line shape of rapid passage: The rapid passage "spike" and Free Induction Decay "wiggles". This was absorption by 0.1 Torr of ammonia, with an absorption line at  $1627.05\text{cm}^{-1}$ . The signal was recorded with 0.5 ns between points.

Also visible in Figure 2.5.1 are "wiggles" on the decaying tail of the emission spike. These are Free Induction Decay (FID) signals. When the laser pulse excites a group of molecules, a phased array of oscillating dipole moments is created. After the pulse, the dipoles continue to rotate and oscillate. As the polarisation of the gas decays and the dipole moments precess, FID wiggles are created by the precession.

The effects of rapid passage make accurate calculation of gas levels difficult, so for most measurement work a cell pressure of 100 Torr has been used to avoid these lineshapes.

## **2.6: Conclusion**

The theory behind the QC laser spectrometer is very straightforward while conventional absorption occurs. It can become more complicated where rapid passage effects are involved for which reason it is important to choose suitable cell pressure and/or chirp rates to ensure normal absorption is occurring.



## Chapter 3: About The Instruments

### 3.1: Introduction

This chapter describes three astigmatic Herriott Cell gas spectrometer systems, and different lasers and detectors used throughout this work. The conversion of recorded signals to calibrated spectra is also described, as is the software written to carry out the analysis. The software to control the portable spectrometer is also explained.

Chapter 3.2 describes the three Herriott cells, along with the different laser systems, photodetectors and amplifiers used and the pressure control / gas selection system.

Chapter 3.3 describes the analysis of recorded signals and the method used to convert them to calibrated transmission spectra using background and etalon signals.

Chapter 3.4 describes some bizarre effects on spectral lines caused by jitter and lack of power in the new laser drive box, and analysis of them to troubleshoot the system.

Chapter 3.5 describes the characterisation of 5 QC lasers acquired for testing through the ACCORD (Advanced Components Cooperation for Optoelectronics Research & Development) program. The original 8  $\mu\text{m}$  laser was similarly tested as a control. After the failure of this laser, its replacement was also put through the same checks.

Chapter 3.6 describes the spectrometer LabVIEW control software, initially written by previous students. For this work, it has been considerably de-bugged, and adapted to cope with both high-speed data acquisition, and running with new laser software.

Chapter 3.7 describes the development and operation of software to accomplish the analysis of recorded signals.

Chapter 3.8 describes the Cascade Technologies 4-laser spectrometer which was acquired during my final year. It is essentially a miniaturised version of the other setups, condensed into a single box run by a laptop.

### 3.2: Instrument Design

The general design of all the laser spectrometer systems used for this work was the same, although various QC lasers, laser drive systems and detectors were interchanged between setups. Both systems could use a computer driven pressure control/valve board to control pressure automatically. The 4-laser Cascade Technologies spectrometer is described separately in Chapter 3.5, as it remained as a complete unit, even through its modifications. It used its own built-in pressure control.

A simple schematic of a Herriott cell and the laser beam paths is shown in Figure 3.2.1.

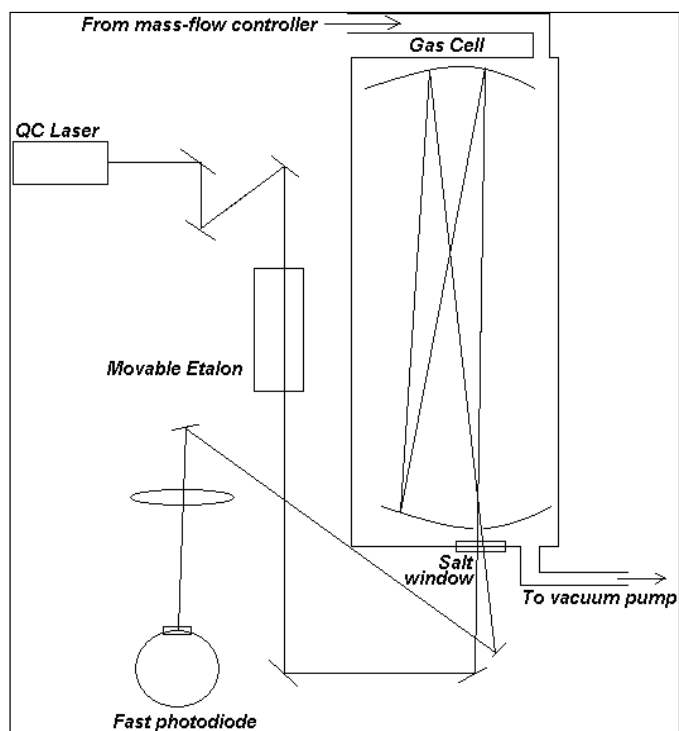


Figure 3.2.1: A simplified drawing of the instrument. The 4-laser system uses the same general design, but has four parallel lasers where the other instruments have only one.

The calibration of the wavenumber scale for all work was carried out using the fringes from a germanium etalon to determine relative wavenumber. This was then converted to absolute wavenumber using the positions of the absorption lines given by HITRAN [49], as discussed in Chapter 3.3.

## Laser Systems

Initially, the laser used was an 8  $\mu\text{m}$  QC laser bought from Alpes Laser and operated by a Cascade Technologies LS-01-D control system. This system was known as "the brick". Later, when the control system failed, this laser was installed in a newer Cascade Technologies LS-03-D system.

Some work on nitric oxide was carried out using a 5  $\mu\text{m}$  QC laser, also supplied by Alpes Laser. It was driven by a Cascade Technologies LS-03-D laser system. This laser was only used a little, but the system later had the 8  $\mu\text{m}$  laser installed when its control system failed. This drive box had some very strange effects on the resolution and lineshape of the laser caused by jitter and a lack of power, which are discussed in detail in Chapter 3.4.

During my final year, 5 QC lasers were supplied by Cascade Technologies through the ACCORD program for testing and evaluation. We also bought a new 8  $\mu\text{m}$  laser from Cascade to replace the original one when it failed. All these lasers were operated by Cascade Technologies LS-03-D laser systems.

The characteristics of all 8 lasers are described in more detail in Chapter 3.5.

## Optical Setup

The QC laser beam is passed through a multipass astigmatic Herriott cell [3] enclosed in a gas chamber. This allows an optical path through a sample gas of up to 99.6 m to be fitted into a space around 50 cm long. For atmospheric gas measurements, the cell was typically kept at a pressure of 100 Torr. The path length allows relatively weak lines such as the water vapour line at  $1275.66\text{ cm}^{-1}$  to be observed. The astigmatic mirrors also refocus the laser beam on each pass of the cell, preventing it from excessive divergence.

The cells used for this work are based on a design by McManus *et al* [60]. The parabolic mirrors have X and Y radii of curvature 77.274 cm and 67.425 cm respectively and are separated by approximately 50 cm. Various multipass solutions

of different lengths are achievable, depending on the input beam angle and position.

The fixed cell in the laboratory which was used for rapid passage studies had a path length of 66.1 m for almost all of this work. A slightly longer path length of approximately 70 m was used briefly before the bench was rearranged to allow for 2-laser spectroscopy. At this point, the best achievable path length dropped to 40 m. This cell consisted of the two astigmatic mirrors mounted on a framework. The framework was then inserted in QVF tubing which was sealed by bolting on end plates, one with a salt window to allow the beam in and out. A photograph of this system is shown in Figure 3.2.2.

The cell used on the portable system [61] (shown in situ in the NERC ARSF aircraft [7] in Figure 3.2.3) initially had a path length of 99.6 m, however for the most recent work in flight from Gloucester Airport, and later comparisons with the Cascade 4-laser system, the best path length achieved was 62.8 m. It consists of the two astigmatic mirrors, which are fixed to mounts attached directly to the baseboard. An end chamber is then placed over each mirror and bolted to the baseboard. Between the end chambers, a thin Pyrex pipe is used to form the cell. This arrangement reduces the weight of the instrument, as well as allowing the mirrors to be adjusted if necessary by removing the cell.

The path length of each cell is measured by positioning the detector in front of the cell window and noting the time between the trigger from the drive box and the detection of the pulse. The detector is then moved to its normal position in the cell output beam and the time from trigger to pulse is again noted. The time difference between the two corresponds to the time the pulse spends within the cell. The pathlength of the cell can then be easily determined by:

$$d = tc \quad (3.2.1)$$

where  $d$  is the optical path length,  $t$  is the time spent in the cell &  $c$  is the speed of light,  $3 \times 10^8 \text{ ms}^{-1}$ .

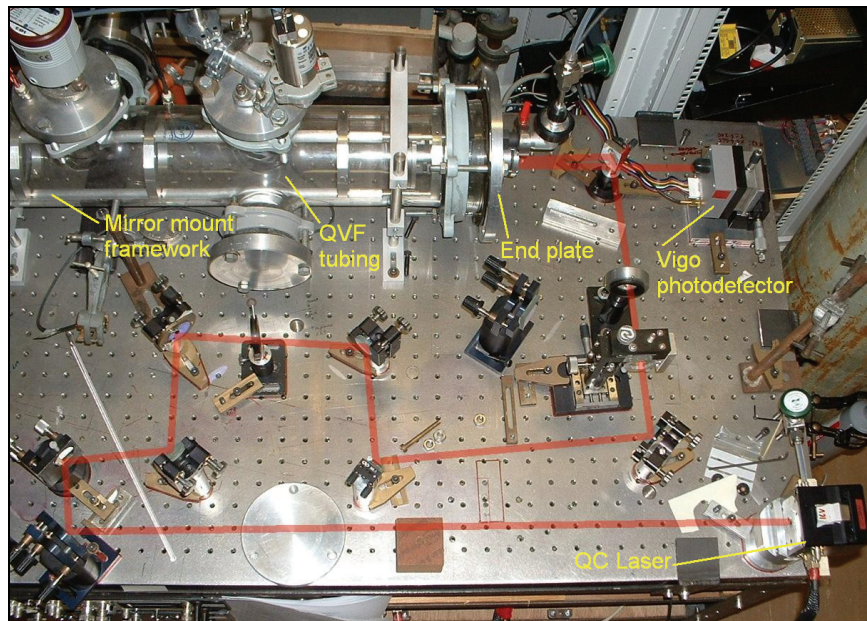


Figure 3.2.2: The fixed Herriott cell used for most of the rapid passage studies. The Herriott cell is in the top left, with MKS Baratron for pressure readout on top. One of the Cascade Technologies QC lasers is at the bottom right. The new Vigo detector is at the top right.

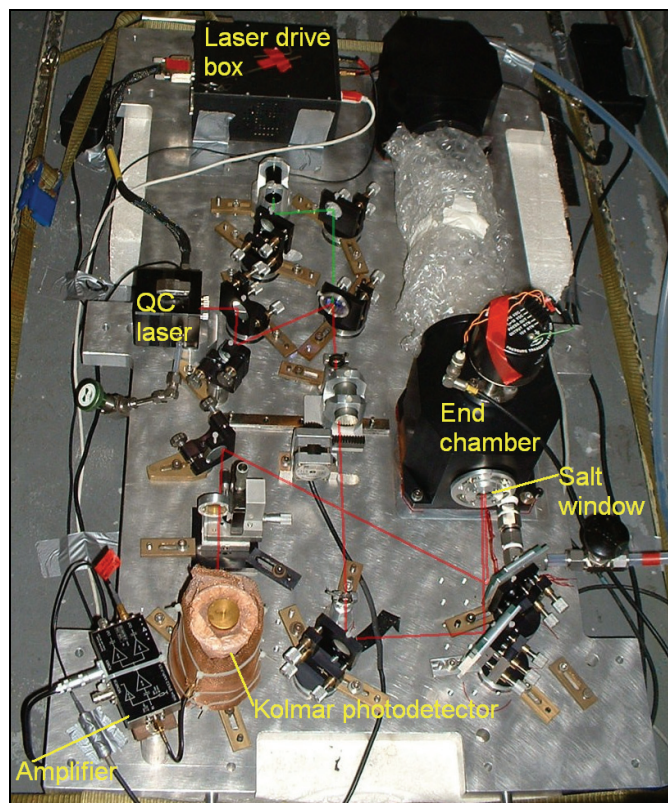


Figure 3.2.3: The portable spectrometer system, seen in situ aboard the NERC ARSF. This shows the original Cascade LS-01-D laser system (top left) and Kolmar 104 detector (bottom left). The laser beam path is shown in red and the alignment laser path in green.

## Photodetectors

Upon exiting the cell, the beam is focussed onto a photodetector.

The photodetector used initially was a liquid nitrogen cooled photovoltaic Mercury Cadmium Telluride (MCT) Kolmar 104. The signal generated was then amplified by an AC coupled amplifier of bandwidth 2 GHz. This introduced a baseline overshoot artefact, which had to be corrected as shown in Figure 3.2.4 before analysing spectra (See Chapter 3.3).

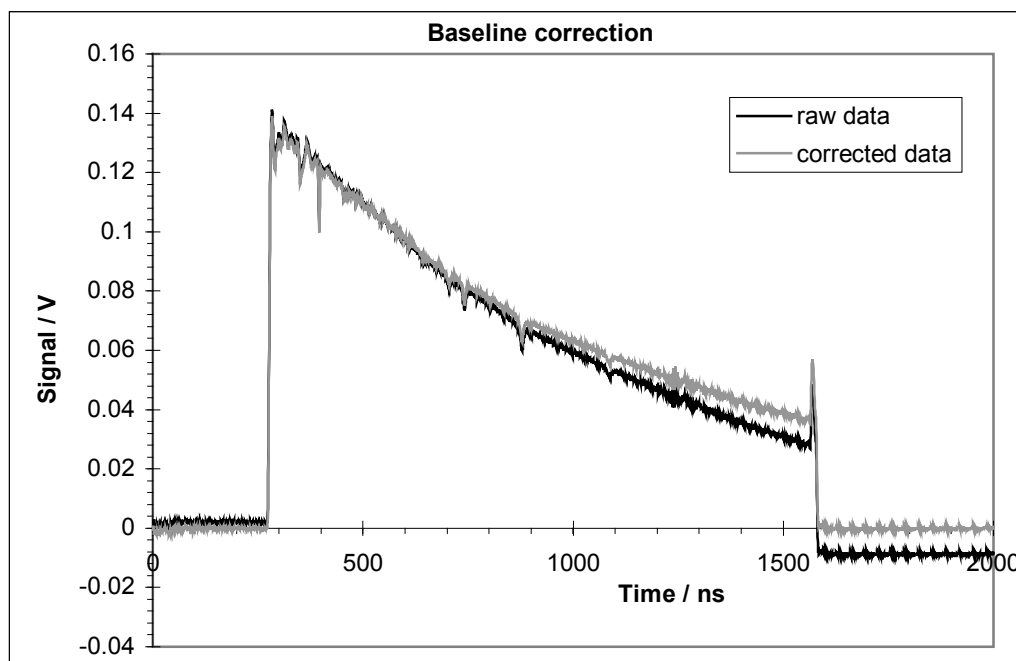


Figure 3.2.4: Raw and corrected signals. It is assumed a linear correction is required, though this assumption has not been tested. This was recorded with 100 Torr of atmosphere in the cell, using 8,000 averages of a 1300 ns pulse applied to the original 8  $\mu\text{m}$  laser.

The Kolmar detector was later replaced by two Vigo PVI-2TE-8 MCT detectors with an immersion lens and built-in amplifier with wider bandwidth. This eliminated the pulse overshoot artefact, as well as considerably improving the signal-to-noise ratio. A specimen signal from each detector is shown in Figure 3.2.5.

Owing to interference effects with an undesired back reflection, there is slight fringing visible on this particular spectrum from the Vigo, but this was eliminated from later spectra following adjustments to the optical setup.

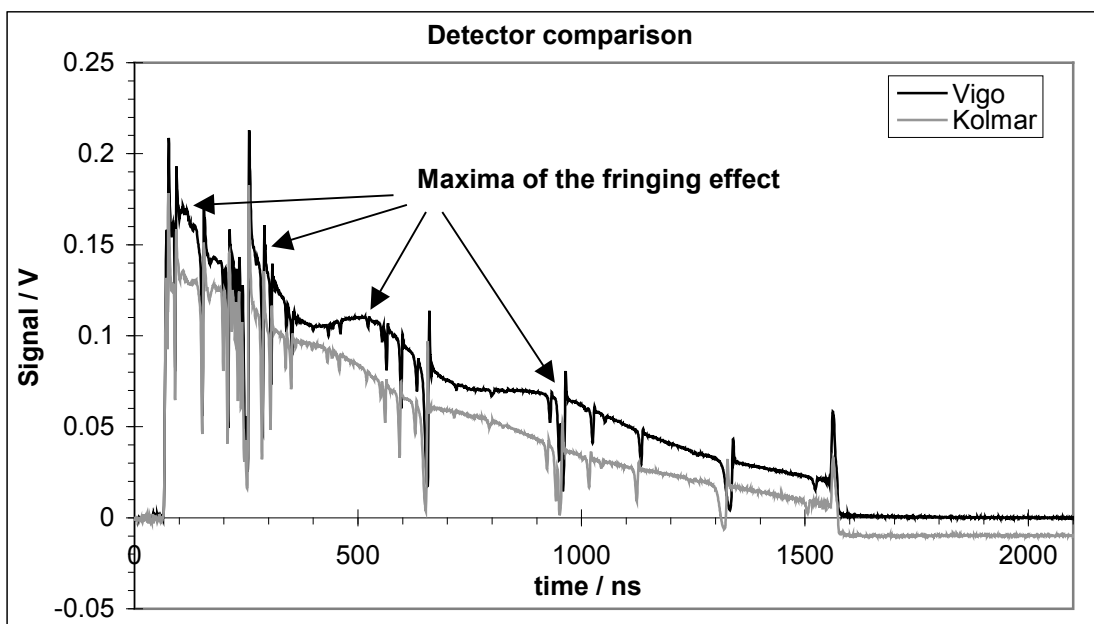


Figure 3.2.5: Sample spectra for each detector, recorded with approx. 1 Torr of acetylene, using 10,000 averages of a 1500 ns, 10.5 V pulse applied to the original 8  $\mu\text{m}$  laser.

### Digitisers

For all work, the signals from the photodetector were fed into the computer through an Acqiris AP200 fast digitiser card (0.5 ns temporal resolution, 8 bits vertical resolution) housed in a PCI slot. This was controlled from LabVIEW 7.1 virtual instruments (VIs) incorporating subVIs supplied by Acqiris (see Chapter 3.5: control software).

During my final year, two Cascade AV1500 averagers were acquired, which connected to a computer through a USB port. They could be driven using LabVIEW 8.5 VIs supplied by Cascade and later modified in house. Having adapted the software to work as required, these digitisers were never used for spectroscopy, but the software modifications are discussed in Chapter 3.6.

### Pressure Control System

The pressure control and gas selection for the cells can be carried out automatically for atmospheric work using electric valves, which are computer controlled through relays, to switch between the atmosphere and zero grade synthetic air for calibration;

and a mass-flow controller to maintain a constant pressure. The pressure control board is shown in Figure 3.2.6. The original board was built at Imperial College (Ascot Research Site) by David Brassington and his students, and has since been modified to be accommodated in a standard 19 inch computer rack although its functionality remained the same. Override switches to bypass the relays have recently been added, allowing the board to be run without a computer if necessary.

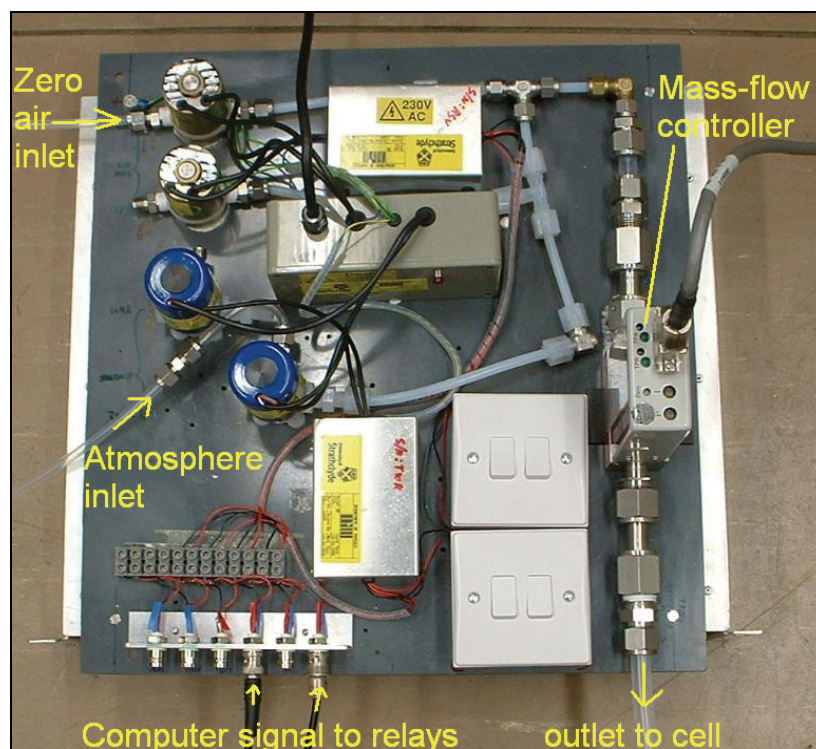


Figure 3.2.6: The pressure control/valve board. There are two single valves, and two two-way valves (left hand side), although only two of the four are used at a time. The mass-flow controller is on the right and the bypass switches at the front.

For rapid passage investigations, the cell pressure was normally controlled manually, with a simple valve between the gas and the cell and a manometer (MKS Baratron) to measure the pressure.



### 3.3: The Data Analysis Process

Throughout the work described in this thesis, the method of obtaining calibrated spectra from the recorded laser signals has remained constant. While recording a series of data, periodically a short break in data logging is taken to allow the recording of a background. The interval between backgrounds varies depending on the experiment.

During atmospheric measurements, backgrounds are usually recorded by flushing the cell through with zero air, which is a synthetic oxygen / nitrogen mix in atmospheric proportions. This removes any remaining measured gases. Once no absorption lines are visible, a signal is saved as a background. This will be saved in the same manner as a non-background spectrum, with the same laser running parameters and the same number of averages.

The backgrounds are used to convert the signals to a transmission spectrum. The transmission is taken as the signal divided by the background and makes the assumption that the laser pulse does not change significantly between the recording of a background and the recording of the final spectrum to use that background. For this assumption to be valid, the time between background scans must be carefully chosen. It is necessary to balance up the desire for as few breaks in data logging as possible with the need for spectra to match the background signal.

Initially transmission calculation was carried out during post-processing of the data, however since the Vigo detectors eliminated the baseline artefact of the Kolmar detector (See Chapter 3.2: Photodetectors), transmission spectra are now calculated during the data recording process.

Figure 3.3.1 illustrates a recorded signal, background spectrum and transmission spectrum. These are plotted in time. Conversion to wavenumber is the final stage in the analysis.

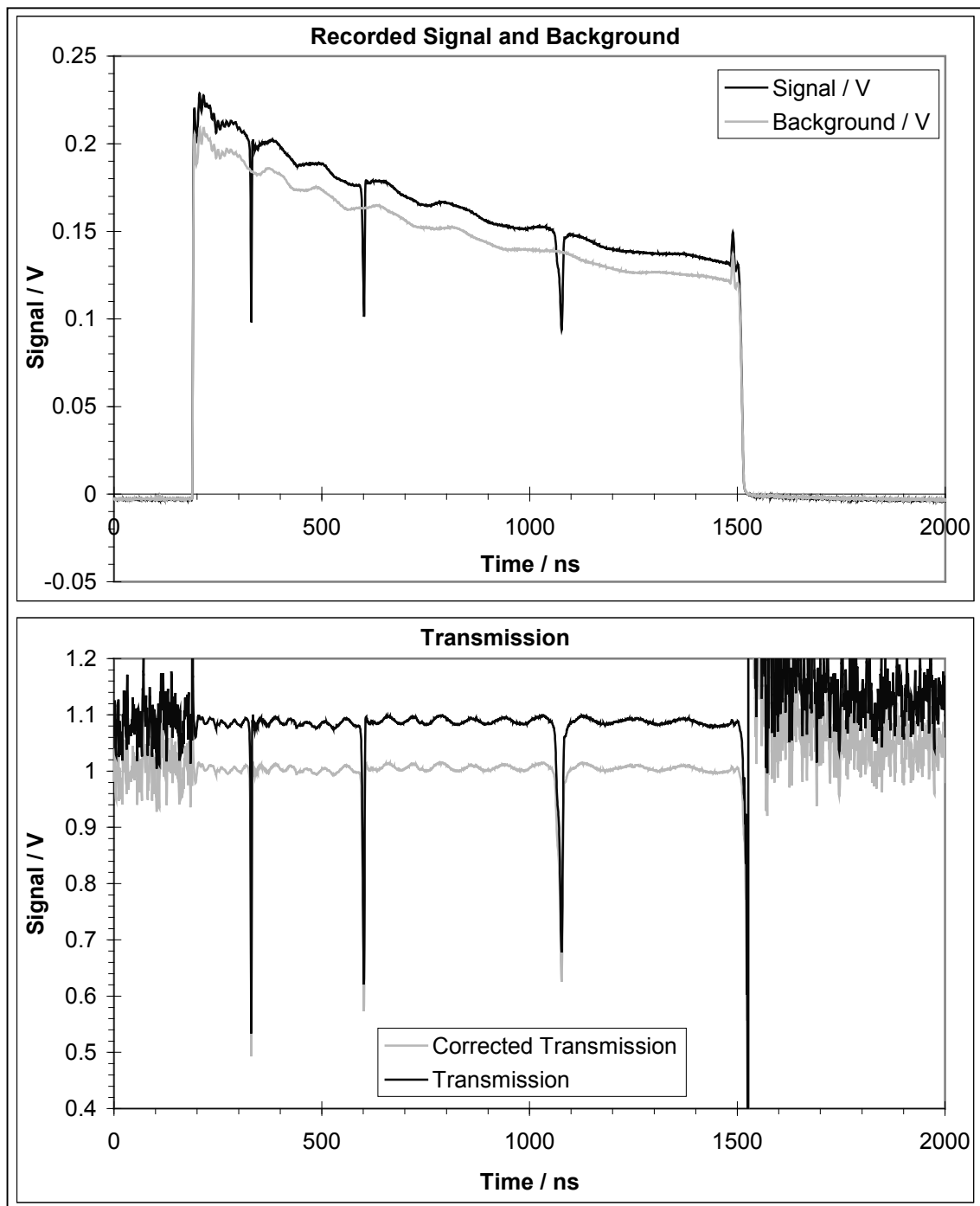


Figure 3.3.1: The raw pulse (top, black) is divided by the background pulse (top, grey) to give the transmission spectrum (bottom, black). This is then divided by its own mean value to set the baseline on 1 (bottom, grey). These spectra were recorded with 5 Torr of CO<sub>2</sub> using laser 60. The laser running parameters were 1300 ns, 20 kHz, 12.5 V, 0 °C.

As can be seen, between recording the background and the signal, the detected power has increased slightly, resulting in a transmission spectrum with a baseline of 1.1. To

correct for this, the mean value of the transmission spectrum between 200 ns and 1500 ns is calculated. The spectrum is then divided by this to fix the baseline on 1. This has an effect equivalent to scaling the background before calculating the transmission, which should not affect the accuracy of the transmission spectra. However some unexplained problem is affecting derivation of accurate mixing ratios from some spectra recorded during fieldwork. It is possible that the rescaling process introduces some form of distortion to the spectra, giving anomalous results.

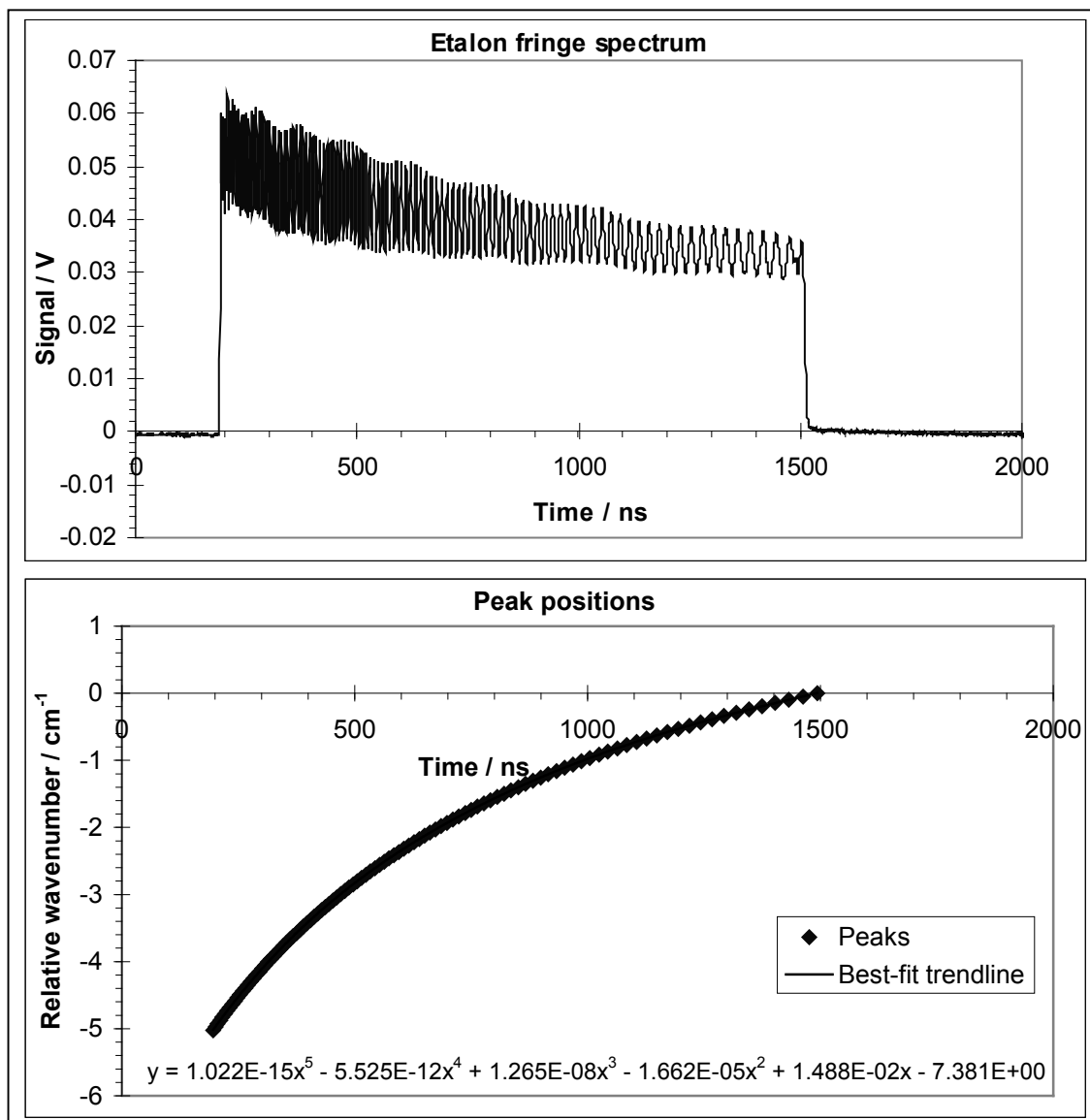


Figure 3.3.2: Etalon fringes (top) and plot of peak positions (bottom). The peaks are separated by a known wavenumber, in this case  $0.0482 \text{ cm}^{-1}$ . At this stage, the end of the pulse is assumed to be at relative wavenumber  $0 \text{ cm}^{-1}$ .

The next step is to use a spectrum of a germanium etalon to characterize the laser

chirp and convert from time to wavenumber. The chirp is stable enough that generally one etalon scan per batch of data is recorded. A batch can be as long as a full day of recording.

Figure 3.3.2 illustrates a set of etalon fringes, and the derivation of a time to wavenumber polynomial conversion based upon the known spacing of the maxima for a given etalon. This time to wavenumber polynomial is then used to calculate a wavenumber for each time coordinate. The spectrum is then converted from relative wavenumber to absolute wavenumber by comparing the positions of the absorption lines to their actual wavenumber according to databases such as HITRAN [49]. The relative wavenumbers can then have a correction factor added to "slide" the spectrum to the correct position. Figure 3.3.3 illustrates the initial and final transmission spectra plotted in time and wavenumber respectively.

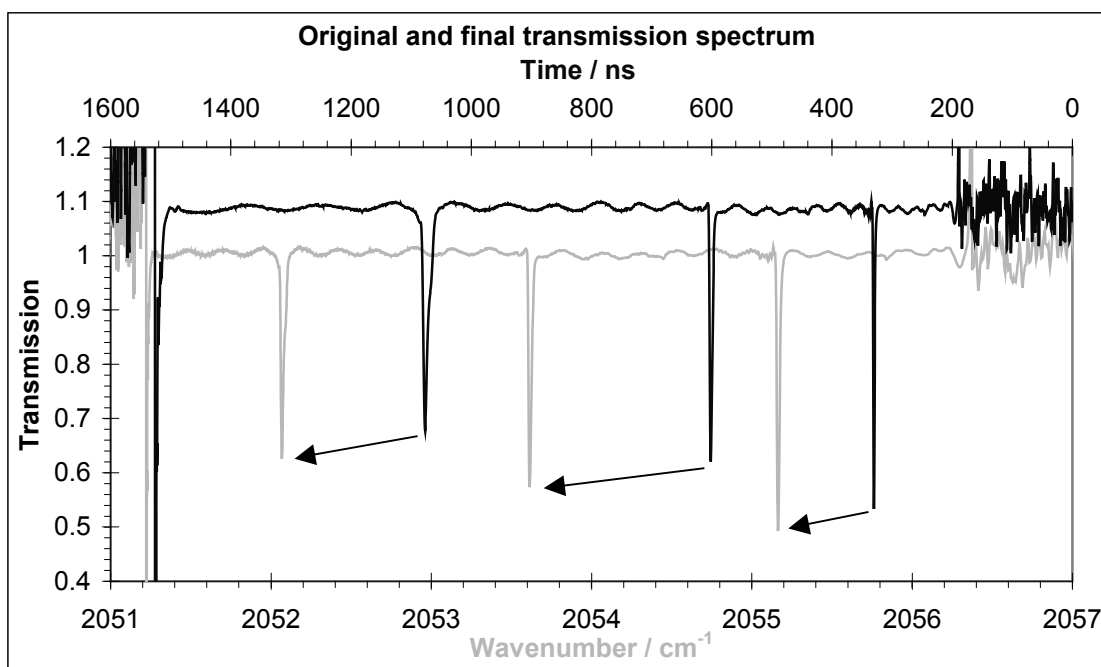


Figure 3.3.3: Original spectrum (black) and calibrated spectrum (grey). The arrows indicate the apparent movement of the lines when converting from time to wavenumber.

As has been described, there is minimal signal processing required to obtain transmission spectra. This is a consequence of the fact that the intra-pulse tuning method does not require any modulation to be applied to the laser. Many other systems do modulate the laser, and consequently require phase-sensitive detection such as lock-in amplifiers, thus introducing the possibility of unwanted phase shifts.

The final stage in the analysis is the derivation of mixing ratios from the spectra. In general, spectra for mixing ratio derivation are recorded with a cell pressure of 100 Torr, or in free space at atmospheric pressure. In either case, the pressure broadening dominates the lineshape, leading to a Lorentzian shape. Each line is separately fitted using standard LabVIEW fitting routines. The fitted lineshape has the form:

$$y = n - h \left( \frac{f}{(x - c)^2 + f^2} \right) \quad (3.3.1)$$

where  $n$  is the baseline level, which should be 1;  $h$  is proportional to the amplitude of the peak;  $f$  is the half-width-at-half-maximum of the line and  $c$  is the line centre. The area under this function, integrated from  $-\infty$  to  $+\infty$ , is simply  $h$ .

For some lower pressure work, a Gaussian fit was used. This has the form:

$$y = n - \sqrt{a^2} e^{-\frac{(x-c)^2}{b}} \quad (3.3.2)$$

where  $n$  is the baseline level, which should be 1;  $a$  is the line strength;  $c$  is the line centre and  $b$  is proportional to the full-width-at-half-maximum. The area under this function, integrated from  $-\infty$  to  $+\infty$ , is given by  $\sqrt{\pi b}$ .

It is easy to determine the mixing ratio of the gas by comparing the calculated area under the fitted line with the known area under the line in question, given in HITRAN [49]. The partial pressure of the absorbing gas,  $P_p$ , is given by

$$P_p = \frac{A_{CALC}}{A_{HITRAN}} \quad (3.3.3)$$

where  $A_{CALC}$  is the calculated area and  $A_{HITRAN}$  is the area according to HITRAN.

The mixing ratio,  $R$ , is given in parts per billion by

$$R = \frac{P_p}{P} \times 1,000,000,000 \quad (3.3.4)$$

where  $P$  is the cell pressure the data were recorded at.

The instrument is a very useful tool for determining relative gas levels. To be certain that the derived levels are accurate, calibration against another instrument, or by

measurement of a certified gas mixture is necessary. During fieldwork, the following steps to calibrate the instrument have been performed.

#### Penicuik field based work – Calibration

See Chapter 4.2 for full details of the work carried out at Penicuik. The original portable system was calibrated for this work by measurement of a standard gas mixture, supplied by BOC. The results indicated that the instrument was under-reading as a consequence of the lower cell pressure. A correction factor was thus added to the routine to adjust all readings to the correct level.

#### In-Flight Atmospheric Measurements – Fitting test

See Chapter 4.3 for full details of the in-flight work. During the first flights from Oxford Airport using the original instrument, no calibration was carried out.

During the second flights from Gloucester, spectra were fitted by the software supplied with the 4-laser system, as well as being analysed using our existing methods. Comparisons between the two methods indicated that the relative levels and the fluctuations of gas levels were real, however the accuracy of the measurements varied from a good agreement between the two fitting methods for N<sub>2</sub>O to a factor of two difference when measuring CO<sub>2</sub>. The reasons for this discrepancy have not yet become apparent.

#### Bus Exhaust Fumes – Zero measurements

See Chapter 4.6 for full details of the bus exhaust fumes work. Following this work, a quantity of background spectra were recorded in the lab, and were later analysed as "blank" spectra to calculate the standard deviation of a zero reading for each gas. For all but one gas, the standard deviation was less than 1% of the highest measured mixing ratio of the gas during the work.

### 3.4: New Laser Drive Box – Power Supply Instability

When the 8  $\mu\text{m}$  QC laser was first installed in the LS-03-D system, the spectra recorded appeared similar to those recorded with the old system. Later, investigations into the use of long pulses to slow the laser chirp rate succeeded in reducing it to 16 MHz/ns. At lower sweep rates it was expected that the form of the signals would change, and when a different type of line shape was observed, this was attributed to novel processes occurring within the gas cell, with a drive voltage only just above threshold. The slowest chirp rate is always at the end of the pulse, as the laser approaches thermal equilibrium, thus slowing the temperature change.

However, following a detailed comparison of the new spectra with those recorded of the same molecule, nitrous oxide, in 2004 by Michael McCulloch and Geoffrey Duxbury [62], the difference between them led to the realisation that the new line shape was not due to hitherto unobserved processes with the gas cell, but was instead caused by the function of the new laser drive system. The reasoning for this conclusion is given below.

In 2004 the measurements were carried out using a spectrometer with a drive system designed by Erwan Normand and Ged Drinkwater. The digitisation used the same Acqiris 0.5 ns digitiser that has been used throughout this work, a liquid nitrogen cooled Kolmar MCT detector, and a 1 GHz bandwidth pre-amplifier. The square current pulse was produced by analogue circuitry. The nitrous oxide spectra shown in Figure 3.4.1 showed very high resolution. The l-doublet, labelled on the figure, was clearly resolved as a doublet. The rapid passage structure of the single strong line was well developed and resolved, with the structure at the lowest pressure being very sharp.

The two lines of the l-doublet each exhibit rapid passage spikes, however the emission spike from the first line lies under the absorption by the second line and is thus unobservable.

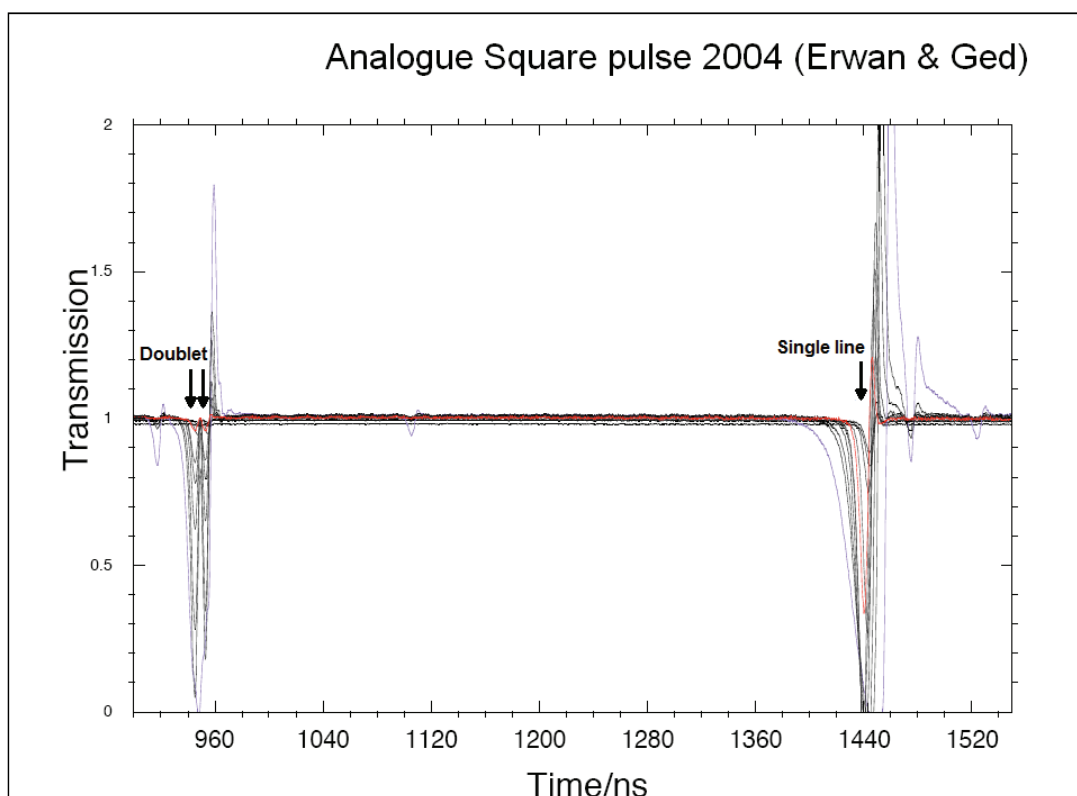


Figure 3.4.1: Various nitrous oxide spectra recorded over a range of pressures between  $1 \times 10^{-4}$  Torr and  $3.13 \times 10^{-2}$  Torr by Duxbury *et al* [62] in 2004, illustrating clear absorption lines and well-defined rapid passage structure.

Equivalent transitions of nitrous oxide recorded during August 2008 show very different structure. Figure 3.4.2 compares spectra recorded using the new laser system at high drive voltage and pulse duration of 1600 ns with those recorded with low drive voltage and pulse duration of 3500 ns.



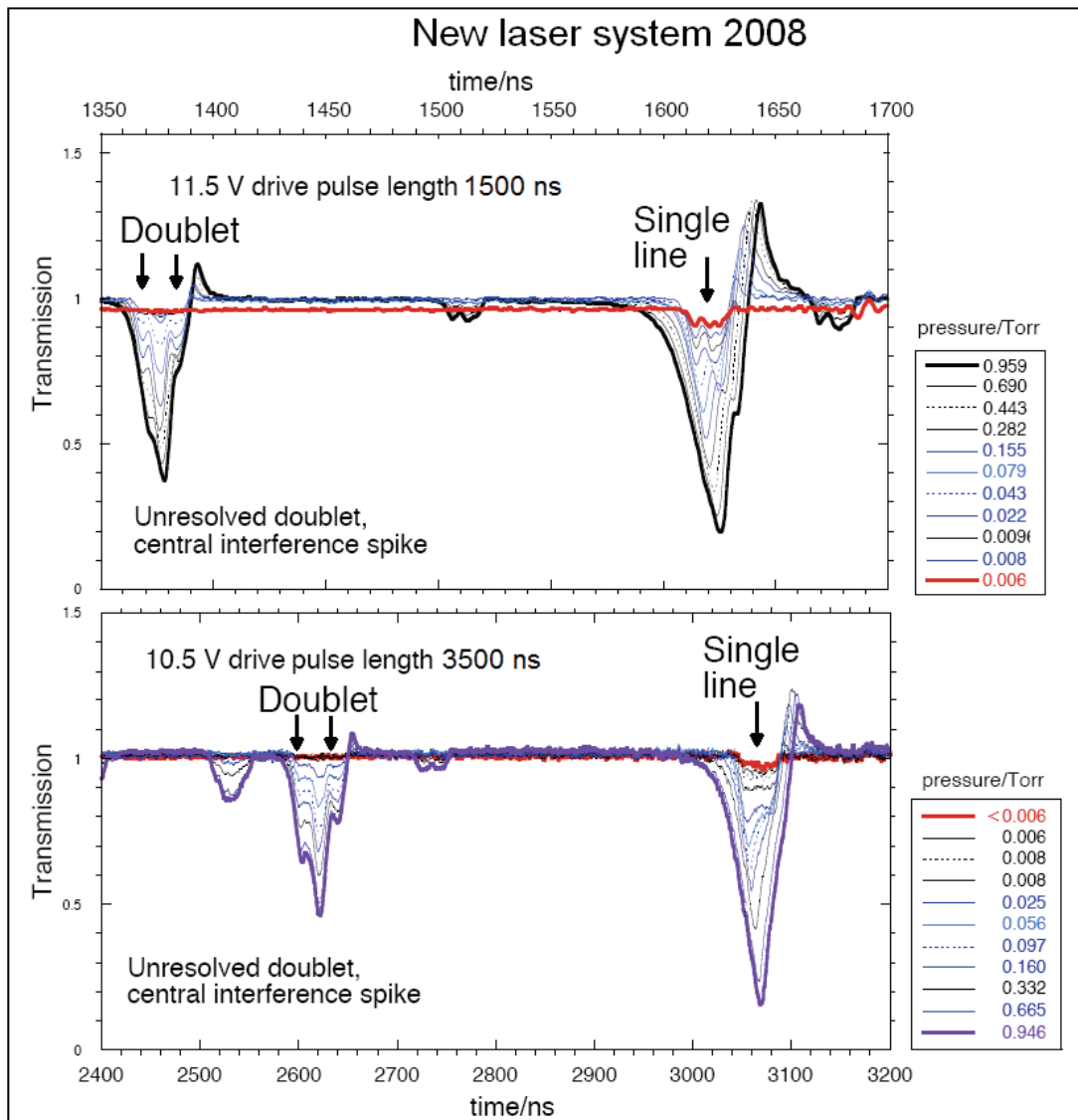


Figure 3.4.2: Various nitrous oxide spectra recorded in 2008, illustrating the merging of the doublet, the smearing of the single line and the drop in intensity of the rapid passage spike. The same doublet and single line are shown in each graph, although they appear differently as the graphs are plotted in time which does not take account of the different chirp behaviour at each set of running parameters.

Regardless of pulse parameters used, the spectra are very similar and show two distinctive features, the doublet being very broad and unresolved and the low pressure spectra of the single line displaying a very distinctive lineshape which is almost rectangular at low pressure. The form of this line shape can be attributed to the functioning of the current pulse generator. Assuming that the low pressure line shape displayed in Figure 3.4.2 represents the instrument function, then the structure

of the whole spectrum can be taken as a convolution of a sharp spectrum such as that shown in Figure 3.4.1 with such an instrument function.

The spectra of the fringes obtained using two germanium etalons with effective fringe spacings of  $0.0485\text{ cm}^{-1}$  and  $0.0200\text{ cm}^{-1}$  were recorded using pulse durations of 1500 ns. One pair were recorded at a laser temperature of  $-5\text{ }^{\circ}\text{C}$ , and the other pair with a laser temperature of  $-20\text{ }^{\circ}\text{C}$  as shown in Figure 3.4.3. For the  $0.0485\text{ cm}^{-1}$  etalon, the contrast and amplitude of the fringes remains approximately constant over the entire duration of the pulse, while that of the  $0.0200\text{ cm}^{-1}$  etalon deteriorates for pulse durations beyond about 800 ns, and is very poor at the end of the pulse. This contrasts with the normal spectra of etalon fringes seen previously when the contrast of the fringes recorded using the  $0.0200\text{ cm}^{-1}$  etalon improved at the slower chirp rate at the end of the pulse.

Similar effects of changed resolution have been seen in the spectra of  $\text{CF}_3\text{CH}_3$  shown in Figure 3.4.4. The spectra obtained with the original laser drive system ("the brick") were well resolved. At the slow chirp rate end of the pulse, the resolution approached the  $0.0018\text{ cm}^{-1}$  resolution of spectra recorded by a previous student on a Bruker Fourier Transform Spectrometer at RAL. However, spectra recorded with the new system exhibit much poorer resolution. The comparison of spectra recorded by "the brick" with the Kolmar and Vigo detectors show that the change in resolution is not due to the use of a different detector.

A comparison of the two sets of etalon fringes with pulse duration, and the "molecular ruler" resolution of Figure 3.4.3 leads to a possible suggestion of the origin of the changes in resolution when using long pulses.

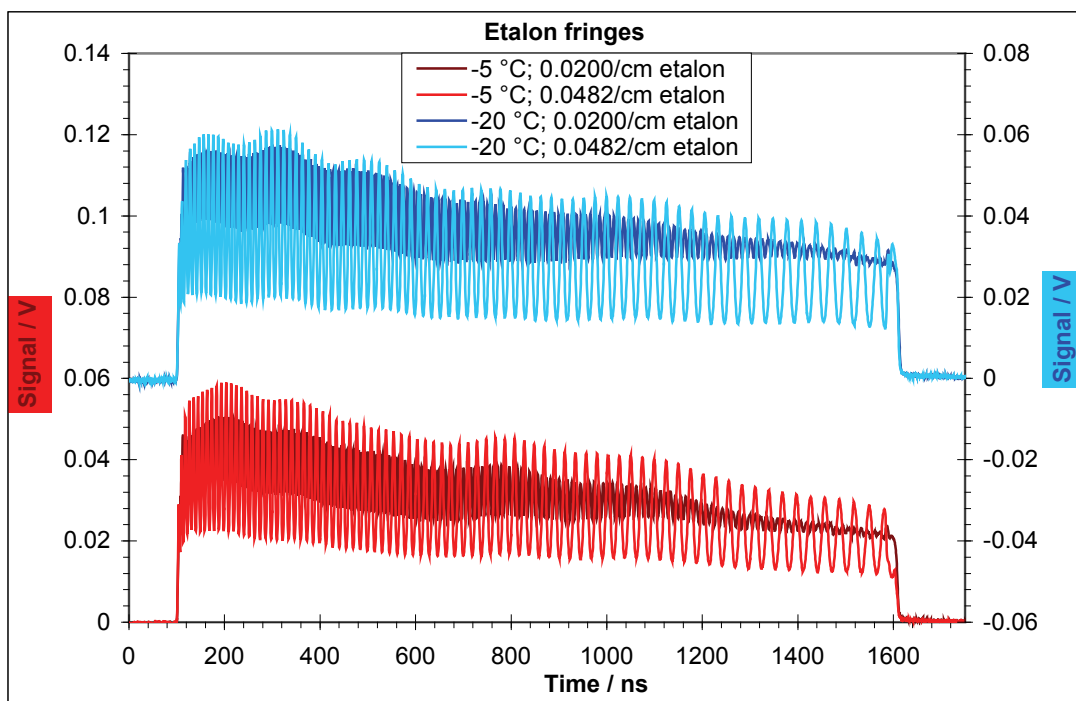


Figure 3.4.3: Comparison of etalon fringe contrast using coarse and fine etalons with different laser temperatures.

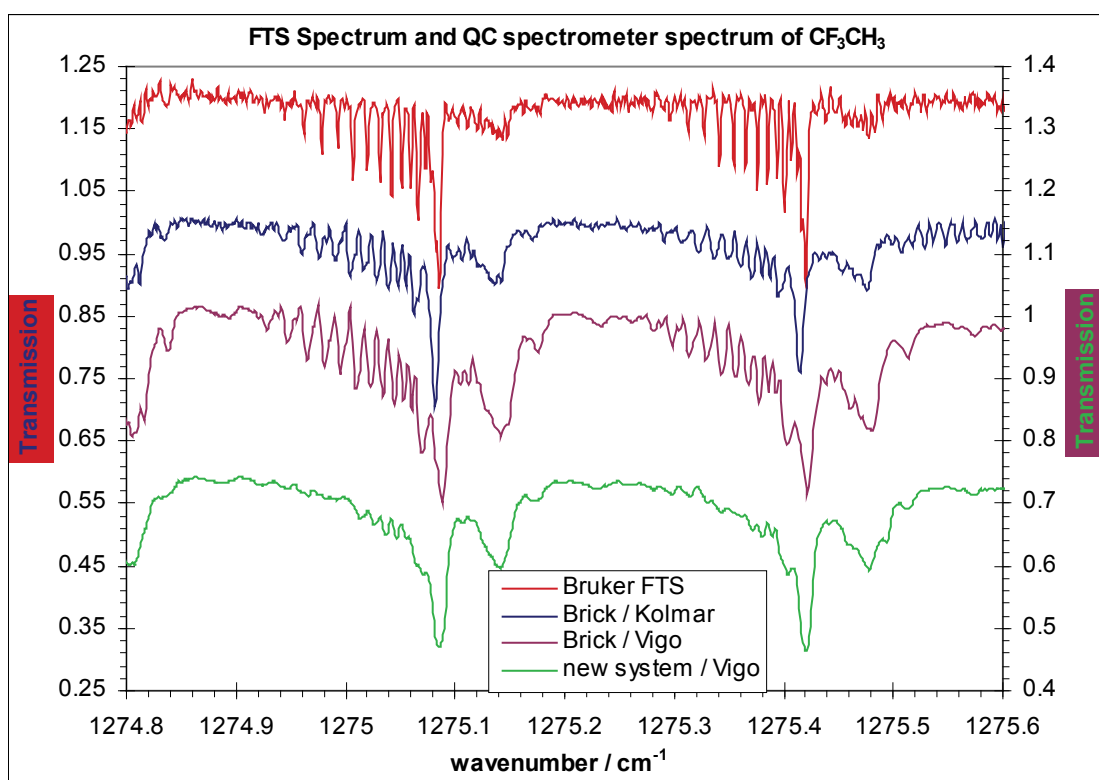


Figure 3.4.4: Comparison of various methods of recording the spectrum of  $\text{CF}_3\text{CH}_3$ . Offsets have been added for clarity. The Bruker spectrum was recorded by a previous student with a resolution of  $0.0018 \text{ cm}^{-1}$ .

The fact that the  $\text{CF}_3\text{CH}_3$  spectrum recorded using the new drive system with short pulses is better resolved than that using the old drive system suggests that the chirp rate of the new system is slower than that of the old system.

Further investigations revealed that reducing either the pulse length or the pulse frequency produced more normal fringes using the  $0.0200\text{ cm}^{-1}$  etalon as shown in Figure 3.4.5. The improvement caused by reducing the frequency was the key to identifying the problem as the laser power supply.

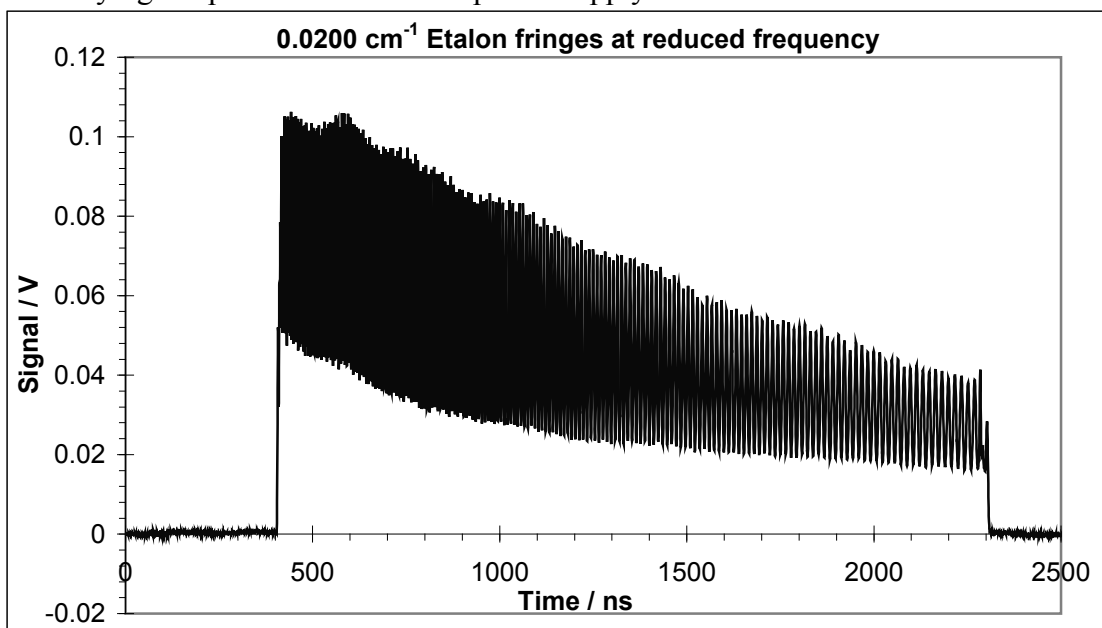


Figure 3.4.5: Etalon fringe contrast using a 1900 ns pulse at 2.5 kHz repetition rate.

Applying a long pulse or a high frequency of short pulses (*i.e.* high duty cycle) to the laser, the power supply lacked the power to properly drive the diode. Consequently the supplied power dropped across the pulse. This affects the heating of the diode and consequently the chirp rate. This caused spectral lines or etalon fringes towards the end of the pulse to jitter back and forth in time. The need to average 20,000 spectra to obtain good quality signals thus averaged 20,000 slightly different line positions, leading to apparent "jitter broadening" of the lineshape. Similarly, the shifting etalon fringes destructively interfere with each other, reducing the contrast.

Subsequent modifications to the new laser drive box by Cascade Technologies rectified the problem by increasing the stability of the power supply.

### 3.5: Laser Characterisation

The lasers acquired through the ACCORD (Advanced Components Cooperation for Optoelectronics Research and Development) program were all given a series of basic tests to characterize them. In the interests of consistency, all the tests were performed with pulse duration 1300 ns; repetition frequency 20 kHz; and voltage at the stated maximum on the laser's specifications sheet. The maximum voltage is temperature independent, whereas the threshold voltage varies with temperature. Some lasers stated a "typical" operating voltage, but as some did not, the maximum voltage was the best choice for consistency.

The tests were: recording the laser emission spectrum using a Bomem Fourier Transform Spectrometer (FTS); determining the frequency chirp using a germanium etalon; recording the temporal and spatial profiles; and measuring the average laser power, all at a laser temperature of 0 °C. Additional FTS spectra at 10 °C and -25 °C were also recorded for each laser.

Our original 8 µm laser was put through most of these tests. A rough spatial profile had been recorded in preparation for profiling all the lasers. Before the full profile could be recorded, the laser failed. The replacement 8 µm laser (laser 51) was also put through the tests.

#### Methodology

The spectra of the lasers were recorded using a Bomem FTS, running with a resolution of 0.05 cm<sup>-1</sup>. To obtain a sensible balance between time to acquire spectra and signal to noise ratio, 20 scans were averaged for each spectrum. As the power and chirp rate of the lasers drop toward the end of the pulse, the Bomem measurement of power at a given frequency has the effect of integrating across a pulse, giving rise to the appearance of a pulse with high power at the low wavenumber end, and lower power at the high wavenumber end, while the temporal profile of the lasers show exactly the opposite. This is most noticeable in the spectra of laser 62 (see Figures 3.5.1 and 3.5.2), which has a very strong signal at the low

wavenumber end of the pulse, while its temporal profile decreases toward the end of the pulse. The laser chirps from high to low wavenumber, so the temporal start of the pulse is at the left of the axis in Figure 3.5.2, but at the right in Figure 3.5.1.

The temporal profiles of the lasers were recorded using one of the Vigo PVI-2TE-8 photodetectors, positioned about 30 cm from the laser aperture. The chirp was characterised by the same setup with the addition of a  $0.0482 \text{ cm}^{-1}$  germanium etalon between the laser and the detector. In both cases, the recorded signal was an average of 8,000 consecutive pulses. The frequency downchirp can be seen in the etalon fringes. Each fringe is separated by  $0.0482 \text{ cm}^{-1}$ . As the chirp slows, the peaks are more spaced out.

The spatial profiles at a distance of 15 cm from the lasers were recorded by scanning a Vigo detector with a  $100 \text{ }\mu\text{m}$  diameter pinhole across the beam at a speed of  $0.07 \text{ mms}^{-1}$  horizontally on a computer controlled translation stage, while recording the peak signal at each 0.01 s. To map out the entire profile this was repeated vertically at 0.1 mm intervals.

The spatial profile of the original  $8 \text{ }\mu\text{m}$  laser was never recorded, however cross sections through the centre of the beam horizontally and vertically were recorded by moving a 1 mm pinhole-covered Vigo detector through the beam about 15 cm from the laser and recording the signal strength every millimetre.

The power was measured using an Ophir model 3A thermal power meter. This measures the average power produced by the laser. Knowing the duty cycle (2.6 %), it is easy to work out the power produced during the actual pulses. This is noted as the peak pulse power.

#### Summary of Characteristics

A summary of the laser characterisation is shown in Tables 3.5.1 and 3.5.2. The full serial numbers shown are shortened to the last two digits to identify the laser.

Laser	Nominal Wavelength / $\mu\text{m}$	Average Pulsetrain Power / mW	Peak Pulse Power / mW
Original 8 $\mu\text{m}$	7.84		
CT-100060	4.87	0.415	15.96
CT-100061	6.15	0.489*	18.81*
CT-100062	6.15	0.907	34.85
CT-100063	7.23	1.163	44.73
CT-100064	7.45	2.160	83.07
CT-200051	7.84	1.485	57.11

Table 3.5.1: The nominal wavelength is given in the laser specification sheet for each laser.

The original 8  $\mu\text{m}$  laser failed before its power could be measured.

\*: Obtained by a demonstration power meter which was on loan for assessment.

Laser	Start chirp rate / MHz/ns	End chirp rate / MHz/ns	Chirp range / $\text{cm}^{-1}$	Temperature tuning / $\text{cm}^{-1}$	Highest wavenumber / $\text{cm}^{-1}$
Original 8 $\mu\text{m}$	151.8	54.2	3.865	6.78	1279.00
CT-100060	321.3	51.2	5.06	9.74	2058.72
CT-100061	72.3	18	1.735	6.31	1630.22
CT-100062	86.8	14.4	1.663	4.98	1629.42
CT-100063	192.8	53.5	4.675	7.88	1388.82
CT-100064	362.17	54.16	5.02	9.64	1345.11
CT-200051	144.87	38.38	2.70	5.53	1277.04

Table 3.5.2: The chirp range is the range covered by a 1300 ns pulse at 0 °C. The temperature tuning is the range from the end of a 1300 ns pulse at 10 °C to the start of a 1300 ns pulse at -25 °C, which is the highest wavenumber.

## Results

The Bomem FTS spectra of the lasers are shown in Figure 3.5.1. The overall pattern of the Bomem spectra is similar for most of the lasers, with a low signal at the high wavenumber end of the pulse, and a high signal at the low wavenumber end of the pulse. This illustrates the effect of the slowing chirp rate, also seen in the etalon fringes of each laser. This means the signal strength recorded by the FTS has little physical meaning and these tests illustrate only the wavelength ranges of the lasers.

The original 8  $\mu\text{m}$  laser seems to shift wavenumber by the same amount between -25 °C and 0 °C as it does between 0 °C and 10 °C. For all the other lasers, the change in wavelength is proportional to change in temperature. This may be a thermal issue as the actual semiconductor chip of the 8  $\mu\text{m}$  laser was roughly twice the size of all the other lasers, and the Peltier struggled to keep it below -25 °C

during other work.

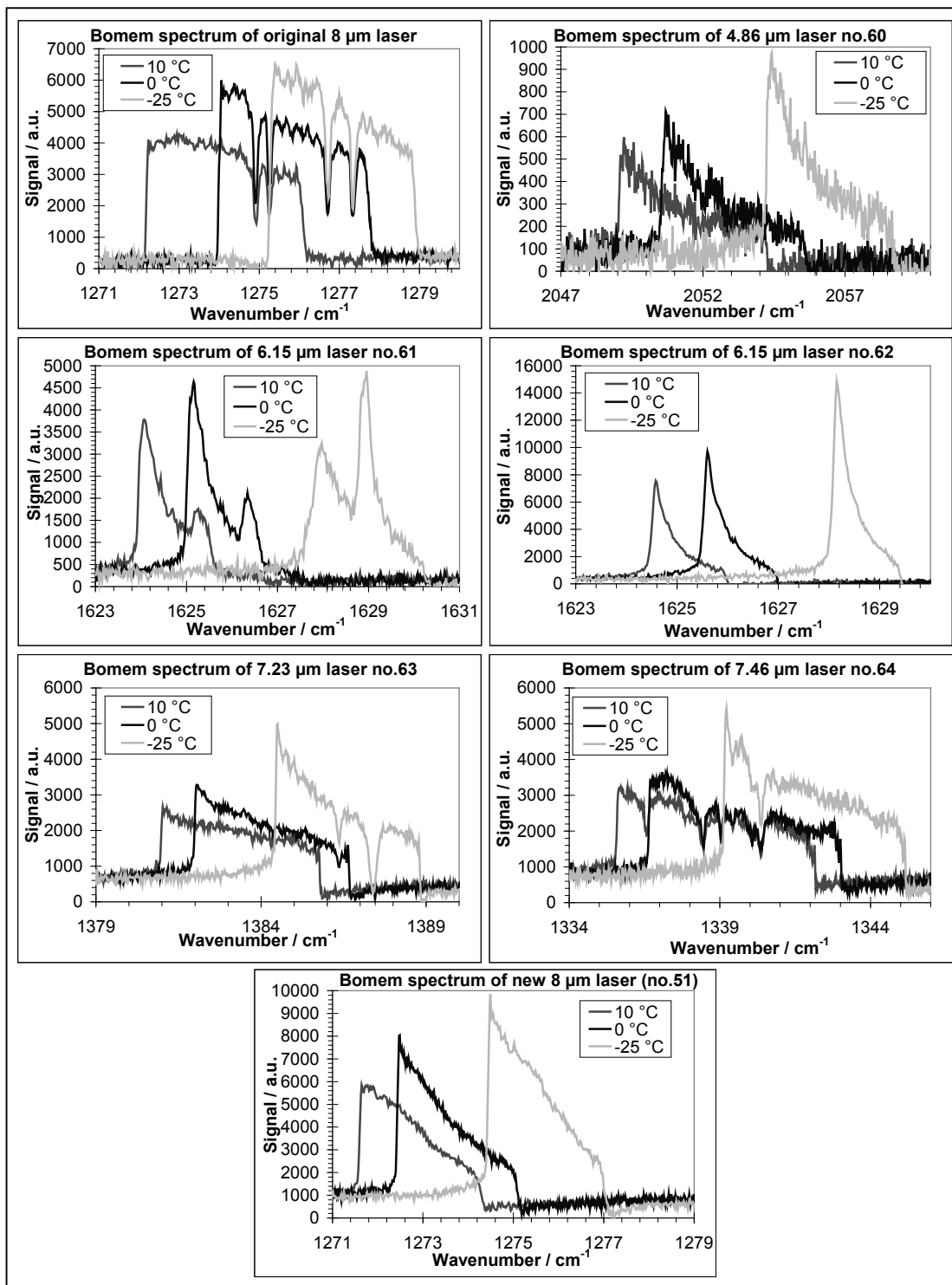


Figure 3.5.1: The laser spectra recorded using the Bomem spectrometer with a resolution of 0.05 cm<sup>-1</sup>. The absorption lines in the original 8 μm laser spectrum are caused by absorption in a 10 cm cell filled with 2.5 Torr of methane which was used as a calibration check. All other absorption lines are caused by the approx. 72 cm of atmospheric water vapour before the beam entered the Bomem.



Laser 61 exhibits two peak wavelengths at each temperature. This is discussed in more detail later (see Laser 61 Bistability).

Laser 64 has an unusually "bumpy" spectrum on account of some strong atmospheric absorption lines. These lines also showed up in transmission spectra, indicating that the frequency of the laser varies slightly from shot-to-shot. It appears that at 13 V, this laser becomes multimode, so it was later run at 11 V where it operates more normally (see Laser 64 High Voltage Behaviour).

The temporal profiles of the seven lasers are shown in Figure 3.5.2.

The temporal profiles are generally fairly similar, most lasers exhibiting the typical trapezoidal pulse. The new 8  $\mu\text{m}$  laser and 6.15  $\mu\text{m}$  laser 62 both have unusually flat profiles, which is useful. A flat profile means that the signal-to-noise ratio will be constant across the pulse, while the trapezoid shape means that there is a lower signal-to-noise ratio at the end of the pulse. This is one advantage of the new 8  $\mu\text{m}$  laser compared to the old 8  $\mu\text{m}$  laser. (See Comparison of the Two 8  $\mu\text{m}$  Lasers)

Lasers 61 and 62 have remarkably strong switch on/off transients, which suggests the laser will be under more stress. During switch on transients, the wavenumber decreases, increases again, then decreases more slowly until the end of the pulse [44].

Laser 64 has an unusually bumpy baseline as a consequence of atmospheric absorption lines. Initially, this was thought to be a symptom of the multimode operation exhibited by this laser at 13V, however further investigations later concluded that it was not. This laser is discussed in more detail later (see Laser 64 High Voltage Behaviour).

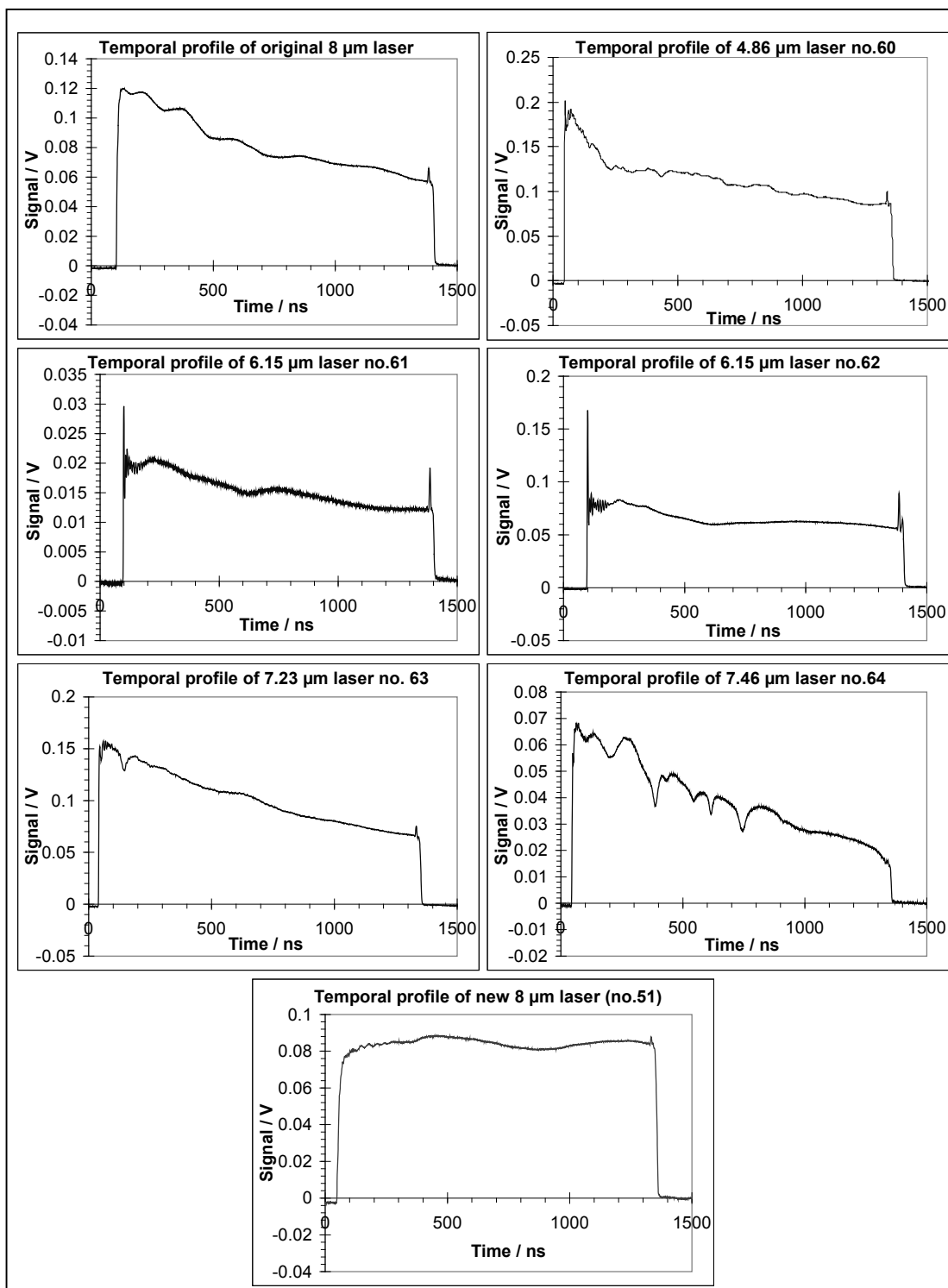


Figure 3.5.2: The temporal profiles using a 1300 ns current pulse. All absorption lines are caused by the approx. 30 cm of atmospheric water vapour between the laser and the detector.

The etalon fringes which demonstrate the downchirp of the lasers are shown in Figure 3.5.3.

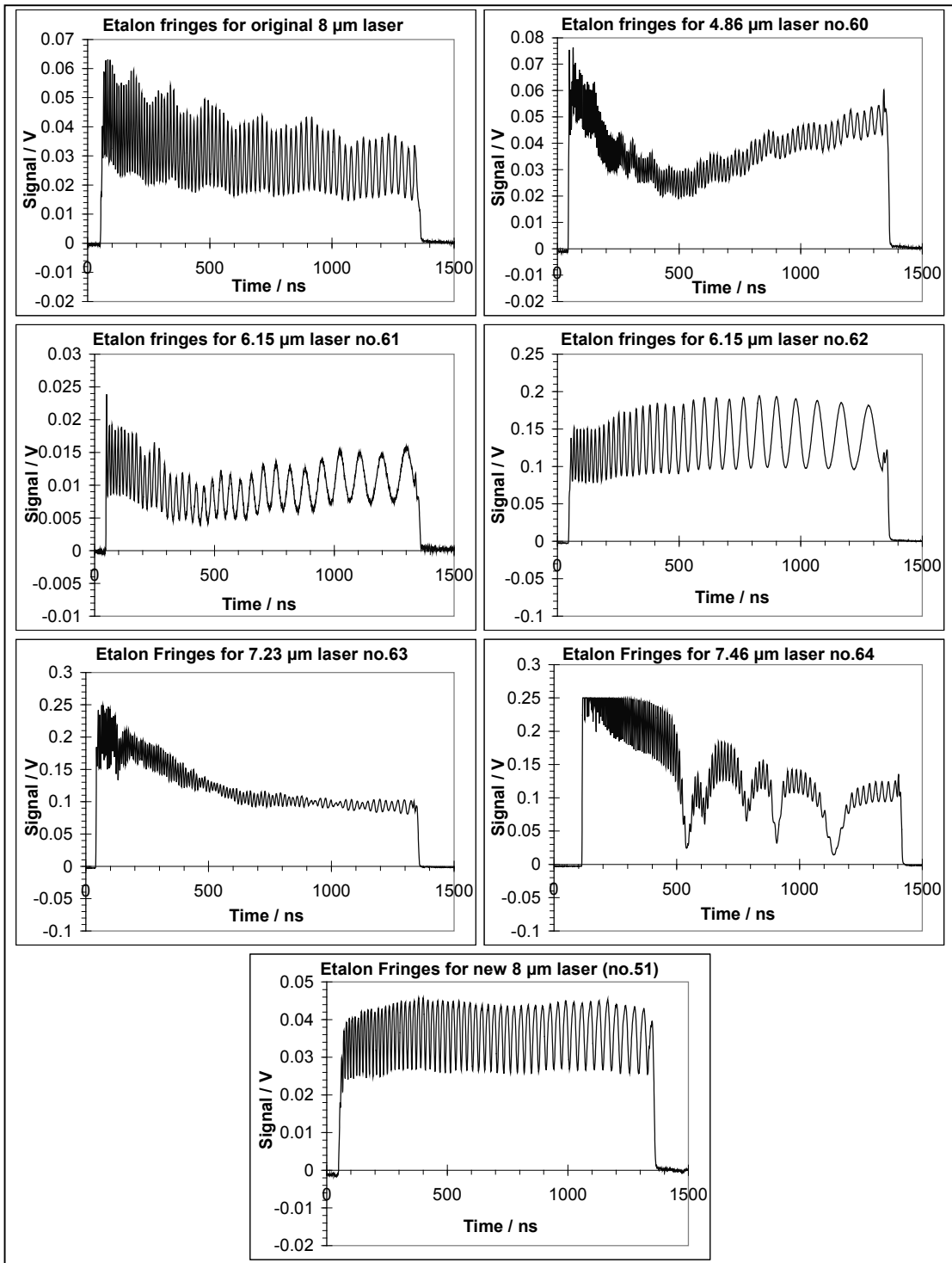


Figure 3.5.3: The etalon fringes. All absorption lines are caused by the approximately 30 cm of atmospheric water vapour between the laser and the detector. The difference in fringe contrast between lasers is a consequence of etalon angle. The etalon used had a free spectral range of  $0.0482 \text{ cm}^{-1}$ .

The downchirps of each laser show similar behaviour – initially a high chirp rate,

slowing as the pulse continues. The actual rates vary hugely between lasers, as shown in Table 3.5.2 in Summary of Characteristics. As well as saturating the detector at the start of the pulse, laser 64 shows poor fringe contrast towards the end of the pulse, which is a sign of multimode operation. See Laser 64 High Voltage Behaviour for more detail.

Horizontal and vertical cross sections through the original 8  $\mu\text{m}$  laser beam are shown in Figure 3.5.4.

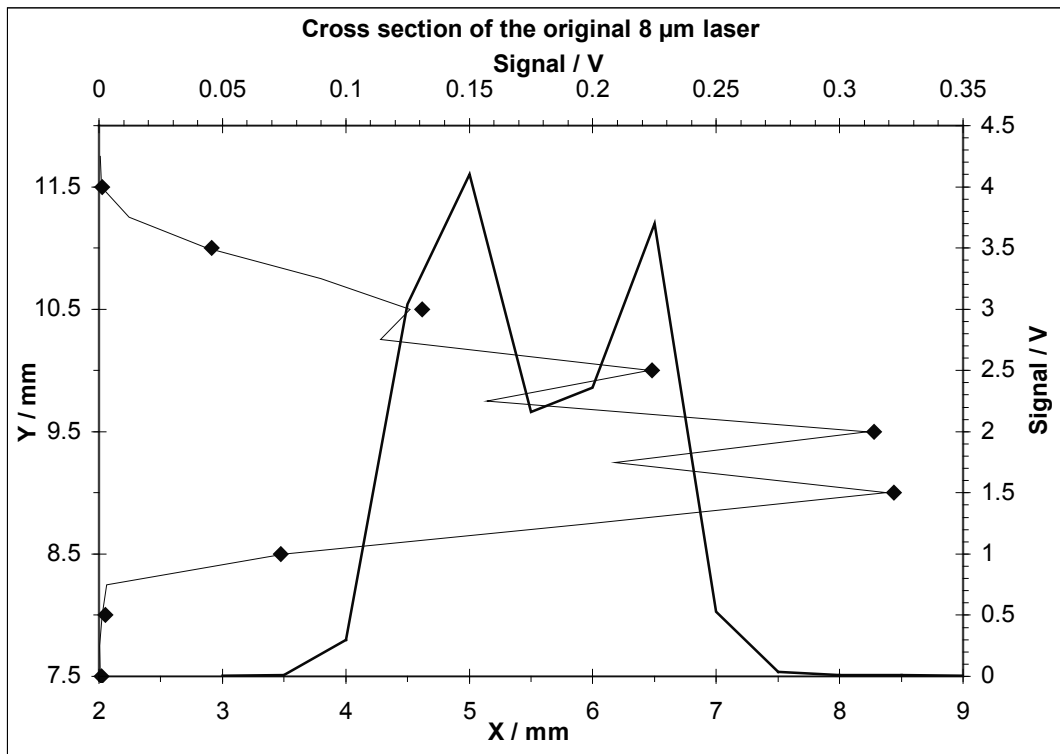


Figure 3.5.4: Horizontal and vertical cross sections of the original 8  $\mu\text{m}$  laser. The points show the original vertical profile recorded with a 1 mm separation between points. The lines show the repeat with 0.5 mm between points.

The original 8  $\mu\text{m}$  laser initially appeared to have two maxima, one beside the other, and a slightly asymmetric vertical cross section. A more detailed (0.5 mm between points) check confirmed the horizontal cross section, but appeared to show fringes in the vertical one. It is not clear whether these fringes are real, or a measurement artefact. This was the last data recorded before the laser failed, so the fringes may have been a symptom of the impending failure.

The full spatial profiles of the six newer lasers are shown in Figure 3.5.5.

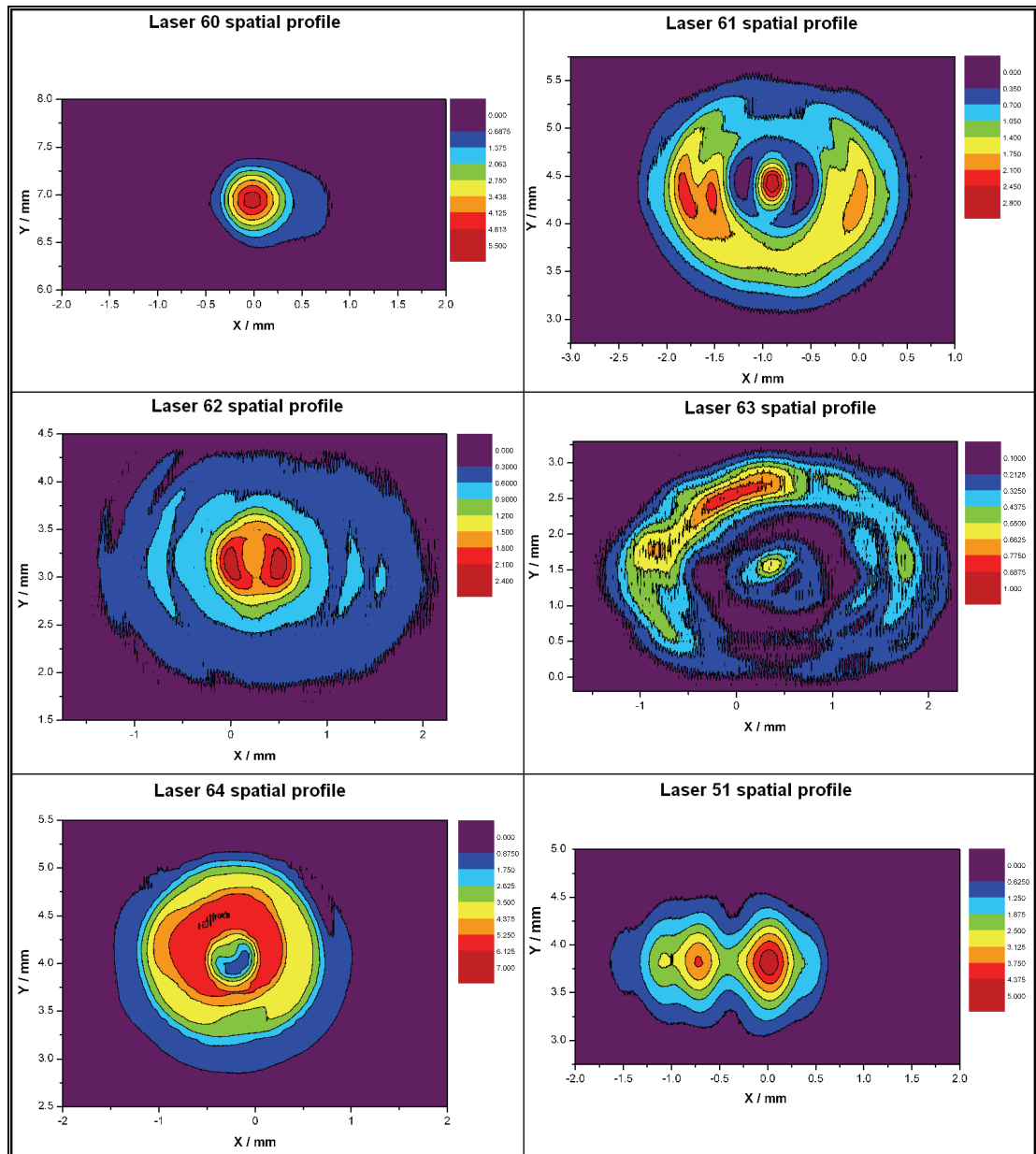


Figure 3.5.5: The spatial profiles of the 6 newer lasers. These were recorded by scanning a Vigo detector with a 100  $\mu\text{m}$  diameter pinhole across the beam at a distance of 15 cm from the laser at a speed of  $0.07 \text{ mm s}^{-1}$  horizontally on a computer controlled translation stage, while recording the peak signal at each 0.01 s. To map out the entire profile this was repeated vertically at 0.1 mm intervals.

The lasers all have different spatial profiles. Laser 60 has an almost perfect Gaussian spatial profile with one clearly defined central peak. Figure 3.5.6 shows a calculated

Gaussian fit vertically and horizontally through the beam, as well as the calculated Mean Squared Error (MSE) of the fit. There is a slight pedestal on the right hand side of the horizontal cross section, which gives it an MSE of 0.02. The vertical fit gives and MSE of only 0.005.

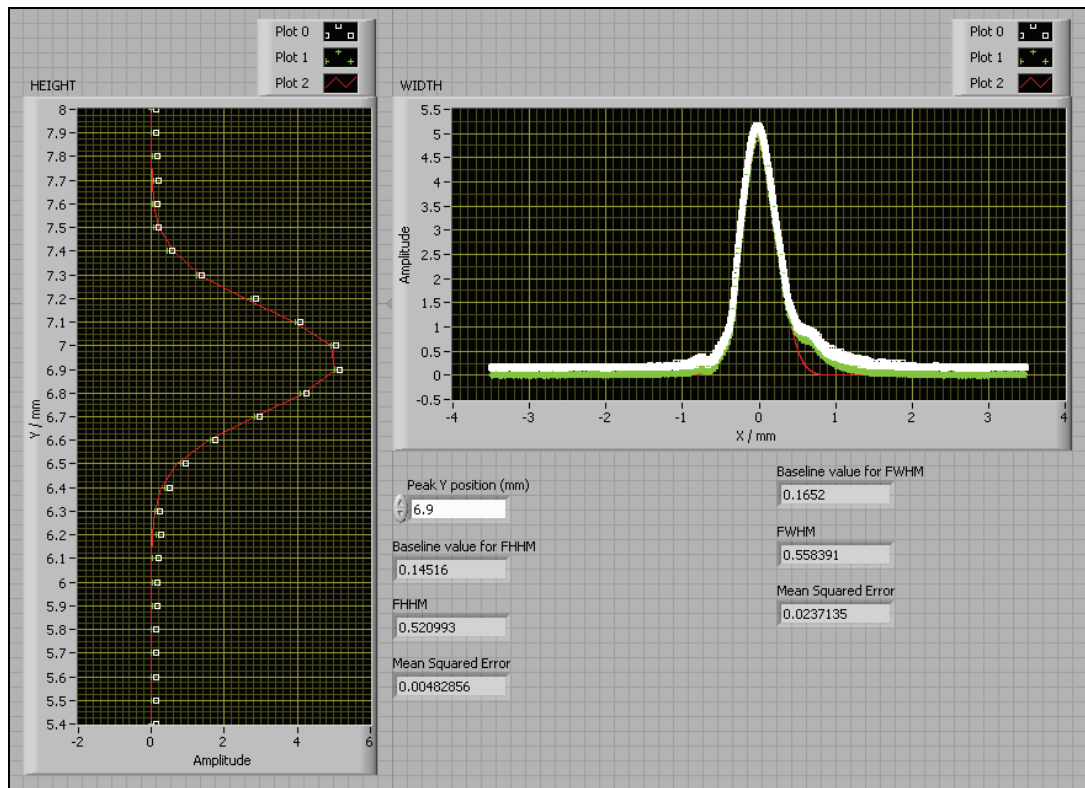


Figure 3.5.6: Gaussian fits to horizontal and vertical cross sections through the centre of the spatial profile of Laser 60.

Laser 61 has a strange profile, with a very strong central "spike" rising out of the hole in the centre of a ring shaped profile. The "spike" is almost a perfect Gaussian, albeit slightly oval. It is possible that the outer ring is one of the two possible laser modes and the central spike is the other. The bistability of this laser is described in more detail later. (see Laser 61 Bistability).

Laser 62 has a symmetrical profile with two maxima. This laser has been successfully used for spectroscopy, and seems to be a very useful laser, despite a slightly untidy spatial profile.

Laser 63 has a particularly strange profile, even compared to all the other lasers. It

resembles a meteorite crater, having a weak central spike surrounded by an incomplete ring. Unusually, the peak power is not the central spike, but is one side of the ring. This profile makes it remarkably difficult to align this laser which thus far has not been used with a Herriott cell.

Laser 64 has a circular profile with a central space. The peak intensity appears to be a plateau, but as this is the level at which the detector saturates, the actual intensity in this area is not known.

Laser 51 has a double-lobed profile, although both of the lobes are reasonably well shaped. Despite this rather odd profile, this laser has been successfully coupled into Herriott cells and used for atmospheric measurements.

#### Comparison of the Two 8 $\mu\text{m}$ Lasers

Laser 51 was not supplied through the ACCORD program, but was purchased from Cascade to replace the original 8  $\mu\text{m}$  laser. The same atmospheric monitoring "window" from 1274.5  $\text{cm}^{-1}$  to 1277.5  $\text{cm}^{-1}$  can be used, however this requires running the laser at a lower temperature than the old one.

Temperature tuning from 10  $^{\circ}\text{C}$  to -25  $^{\circ}\text{C}$  gave the old 8  $\mu\text{m}$  laser a tuning range from 1272  $\text{cm}^{-1}$  to 1279  $\text{cm}^{-1}$ . Laser 51 has a narrower range, and can be tuned between 1271.5  $\text{cm}^{-1}$  and 1277  $\text{cm}^{-1}$ . The Bomem spectra in Figure 3.5.1 illustrate this.

The temporal profile of the new laser is flatter than the old one, without the power dropping off toward the end of the pulse. In principle this should make it possible to use longer pulses to reach very low chirp rates. The old laser was successfully run with 3  $\mu\text{s}$  pulses applied, however the new one has not yet been tried out for long pulse work.

The chirp rate of laser 51 is slower, so the laser only chirps through two thirds of the range of the old laser when using a 1300 ns pulse. This is wide enough to pick up 3

nitrous oxide, 3 methane and 2 water vapour absorption lines between  $1274.62\text{ cm}^{-1}$  and  $1276.84\text{ cm}^{-1}$ . A typical atmospheric absorption spectrum is shown for each  $8\text{ }\mu\text{m}$  laser in Figure 3.5.7.

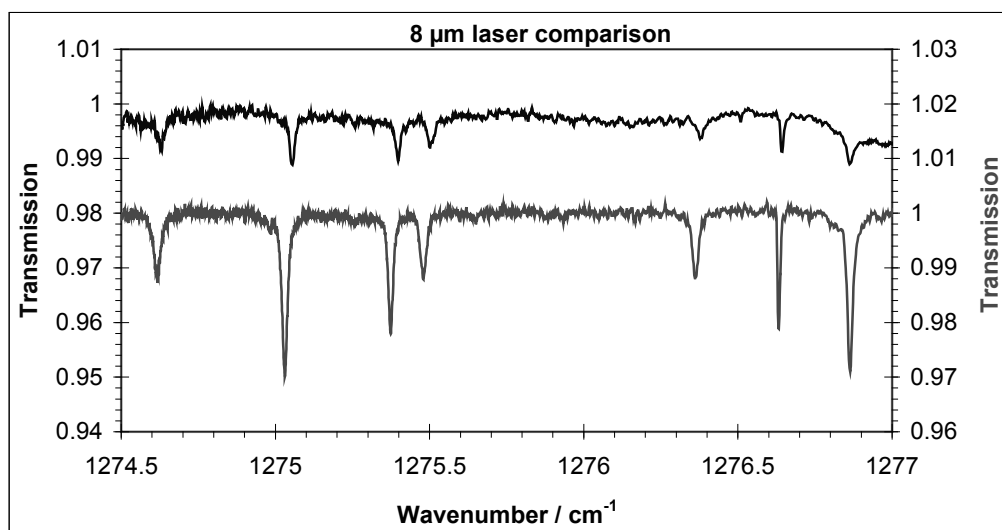


Figure 3.5.7: Atmospheric spectra recorded at 100 Torr comparing the two lasers.

Top: Recorded using the original  $8\text{ }\mu\text{m}$  laser in its original drive box. The chirp rate based resolution scans from  $0.006\text{ cm}^{-1}$  to  $0.013\text{ cm}^{-1}$  left to right.

Bottom: Recorded using the new  $8\text{ }\mu\text{m}$  laser. The chirp rate based resolution scans from  $0.006\text{ cm}^{-1}$  to  $0.011\text{ cm}^{-1}$  left to right.

The two spectra show similar performance as far as resolving the lines and signal-to-noise ratio are concerned. The new laser gives a flatter baseline, indicating that the pulse shape has changed less between recording the background and the signal.

The spectrum recorded using the original  $8\text{ }\mu\text{m}$  laser were originally recorded as a system test during cell alignment. The cell path length used was not noted, but given the discrepancy in linestrength between the two spectra, it was evidently less than the  $62.8\text{ m}$  path later used to record the spectrum using the new laser.

### Laser 61 Bistability

The spectrum of laser 61 showed two peak wavelengths, unlike all the other spectra. Later investigations showed that the laser was bistable, and each pulse could take one of two starting wavelengths. Averaging several spectra gives a spectrum of each mode superimposed on each other, as occurred with the Bomem spectra.



Which mode lases appears to be random, although the ratio of mode 1 pulses to mode 2 pulses varies with temperature, voltage, and drive frequency. At 0 °C and 10 °C, the lower wavenumber mode is dominant, however at -25 °C the higher wavenumber mode dominates. The pulses are pretty flat and show a normal increase in gain as the temperature drops. Looking at individual pulses on the oscilloscope, there appeared to be very little difference in the temporal profiles of the two modes.

By running the laser at -5 °C and 500 ns, it was possible to differentiate the two modes. At these settings, one mode was lasing just below the frequency of a broad, strongly absorbing water vapour line which lies at  $1627.7\text{ cm}^{-1}$ , with the wing visible at the start of the pulse, while the other mode is lasing just above the water line with the wing visible at the end of the pulse. This is shown in Figure 3.5.8.

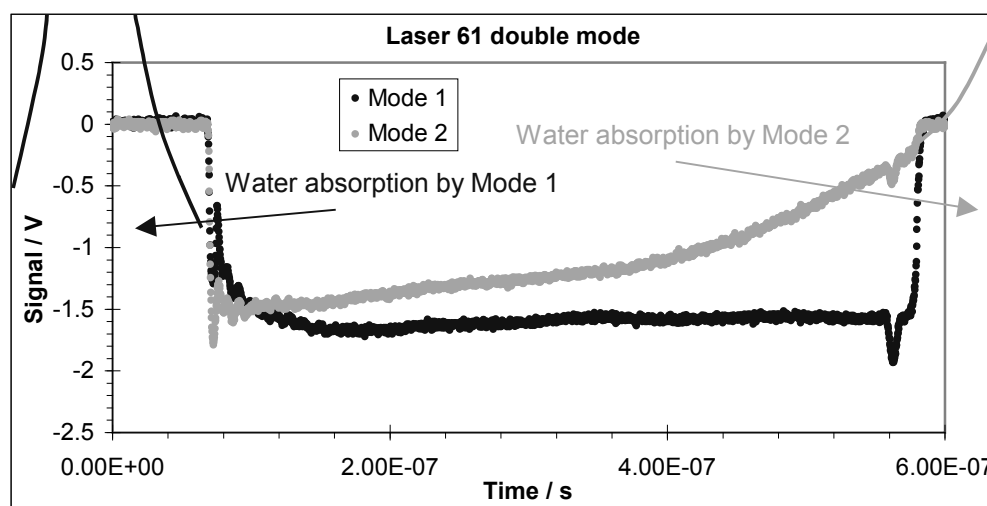


Figure 3.5.8: The two modes of 6.15  $\mu\text{m}$  laser 61 running at -5 °C and 500 ns to show water absorption in each mode. An approximation of the absorption has been drawn on outside the pulses to illustrate the position of the water line in each mode.

This laser beam was later passed through a monochromator (Jobin-Yvon H25 with the grating replaced with a 58038110 grating designed for use at 10  $\mu\text{m}$ ) to pick out the lower wavenumber (more frequent) mode. By capturing a series of pulses on the oscilloscope, it was possible to estimate that the ratio of pulses on mode 1 to those on mode 2 was slightly more than 4:1. This ratio varies with pulse length, temperature and drive voltage. The pulsetrain is shown in Figure 3.5.9.

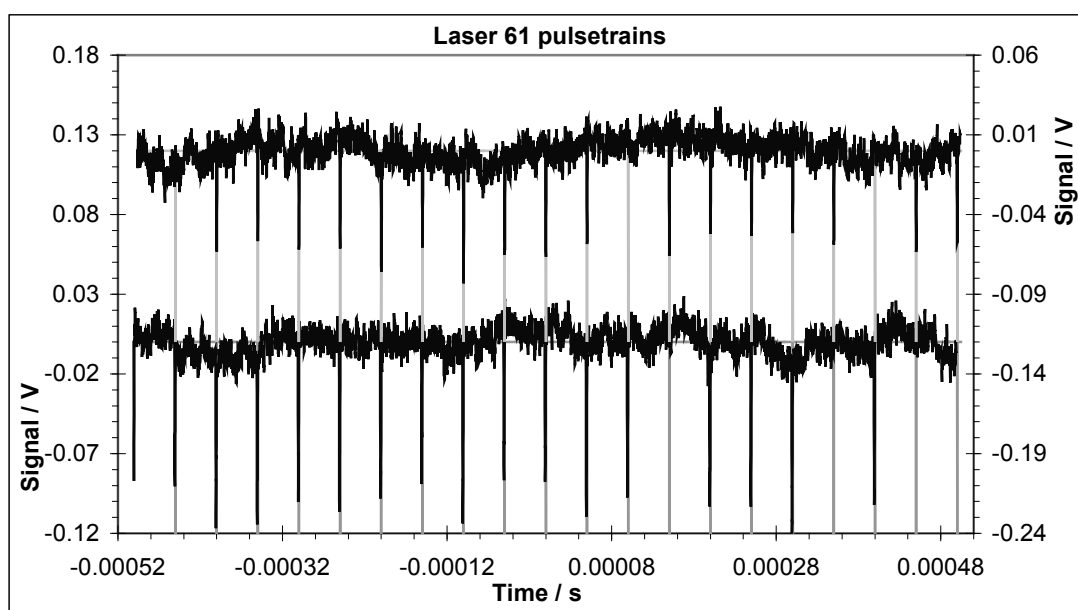


Figure 3.5.9: The pulsetrain of laser 61. The grey lines indicate where the laser pulsed. If no pulse is overlapping the grey line, then on that occasion, mode 2 fired. The monochromator was set to 611.93 nm, as the dial is calibrated for a He:Ne laser, and the output detected is thus the tenth harmonic at around  $1630\text{ cm}^{-1}$ .

The etalon fringe spectrum shown in Figure 3.5.3 is an average of 8,000 pulses and consequently of both modes. Regardless of the starting frequency, both modes have similar chirp behaviour, so averaging does not have an adverse effect on the fringes.

The unpredictable dual mode behaviour of this laser renders it completely useless for spectroscopy, unless measuring some gas with very few lines and a reliable way to tell how many pulses of each mode have been averaged together.

#### Laser 64 High Voltage Behaviour

Laser 64 became multimode at 13 V (its maximum) so the tests on it were repeated at 11 V. This reduction in voltage halved its chirp range. A comparison of the lasers performance at each voltage is shown below in Tables 3.5.3 and 3.5.4.

Voltage / V	Start chirp rate / MHz/ns	End chirp rate / MHz/ns	Chirp range / $\text{cm}^{-1}$	Temperature tuning range / $\text{cm}^{-1}$	Highest wavenumber / $\text{cm}^{-1}$
11	141.33	31.49	2.85	6.59	1345.41
13	362.17	54.16	5.02	9.64	1345.11

Table 3.5.3: Laser 64 compared at 11 V and 13 V.

Voltage / V	Average Pulsetrain Power / mW	Peak Pulse Power / mW
11	1.011	38.88
13	2.160	83.07

Table 3.5.4: Power output comparison.

The repeated tests are shown in Figure 3.5.10, illustrating the differences between the two voltages.

The Bomem spectra show that at 13 V, the initial wavenumber of the laser is the same as for 11 V, but the range covered is almost twice as wide.

From the output temporal profiles, it can be seen that at 13 V, the initial pulse power is higher than at 11 V, and the power also drops off more rapidly.

The etalon fringes show that the chirp rate also varies with drive voltage, although rates at either chirp are fairly typical. At 13 V, the start chirp rate is 170.12 MHz/ns and the end chirp rate is 46.65 MHz/ns, while at 11 V the laser chirps slightly faster at first (180.75 MHz/ns) but slows more, ending up at a chirp rate of 38.9 MHz/ns. Running at 13 V gives a chirp range of  $6.12 \text{ cm}^{-1}$ , which is almost double the 11 V chirp range of  $3.66 \text{ cm}^{-1}$ .

This laser has a circular profile with a central space. At 13 V, the top appears to plateau, but this is in fact the level at which the detector saturates. The 11 V profile suggests that the profile is not in fact symmetrical, but has a weak spot at the bottom of the beam. It seems likely that if the detector had not saturated, the 13 V profile would be similar to the 11 V profile, but stronger. The average power output at 13 V was 2.160 mW, while at 11 V, only 1.011 mW output power was achieved, so in principle the 13 V spatial profile should have been twice the power of the 11 V one.

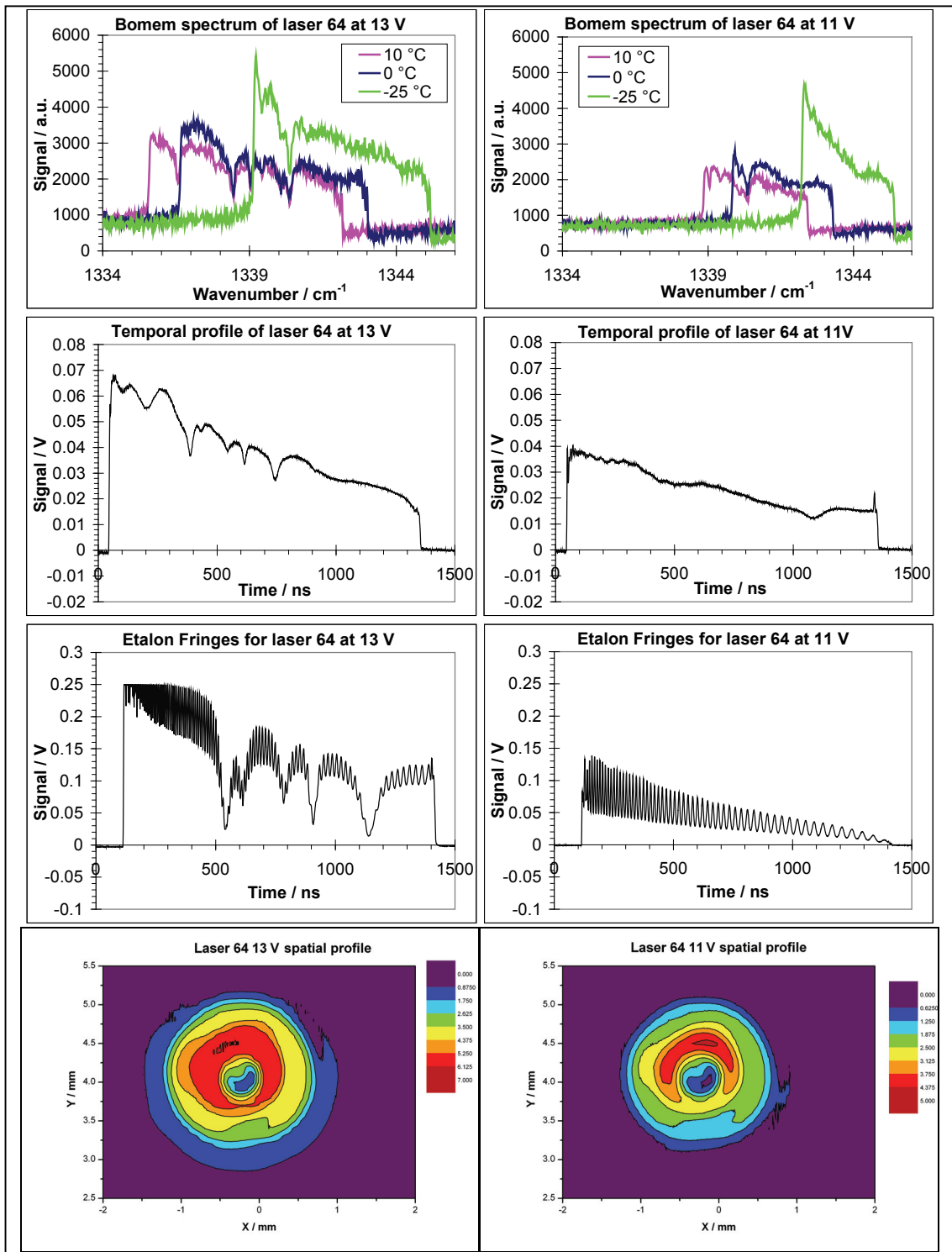


Figure 3.5.10: Laser 64 performance at 13 V and at 11 V. The peaks of the 13 V etalon fringes at the start of the pulse saturated the detector.

Additional etalon fringe spectra were recorded using a  $0.02 \text{ cm}^{-1}$  etalon. These are shown in Figure 3.5.11.

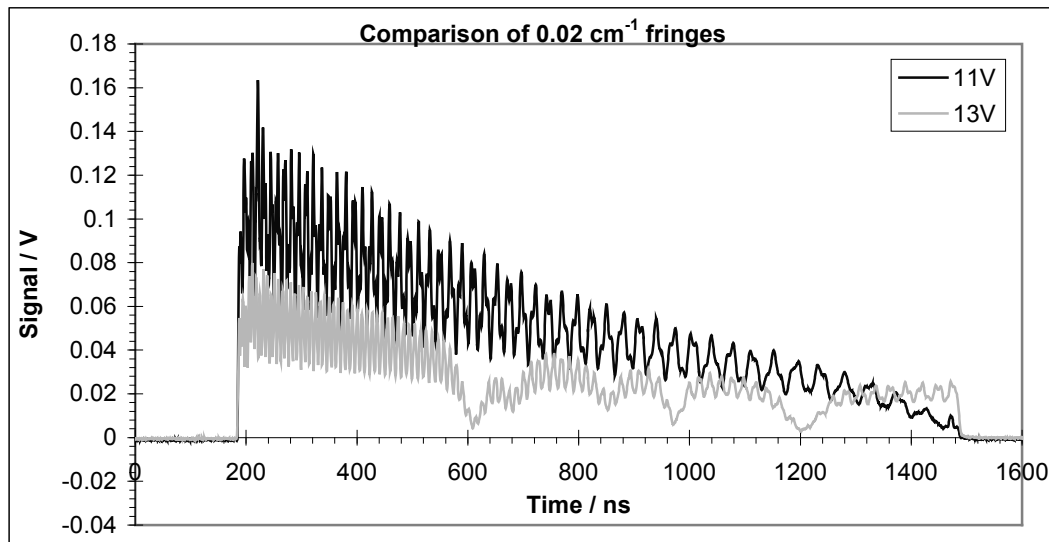


Figure 3.5.11: Laser 64 etalon fringes at 13 V and at 11 V.

These fringes show what appears to be a beat frequency between two sets of fringes. This occurs at both 13 V and at 11 V. The fringe contrast is poorer at the end of the pulse than at the start, similar to that seen in Chapter 3.4. As the drive boxes have been repaired, and this effect is not seen with any of the other lasers, the cause this time has to be multimode operation of Laser 64. The beat between the two waves allows us to determine the difference is  $0.02 \text{ cm}^{-1}$  in 3 fringes, or  $0.007 \text{ cm}^{-1}$  per fringe. This is only slightly more than the resolution of the laser, as determined by the square root of the chirp rate, which means the multimode operation will not have a visible effect on absorption lines except at very slow chirp rate.

### 3.6: Control Software

The spectrometer is controlled by interpretive programs, written and run under LabVIEW 7.1 as virtual instruments (VIs) running on a PC. There are two basic versions of the program, one simple data acquisition program, and a more complex version which controls all the electronics necessary to run the spectrometer in an aeroplane from one PC. Both use subVIs supplied by Acqiris to control the AP200 digitiser built into the computer PCI slot. Both versions have been modified occasionally to fix bugs and improve performance. The biggest change, which only affected the flight program, occurred when the original laser drive system broke. The replacement system is incompatible with the LabVIEW laser drivers, so the program had all laser control features removed, allowing the laser to be separately controlled.

#### Acquisition Only.vi

The simple program (Acquisition Only.vi) was written by previous PhD students, and needed very little modification. The user interface is shown in Figure 3.6.1.

The program acts as a virtual oscilloscope (top graph), recording the raw pulse signal received by the Acqiris PCI card within the computer. The trigger and acquisition settings can be adjusted in the box at the right. The program can be used as an oscilloscope, displaying spectra without saving. If a background spectrum has been saved by clicking "save to graph", the current signal is divided by the saved background to give an on-the-fly transmission spectrum (bottom graph).

The user can choose where to save data using the "select dir" button in the box at the top right. Once a saving location has been chosen, clicking on "Autorun" will start spectra being saved as text files.

Originally, the saved data consisted of the raw pulse and a timestamp. Soon after starting to use the Vigo detector, it was clear that the "on-the-fly" transmission spectra were accurate enough to use without having to recalculate them (the Vigo eliminated distortion which used to need removed, see Chapter 3.2: Photodetectors).

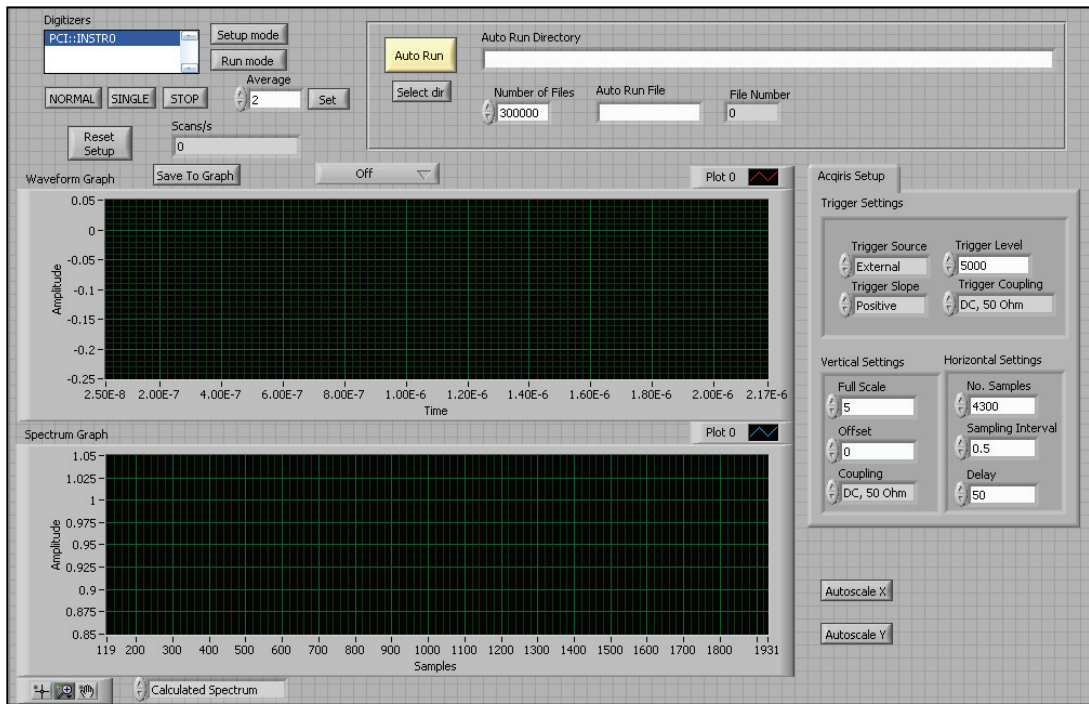


Figure 3.6.1: User interface for Acquisition Only.vi.

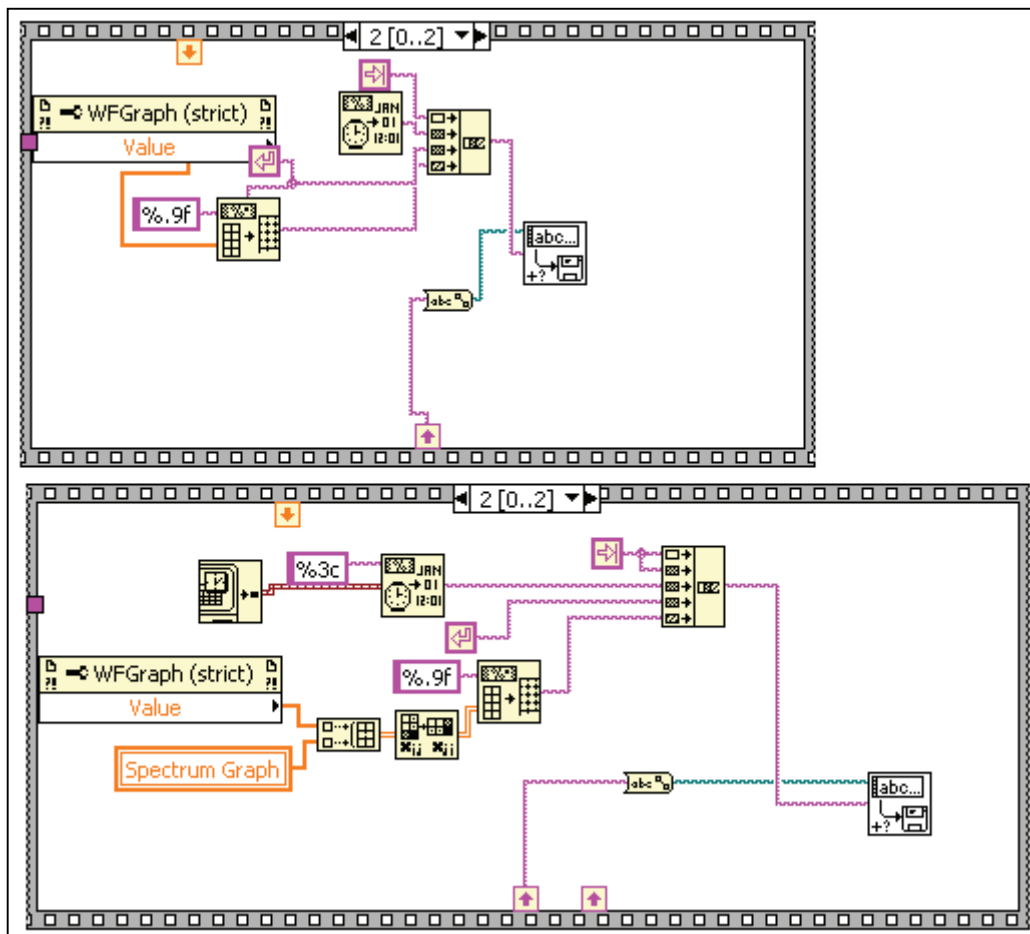
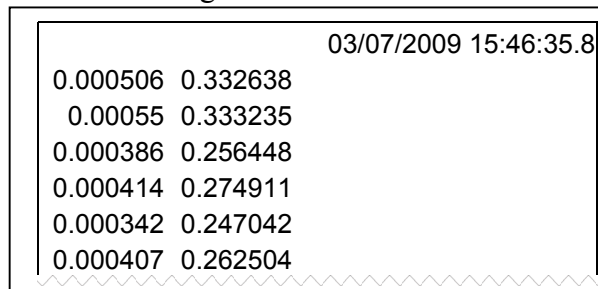


Figure 3.6.2: Original (top) & new (bottom) data saving frame from Acquisition Only.vi.

The program was modified to save the transmission spectrum as well as the raw pulse. At the same time, the timestamp format was modified to include seconds as a decimal number, rather than an integer. For fast recording, this allowed us to save subsecond spectra with accurate datestamps. The old and new versions of the spectrum saving frame of the program are shown in Figure 3.6.2. WFGGraph (strict) is the waveform corresponding to the raw pulse. Spectrum Graph is the calculated transmission spectrum, which is present as a global variable. This allows data to "tunnel" from one frame of the program to another.

The saved file is a text file with extension .awd, which can then be opened by Excel as a spreadsheet, or again by LabVIEW as a text file for further analysis. The first few lines of a file are shown in Figure 3.6.3.



		03/07/2009 15:46:35.8
0.000506	0.332638	
0.00055	0.333235	
0.000386	0.256448	
0.000414	0.274911	
0.000342	0.247042	
0.000407	0.262504	

Figure 3.6.3: Part of a saved spectrum. First column: raw spectrum. Second column: transmission spectrum. First cell in third column: timestamp.

If a background file has not been saved, the second column is filled with zeroes.

### Flight Program.vi

The flight program is a more sophisticated version of Acquisition Only.vi, which has always been able to save transmission spectra. This program controls all the electronics illustrated in Figure 3.6.4, and is responsible for ensuring the correct sequence of operations necessary to record data.

Flight Program 5.1.vi was initially written by previous members of the group, but it was never properly debugged until returning from the Oxford Airport based work where it was necessary to use some very convoluted workarounds to make the program run. The revised version became Flight Program 6.vi.



All variables are set from the front panel, shown in Figure 3.6.5, then the VI can run.

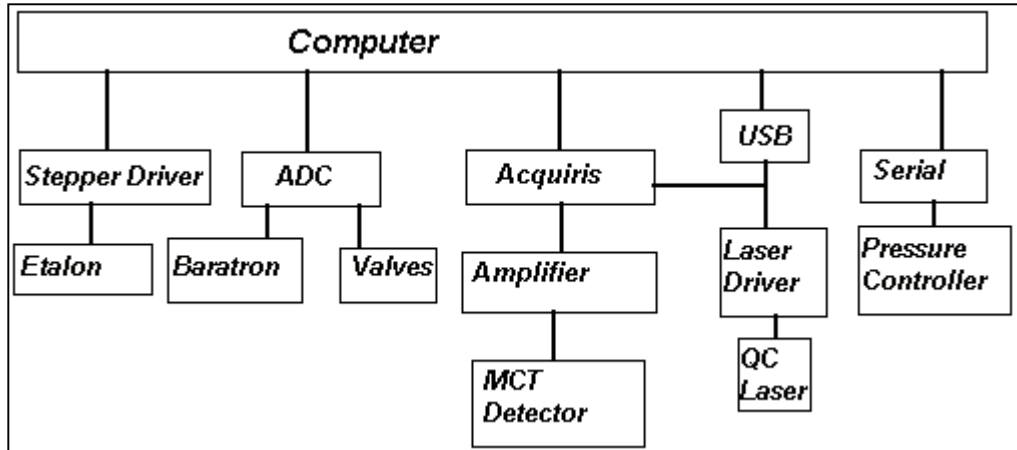


Figure 3.6.4: Electronics controlling the spectrometer. The MCT detector amplifier was only used with the Kolmar detector. The Vigo detector had its own built-in amplifier.

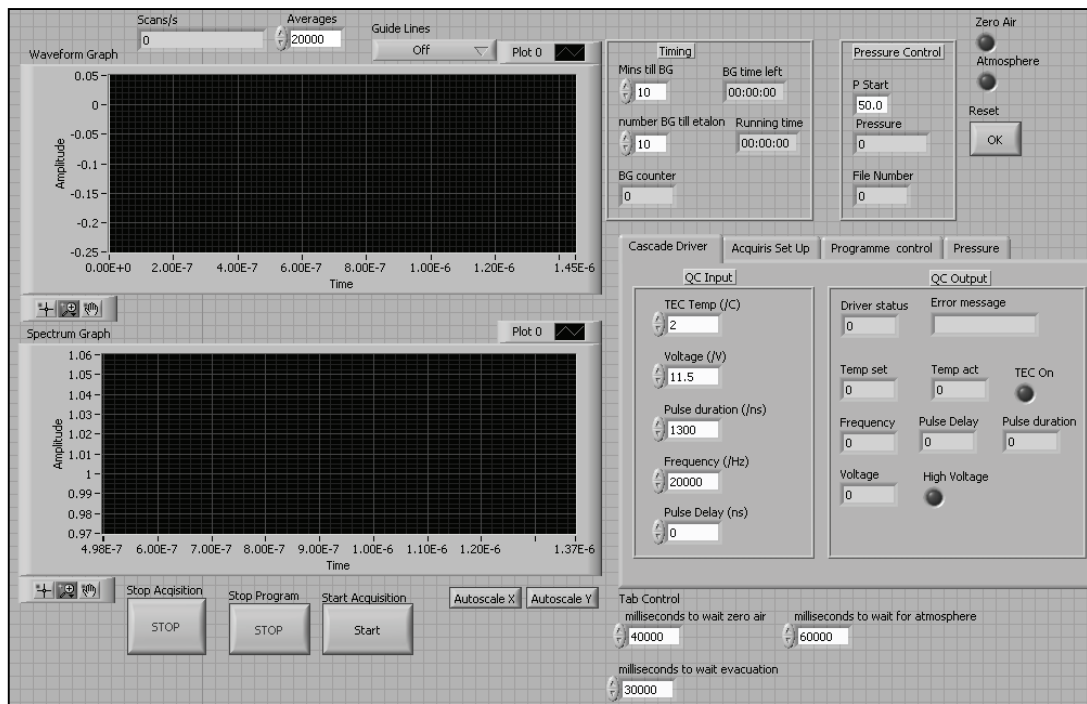


Figure 3.6.5: LabVIEW Control Panel for Data Acquisition and Instrument Control.

The program runs in a continuous loop. Once initialisation is complete, it can be left unattended. During the Oxford flights, the instrument was monitored. The graphs in Figure 3.6.5 plot the raw spectrum, and the "on-the-fly" transmission, which can be recalculated more accurately in post-processing the spectra. In this respect, the program is very similar to Acquisition Only.vi. A schematic diagram of Flight Program.vi is shown in Figure 3.6.6.

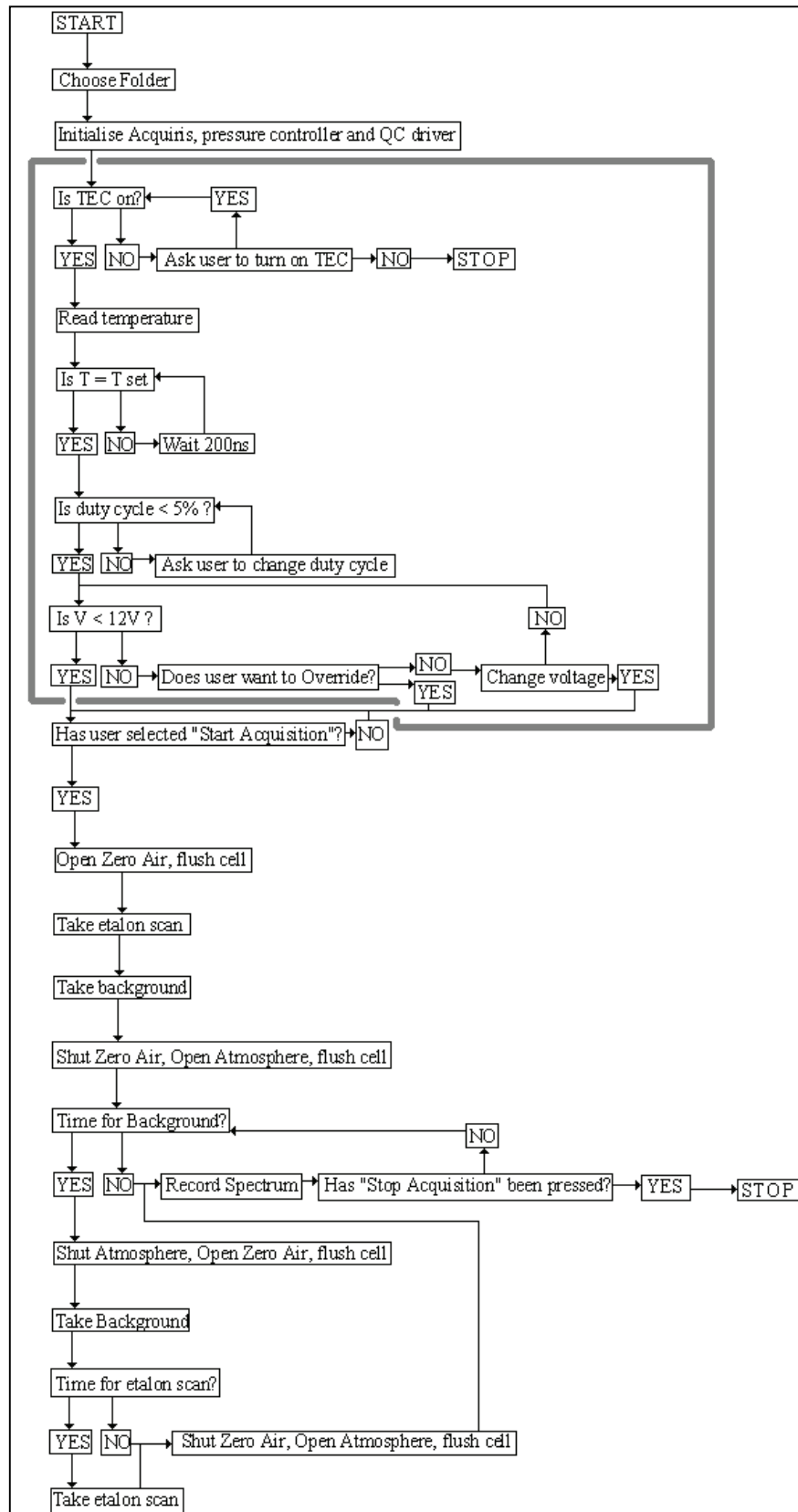


Figure 3.6.6: Operational sequence of Flight Program.vi. The parts in the grey box were later removed to run the program while driving the laser from newer laser drive software.

The main bug which required to be fixed in Flight Program 5.1.vi was a recurring error in initialising the Acqiris data acquisition card. The problematic frame is shown in Figure A.1.1 in the Appendix.

In version 5.1 of the program, Initialise Acqiris.vi generated a numerical output, which was fed into Query Horizontal Settings.vi. As these two subroutines were in the same frame, Query Horizontal Settings.vi attempted to use the number before Initialise Acqiris.vi had generated it. This crashed the flight program, but before the crash, the Acqiris would have been successfully initialised. This meant that on the second run, the numerical output was already there, ready to feed into Query Horizontal Settings.vi.

In order to remove the need to start the program twice, this frame was split in two, with a time delay of 1 s.

Following these repairs, the later removal of the laser drive functions created an even newer version, Flight Program 6 For New Lasers.vi, which has been functioning satisfactorily ever since.

The above is an overview of the in-house control software which was modified for this work. For a detailed description, see the PhD theses by Michael McCulloch [63] and Stephen Wright [64] who originally wrote the in-house software.

#### Acquisition Only for New Digitisers.vi

The only other control software modification required for this work, other than the controls for the Cascade 4-laser spectrometer which are discussed in Chapter 3.8, was the adaptation of Cascade Technologies' drive VIs for their AV1500 digitiser. Their digitiser software allowed the digitiser to act as a simple virtual oscilloscope, displaying signals with a limited saving ability of one file. Each file had to be manually saved.

To allow this digitiser to be used in a similar fashion to the Acqiris, automatic

sequential saving of files was necessary, as was the addition of an ability to save background graphs and calculate on-the-fly transmission spectra.

All these modifications took place within one frame of the program, which in the original version displayed the incoming signal. This frame is shown in Figure A.1.2 in the Appendix which compares the original program to the modified one.

Waveform Graph is the original spectrum display. This is now additionally fed into a "save background" case structure, operated by a toggle switch. Once a background has been saved, it is fed into a shift register and reused on each subsequent loop. When the toggle switch has not been pressed, the "save background" case structure changes to false and the same spectrum is returned for subsequent loops.

The waveform spectrum is divided by the saved background to give a transmission spectrum, which is plotted as Waveform Graph 2. If Autosave is selected, both spectra are then saved in the desired folder with the filename AVrun#.awd, where # is the filename. On each run of the loop, while files are being saved, the filename is increased and fed into a shift register. If Autosave is not selected, the filename remains constant.

Currently, the output file does not include a timestamp. To use the new digitisers for data acquisition, this feature would have to be added, which would be fairly simple.

### 3.7: Data Analysis Software

#### Datafix.vi

Datafix.vi is a LabVIEW virtual instrument (VI) designed to process data created by the LabVIEW data acquisition software described in Chapter 3.6. It was originally designed to adjust the baseline of spectra recorded using the Kolmar detector (see Figure 3.2.3), before recalculating the transmission spectra, then scaling them to take account of any loss of signal strength between recording the background and the signal.

The replacement of the Kolmar detector with the Vigo detectors has rendered the baseline correction and transmission calculation obsolete, although the transmission spectrum rescaling is still sometimes necessary if the signal strength changes between recording the background and recording the spectrum. This most commonly occurs when background spectra are recorded in the lab before or after field data is recorded. It is common for the detected signal to change slightly, either as a consequence of mechanical disturbance or environmental factors such as temperature.

The rescaling has an effect equivalent to scaling the background before calculating the transmission, which should not affect the accuracy of the transmission spectra. However some unexplained problem is affecting derivation of accurate mixing ratios from some spectra recorded during fieldwork. It is possible that the rescaling process introduces some form of distortion to the spectra, giving anomalous results.

The data to be processed should all be in one folder, with sequentially numbered filenames of the form title#.awd where title is set before acquisition and # represents the filename. Background files should be called titleB#.awd, B standing for background. They should be numbered to coincide with the filenames of regular files when they were recorded.

The Datafix.vi front panel shows 4 graphs which display the analysis in progress.

The block diagram of Datafix.vi is shown in Figure A.1.3 in the Appendix. It consists of a sequence of loops calling subVIs. Each subVI has also been made as a standalone routine in case only some parts of the analysis are necessary.

After asking for the folder where the data is located, the file title, and the number of files, the program works through each subVI, saving the revised data after each step.

Frame 0 reads the background files using BGfix.vi, and straightens out the baseline. The revised data is output as an array which then feeds into the case structure containing Polyfitta.vi. This is the only optional subVI, which can be used to substitute a polynomial fit for the original data. This option does not give very good results, so it is no longer used. If the user selects "yes" when asked "Do you want to fit a polynomial to the background?", the case structure containing Polyfitta.vi will run at "True", and the array will be fed into Polyfitta.vi for fitting. The fit is then output as an array. Otherwise it will run at "False", and the data will not be changed, the output array being the same as the input one.

The array is then written to a file named titleFB#.awd in the original folder. Although frame 0 is not supposed to output data corresponding to nonexistent files, a bug allows it to save an array of zeroes with filename 0. This is prevented by the case structure containing the "save as spreadsheet file" icon. If the filename is 0, this runs at "True" and no data is written to file. If a real filename is present, the data is saved, as well as being plotted to graph. When all files have been processed, BGfix.vi outputs "True" to the stop loop condition. The loop stops and Datafix.vi moves on to the second frame.

### BGfix.vi

BGfix.vi is shown in Figure A.1.4 in the Appendix. The Loop Iteration input comes from the WHILE loop in Datafix.vi. This gives the current filename. When this equals the desired number of files, the = function sends a True output to "WHILE condition to STOP", which stops the loop.

The "Open File" function (1) attempts to open the file. If the file exists, it opens it. If the file does not exist, it outputs an error. This feeds into the "select" triangles, which then output the last successful filename and corresponding filename. If there is a file, the error output returns False, so the new filename and filename are selected. If the previous filename is returned, the = function (2) returns True and the case structure does nothing with the data and the next iteration then begins. If a new filename is returned, the = function (2) outputs False, and the case structure analyses the data.

The circled area reads the data file and selects column 0, the raw spectrum, and splits it into chunks: 1, 2 and 3. Parts 1 and 3 are noise recorded before and after the pulse. They have their mean values calculated and subtracted to fix them on a baseline of 1. This is illustrated by the two MEAN and – functions in the grey boxes. Part 2 is the raw laser pulse which needs a baseline correction. This is assumed to be a linear correction, which is calculated by the functions in the blue box. The X values are read in from a file (Indices.awd) which is simply a list of the numbers 0 to 4000 in order. These X values are also used to plot the graph. This baseline correction actually has almost no visible effect in the final transmission spectra and could probably have been neglected.

The revised spectrum is then substituted back into the original array (black hexagonally boxed area). It is then output as an array and as a graph.

#### Polyfitta.vi

Polyfitta.vi is a simple program. The output data from BGfix.vi is read in as an array, and again split into 3 parts. This time, only the central part is needed. A polynomial fit is made to this part, which is then substituted for the original central data.

#### Graphfix.vi

The next stage of analysis is to similarly correct the baselines of the data files. Graphfix.vi in Frame 1 accomplishes this in the same manner as BGfix.vi treats the backgrounds. One additional step is to remove the leading blank cells at the top of

columns 1 and 2 where the timestamp is located in column 3. As there are files corresponding to every filename, the case structure to ignore nonexistent files is not included. The spectra are read in from files named title#.awd, and the corrected data saved to files named titleS#.awd. Once this is complete, a True output is sent to Datafix.vi, terminating the loop and moving on to the next frame.

Frame 2 of Datafix.vi then divides the corrected signal spectra by the corrected background spectra, to give a more accurate transmission spectrum using a subVI called Drawgraph.vi.

#### Drawgraph.vi

Drawgraph.vi is shown in Figure A.1.5 in the Appendix. The area in the blue box assembles the correct filenames for the input data (titleS#.awd), input background (titleFB#.awd) and output transmission spectra (titleA#.awd). The same check/select method (red box) of determining if a background exists is used as in Datafix.vi. (1) attempts to open a file, and if it can't, an error = True message forces (2) to choose the previous background again.

The signal is then divided by the background to give a transmission spectrum, which is then graphed and saved to a spreadsheet (black box) with filename titleA#.awd.

#### Basefix.vi

The final stage of the initial corrections uses Basefix.vi to fix the baseline of the transmission spectrum on 1. This corrects any increase or decrease in signal strength between the background and the signal. The transmission spectra are read in with filenames titleA#.awd, and again split into 3 as illustrated by BGfix.vi: noise before and after the laser pulse, and the actual data. The central part then has its mean value calculated. As atmospheric spectra only have a few, weak absorption lines, the lines themselves do not overly affect the mean value. The central part is then divided by the mean value, fixing the baseline on 1. This corrected data is substituted back into the original array, which is then saved as titleSA#.awd.



Basefix.vi is also used as a standalone VI to correct more recent data recorded by the Vigo photodetector, as the loss/gain of signal strength, often caused by beam wander, is still an occasional problem during fieldwork.

The rescaling has an effect equivalent to scaling the background before calculating the transmission spectrum. Either method should have no effect on the accuracy of the transmission spectrum, being equivalent to having recorded a background spectrum at the same power level as the absorption spectrum in the first place.

### 9-Point Savitzky-Golay.vi

When using the Kolmar detector, to reduce the noise in the transmission spectra, it was often necessary to smooth the data. This was accomplished using a 9-point Savitzky-Golay smoothing routine [65], which is effectively a weighted average of 9 points, centred on each point in the array in turn. The baseline corrected data files (titleSA#.awd) were opened in similar fashion to the subVIs of Datafix.vi, then the data array was fed through "9-Point Savitzky-Golay.vi", illustrated in Figure A.1.6 in the Appendix.

The routine works as a subVI, so the input and output data are fed in from another VI. This allows this subVI to be placed into any VI where smoothing of data is required. The input array is worked through point by point. At each point,

$$Y'_i = \frac{-21(Y_{i-4} + Y_{i+4}) + 14(Y_{i-3} + Y_{i+3}) + 39(Y_{i-2} + Y_{i+2}) + 54(Y_{i-1} + Y_{i+1}) + 59Y_i}{231} \quad (3.7.1)$$

where  $Y$  is the old value and  $Y'$  is the new value. This implementation of the smooth means that the first and last 4 points of the array will be distorted. For spectra, as the first and last few hundred points are noise on either side of the laser pulse, this does not matter. For other uses, it could be an issue

### Fitting peaks

The next stage in the data analysis is the fitting of any absorption lines with a Gaussian or Lorentzian lineshape. While a Voigt profile would be the most accurate fit, for most work, a Lorentzian is a close enough approximation. Accurately fitting a

Voigt profile is not easily accomplished in LabVIEW. For the unexpectedly low pressure spectra from Penicuik, a Gaussian fit was a closer approximation. Figure 3.7.5 shows a fitting frame of "Fit Peaks Penicuik.vi" for a methane line.

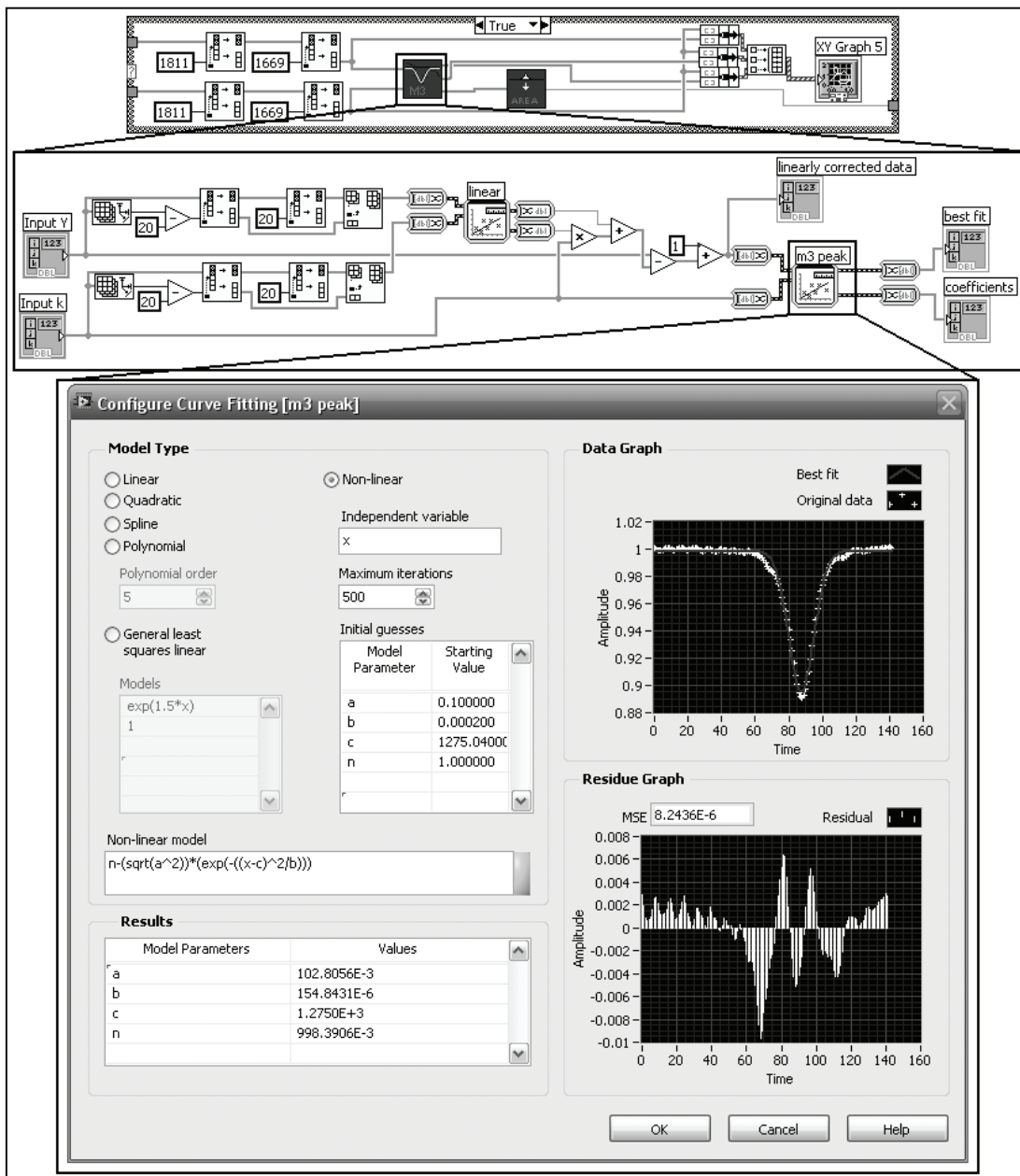


Figure 3.7.5: Fitting spectral lines in LabVIEW.

The transmission spectra are opened as described above to obtain an array of Y data. A corresponding array of calibrated wavenumbers is obtained from a saved file Kindices.awd. The region containing a spectral line is then cut from the rest of the array by the yellow boxes in the frame. There is one copy of this frame for each line

to be fitted, each cutting a different piece of the data.

The selected K and Y data are fed into a subroutine. Each individual line has its own subVI with different constants but the same structure. The subroutine for methane line 3 is shown below the fitting frame. The subroutine uses the first and last 20 points of the data to be fitted to create a straight line fit to the baseline. This is necessary to remove any baseline distortion remaining after the earlier processing. This is subtracted from the data to give a baseline of 0. This then has 1 added to fully correct the transmission spectrum baseline.

The "m3 peak" fit is then used to fit a Gaussian curve of the form:

$$y = n - \sqrt{a^2} e^{-\frac{(x-c)^2}{b}} \quad (3.7.2)$$

where  $n$  is the baseline level, which should be 1;  $c$  is the line centre;  $a$  is the line strength and  $b$  is proportional to the full width at half maximum. The fit function outputs an array consisting of  $a, b, c, n$ , from which "Area Gaussian.vi" can determine the integrated intensity of the fitted lineshape from  $-\infty$  to  $+\infty$ . From this it is easy to determine the mixing ratio of the gas by comparing this intensity to HITRAN [49] as described in Chapter 3.3. The original data, baseline corrected data and fit are plotted in a graph.

The descriptions above cover the main steps in analysing spectra using LabVIEW VIs. Numerous variations of these have been used for different batches of data, and assorted VIs for specialised processing of awkward data have been written, but the above covers the basic methodology used throughout. The software used for the 4-laser spectrometer is discussed toward the end of Chapter 3.8, although it too used much of the same basic programming as the above routines.

### 3.8: The 4-Laser Miniature Spectrometer

#### Original Design

The Cascade CT2400 4-laser system was used in its original form for the flight based work carried out from Gloucester Airport. Although this flight was successful, some limitations were discovered which required improvements to the design of the system. The modifications are discussed later.

In its original design, the spectrometer consisted of a sealed box containing 4 QC lasers (Table 3.8.1 lists the characteristics of these lasers), electronics to drive the lasers, a pressure controller, 76 m gas cell and built in pump. The drive electronics include a Cascade AV1500 digitiser as described in Chapter 3.2: digitisers and Chapter 3.7. The box is shown in Figure 3.8.1 with some of the side panels removed to show the inside. Figure 3.8.2 shows the other end of the box with gas inlet and exhaust visible.

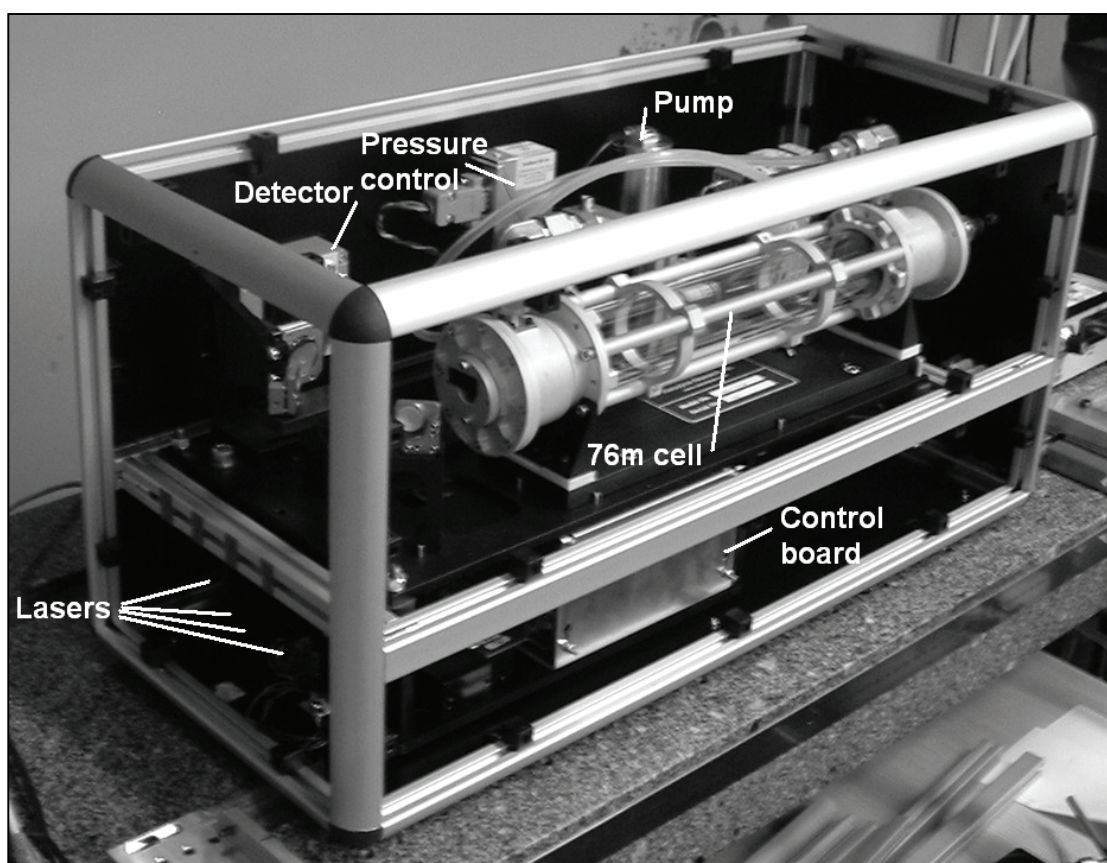


Figure 3.8.1: The original design of the 4-laser system.

Laser	Nominal Wavelength / $\mu\text{m}$	Gas detected on-the-fly	Other gases in range	Set temperature / $^{\circ}\text{C}$	Voltage / V	Pulse length / ns
0	6.14	$\text{NO}_2$	$\text{H}_2\text{O}$	23	11.4	500
1	4.87	$\text{CO}_2$	CO	24	9.5	500
2	7.84	$\text{N}_2\text{O}$	$\text{CH}_4$	11	9.4	800
3	5.26	NO		24.5	9.0	600

Table 3.8.1: Vital statistics of the 4 lasers originally used in the 4-laser system.

The system measures 62 cm x 34 cm x 40 cm and weighs 22 kg. The power consumption is a maximum of 600W. The system is driven by a laptop, partitioned so as to be able to run either Windows XP or the Ubuntu implementation of Linux. There are two possible ways to operate the 4-laser system. By using the alignment software (either compiled C++ running under Ubuntu or LabVIEW running under Windows), it is possible to run one laser and view its pulse. By modifying the LabVIEW VI (Alignment.vi), a version of Acquisition Only was built for this system, using only one laser at a time. This makes it possible to use one laser to give us a more compact version of the portable spectrometer.

Alternatively, the full control program for the system is compiled C++, and can be run from the Ubuntu partition of the laptop. This is the software which would be commercially available with the system, which runs each laser for 500 pulses which are then averaged. The averaged spectrum from each laser is then fitted with a calculated line shape to derive the concentrations, which are then plotted. An additional logging function, normally deactivated on commercial systems, saves the 500-average spectrum for each of the 4 lasers, various intermediate stages in the fitting process, the 4 gas concentrations, the set pressure, the box temperature and a timestamp in an xml file.

The operating pressure of the cell is set by a plug-in LM1117-T voltage regulator. The fixed voltage generated sets the pressure independently of the software. The standard pressure of the system is 152 Torr with a 2.5 V regulator, which can be changed by using a different voltage.

The control software is discussed in more detail later, along with the data analysis software.

### Modifications

The most noticeable issue during the first flight with the 4-laser system was the rise in temperature inside the box. As the flight was in February, the initial temperature was unusually low (5 °C) so the 12 °C rise to 17 °C did not have any serious effects on the system. Nonetheless, this indicated a clear need for additional cooling of the system.

To this end, a "cooling cube" from Farnell was clamped to the baseplate with a layer of thermal contact paste between to ensure good conduction. The cooling cube was effectively a box of fine aluminium wires. With computer fans bolted on each end to force air through, it made an effective heatsink. The fans were wired to a jack which was mounted on the end panel. This allows them to be run from a 12 V transformer.

As the baseplate was at the bottom of the box, the cooling cube made the spectrometer too big to fit in the box. It was necessary to buy extra lengths of aluminium extrusion to extend the box by approx. 10 cm. The extended box is shown in Figure 3.8.2. This photo was taken from the other end and also shows the gas inlet and exhaust.

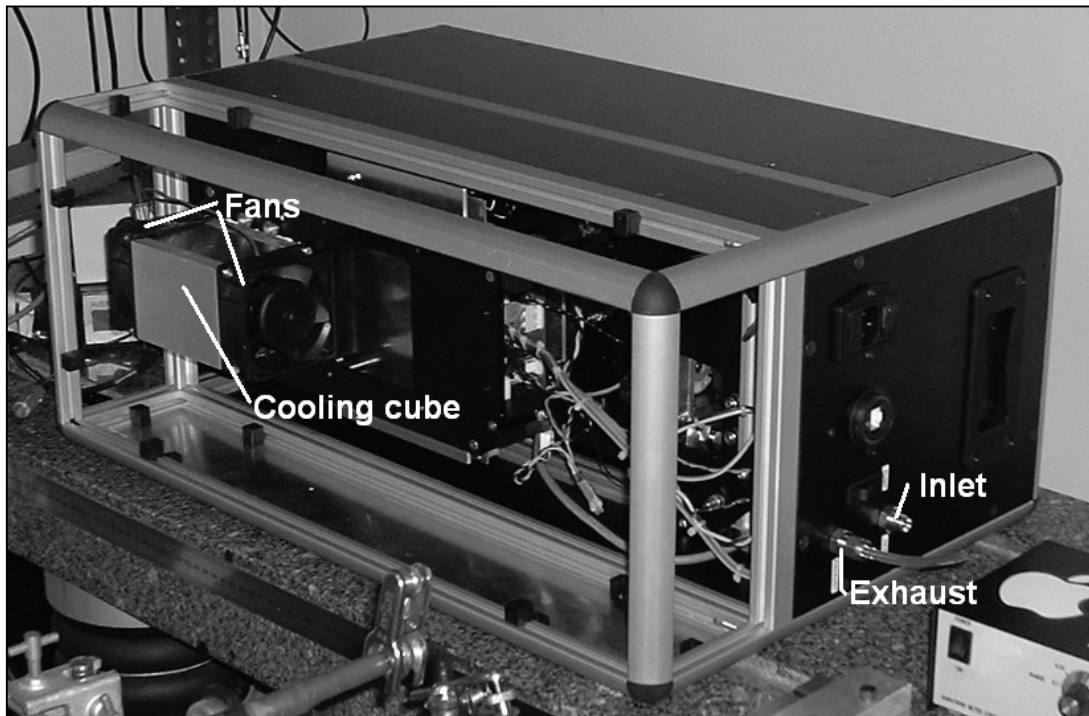


Figure 3.8.2: The extended box, with the cooling cube in place.

Of the panels removed for the photo, the original base panel was reused, the long sides were aluminium cut to size, one of which is shown, and the two short sides were mesh sheeting to ensure good airflow through the box. A new top panel was also made up in mesh to allow convection to dissipate heat generated by the pump.

The main modification was carried out by Cascade Technologies, and involved "packaging" the lasers to enclose them from the atmosphere. This should, in addition to improving the electrical contacts' resistance to vibration, allow the lasers to be run at colder temperatures without any problems with condensation. At the same time, the 6.14  $\mu\text{m}$  laser (Laser 0), which was showing early signs of failure, was replaced with a similar laser. The packaging also resulted in slight changes being required to some lasers operating parameters. Table 3.8.2 lists the revised laser parameters.

Laser	Nominal Wavelength / $\mu\text{m}$	Gas detected on-the-fly	Other gases in range	Set temperature / $^{\circ}\text{C}$	Voltage / V	Pulse length / ns
0*	6.13	$\text{NO}_2$	$\text{H}_2\text{O}$	15	7.5	500
1	4.87	$\text{CO}_2$	CO	24	9.5	500
2	7.84	$\text{N}_2\text{O}$	$\text{H}_2\text{CO}$ , $\text{CH}_4$	9	9.4	800
3	5.26	NO		28	9.0	600

Table 3.8.2: Vital statistics of the 4 lasers now used in the 4-laser system. \*: This is the replacement  $1631\text{ cm}^{-1}$  laser

As noted earlier, the pressure was originally maintained at 152 Torr by means of a 2.5 V voltage regulator of type LM1117-T. This was later replaced by a 1.8 V regulator of the same type which reduced the cell pressure to 108 Torr. This reduced pressure broadening, leading to less line overlap without being so low to allow rapid passage effects to cause difficult line shapes.

### Software

As mentioned above, there are two methods of controlling the system, either running in full automatic recording mode using compiled C++ running on the Ubuntu partition of the laptop, or running one laser at a time using software originally designed for aligning the system. This alignment software is written both in compiled C++ for the Ubuntu partition, and as a non-compiled LabVIEW VI for the Windows partition of the laptop. Both methods are discussed below, as are the routines required to retrieve data.

The C++ alignment software is identical in function to the original LabVIEW version, so it is not separately described since the LabVIEW version was always used to align and test the box. A very early modification to this software was the addition of the ability to save data from the LabVIEW alignment VI.

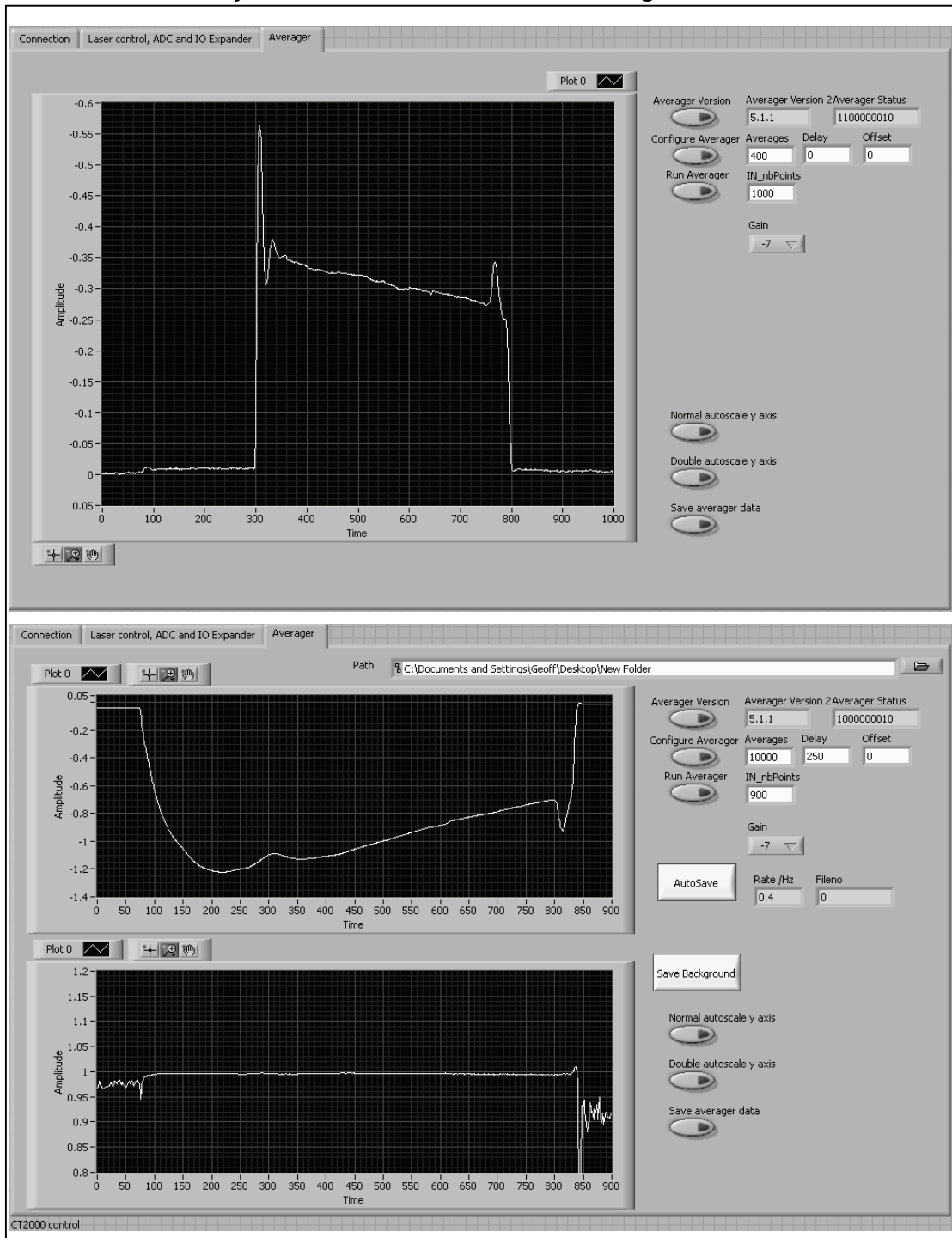


Figure 3.8.3: Initial and modified front panel of Alignment.vi.



Alignment.vi and its modified version, Acquisition by Gas Sensorwith date.vi both allow one laser to be run, and its output pulse as detected by the box's built-in Vigo to be displayed. The modifications to the program entailed building in the ability to save sequential files, and to store background graphs. The original and modified Averager panes of the front panel of Alignment.vi are shown in Figure 3.8.3.

The main visible changes are the addition of the filepath selection box, the second (transmission spectrum) graph and the "Save background" and "AutoSave" buttons. The method of adding in the saving is identical to that used for the Cascade digitiser programs (see Chapter 3.6: Acquisition Only for New Digitisers.vi). This program, however, does include a datestamp. The "Autosave= True" frame is shown in Figure 3.8.4, illustrating the datestamping.

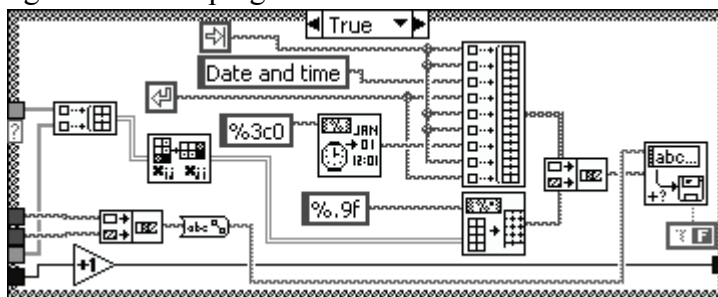


Figure 3.8.4: Datestamping in Acquisition by Gas Sensorwith dates.vi.

This saves the data in the same format as Acquisition Only.vi and Flight Program.vi, allowing existing analysis routines to be used to process the data.

The compiled C++ software to run all the functions of the gas sensor is described in detail in the user manual [66]. It triggers 500 pulses from Laser 0, which are then averaged, followed by 500 pulses from Laser 1, which are then averaged, followed by Laser 2, then Laser 3. The 4 averaged spectra each contain 1 line which is analysed on-the-fly. A synthetic 2nd order polynomial baseline is calculated to generate a transmission spectrum, the data is converted from time to wavenumber using a calibration calculated by Cascade for each laser, then the line is fitted with a lineshape calculated for the original pressure (152 Torr). Both the baseline and the peak fitting use a least-squares method. The accuracy of the concentrations calculated by the supplied software is  $\pm 5\%$ .

With the pressure now set to 108 Torr, there is a slight discrepancy between the real data and the fit. As this fit is generally only used as an indication while logging, the final mixing ratios derived in post-processing which use the correct pressure, are unaffected.

The 4 averaged spectra, 4 concentrations, box temperature and pressure are all saved in an xml file along with the intermediate stages in the fitting of the lines. Originally the set pressure was saved, but following the modifications to the hardware described earlier, Cascade modified the software to record the actual cell pressure. The saving ability is intended as a diagnostic tool for Cascade, but it also gives us the ability to check other spectral lines which are not fitted on-the fly.

The calculated concentrations are displayed on a graph which shows up to 30 minutes of data. The concentrations are also saved in a database file from which they can be retrieved by a Cascade program, Data Explorer. Normally the original spectra are used to recalculate mixing ratios as a double check.

The original spectra can be extracted from the xml files where they are saved as `real_data_shifted`. This is accomplished using a VI supplied by Cascade, called `ExtractXML.vi`. This populates a spreadsheet with the raw spectra, one spectrum in each column, leading to a very large file. It is also necessary to retrieve the timestamps. The files are named `fit.YYYY-MM-DD_hh-mm-ss-ddd` where YYYY is the year, MM the month, DD the day, hh the hour, mm the minute, ss the second and ddd the first three decimal places of the second. The timestamps can be retrieved from the filenames using `ExtractXML Timestamps.vi`, which is based on `ExtractXML.vi`. This routine is shown in Figure A.1.7 in the Appendix.

The extracted spectra are split into separate files, and then transmission spectra are calculated using a variation of `Drawgraph.vi` (See Chapter 3.7). This requires background spectra which should be recorded each time the spectrometer is run. The transmission spectra are then processed as described in Chapter 3.7. All lines are fitted, allowing more than the 1 gas per laser plotted at the time to be measured.

### **3.9: Conclusion**

Our instruments have been continually improving across the course of this work, building up from "the brick" driving a single laser with signals detected by a liquid nitrogen cooled detector to the newer drive system with signals picked up by a Peltier cooled detector, eliminating the need to use liquid nitrogen, and greatly improving the signal to noise ratio.

For fieldwork, the Cascade 4-laser system offers us the ultimate refinement to date, allowing us to use more than one laser simultaneously for measurements, while still saving whole spectra which can later be processed to retrieve at least 11 spectral lines at default parameters. It is probable that there will be more detectable lines, depending on the gases being studied.

## Chapter 4: Experimental Results

### 4.1: Introduction

Over the course of this research, in addition to lab based work, several field based projects have been carried out. These projects are described in chapters 4.2 to 4.6.

Chapter 4.2 describes the operation of the spectrometer at the Easter Bush field site of the Centre for Ecology and Hydrology near Edinburgh. The aim was to investigate the effect of spreading an artificial nitrate fertilizer on the field surrounding the test site had on the nitrous oxide level in the air. This work was carried out in parallel with the lead salt laser spectrometer which Famulari *et al* [12] use to perform similar measurements, on an annual basis.

Chapter 4.3 describes in-flight measurements. Initial results were of methane, water vapour and nitrous oxide mixing ratios throughout a return flight from Oxford to Haverfordwest and a circuit of Oxfordshire. The portable spectrometer was installed in the NERC ARSF aircraft [7] to perform these measurements. Another flight was carried out later, using the Cascade 4-laser system to measure methane, nitrous oxide, carbon dioxide, carbon monoxide and water vapour mixing ratios during a flight from Gloucester to Haverfordwest and back.

Chapter 4.4 describes single-pass spectroscopy of a carbon / argon / hydrogen plasma used for chemical vapour deposition of artificial diamond. This work was carried out in collaboration with Prof. Mike Ashfold's group in the Chemistry department at Bristol University.

Chapter 4.5 describes single pass free-space spectroscopy through the exhaust plume of a Rolls-Royce turbojet engine. This work was carried out in collaboration with Rolls-Royce and Scitech Consultants.

Chapter 4.6 describes the first field tests of the modified Cascade 4-laser system, measuring exhaust emissions from diesel bus engines across the twentieth century.

Chapter 4.7 describes laboratory investigations of nonlinear effects including rapid passage and free induction decay in water vapour, acetylene, ammonia, methane and nitrous oxide.

Chapter 4.8 describes a small amount of laboratory work using two lasers, one triggered from the other to give a "spectrum" consisting of two pulses, one from each laser. This allows us to probe two separate regions of the spectrum simultaneously.

## 4.2: Nitrous Oxide During Field Fertilization

During May 2007, the spectrometer was operated at the Easter Bush field site of the Centre for Ecology and Hydrology (CEH) near Edinburgh. The object of this work was to measure the atmospheric level of nitrous oxide before and after the spreading of an artificial nitrate fertilizer on the field. Nitrate fertilisers are frequently used in agriculture, and usually have to be overapplied as a considerably quantity of the nitrates are later lost to the air. CEH have been monitoring the nitrous oxide level during previous years [11, 67, 68] using a lead salt diode based laser absorption spectrometer, later replaced by a QC laser system using the inter-pulse tuning method [69] and have observed increases in the airborne nitrous oxide level following field fertilisation using micrometeorological methods [70].

Nitrous oxide emission as a consequence of fertilisation of soil has also been measured by Kaiser *et al* [71] using soil cover box systems, analysing the N<sub>2</sub>O concentration using a <sup>63</sup>Ni-electron capture detector equipped with an automatic sample injector system [72]. Gas chromatography has also been used with the closed chamber technique by Hellebrand *et al* [73].

This work utilised the original portable spectrometer system, using the Kolmar detector. In an attempt to obtain a high flow rate through the cell, two Edwards rotary pumps in parallel were used. This gave a flow rate of 4.5 L/min through the cell. Unfortunately the use of these pumps also caused a drop in cell pressure, affecting the lineshape. With the cell pressure around 35 Torr, the flush time for the cell was approx. 2 s. The instrument was running continuously during daytime with background scans taken at half hourly intervals.

Easter Bush is south of Edinburgh to the east of the Pentland Hills. The prevailing wind direction is southeast, so there is relatively little urban pollution from Edinburgh at the site. The approximate position of the site is shown in Figure 4.2.1.

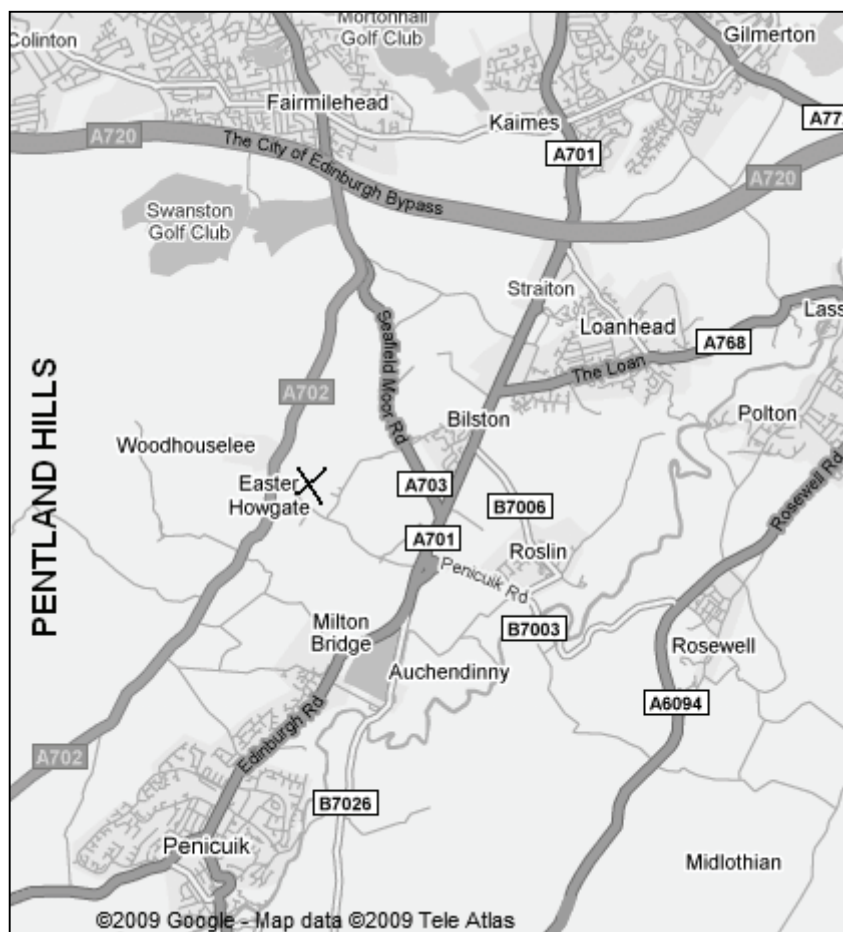


Figure 4.2.1: Location of the field site (marked by the X), south of Edinburgh.

With very little urban pollution from Edinburgh, the methane level was very close to background level. Figure 4.2.2 illustrates a typical spectrum recorded at Easter Bush, run at around 35 Torr and a simulated spectrum at 35 Torr using the Northern Hemisphere background levels: 319 ppb N<sub>2</sub>O; 1852 ppb CH<sub>4</sub>; 8000 ppm H<sub>2</sub>O. The methane peaks at Easter Bush are very close to the Northern Hemisphere background level [74].

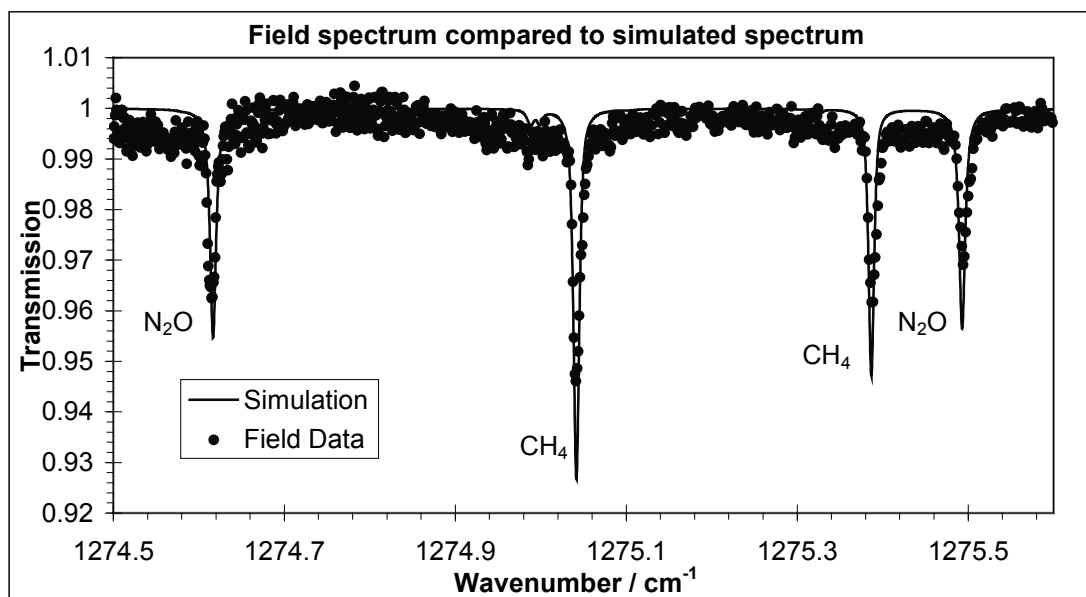


Figure 4.2.2: Simulated background level spectrum (line) compared to field data (points).

The simulated spectrum has been offset slightly to accurately align the baselines.

A short set of calibration data was recorded by flowing gas from a gasbag through the cell. This gas was supplied by BOC with a calibrated content of 303 ppb of N<sub>2</sub>O. The measurements obtained are shown in Figure 4.2.3 below. With an average mixing ratio measured to be 231 ppb, a correction factor of 1.31 was therefore applied to all results calculated from the field data. The need for this correction may be a result of the rescaling (see pages 43 and 77).

Following this correction, the values measured were typically between 300 ppb and 400 ppb. The Northern Hemisphere background level is 322 ppb [5], which is in good agreement with these measurements, although the variation within these results is less likely to be real and is probably a consequence of the poor fit to the absorption lines at low pressure.



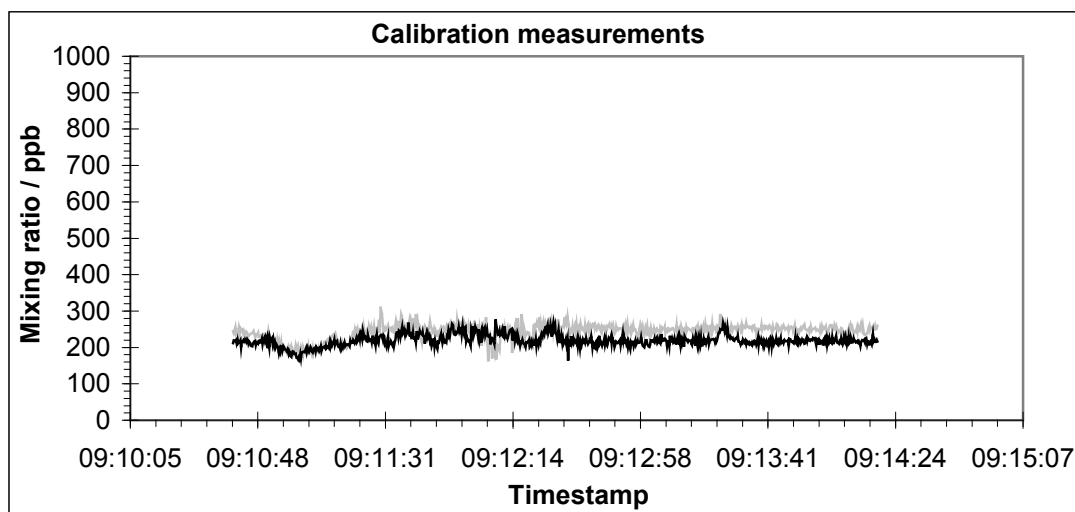


Figure 4.2.3: Mixing ratios of nitrous oxide derived from the 1274.22  $\text{cm}^{-1}$  line (black) and the 1275.49  $\text{cm}^{-1}$  line (grey) while measuring a calibration mixture containing 303 ppb.

On May 16, a farmer spread an artificial nitrate fertilizer on the field surrounding the test site. Following the fertilization, there was no change in the nitrous oxide level until after it rained at the weekend. During the week commencing 21 May, there was a continual increase in nitrous oxide level. (See Figure 4.2.4). Similar increases have been observed in previous years by the group at CEH [11, 67]. Over the course of measurements, the methane level remained stable, with fluctuations presumably corresponding to changes in wind speed, as discussed later.

The occasional spikes seen in Figure 4.2.4, particularly toward the end of the month are artificial, and occur when the laser has drifted so far from the background spectrum that the transmission spectrum is impossible to fit within the constraints of the fitting routine used. This can either occur when the signal to noise ratio becomes too low, usually caused by the signal strength dropping as a result of thermal creep, vibration or condensation; or when the transmission baseline is insufficiently close to flat which can occur if the laser shifts wavelength slightly or changes temporal profile slightly.

The increase in nitrous oxide following a weekend of rain indicates that a considerable quantity of nitrogen added to the soil in fertilizer must then be lost to the air. This necessitates overfertilizing of farmland to ensure sufficient nitrates

remain in the soil to successfully fertilize crops. Soil processes contribute about 70% of annual nitrous oxide emissions to the atmosphere [75], so farming is a serious source of airborne nitrous oxide pollution.

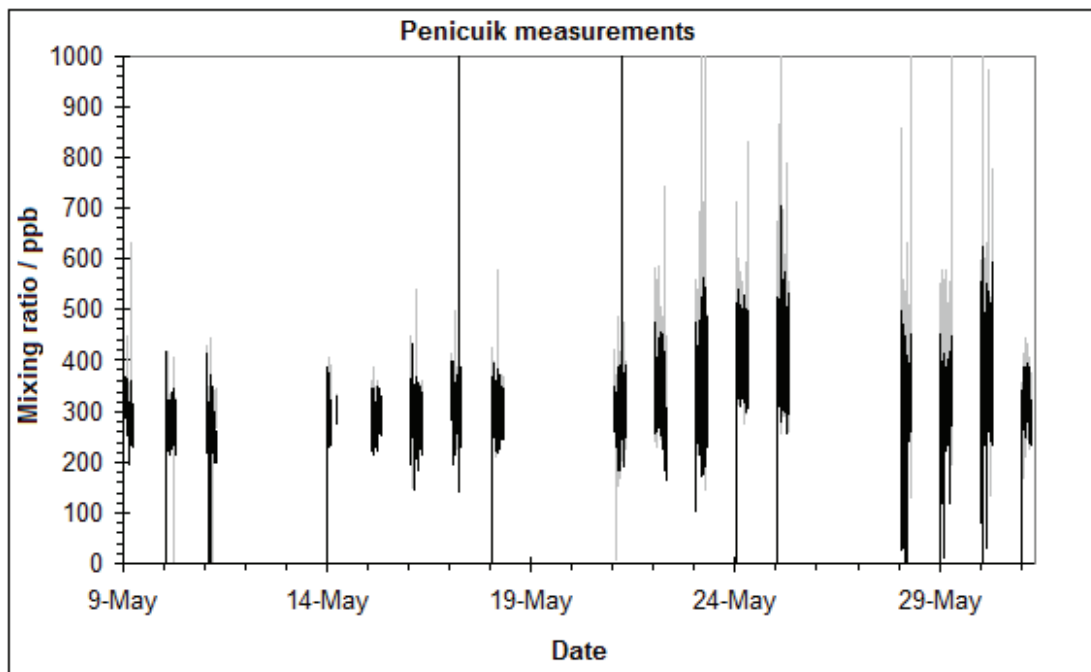


Figure 4.2.4: Mixing ratios of nitrous oxide derived from the  $1274.22\text{ cm}^{-1}$  line (black) and the  $1275.49\text{ cm}^{-1}$  line (grey).

The original intention of this work was to compare results from our instrument with those obtained by the lead salt laser spectrometry which Famulari *et al* [12] were running at the same time. Their analysis is still ongoing so no comparison is yet possible. Their instrument recorded 10 readings per second. We attempted to obtain 5 spectra per second to approach their data acquisition rate. To achieve this, it was necessary to maintain a high flow rate through the cell.

The attempt to speed up the flow by using two pumps in parallel exceeded the limit of the mass-flow controller. The cell reached equilibrium between the high rate of pumping and the influx of air through the narrow bore piping at around 30 Torr. At this low a pressure, lineshapes were distorted by rapid passage effects (see Chapter 2.5). If the wind happened to blow directly into the inlet, the ram effect meant the equilibrium pressure was higher, and lineshapes were closer to the Lorentzian shape. With such a large quantity of data, it would have been impractical to calculate a

specific rapid passage lineshape for each of the lines in the spectrum for every individual spectrum. For this reason, a Gaussian fit was used as an approximation. The accuracy of this fit varied with cell pressure as described, so variations in wind speed cause fluctuations in the measurements.

The volume of data generated by subsecond measurements also caused some difficulties. Throughout this work, 4 spectra were recorded per second. Initially these were saved as two-column text files. After a few hours of data acquisition, the recording slowed drastically. It seems that Microsoft Windows XP assigns a certain "block" of memory to a subfolder when it is created. Once the data being saved exceeds this memory space, data are scattered through the hard drive wherever space can be found. This slows the computer down.

In an effort to avoid this, on the 15th and 16th of May, spectra were saved as one row of data in one big text file covering 30 minutes. This did reduce the memory space, but created some files which were too big for any normal Windows program to open. It is possible to split text files without opening them under Linux, which proved successful on the oversize files. Using a LabVIEW VI, the split files were then further split back to individual spectra which were then analysed using existing LabVIEW routines.

From the 17th May onwards, spectra were again saved as individual files, and the acquisition VI was modified to change folder every 30 minutes when a new background was recorded. This proved to be a satisfactory compromise, although it was necessary to manually create around 15 sequentially numbered folders every morning before starting recording.

As a result of a loose connection to the Baratron, no pressure data was recorded for the 24th, 25th and 30th of May. It was necessary to derive the pressure from the methane lines, assuming a constant methane level was present across these days. The fitting routine was used in reverse to derive pressures for a fixed (assumed) mixing ratio of methane. These derived pressures were then used to calculate the nitrous

oxide mixing ratio. This approach gave readings consistent with the surrounding days, the only drawback being that the methane mixing ratios cannot be determined.

The results obtained by deriving the pressures from the methane lines were in good agreement with the results obtained from measured pressures on other days, suggesting that this method could well be used in some other setup if pressure recording was not practical.

Other than the anticipated increase in nitrous oxide following the fertilization, the main conclusions from this work were discovering limitations and troubleshooting dodges of the spectrometer system [76], which can be summarized as follows.

Subsecond resolution of gas levels is impractical, as it is hard to change the full cell volume (approx. 3 L) in less than a second. In order to do so, it is necessary to pump so hard that the mass-flow controller cannot open wide enough to maintain the pressure. Consequently, to gain subsecond sampling, a smaller volume cell is necessary, such as the 0.5 L cell in the Cascade 4-laser system. Even using this, to be able to flush the cell in 0.5 s requires running at a pressure of 57 Torr. This is close to the limit of normal absorption lines before rapid passage effects are seen in some gases. Further experiments would be necessary to ascertain whether accurate results can be obtained under these conditions.

Measurement of gas mixing ratios by fitting absorption lines becomes difficult below around 50 Torr, as a consequence of the rapid passage lineshape. It is easier to work above 50 Torr and fit a Gaussian or Lorentzian lineshape as appropriate.

Taking excessive time between backgrounds leads to unfittable spectra. No experiments to determine maximum time between backgrounds have been performed. While the airborne work in the next chapter used 10 mins between backgrounds and gave useful results, this work only took backgrounds every half hour, which led to spikes in the results caused by poor fitting.

### 4.3: In-Flight Atmospheric Measurements

Atmospheric levels of pollution can, in many cases, be most accurately measured by instruments which are airborne and thus in the atmosphere. Atmospheric gases which contribute to global warming include methane, carbon dioxide, water vapour and nitrous oxide.

Other flight based measurements of atmospheric gases include measurements of  $\text{NO}_x$  and CO during the Australian monsoon [77], investigating the effect of lightning on the  $\text{NO}_x$  mixing ratios. These measurements were carried out using an instrument designed to detect the chemiluminescence of NO in the presence of ozone, catalysing  $\text{NO}_2$  to NO by a gold surface [78]. CO was meanwhile measured by a fast-response resonance fluorescence instrument [79].

The above instruments were also used aboard the FAAM aircraft [80], conducting measurements of emissions from Lagos [81]. CO and  $\text{NO}_x$  were measured as described above, while canisters of air were also collected for later analysis using a dual channel gas chromatograph with flame ionisation detectors to calculate the levels of benzene and acetylene present.

Stratospheric measurements of methane and nitrous oxide have been carried out using a CW QC laser spectrometer operated in a fast repetitive-sweep mode aboard the NASA ER-2 high altitude aircraft [82]. Measurements were performed at heights of up to 20 km, with the instrument capable of detecting methane present at levels around 2 ppb.

Other measurements carried out aboard the NERC Dornier [7] include observations of a chemical equator in the atmosphere [83], measuring CO using a fast-response fluorescence detector; ozone using ultraviolet absorption spectroscopy and volatile organic compounds (VOCs) by collection of samples which were later analysed by gas chromatography.

### Oxford Airport Based Flights

On 19 October 2006, the spectrometer was set up in the NERC ARSF Dornier aircraft [7] to conduct measurements on methane, water vapour and nitrous oxide spectral lines throughout a return flight from Oxford to Haverfordwest and a circuit of Oxfordshire [84, 85]. The outward flight was at an altitude of 600 m, and the return flight and Oxford circuit at 2000 m. Owing to air traffic control, the plane was unable to follow the same route in both directions for most of the flight. The objective was to assess the performance of the instrument while in flight, and endeavour to discover noticeable differences flying over pollution sources such as exhaust plumes above main roads.

The atmosphere was sampled through a forward facing sampling inlet at the front of the aircraft, shown in Figure 4.3.1.



Figure 4.3.1: The snorkel on the aircraft roof, as used to sample the atmosphere in flight.

A schematic of the vacuum system is shown in Figure 4.3.2. The constant flow through the cell created by the pump was improved in flight by the ram effect of the motion of the plane.

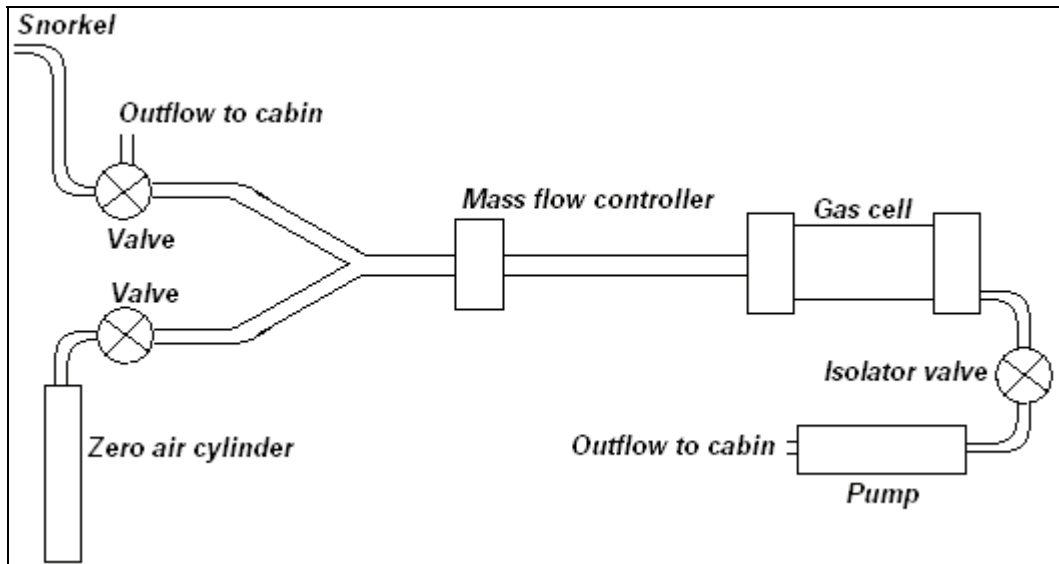


Figure 4.3.2: Schematic of vacuum system.

The pump used in the plane is oil-less (Rietschle Thomas VTE6), with a maximum flow rate of 100 L/min and 150 mBar vacuum capability. The actual flow rate through the cell was not measured, but the constricting effect of the associated pipework means it would be considerably less than 100 L/min. During laboratory tests, the time to completely change the air in the cell was calculated as 2 s using a similar pump.

The incoming air was either allowed through the mass flow controller, or diverted into the cabin while background spectra were taken. To take a background, with the inflow diverted to the cabin, the cell was evacuated for 30 s. Another valve was then opened to a cylinder of zero grade air. A 60 s delay was used to allow the zero air to flush out any remaining atmospheric gases, then the background spectrum was taken. The valve to the atmosphere was then reopened, and following a 40 s flushing delay, spectrum recording started again.

The laser was operated in pulsed mode, a 1300 ns top-hat shaped current pulse being applied to the QC laser operating at 8  $\mu\text{m}$  (around 1270  $\text{cm}^{-1}$ ). The resultant frequency downchirp gave a scan range of approx. 3.5  $\text{cm}^{-1}$ . To ensure that the spectral output covered several methane, nitrous oxide and water absorption lines during each pulse, the substrate temperature of the QC laser was set to 2  $^{\circ}\text{C}$ . The

pulse duration was 1300 ns, the pulse repetition frequency 20 kHz, and the operating voltage 11.5 V. 20,000 successive spectra were averaged. Software limitations led to a time interval of two seconds between each recorded spectrum.

The absorption lines visible using the above parameters are shown in Table 4.3.1, which also lists the instrumental and pressure broadening contributions to the linewidths of the lines from which mixing ratios were derived.

Label	Molecule, label	Wavenumber <sup>a</sup>	Observed FWHM <sup>b</sup> (linewidth /cm <sup>-1</sup> )	Calculated FWHM (Doppler)	Calculated FWHM <sup>c</sup> (Chirp rate)	Calculated FWHM <sup>a</sup> (Air broadening)
w1	H <sub>2</sub> O	1276.62804	Not measured.			
w1	H <sub>2</sub> O	1276.62619	Not measured.			
w2	H <sub>2</sub> O	1275.66245	0.024	0.0037	0.0068	0.0215
m1	CH <sub>4</sub>	1276.84431	Not measured.			
m2	CH <sub>4</sub>	1275.38678	0.018	0.0040	0.0064	0.0140
m3	CH <sub>4</sub>	1275.04168	0.018	0.0040	0.0059	0.0154
n1	N <sub>2</sub> O	1276.36576	Not measured.			
n2	N <sub>2</sub> O	1275.49287	0.024	0.0024	0.0067	0.0206
n3	N <sub>2</sub> O	1274.61651	0.021	0.0024	0.0052	0.0204

Table 4.3.1: Contributions to the full width at half maximum (FWHM) (cm<sup>-1</sup>), of the absorption lines at a reduced atmospheric pressure of 96 Torr. The line labels are used in subsequent figures. w1 is a Dicke narrowed [86] pair of lines which cannot be separately resolved. Lines w1, m1 and n1 were not used for calculations of mixing ratios. <sup>a</sup>See reference [49]. <sup>b</sup>Measured using the spectra shown in Figures 4.3.11 and 4.3.12. <sup>c</sup>Assuming a Gaussian instrument function, see reference [43].

The flight path and altitude were recorded as Receiver Independent Exchange Format (RINEX) files using the Global Positioning System (GPS) data logging system within the aircraft. This was then post-processed using the P4 software which forms part of the GPS RINEX Generator (GRINGO) package produced by the Institute of Engineering, Surveying and Space Geodesy at Nottingham University, then plotted using ArcMap v9.1 from the ESRI ArcGIS 9 software suite. A map of the flight paths is shown in Figure 4.3.3.

The altitudes for each of the flights, logged by the GPS system in the plane, using Greenwich Mean Time (GMT), are shown in Figures 4.3.4 to 4.3.6. The variation of the pressure within the absorption cell during the flights is also plotted, using the computer time system, British Summer Time (BST). The latter plot is adjusted owing



to an error in the computer clock, which was 3 minutes slow.

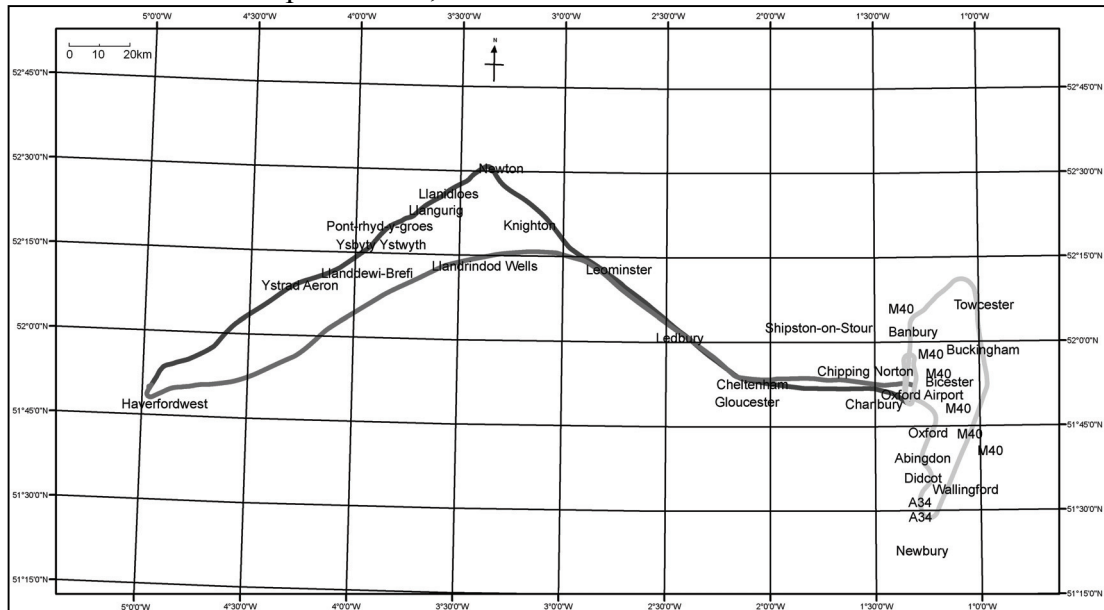


Figure 4.3.3: Flight paths. Dark grey: Oxford-Haverfordwest.

Mid Grey: Haverfordwest-Oxford. Light grey: Oxfordshire circuit

It may be noted that the pressure fluctuations observed during the flight are much larger in the outbound low altitude leg, where the flight conditions were quite turbulent. The instrument remained unaffected by the turbulence, so this was a very good demonstration of the robustness of the design. The long-term pressure variation measured during the flight is reversed in the return leg, and is probably due to the variation in atmospheric pressure between Oxford airport and Haverfordwest. In a subsequent closed loop flight from Oxford airport the long-term variation was absent.

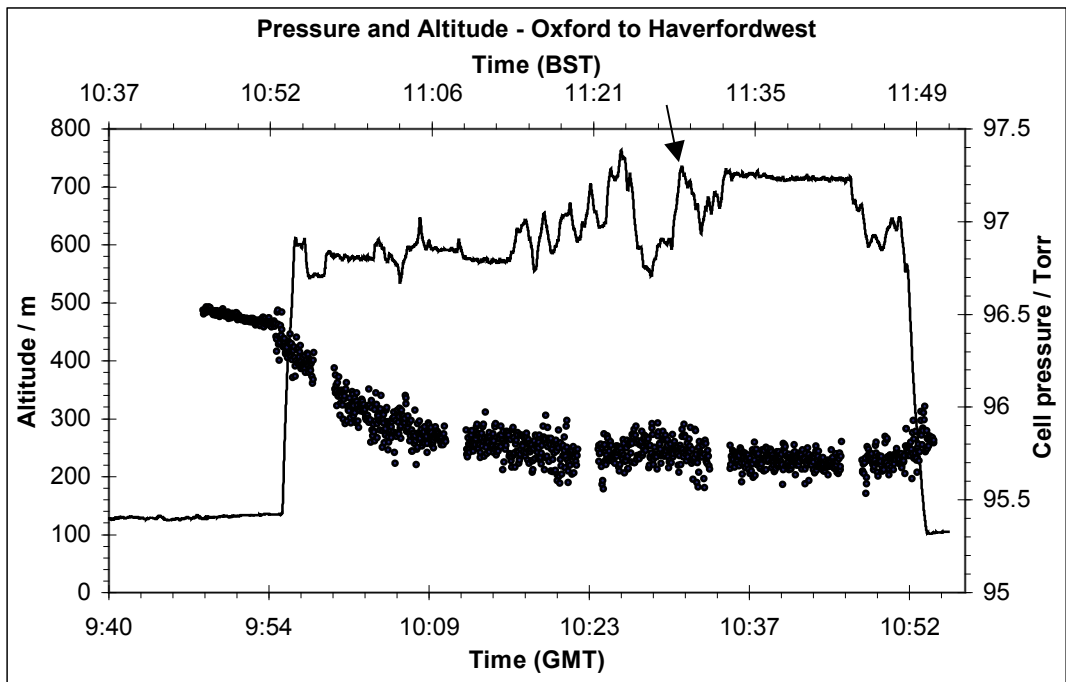


Figure 4.3.4: Altitude of plane (line) and smoothed cell pressure (dots) during the outward flight. The arrow marks the point when a methane spike was detected.

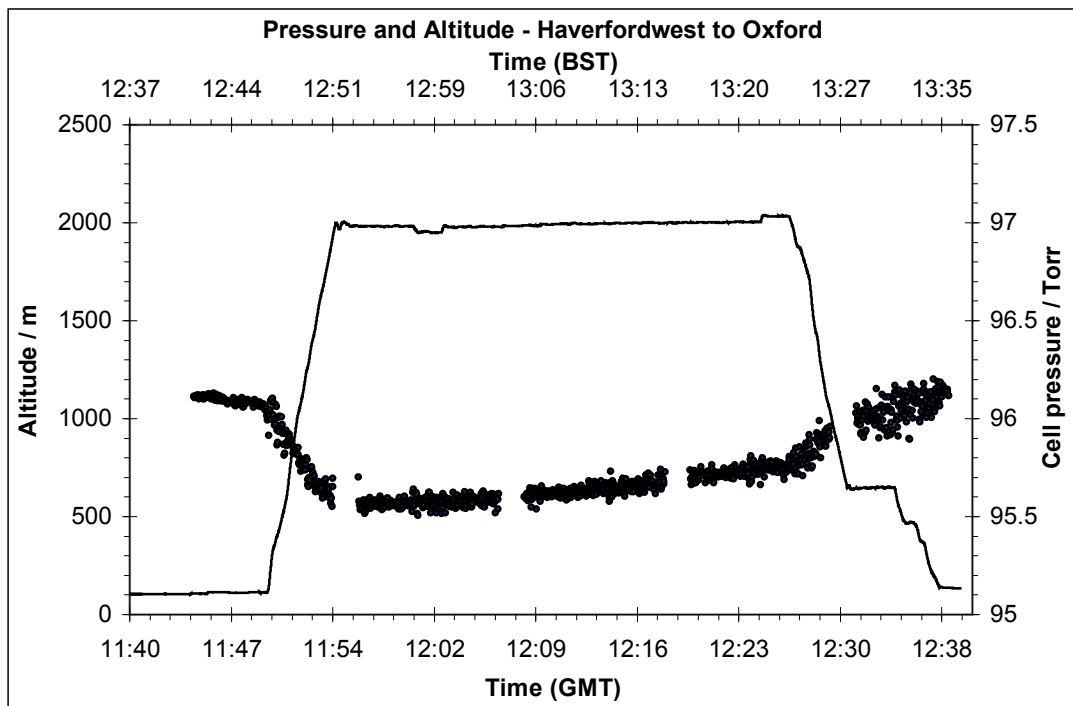


Figure 4.3.5: Altitude of plane (line) and smoothed cell pressure (dots) during the return flight.

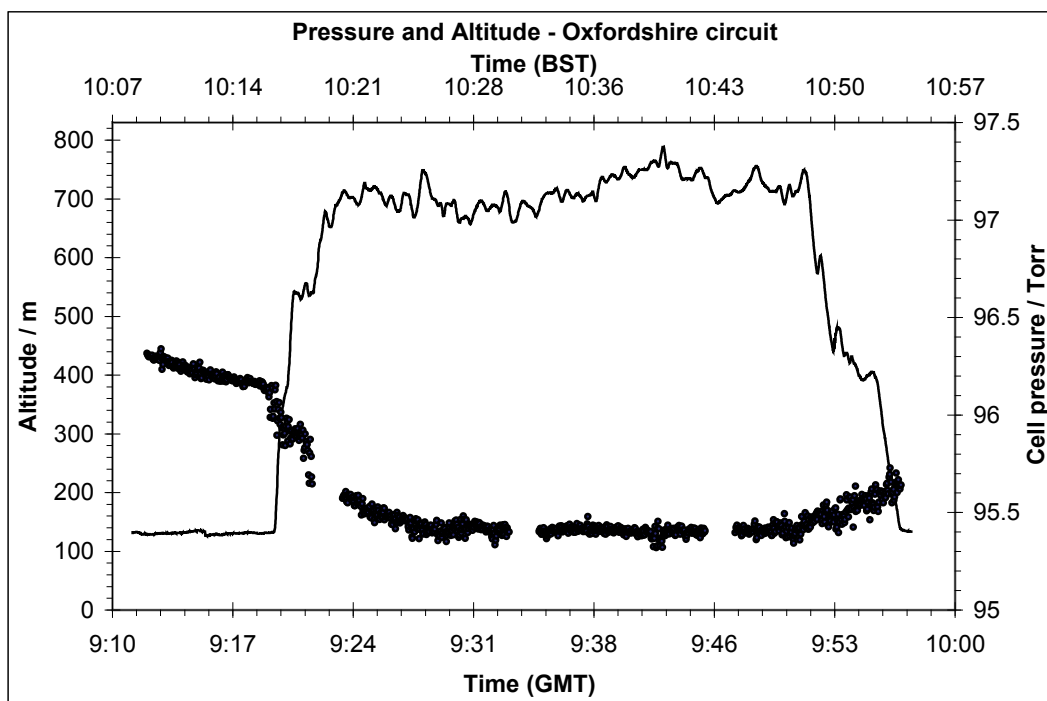


Figure 4.3.6: Altitude of plane (line) and smoothed cell pressure (dots) during the Oxfordshire circuit.

The average cell pressure of approx. 96 Torr was less than the 100 Torr set on the mass flow controller, and varied most on takeoff when the ram effect changed rapidly as the plane gathered speed. This pressure change is not as evident on landing as the spectrometer acquisition had to be switched off soon after touchdown, when the aircraft was still travelling at high speed. The ram effect also helped to speed the flow through the cell. The time to completely change the air in the cell was calculated as 2 s.

During the outward flight from Oxford to Haverfordwest, the valve to the zero air cylinder malfunctioned, with the result that the "background" spectra were in fact taken with atmosphere in the cylinder. These spectra were later post-processed to remove the unwanted lines.

Most of the noise in the spectra is a consequence of the digitisation process carried out by the Acqiris card. In order to derive an accurate background spectrum, this artefact must be removed, and then reinstated following the removal of the unwanted

spectral lines, in order to be cancelled out during calculation of the transmission spectrum. To accomplish this, the spectrum was smoothed by a 9-point Savitzky-Golay smoothing algorithm [65]. The ratio of the original signal to the smoothed signal was taken to give a roughening, or noise function. It was then relatively straightforward to fit short lengths of straight line across each of the unwanted absorption lines in the smoothed spectrum. The revised spectrum was then re-roughened to give a more accurate background. At the start of the spectrum, the baseline could not be approximated by a straight line, so the first 3 lines visible in Figure 4.3.7 (lines m1, w1 and n1) are ignored in the rest of the analysis.

As a result of the AC coupling between the photodiode amplifier and the digitiser, all spectra required a correction to the baseline. The mean baseline value before and after the pulse, and a calculated baseline correction, assumed to be linear across the pulse are subtracted. See Figure 4.3.7 for before and after views.

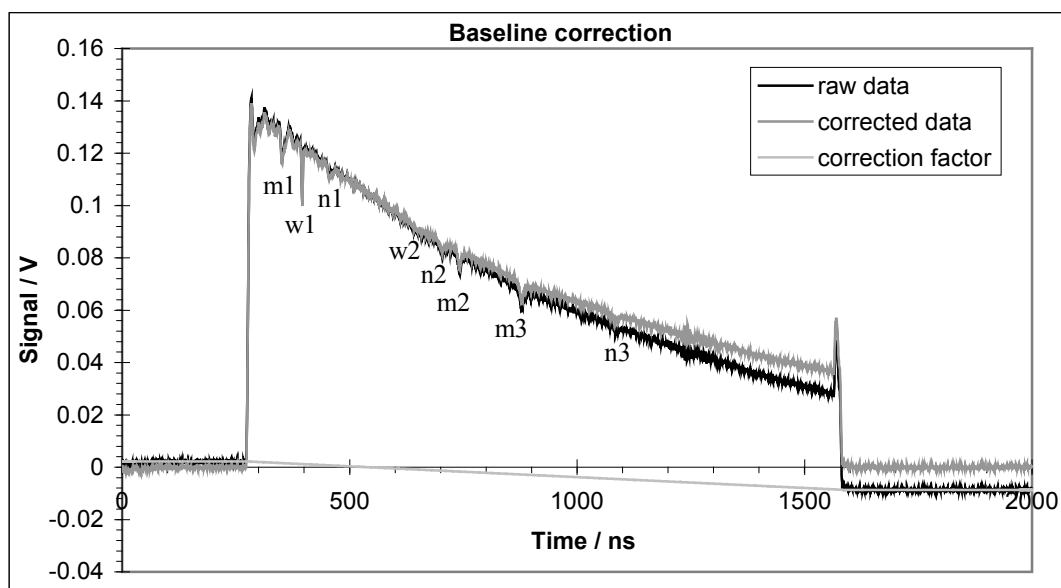


Figure 4.3.7: Original spectrum (black), assumed correction factor (light grey) and corrected spectrum (dark grey).

The transmission spectrum is then calculated by taking the signal to background ratio. This is divided by its own mean value to fix the baseline on 1. Finally, the spectra are converted from pixel to wavenumber, using the etalon fringes as a guide, and the lines themselves as a calibration, as discussed in Chapter 3.3.

A peakfitting program is then used to remove any remaining slope in the baseline and fit a Lorentzian function to each peak. Although the Voigt function is a more accurate description of the line shape, at the gas pressure used for the experiments the dominant source of line broadening is due to collisions of the trace gas molecules of water, methane and nitrous oxide with the background of nitrogen and oxygen, leading to a predominantly Lorentzian shape. The other source of broadening is instrumental and is due to the rapid laser down-chirp, and is proportional to the square root of the chirp rate [43]. The calculated contributions of the Doppler effect, foreign gas broadening and instrumental broadening are given in Table 4.3.1.

The parameters used to fit the lineshape are used to calculate the integrated intensity of the peak, and thus the mixing ratio of gas. The program output consists of a list of timestamps and mixing ratios calculated from each spectral line. All of the data analysis was carried out using our group's own LabVIEW 8.0 virtual instruments, written specifically for the purpose.

The mixing ratios of methane derived from the m2 and m3 spectral lines at  $1275.39\text{ cm}^{-1}$  and  $1275.04\text{ cm}^{-1}$  respectively, and of nitrous oxide derived from the n2 spectral line at  $1275.49\text{ cm}^{-1}$  are shown in Figures 4.3.8 to 4.3.10.

There are clear variations in gas levels during the flights, the most prominent feature being the initial drop from high levels. This was most noticeable on takeoff from Oxford where the level dropped from 3200 ppb to 2200 ppb of methane. Oxford Airport is surrounded by busy roads, which would tend to give a high methane reading. Additionally, prior to lift off, the plane was sitting in its own cloud of pollution until the instrument began running. From switching on the plane engines until the spectrometer starts recording took 5 minutes, and this allowed a lot of pollution to enter the cell, which took around 8 minutes to fully drop back to normal background levels.

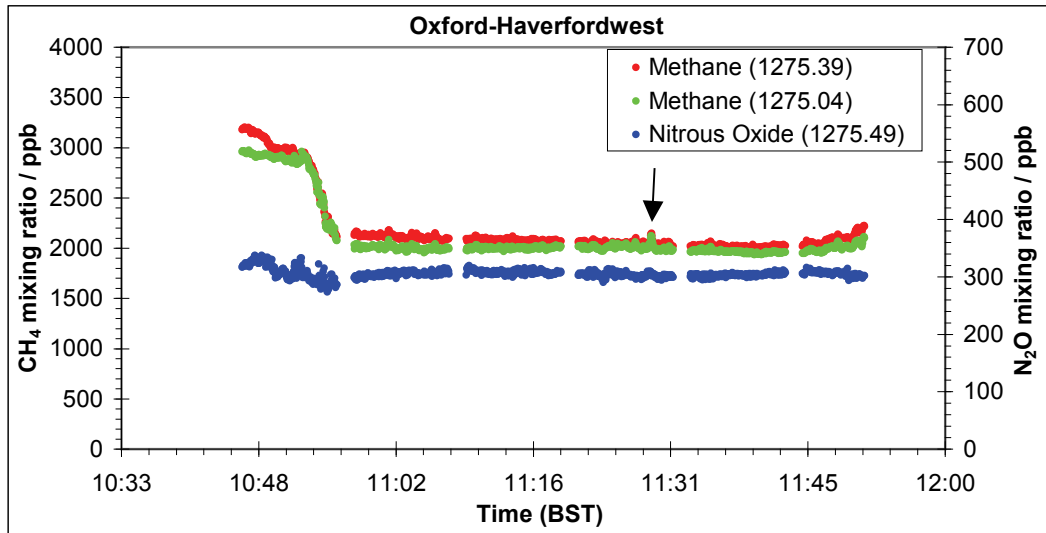


Figure 4.3.8: Methane and nitrous oxide mixing ratios during the outward flight. The arrow indicates a strong methane peak which is discussed later.

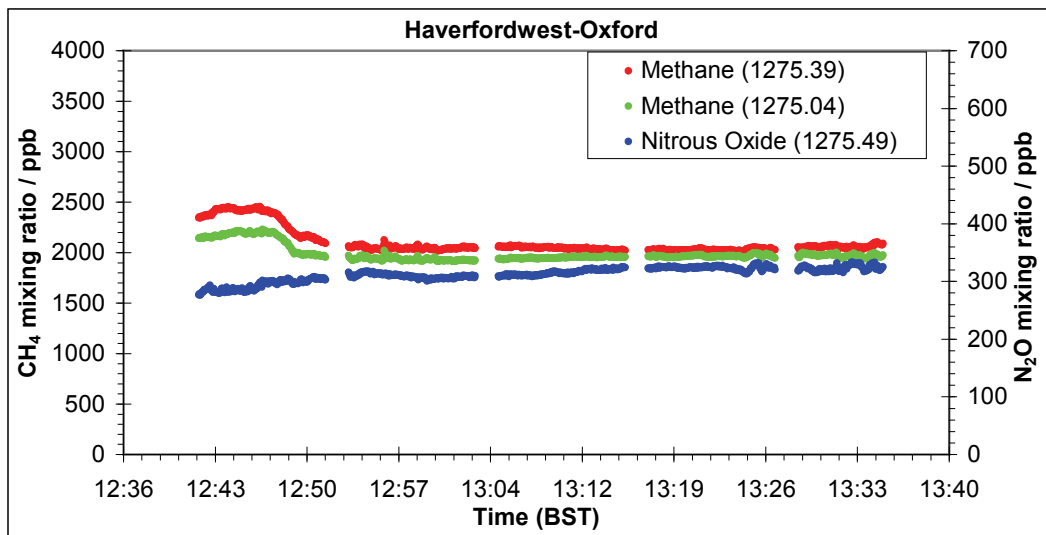


Figure 4.3.9: Methane and nitrous oxide mixing ratios during the return flight.

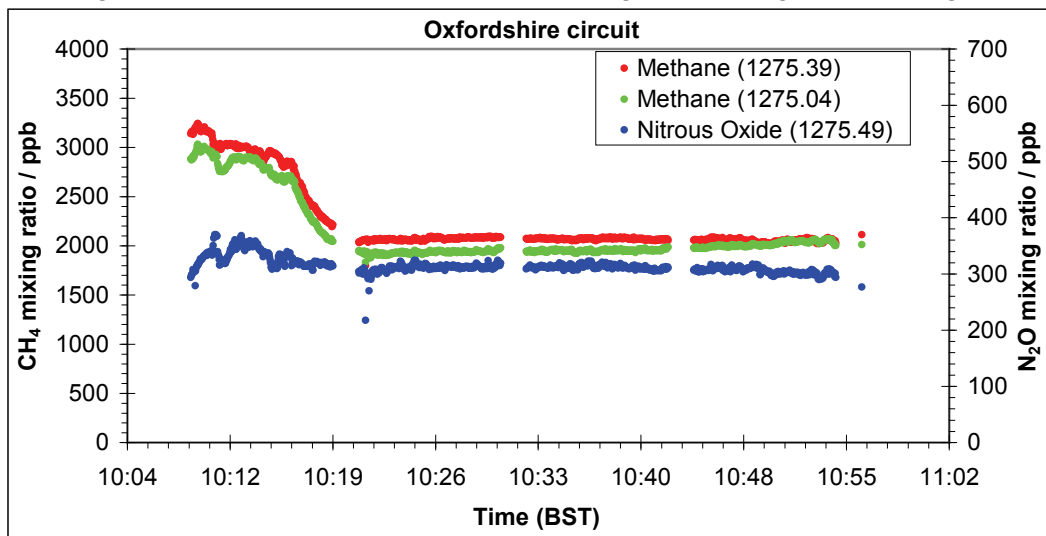


Figure 4.3.10: Methane and nitrous oxide mixing ratios during the Oxfordshire circuit.

Nonetheless, the initial level of 3200 ppb seems unrealistically high. While levels around 3000 ppb have previously been observed near Schiphol Airport in Amsterdam [87], these were only very brief spikes against a typical level around 2100 ppb. The mixing ratios measured by our instrument could be validated in a number of ways, including filling jars from the cell outlet at intervals to be later tested by another method. Alternative methods of measuring methane levels include gas chromatography [87], flame ionisation detection [88, 89] and Fourier Transform spectroscopy [90]. The nitrous oxide level measured during flight was typically 320 ppb to 340 ppb, slightly higher than the Northern Hemisphere background level of 322 ppb. Urban pollution in various regions of the route, and emissions from vehicles are the most likely explanation for this increased level.

Typical spectra from takeoff and landing are shown in Figures 4.3.11 and 4.3.12. These highlight the change in methane level.

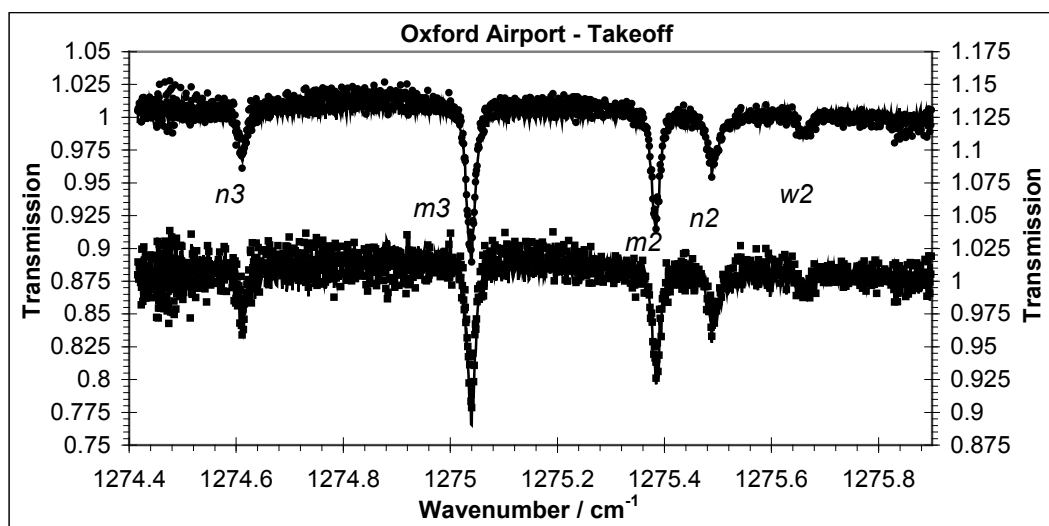


Figure 4.3.11: Sample spectra during takeoff. The top spectra were early in the takeoff. The bottom spectra were later in the takeoff. The line labels match those in Table 4.3.1.

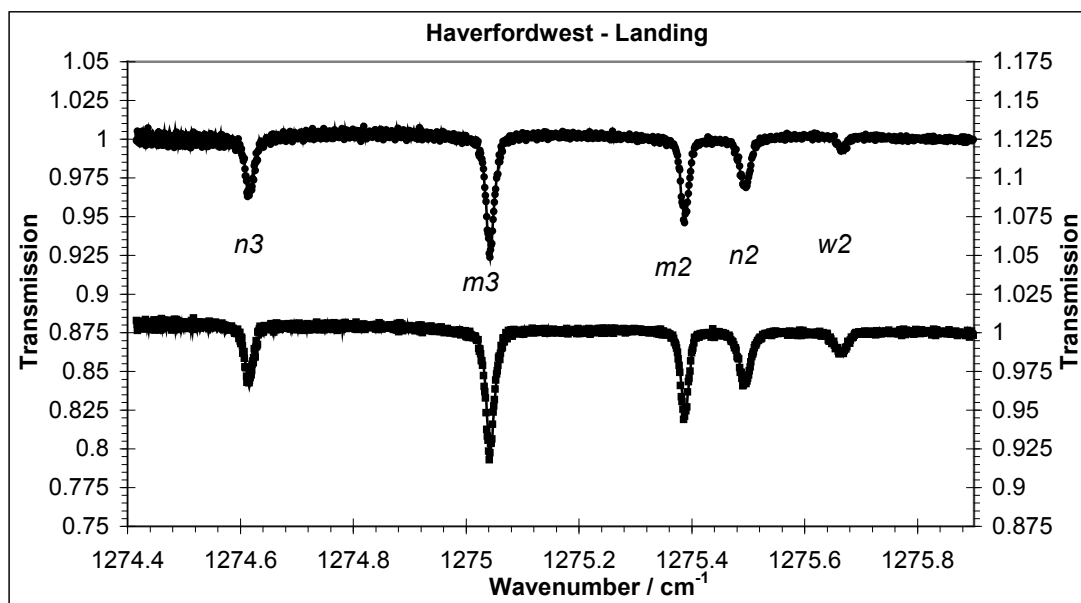


Figure 4.3.12: Sample spectra during descent. The top spectra were early in the descent. The bottom spectra were later in the descent. The line labels match those in Table 4.3.1.

The variation in water vapour level can also be examined. As shown in Figure 4.3.13, during the descent, there is a significant increase in absorption, and consequently concentration, observed with only minor changes in the methane and nitrous oxide concentration. The water line is only distinguishable from the noise at high water vapour concentration, and on the cleanest spectra. Attempting to calculate accurate measurements from this line throughout the flight was impractical.

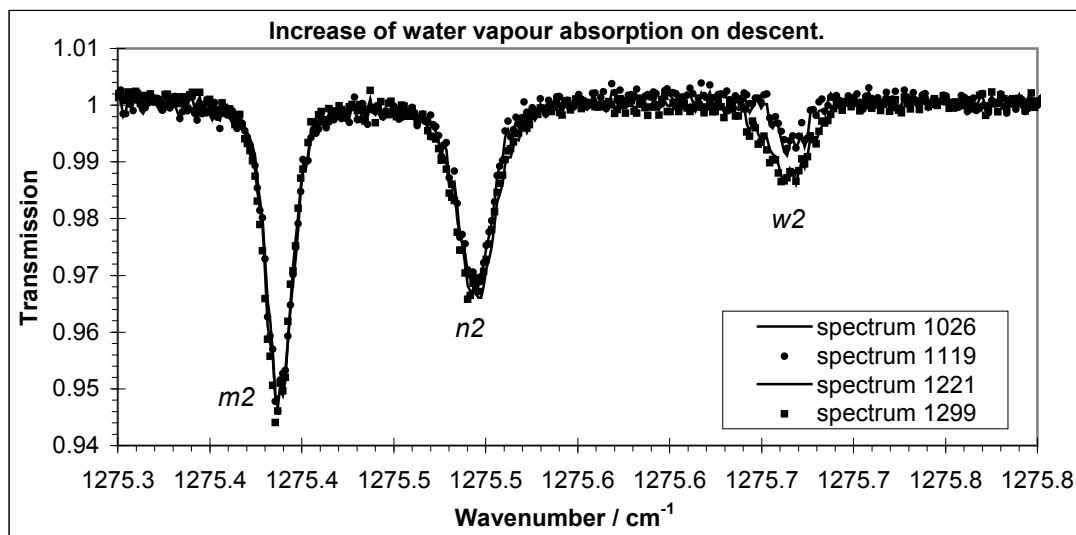


Figure 4.3.13: Increase of water vapour absorption on descent. The line labels match those in Table 4.3.1.



At 11:29, there was a clear methane spike (arrowed on Figure 4.3.8). Methane has previously been shown to be emitted by vehicles [88, 89, 90]. At the time the spike was detected, the plane was flying across a funnel shaped set of hills near a junction on a major tourist route (see Figure 4.3.14). It is logical to assume the pollution was generated by traffic and was concentrated across the flightpath by the funnel effect, which also resulted in the plane being pushed upwards, as arrowed on Figure 4.3.4.

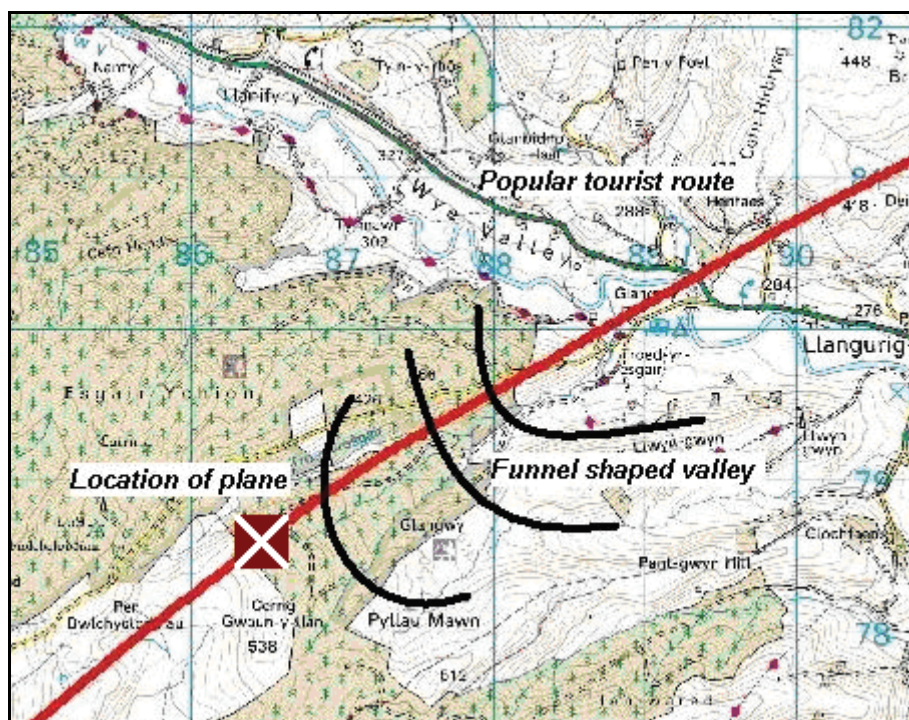


Figure 4.3.14: Location of plane while detecting methane spike.

© Crown Copyright/database right 2010. An Ordnance Survey/EDINA supplied service.

### Gloucester Airport Based Flight

On the 4th of February 2009, further airborne measurements in the NERC Dornier [7] were carried out. On this occasion, the Cascade 4-laser spectrometer was used in its original form as described in Chapter 3.6. The 4 lasers were all run, however only three of them were able to detect any useful absorption lines. It was thus possible to measure carbon monoxide, carbon dioxide, nitrous oxide, methane and water vapour.

The H<sub>2</sub>O line at 1627.83 cm<sup>-1</sup> was measured by Laser 0; the CO line at 2050.85 cm<sup>-1</sup> and the CO<sub>2</sub> line at 2050.87 cm<sup>-1</sup> by Laser 1; the N<sub>2</sub>O line at 1274.62 cm<sup>-1</sup> and CH<sub>4</sub> lines at 1275.40 cm<sup>-1</sup> and 1276.84 cm<sup>-1</sup> by Laser 2. Laser 3 did not measure any lines

which were detectable in the atmosphere during this work.

The outward flight followed the approximate path of the flights from Oxford Airport, and was at an altitude of 800 m. After a short distance flying over Milford Haven at 500 m, the return light was on a more direct route at around 900 m.

The atmosphere was again sampled through a "snorkel" at the front of the aircraft, similar to the one shown in Figure 4.3.1.

The pressure control and pumping were carried out by the system's internal pressure system, described in Chapter 3.6. The pressure was set to 152 Torr, although it is likely that this fluctuated during flight. At the time, the program did not include a pressure readout, although it has since been modified.

The lasers were operated in pulsed mode with the following default parameters:

Laser	Nominal wavelength / $\text{cm}^{-1}$	Pulse duration / ns	Voltage / V	Temperature / $^{\circ}\text{C}$
0	1631	500	11.4	23
1	2051	500	9.5	24
2	1274	800	9.4	11
3	1904	600	9	24.5

Table 4.3.2: Default parameters for running the lasers in the Cascade laser box

Each laser operated at 5 kHz, and 500 successive spectra were averaged. The processing to calculate concentrations led to a time interval of three seconds between each recorded set of 4 spectra.

The flight path, altitude and atmospheric pressure and temperature were recorded by the Aircraft Integrated Meteorological Measurement System (AIMMS) GPS system within the aircraft. A map of the flight paths is shown in Figure 4.3.15, overlaid on the previous flights from Oxford.

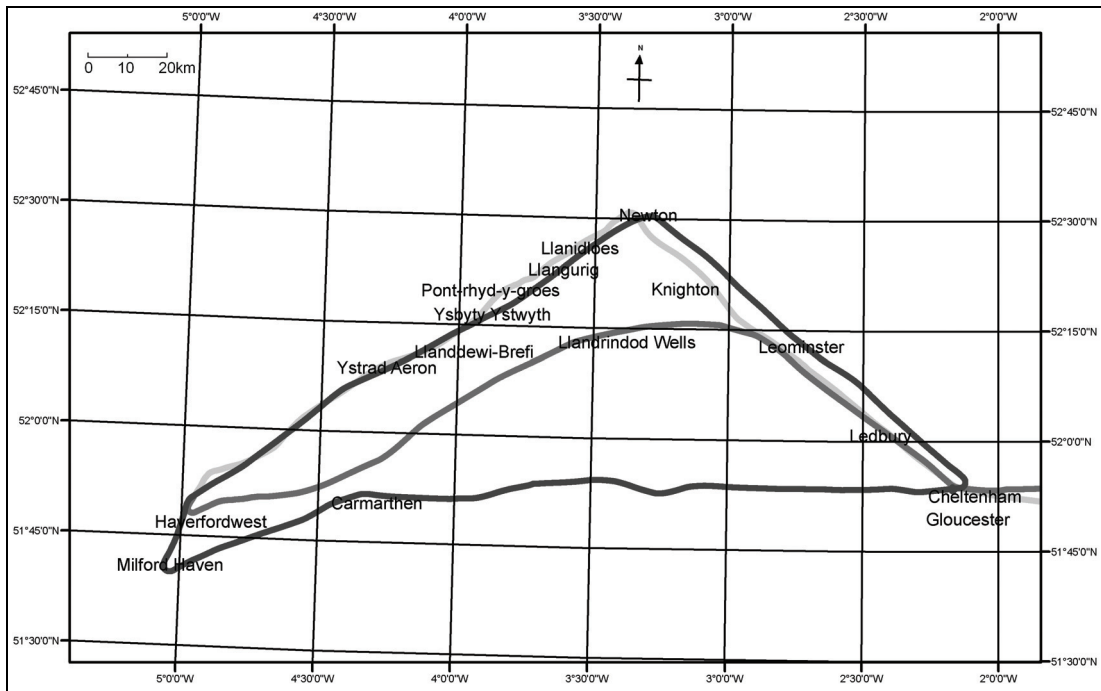


Figure 4.3.15: Flight paths. Light grey: Oxford-Haverfordwest. Mid Grey: Haverfordwest-Oxford. Dark grey: Gloucester-Milford Haven return.

The altitude of the plane during the flight is shown in Figure 4.3.16. The variation of atmospheric temperature during the flights is also plotted. This illustrates the contrast between lower altitude (warm) and higher altitude (cold).

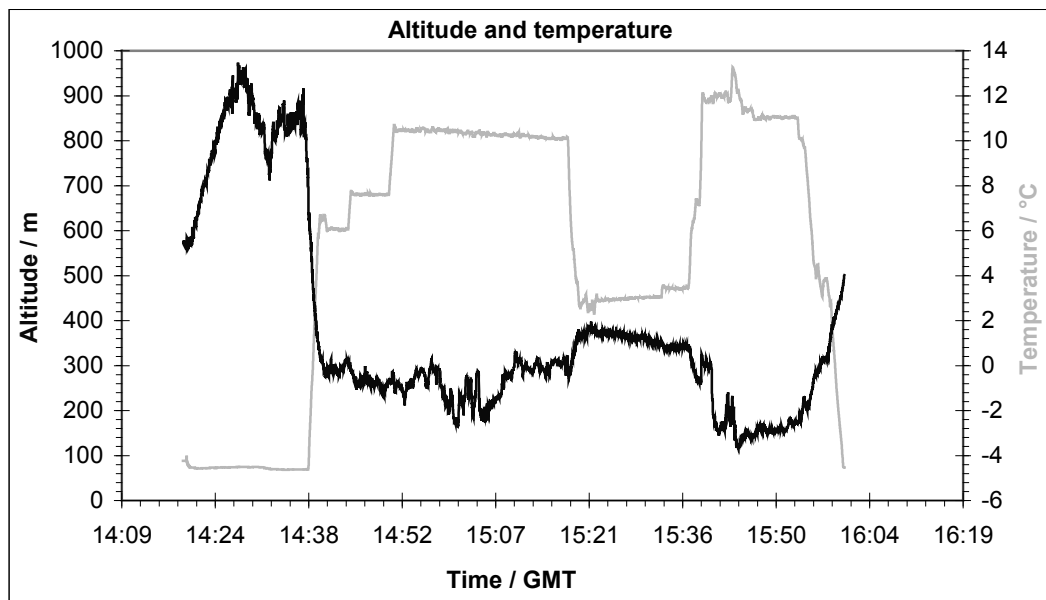


Figure 4.3.16: Altitude (grey) and outside temperature (black) throughout the flight.

This flight, even at low altitude, was considerably smoother than the low altitude trip from Oxford Airport to Haverfordwest in 2006.

Each file recorded by the control software includes the spectrum recorded by each of the 4 lasers, the derived concentrations of CO<sub>2</sub> and N<sub>2</sub>O along with NO and NO<sub>2</sub>, although neither of these were detected during this work. Various intermediate stages in the calculations are also saved to file. In flight, the fitting method used encountered some difficulties, mostly relating to fluctuations in laser signal strength caused by vibration or thermally caused creep in the mirror mounts. The mixing ratios were recalculated later, along with mixing ratios of CH<sub>4</sub>, CO and H<sub>2</sub>O. In order to improve the accuracy of the fit, background spectra were recorded in the laboratory using zero air. The recorded spectra were then divided by the background spectra to give transmission spectra similar to these recorded by the other instruments. To calibrate the spectra, a set of etalon fringes was recorded, again in the laboratory.

A slightly modified version of our peakfitting program was then used to remove any remaining slope in the baseline and fit a Lorentzian function to each peak. Above 100 Torr, a Lorentzian is a reasonably accurate approximation to the pressure broadened lineshape. The parameters used to fit the lineshape are used to calculate the integrated intensity of the peak, and thus the mixing ratio of gas. The program output consists of a list of timestamps and mixing ratios calculated from each spectral line.

The mixing ratio of water vapour derived from the spectral line 1627.83 cm<sup>-1</sup> is shown in Figure 4.3.17, along with the altitude of the plane.

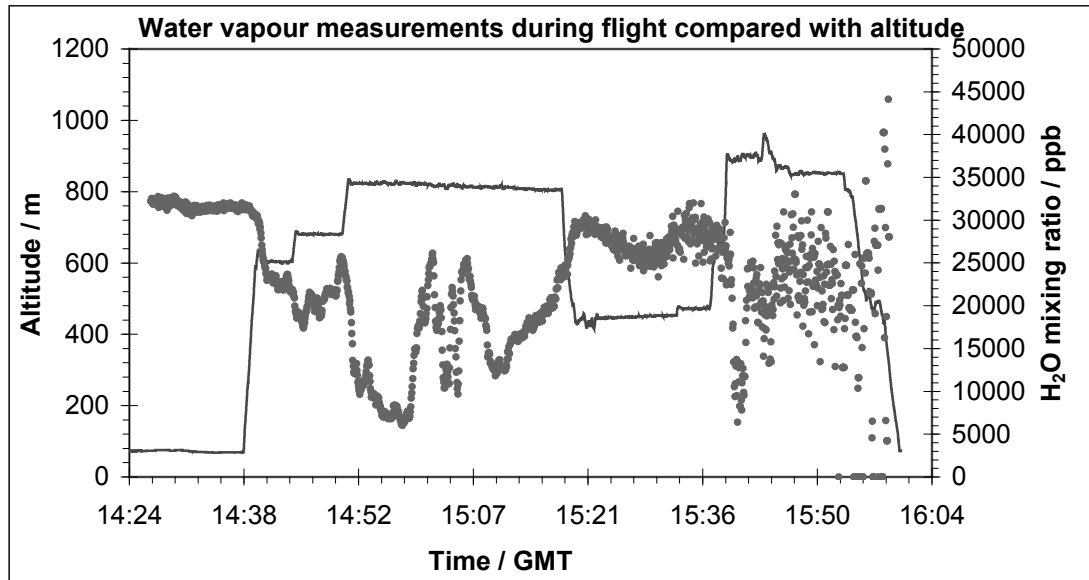


Figure 4.3.17: In-flight variation of water vapour (points) and altitude (line).

As can be seen, the water level varies considerably during the flight, most notably on takeoff at 14:36. The levels measured are unrealistically low, being an order of magnitude less than the average water vapour level in the Sahara Desert [91]. The variation in level is believed to be real since it is correlated with altitude, with lower levels being measured at higher altitude. Towards the end of the flight, readings became quite random as a consequence of the laser becoming misaligned. It is uncertain whether this was an effect of vibration, or of thermal creep. The temperature inside the spectrometer increased by over 10 °C during the flight as shown in Figure 4.3.18.

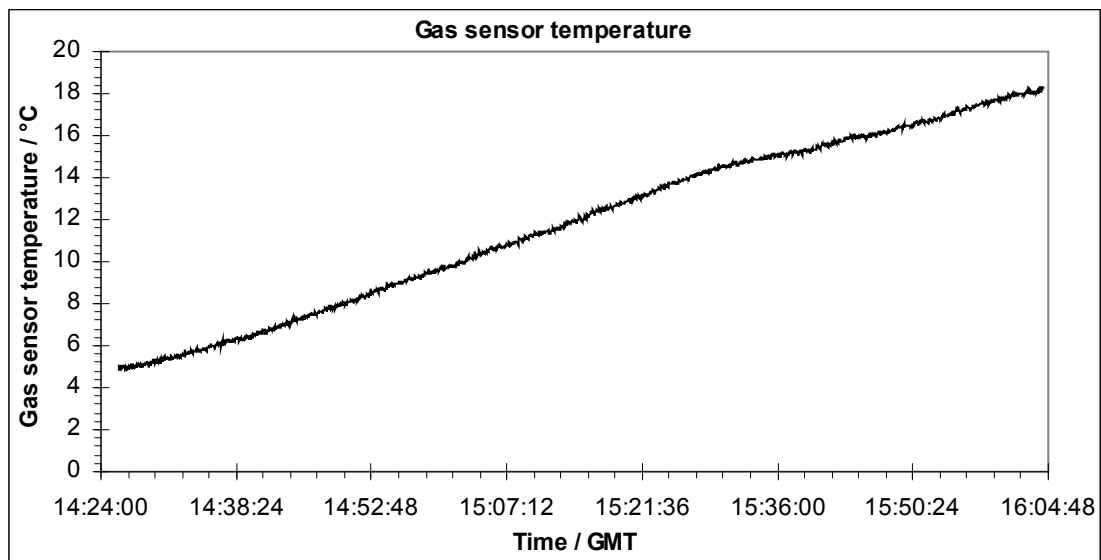


Figure 4.3.18: Gas sensor internal temperature during flight.

The mixing ratio of carbon monoxide derived from the spectral line at  $2050.85\text{ cm}^{-1}$  is shown in Figure 4.3.19.

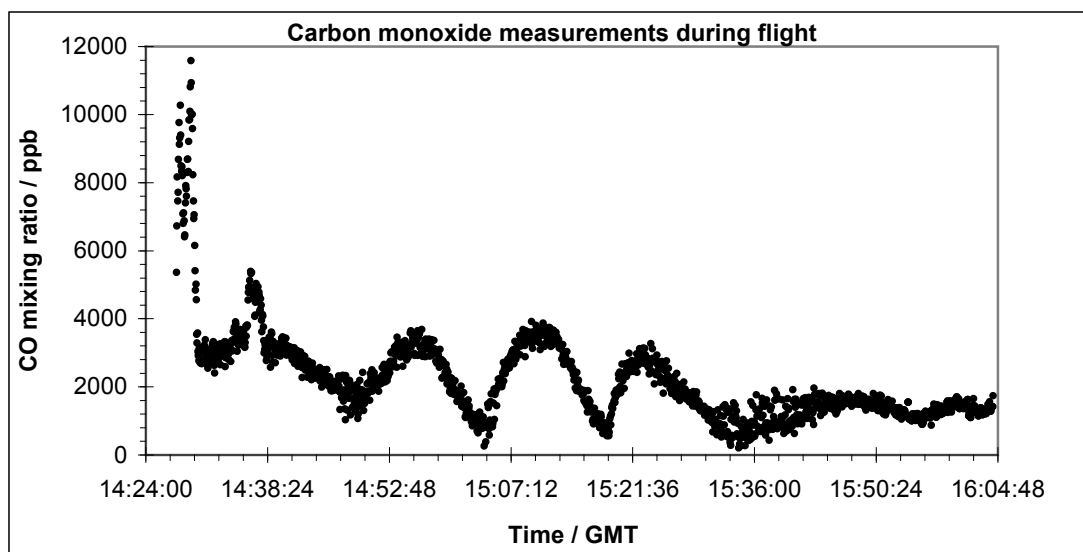


Figure 4.3.19: In-flight variation of carbon monoxide.

The measurements of carbon dioxide are shown in Figure 4.3.20. This compares the mixing ratios derived from the spectral line at  $2050.87\text{ cm}^{-1}$  using our fitting method to the concentrations calculated on-the-fly by Cascade's gas sensor control program.

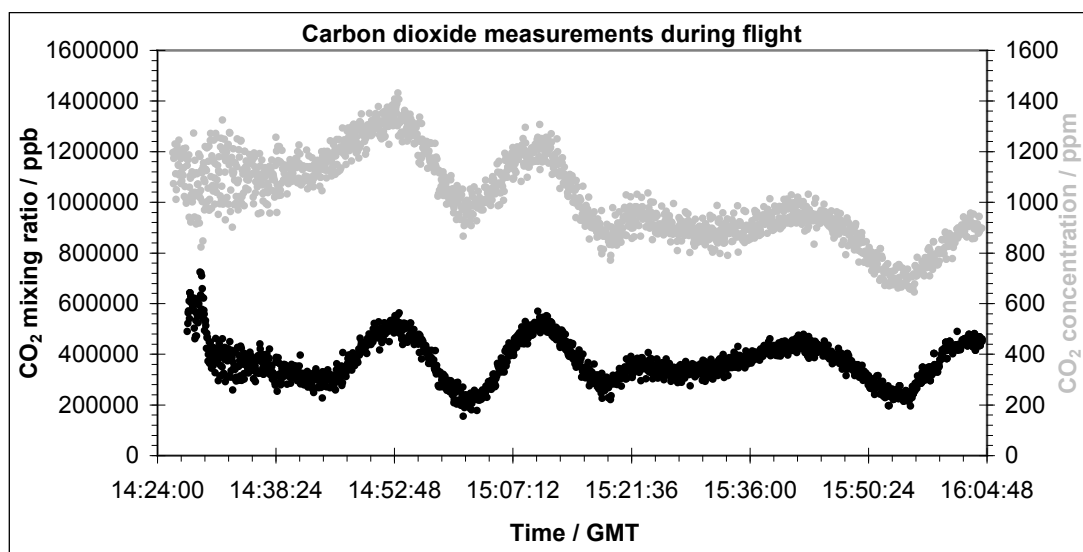


Figure 4.3.20: In-flight variation of carbon dioxide, calculated on-the-fly by the control program (grey) and calculated by our own fitting methods during post-processing (black).

The carbon dioxide and carbon monoxide levels both show maxima at 14:52 and 15:10. The first maximum occurred at a course change over Newtown, and may correspond to pollution from burning hydrocarbons. The second occurred over rural

ground in Wales and has no obvious source from the map. Although the maxima are similar in appearance, they are not identical, and are thus unlikely to be laser fluctuations. There is another carbon monoxide peak at 14:36, corresponding to the plane taking off, which does not correspond to any carbon dioxide increase. The Northern Hemisphere background level of CO<sub>2</sub> is 400ppm [5] which compares well to the values derived from our peakfitting. The Cascade fitting method leads to levels more than double this. The CO level however seems to be excessively high. Previous studies in China measured a level of 393 ppb in a relatively polluted area [92].

The mixing ratios of methane derived from the spectral lines at 1275.40 cm<sup>-1</sup> and 1276.84 cm<sup>-1</sup> are shown in Figure 4.3.21. The results derived from the two peaks are generally in agreement about the level of methane, although they do fluctuate relative to each other. The only place where the two lines show a conclusive variation in methane level is between 15:21 and 15:30 where both lines drop. This corresponds to some low flying near Milford Haven. The Northern Hemisphere background level of methane is 1865 ppb, which is broadly in agreement with the levels measured.

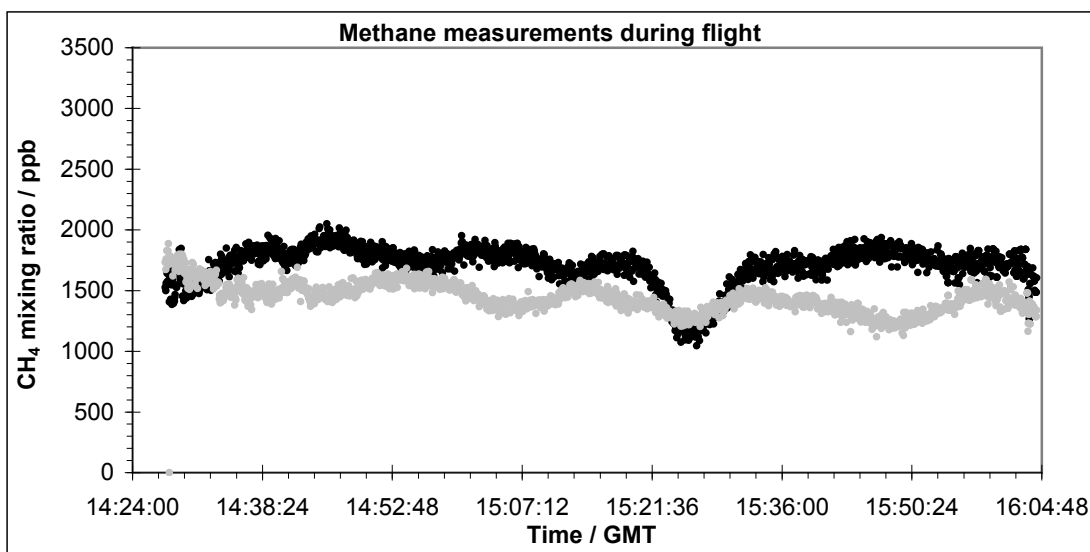


Figure 4.3.21: In-flight mixing ratios of methane derived from the absorption lines at 1275.40 cm<sup>-1</sup> (black) and 1276.84 cm<sup>-1</sup> (grey).

The degree of variation in the measurements, in particular the lack of correlation between mixing ratios derived for each line, suggests that the derived mixing ratios from this laser are less reliable than the mixing ratios of CO and CO<sub>2</sub>. The main

difference was the quality of match between the laboratory recorded background spectra and the field spectra. For the CO/CO<sub>2</sub> laser, this was a good match while for the CH<sub>4</sub>/N<sub>2</sub>O laser was less so. This tended to lead to baselines which were not flat in the transmission spectra, which may have led to inadequate fitting of the absorption lines.

The mixing ratios of nitrous oxide derived from the spectral line at 1274.62 cm<sup>-1</sup> are shown in Figure 4.3.22, again compared to the concentrations calculated on-the-fly by the control software. The nitrous oxide level shows an increase, followed by a sharp drop at 15:07. This corresponded to flying out of snow covered ground and over uncovered ground. Until this point, both methods of deriving results gave similar values, however after this the values diverge. This is likely to be an effect of the increasing temperature causing the laser signal to deviate from the background signal, giving non flat baselines in the transmission spectra, which the fitting routine cannot handle properly. The levels are generally above the Northern Hemisphere background level of 322 ppb of nitrous oxide [5], but the extent by which they exceed it casts some doubt on the accuracy of the measurements, particularly toward the end of the flight.

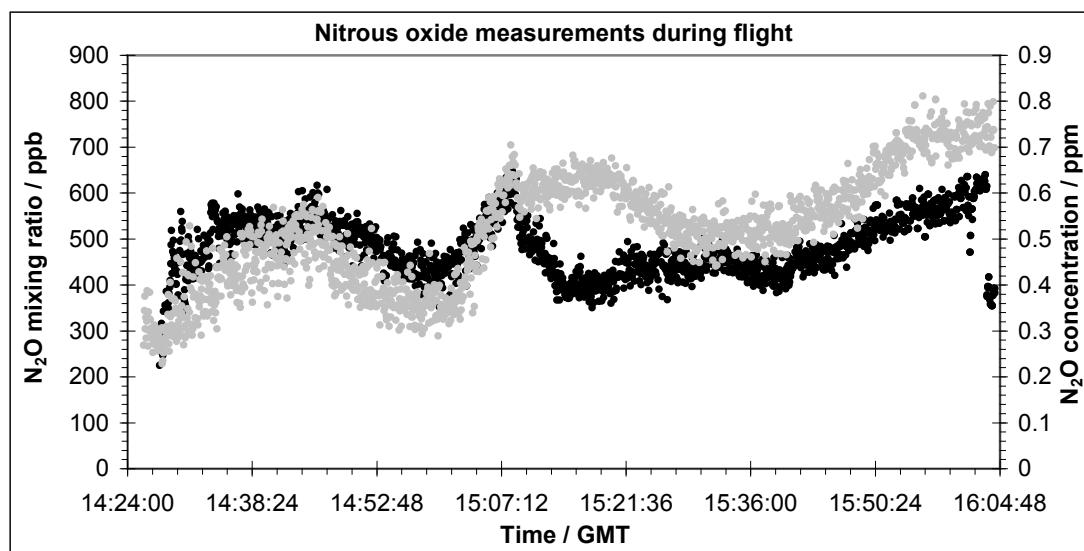


Figure 4.3.22: In-flight variation of nitrous oxide, calculated on-the-fly by the control program (grey) and calculated by our own fitting methods during post-processing (black).

The main difference between these results, and those obtained using the older system



was the lack of fast variations in gas levels. Later laboratory tests demonstrated that the built in pump in the 4-laser system gave the cell a dwell time of around 40 s, while using an external pump could reduce this to around 8 s, *i.e.* one point records a high reading, while the points 4 s before it and 4 s after it show normal. The dwell time with the internal pump would smear any fast variations such as an exhaust plume or an updraught across 40 s, and correspondingly reduce the strength of the change, rendering it invisible.

This flight proved successful overall, although some further development to the system's cooling and pumping capabilities was required before any further flight based work could be attempted. The accuracy of some of the measurements was less than ideal. Future work will also have to focus on improving the analysis methodology to improve reliability of results.

#### 4.4: Hot Acetylene and Methane in a CVD Reactor

Chemical Vapour Deposition (CVD) is used in the processes of semiconductor growing and artificial diamond manufacture. It is a very precise process, allowing thin layers of a substance to be deposited on some substrate. Artificial diamonds have two major uses in industry. The hardness of diamond makes them ideal for cutting and grinding, while the fact that diamond is an electrical insulator but a thermal conductor makes them perfectly suited to high-quality heatsinks.

Electron density and energy measurements within a plasma have been carried out using a fine tungsten wire probe [93], while simultaneous measurements of ions present within the plasma utilised a hole in the chamber to extract ions to a mass spectrometer. A similar method using a double probe has also been used [94], this time in conjunction with a noninvasive method: emission spectroscopy [95], viewing the spectra of  $C_2$  and CH through an optical fibre connected to either a scanning monochromator or a spectrum analyser. It was observed that the spectrum varied widely in different regions of the plasma, highlighting the spatial variance of the plasma itself.

Like emission spectroscopy, absorption spectroscopy has an advantage in that it is a noninvasive process and consequently does not affect the processes occurring within the plasma, provided low power lasers are used. Extremely intense lasers can be used to accelerate particles within a plasma [*e.g.* 96]. Ultraviolet absorption spectroscopy has been performed on an atmospheric pressure diamond deposition reactor [97], again with the intention of determining which reactions are taking place in different regions of the plasma. Many radicals are present including C, H, CH, and  $C_2$ . Measurements of CH have been carried out by cavity ring-down spectroscopy [98] in a similar plasma to that discussed in this chapter.

The deposition process depends upon the reactions occurring within the plasma, so it is vital to understand these reactions before the deposition process can be improved.

During February 2008, in collaboration with Bristol University School of Chemistry, measurements of hot acetylene and methane levels in a noble gas / hydrogen / hydrocarbon plasma in a CVD diamond reactor [99] were performed. The plasma in this reactor has previously been modelled [100]. By measuring levels of different gases in different regions of the plasma, it is possible to improve the model of the reaction process thus improving the understanding of how to best perform the chemical vapour deposition process.

A custom built microwave reactor with a 2 kW 2.45 GHz Muegge power supply and microwave generator was used. The multipass cell was not used for this work, which was the first time the Vigo photodetector, and the last time that the "brick" drive system were used in a field trial. The experimental setup is shown in Figure 4.4.1.

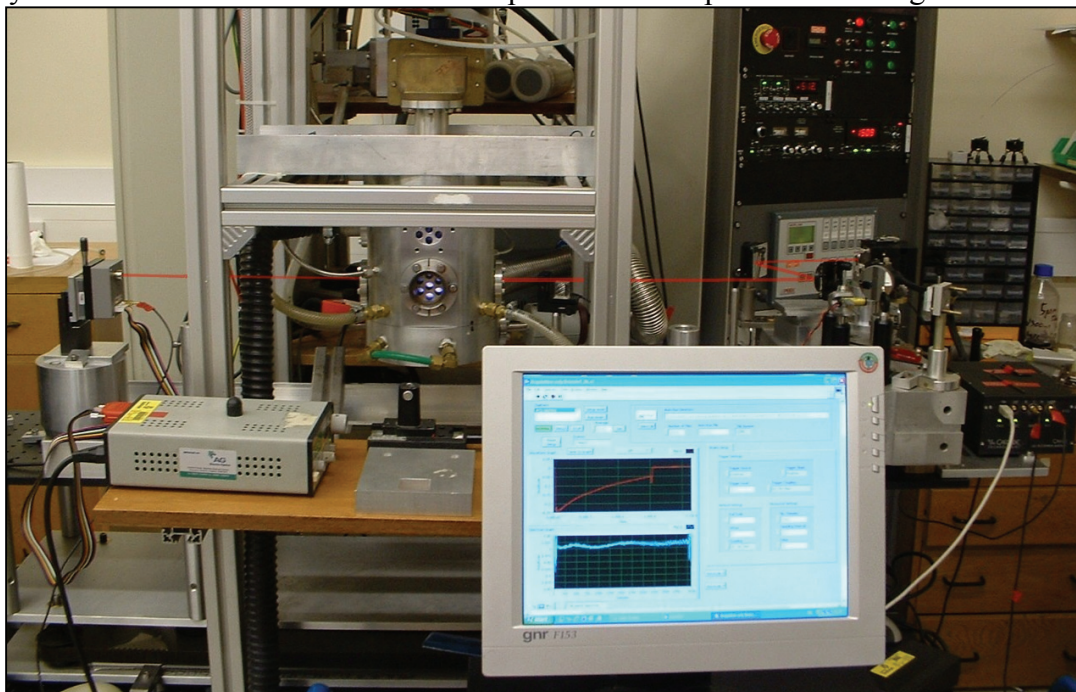


Figure 4.4.1: The Bristol plasma reactor, with the laser path drawn in red. The QC laser is on the right, and the Vigo photodetector on the left. The argon / hydrogen plasma can be seen as a purple glow through the viewing port.

The laser and photodetector were mounted on a table which could be jacked up and down, allowing the beam to pass through any of 3 windows in the side of the plasma chamber. These windows are recessed by 2.5 cm into the reactor walls. Their centre lines are 1 mm, 11 mm, and 21 mm above the substrate surface. These windows cut

down the length of cold gas which the laser beam must traverse on either side of the plasma. This, and the use of the Vigo detector replacing the Kolmar, gives improved spectral quality compared to previous work by Cheesman *et al* [101], and Ma [102].

The temperature of the plasma at 11 mm above the substrate is illustrated in Figure 4.4.2. The region between the edges of the recessed windows (bold line) and the dotted line where the plasma temperature exceeds 1500 K contains the gas which could be detected. Although this is hot gas, it is the cooler outer sheath of the plasma ball, and not the central hot zone. Within the hot zone, the Maxwell-Boltzmann distribution of particles means that there are relatively few particles in each of a large number of excited energy levels. As absorption from an energy level depends on the population of that level, this ensures that in the centre of the plasma, all absorption lines are very weak and are unable to be detected with the setup used here.

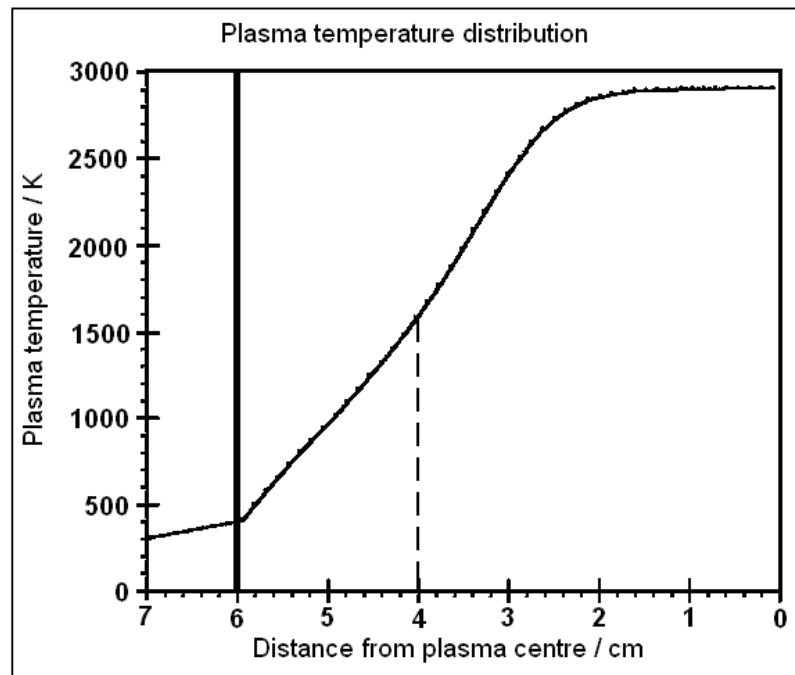


Figure 4.4.2: Plasma temperature within the reactor. Taken from [100].

The observed lines are illustrated in Figures 4.4.3 (Acetylene) and 4.4.4 (Methane). The spectra used to illustrate these were recorded with a higher pressure of cold gas, with the reactor switched off. This saturates absorption by the stronger cold lines, while increasing the strength of the hot bands such that they are visible at room temperature. The line intensities of these lines are tabulated in Tables 4.4.1 and 4.4.2.

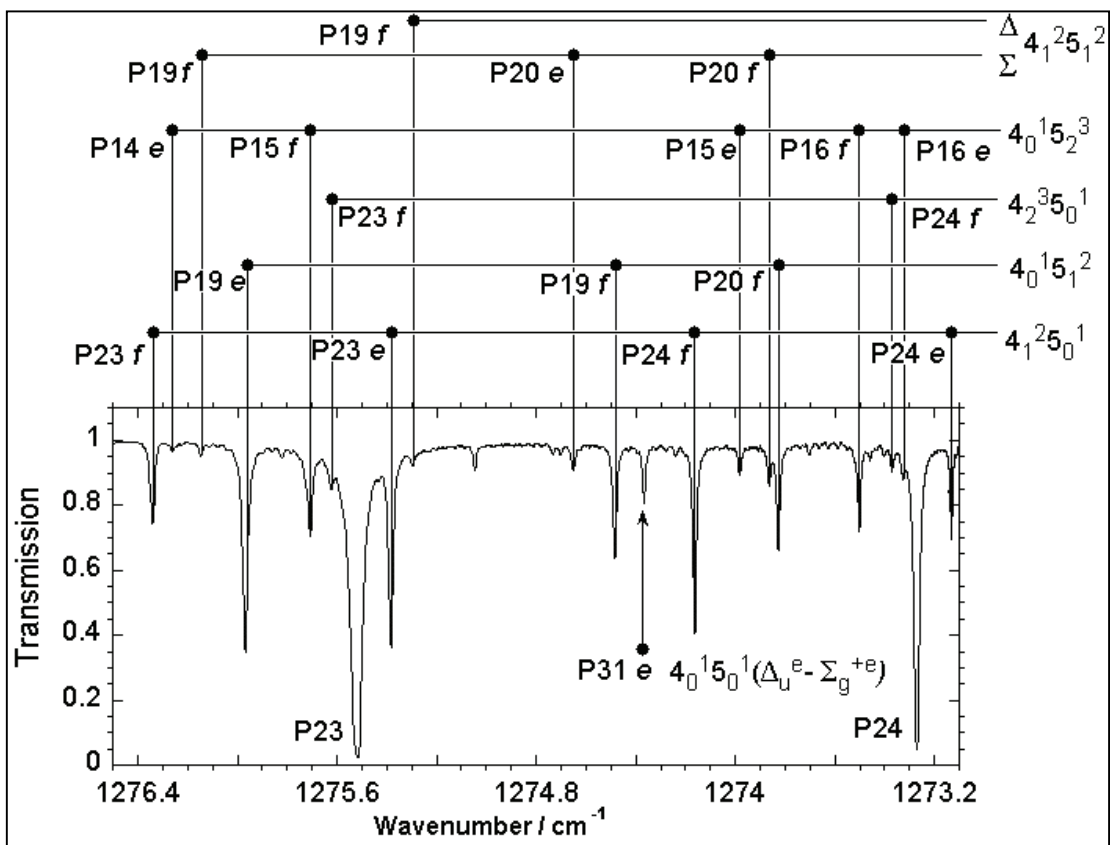


Figure 4.4.3: Assignment of the acetylene lines. These are tabulated in Table 4.4.1.

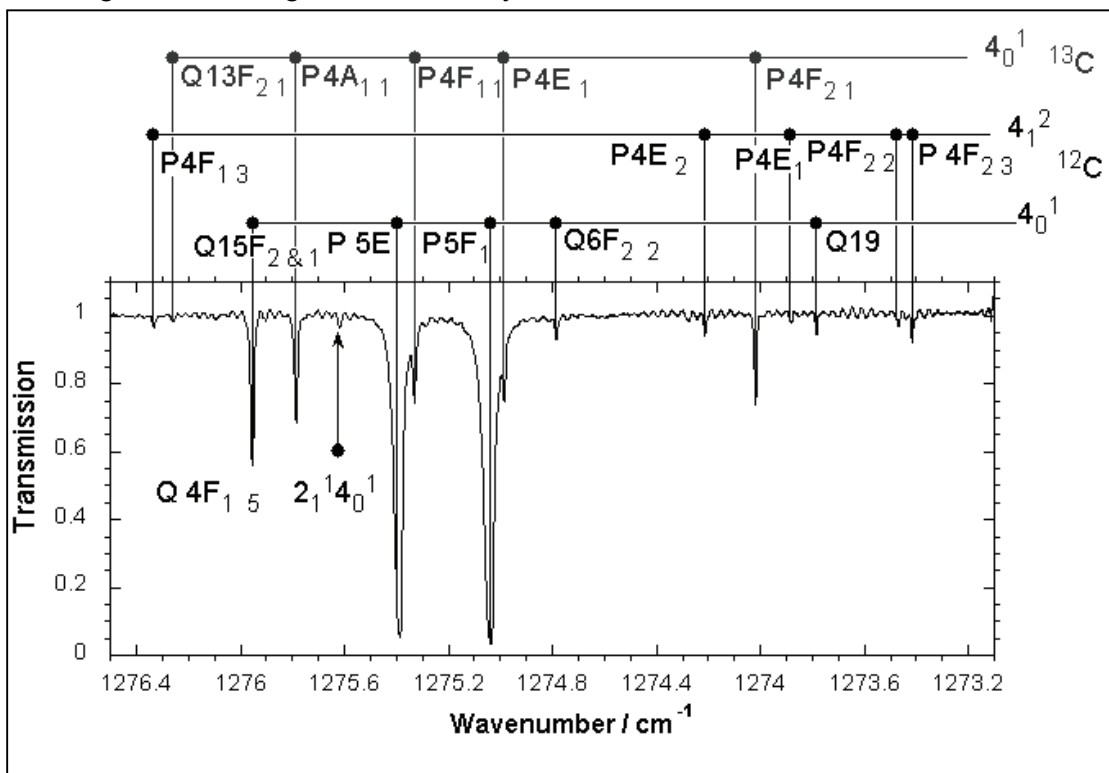


Figure 4.4.4: Assignment of the methane lines. These are tabulated in Table 4.4.2. The lines labelled on the top row are isotopic  $^{13}\text{CH}_4$ .

Line label	Wavenumber/ cm <sup>-1</sup> <sup>a,b</sup>	E <sup>n</sup> /cm <sup>-1</sup> <sup>c</sup>	Vibrational transition	Spin weighting	Rotational transition <sup>d</sup>
	1273.10387	1319	$4_1^2 5_0^1 (\Pi_u - \Pi_g)$	1	P(24, <i>e</i> )
	1273.26195	706	$4_0^1 5_0^1 (\Sigma_u^+ - \Sigma_g^+)$	1	P(24)
	1273.31971	1781	$4_0^1 5_2^3 (\Delta_u - \Delta_g)$	1	P(16, <i>e</i> )
	1273.36660	1937	$4_2^3 5_0^1 (\Delta_u - \Delta_g)$	3	P(24, <i>f</i> )
	1273.45272	1995	$4_2^3 5_0^1 (\Sigma_u^+ - \Sigma_g^+)$	3	P(25, <i>e</i> )
	1273.51679	1781	$4_0^1 5_2^3 (\Delta_u - \Delta_g)$	3	P(16, <i>f</i> )
a16	1273.81972	1225	$4_0^1 5_1^2 (\Pi_g - \Pi_u)$	1	P(20, <i>f</i> )
a15	1273.85701	1822	$4_1^2 5_1^2 (\Sigma_g - \Sigma_u)$	1	P(20, <i>f</i> )
	1273.97456	1732	$4_0^1 5_2^3 (\Sigma_u - \Sigma_g)$	3	P(15, <i>e</i> )
	1274.15639	1318	$4_1^2 5_0^1 (\Pi_u - \Pi_g)$	3	P(24, <i>f</i> )
	1274.36203	1167	$4_0^1 5_0^1 (\Delta_u^e - \Sigma_g^{+e})$	3	P(31, <i>e</i> ) <sup>e</sup>
	1274.47950	1177	$4_0^1 5_1^2 (\Pi_g - \Pi_u)$	3	P(19, <i>f</i> )
	1274.64740	1822	$4_1^2 5_1^2 (\Sigma_g - \Sigma_u)$	1	P(20, <i>f</i> )
	1275.28862	1792	$4_1^2 5_1^2 (\Delta_g - \Delta_u)$	1	P(19, <i>f</i> )
	1275.37466	1262	$4_1^2 5_0^1 (\Pi_u - \Pi_g)$	3	P(23, <i>e</i> )
	1275.42325	1792	$4_1^2 5_1^2 (\Delta_g - \Delta_u)$	1	P(19, <i>e</i> )
	1275.51222	649	$4_0^1 5_0^1 (\Sigma_u^+ - \Sigma_g^+)$	3	P(23, <i>e</i> )
	1275.56659	1743	$4_0^1 5_2^3 (\Delta_u - \Delta_g)$	3	P(15, <i>e</i> )
	1275.58094	1881	$4_2^3 5_0^1 (\Delta_u - \Delta_g)$	3	P(23, <i>e</i> )
	1275.61495	1881	$4_2^3 5_0^1 (\Delta_u - \Delta_g)$	1	P(23, <i>f</i> )
	1275.71661	1743	$4_0^1 5_2^3 (\Delta_u - \Delta_g)$	1	P(15, <i>f</i> )
	1275.95859	1177	$4_0^1 5_1^2 (\Pi_g - \Pi_u)$	3	P(19, <i>e</i> )
	1276.14079	1775	$4_1^2 5_1^2 (\Sigma_g - \Sigma_u)$	3	P(19, <i>f</i> )
	1276.25806	1708	$4_0^1 5_2^3 (\Sigma_u - \Sigma_g)$	1	P(14, <i>e</i> )
	1276.33663	1262	$4_1^2 5_0^1 (\Pi_u - \Pi_g)$	1	P(23, <i>f</i> )

Table 4.4.1: Assignment of the acetylene lines illustrated in Figure 4.4.3. Taken from [103].

a15 and a16 are weak lines caused by absorption from hot acetylene which are analysed in more detail later. <sup>a</sup>See reference [49]. <sup>b</sup>See reference [104].

<sup>c</sup>Approximated using values of rotation constants and band origins in [49].

<sup>d</sup>*e* and *f* indicate the *l*-doubling components of the  $\Pi$  and  $\Delta$  vibrational states.

<sup>e</sup>Transition is due to rotational *l*-resonance between  $\Delta_u^e$  and  $\Sigma_u^{+e}$  sublevels of the same *J* value, see reference [105].

Line label	Wavenumber/cm <sup>-1</sup> <sup>a</sup>	Line intensity / 10 <sup>-24</sup> 300K	Line intensity / 10 <sup>-24</sup> 3000 K	E <sup>v</sup> /cm <sup>-1</sup>	Vibrational transition	Rotational transition	C isotope
	1276.33105	118	8.21	1433.9722	4 <sub>1</sub> <sup>2</sup>	3F <sub>2 5</sub> - 4F <sub>1 3</sub>	12
	1276.26206	23	0.19	949.8879	4 <sub>0</sub> <sup>1</sup>	13F <sub>1 4</sub> - 13F <sub>2 1</sub>	13
	1275.94566	547	17	1250.8364	4 <sub>0</sub> <sup>1</sup>	15F <sub>2 4</sub> - 15F <sub>1 1</sub>	12
	1275.94776	547	17	1250.8373	4 <sub>0</sub> <sup>1</sup>	15F <sub>1 5</sub> - 15F <sub>2 1</sub>	12
		Sum 1094	Sum 34				
	1275.77928	676	0.14	104.7777	4 <sub>0</sub> <sup>1</sup>	3A <sub>2 1</sub> - 4A <sub>1 1</sub>	13
	1275.62160	1.45	0.25	1639.6508	2 <sub>1</sub> <sup>1</sup> 4 <sub>0</sub> <sup>1</sup>	4F <sub>2 9</sub> - 4F <sub>1 5</sub>	12
	1275.38678	2460	6.34	157.1372	4 <sub>0</sub> <sup>1</sup>	4E <sub>2</sub> - 5E <sub>1</sub>	12
	1275.32654	404	0.08	104.7796	4 <sub>0</sub> <sup>1</sup>	3F <sub>2 2</sub> - 4F <sub>1 1</sub>	13
	1275.04168	3690	9.53	157.1389	4 <sub>0</sub> <sup>1</sup>	4F <sub>2 3</sub> - 5F <sub>1 2</sub>	12
	1274.98482	269	0.06	104.7809	4 <sub>0</sub> <sup>1</sup>	3E <sub>2</sub> - 4E <sub>1</sub>	13
	1274.78613	86.8	0.03	219.9368	4 <sub>0</sub> <sup>1</sup>	6F <sub>1 1</sub> - 6F <sub>2 2</sub>	12
	1274.21393	76.5	5.28	1432.524	4 <sub>0</sub> <sup>1</sup>	3E <sub>3</sub> - 4E <sub>2</sub>	12
	1274.01690	401	0.09	104.7849	4 <sub>0</sub> <sup>1</sup>	3F <sub>1 3</sub> - 4F <sub>2 1</sub>	13
	1273.88163	33.5	2.09	1409.3759	4 <sub>1</sub> <sup>2</sup>	3E <sub>2</sub> - 4E <sub>1</sub>	12
	1273.87525	1.54	19.7	2623.6592	4 <sub>0</sub> <sup>1</sup>	22A <sub>2 3</sub> - 22A <sub>1 1</sub>	12
	1273.86456	0.93	11.8	2623.6770	4 <sub>0</sub> <sup>1</sup>	22F <sub>2 8</sub> - 22F <sub>1 2</sub>	12
	1273.85875	0.62	7.90	2623.6865	4 <sub>0</sub> <sup>1</sup>	22E <sub>5</sub> - 22E <sub>2</sub>	12
		Sum 3.09	Sum 39.4				
	1273.84015	10.5	5.12	1878.4236	4 <sub>1</sub> <sup>2</sup>	10A <sub>1 3</sub> - 10A <sub>2 2</sub>	12
	1274.78613	86.8	0.03	219.9368	4 <sub>0</sub> <sup>1</sup>	6F <sub>1 1</sub> - 6F <sub>2 2</sub>	12
m9	1273.782404	12.9	23.9	1975.015	4 <sub>0</sub> <sup>1</sup>	19E <sub>4</sub> - 19E <sub>1</sub>	12
	1273.782485	19.3	14.4	1975.0127	4 <sub>0</sub> <sup>1</sup>	19F <sub>1 7</sub> - 19F <sub>2 2</sub>	12
	1273.782563	32.2	9.56	1975.0082	4 <sub>0</sub> <sup>1</sup>	19A <sub>1 3</sub> - 19A <sub>2 1</sub>	12
		Sum 64.4	47.9				
	1273.469769	50.4	3.13	1409.007	4 <sub>1</sub> <sup>2</sup>	3F <sub>1 4</sub> - 4F <sub>2 2</sub>	12
	1273.418313	116	7.99	1432.1805	4 <sub>1</sub> <sup>2</sup>	3F <sub>1 5</sub> - 4F <sub>2 3</sub>	12

Table 4.4.2: Assignment of the methane lines illustrated in Figure 4.4.4. Taken from [103].

<sup>a</sup>See reference [49]. m9 is a clump of weak lines caused by absorption from hot methane which is analysed in more detail later.

Background spectra were recorded with a pure noble gas / hydrogen plasma before any hydrocarbon was added. This gave us spectra free of absorption lines while ensuring the optical path within the chamber was as close as possible to the measurement conditions. Spectra were then recorded as the carbon flow rate was increased to running level, and for a few minutes while the plasma remained in equilibrium. The hydrocarbon supply was then cut off, and spectra continued being recorded until no more absorption lines were visible.

Typical parameters for running the plasma are as follows:

Beam height: 11 cm above substrate (middle window).

Noble Gas: Argon.

Noble Gas flow rate: 40 sccm.

Microwave Power: 1.5 kW.

Pressure: 150 Torr.

Unless otherwise stated, these parameters were used. The hydrocarbon flow rate could be high, medium or low as detailed in Table 4.4.3. In practice, the low flow rate made the weak lines too weak to be easily used, so most of the analysis focussed on high and medium flow rate spectra.

Hydrocarbon	High flow rate / sccm	Mid flow rate / sccm	Low flow rate / sccm
Acetylene	24.8	15.5	3.1
Methane	40	25	5

Table 4.4.3: Hydrocarbon flow rates. The flow rate of carbon is the same, regardless of the hydrocarbon used.

Analysis of the data focussed on the narrow spectral range between  $1273.7\text{ cm}^{-1}$  and  $1274.0\text{ cm}^{-1}$ . This region contained 3 weak lines, all hot bands (*i.e.* lines which result from absorption from a highly excited energy level) with high J values. Two are acetylene P20 lines at  $1273.857\text{ cm}^{-1}$  (line a15) and  $1273.819\text{ cm}^{-1}$  (line a16), and the other a set of Q19 methane lines at  $1273.782\text{ cm}^{-1}$  (line m9). The main significance of these lines is that they are clear from overlaps with any cold gas absorption lines. Plotting the strength of these lines therefore gives a valuable indicator of the hot-band behaviour of the plasma. A typical plasma spectrum is shown in Figure 4.4.5.

Under plasma conditions, these lines are weak enough that fitting a lineshape to them is almost impossible. However, in the weak line regime, it is acceptable to assume that the line height is proportional to its integrated intensity.

The height of each of the three weak lines was therefore retrieved from the saved spectra, and plotted out for various plasma conditions, as discussed below.



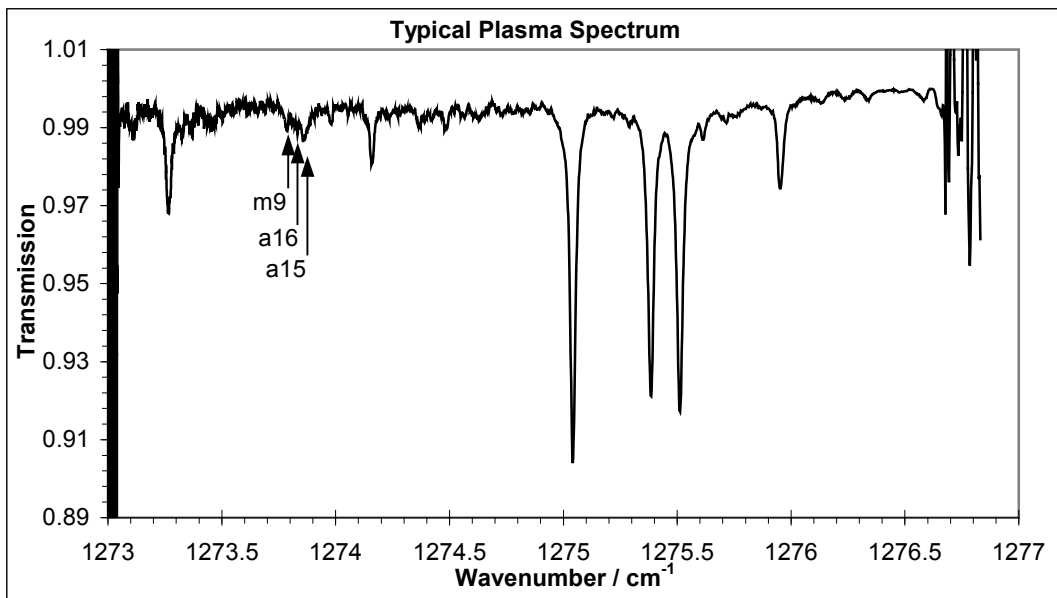


Figure 4.4.5: A typical plasma spectrum, with the "footprint" a15, a16 and m9 lines labelled.  
See Tables 4.4.2 and 4.4.2 for a description of these lines.

Figure 4.4.6 illustrates the strengths of the 3 lines under typical plasma conditions for high and medium flow rates of methane and acetylene.

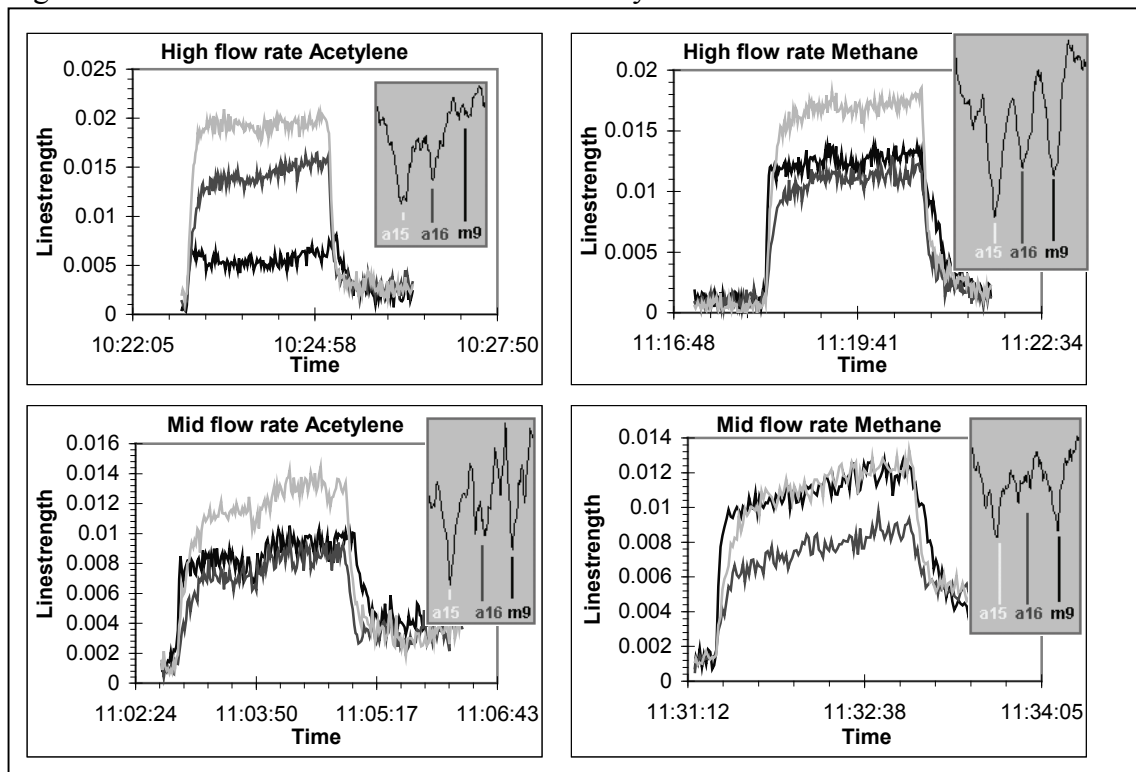


Figure 4.4.6: Linestrength plots for typical plasma parameters.

At standard parameters, regardless of flow rate or hydrocarbon used, the m9 line

appears first and vanishes last. This indicates that hot band methane is formed before hot band acetylene, and it also lingers for longer as the plasma runs out of carbon feedstock. The a16 line always appears last, although only marginally after the a15 line. The a16 line also decays slightly slower than a15.

By comparing the medium and high flow rate runs, it is clear that increasing the carbon flow rate increases the strength of the two acetylene lines, regardless of which carbon feedstock is used.

By comparing the acetylene fed runs to the methane fed runs, the methane line is stronger if the carbon feedstock is methane. This is expected behaviour. The high flow rate methane plasma looks very similar to the medium flow rate acetylene one.

The relative strength of the acetylene lines remains constant throughout, other than the slight difference in buildup and decay times. As these lines are from similar energy levels, there should be almost equal abundances of molecules to be excited.

Figure 4.4.7 shows the effect of varying the plasma pressure on mid flow rate methane and acetylene plasmas. Reducing the plasma pressure lowers the strength of the methane line compared to the acetylene lines, regardless of which carbon feedstock is used. The methane line starts out stronger when methane is used, but drops regardless of which gas is feeding the plasma.

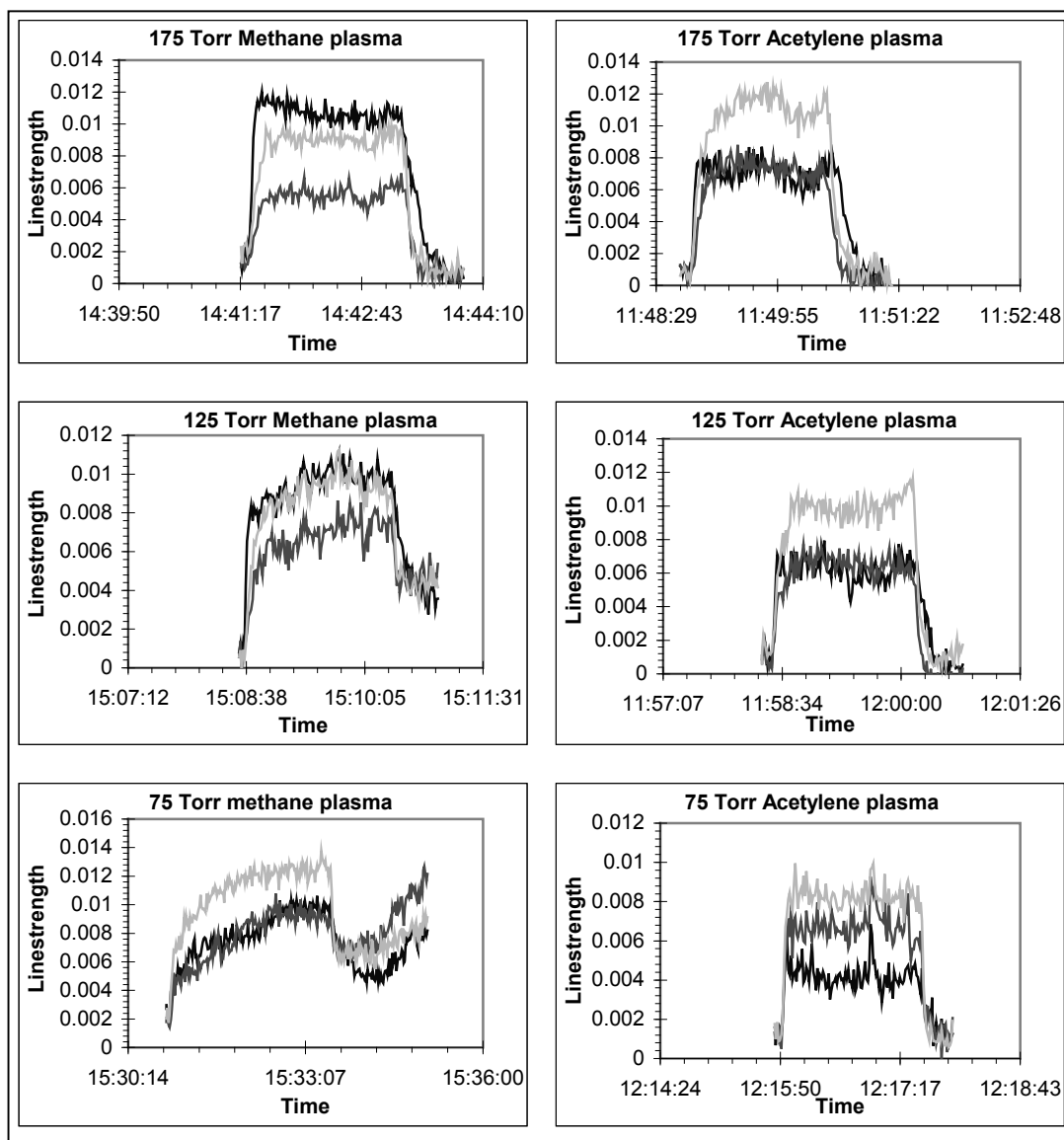


Figure 4.4.7: Linestrength plots for various plasma pressures. black: methane line 9. light grey: acetylene line 15. dark grey: acetylene line 16.

The microwave power was only varied for acetylene feedstock, and made little difference to the relative linestrengths. The acetylene lines appeared to get slightly stronger at low power, but this was not statistically significant and may be an effect of random error.

The noble gas used in the plasma seems to have no effect. Argon based and neon based plasmas exhibit similar behaviour. Altering the noble gas flow rate has quite a strong effect on the plasma. It is unclear how much of this is directly due to the

change in flow rate, and how much is indirect, due to the change in temperature which the alteration of the flow rate causes. At high noble gas / low hydrogen, the plasma was considerably hotter than for low noble gas / high hydrogen. This is a consequence of noble gas having poorer thermal conductivity than hydrogen [99]. Figure 4.4.8 illustrates the behaviour of the plasma for a mid flow rate methane plasma with various different argon flow rates. The hydrogen flow rate was altered so that the total argon + hydrogen flow rate was always 540 sccm.

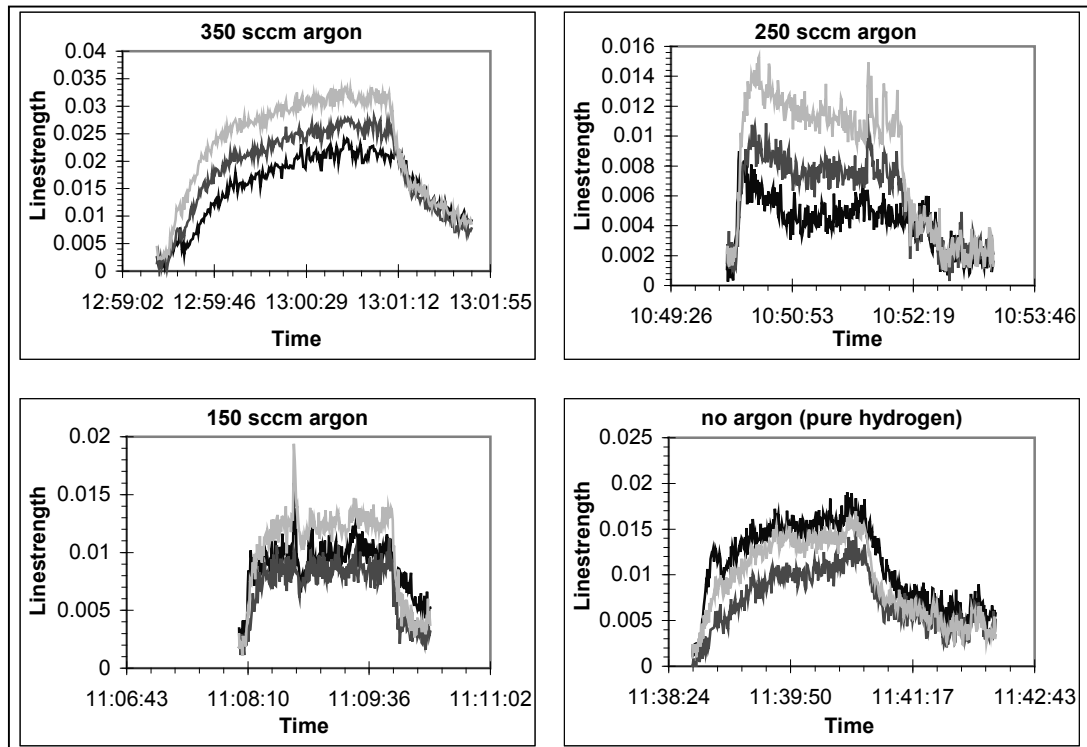


Figure 4.4.8: Linestrength plots for various argon flow rates. black: methane line 9. light grey: acetylene line 15. dark grey: acetylene line 16.

As the argon flow rate drops, and the hydrogen flow rate increases, the methane line becomes stronger compared to the acetylene lines. Also, with no argon, the methane line drops off more slowly. This tallies with observations made at the time: The strong (cold band) methane lines in the spectrum took a lot longer to disappear with low argon levels. With no argon, one test required a full 3 minutes for the cold band methane to clear. Obviously the weak lines drop off faster, but they still linger noticeably with no argon, compared to their drop off with some argon. As stated earlier, these trends were also observed if neon was substituted for argon. The blip

during the 150 sccm argon run is a consequence of some strong interference fringes observed at that point. The cause of the fringes is thought to be a refractive index change within the plasma, probably caused by a carbon deposit on the substrate vaporising and reentering the plasma.

The QC laser spectrometer has shown itself to be a useful tool for probing the outer, cooler layer of a CVD plasma. Within the hot central zone, the Maxwell-Boltzmann distribution of particles means that there are relatively few particles in each of a large number of excited energy levels. As absorption from an energy level depends on the population of that level, this ensures that in the centre of the plasma, all absorption lines are very weak and are unable to be detected with the setup used here. The measurements of the outer layer have still proved useful and informative.

By measuring levels of different gases in different regions of the plasma, it is possible to improve a model [100] of the reaction process. As the reaction process is critical to the deposition of diamond, by building up a model to explain exactly what occurs under different plasma conditions, it will be possible to improve the quality of the deposited diamonds.

#### 4.5: Jet Engine Exhaust Plume Measurements

On 23 July 2009, Laser 60 (see Chapter 3) was used to measure H<sub>2</sub>O, CO and CO<sub>2</sub> present in the exhaust plume of a Rolls-Royce turbojet engine [106]. The engine was fixed in a testbed at Rolls-Royce's base in Ansty.

Pollution from aircraft engines has a major effect on the atmosphere, and the number of aircraft-miles per year is increasing, as is total aviation fuel consumption. [107].

A wide variety of measurements of emissions from aircraft was carried out by Spicer *et al* [108]. Several different measurement methods were used including chemiluminescence, infrared absorption, flame ionisation and proton transfer reaction mass spectrometry. These measurements were taken from US military aircraft running at various engine speeds, while on the ground. Gas was sampled through a pipe in the exhaust flow some distance from the engine to ensure the gases had cooled to a temperature which would not damage the instruments, or distort the readings. Similar work by Agrawal *et al* [109] measured emissions at a distance of 1 m behind a selection of 4 commercial aircraft engines.

Schäfer *et al* [110] have measured the exhaust gases immediately behind the exhaust nozzle of a static aero engine in a test rig using infrared Fourier Transform spectroscopy. Their measurements of beam cross-section show the exhaust plume to have a generally similar shape to the plume described in this chapter. Further analysis of the data presented here will likely improve the cross sections and enable a better comparison.

Gas / liquid chromatography has been used to measure the hydrocarbon emissions from a jet engine in a test rig during simulated supersonic flight conditions at high altitude [111]. These tests simulated altitude by running the engine under lower pressure than ground level.

For this work, the laser and detector were mounted on a traverse beside the engine exhaust, with the beam crossing the exhaust plume. At the other side, a corner cube reflector was used to return the beam to the detector. A parabolic mirror was used to ensure that the signal would still be detected if the beam shifted on account of turbulence in the plume. The laser and detector drive boxes were strapped to an adjacent table, while the control computer was in the control room next to the test bed. This arrangement required the use of 15m of USB and BNC leads between the PC and the laser and detector. A photograph of the setup is shown in Figure 4.5.1.

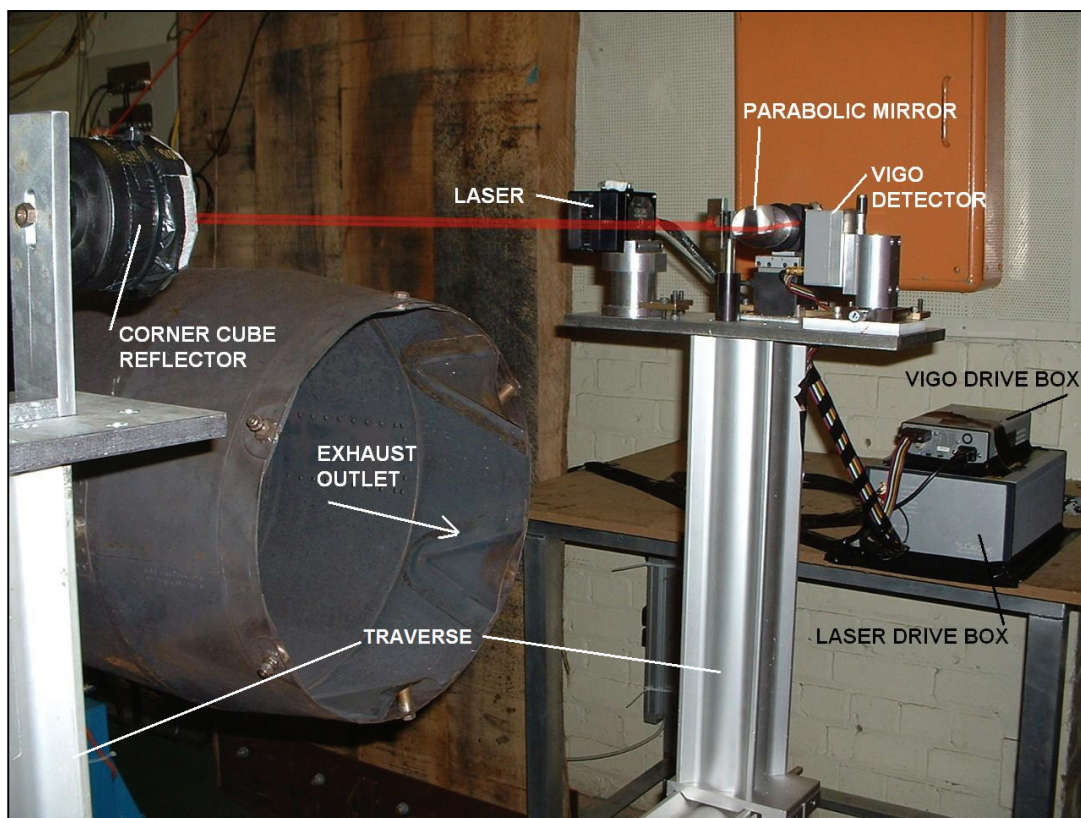


Figure 4.5.1: Laser mounting arrangements in Ansty. In this photo, the traverse had been jacked up clear of the plume to test the height adjustment. The laser beam is drawn in red.

The laser was run at  $-20\text{ }^{\circ}\text{C}$  with a 1300 ns, 12 V pulse at a frequency of 20 kHz. This resulted in a frequency downchirp between  $2058.84\text{ cm}^{-1}$  and  $2055.00\text{ cm}^{-1}$ , which allowed us to probe a strong CO absorption line at  $2055.4003\text{ cm}^{-1}$ , along with a weak CO line at  $2056.0476\text{ cm}^{-1}$ , 3 weak CO<sub>2</sub> lines at  $2055.1639\text{ cm}^{-1}$ ,  $2056.70109\text{ cm}^{-1}$  and  $2058.24037\text{ cm}^{-1}$ , and one H<sub>2</sub>O line at  $2057.5\text{ cm}^{-1}$ . With the engine idling at equilibrium, these are the only lines visible.

During acceleration, several other hot bands appear and at high engine revs, additional water vapour absorption is observed. During acceleration, the number of overlapping lines makes retrieval difficult as shown in Figure 4.5.2.

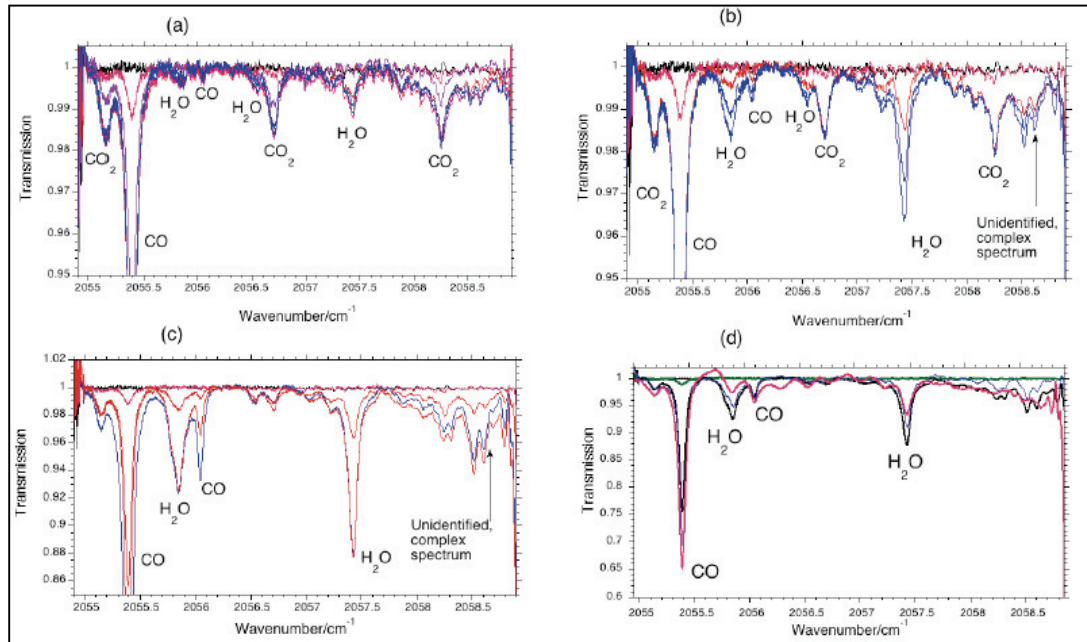


Figure 4.5.2: Engine accelerating from startup to 12,700 rpm. (a) 1 s after ignition. (b) 2 – 5 s after ignition, showing weak CO<sub>2</sub> increasing then decreasing again. (c) The next 20 s, showing an increase in an unidentified, set of lines at the right hand side. (d) Engine approaching equilibrium at 12,700 rpm.

An attempt to marry traverse height to line strengths was carried out. As the work was carried out at atmospheric pressure, a Lorentzian lineshape was used to fit the lines which had least overlaps. These were the CO line at  $2055.4003 \text{ cm}^{-1}$  and the H<sub>2</sub>O line at  $2057.41933 \text{ cm}^{-1}$ . The pressure broadened width of the lines was taken from HITRAN [49]. Without knowing the gas distribution within the plume, an effective path length cannot be chosen, and without knowing the temperature distribution, the line intensities cannot be determined. Therefore the results were left as line-integrated areas, rather than being converted to mixing ratios, as has been the case hitherto. The traverse height is in millimetres, with 0 corresponding to the laser beam passing through the centre of the exhaust plume.



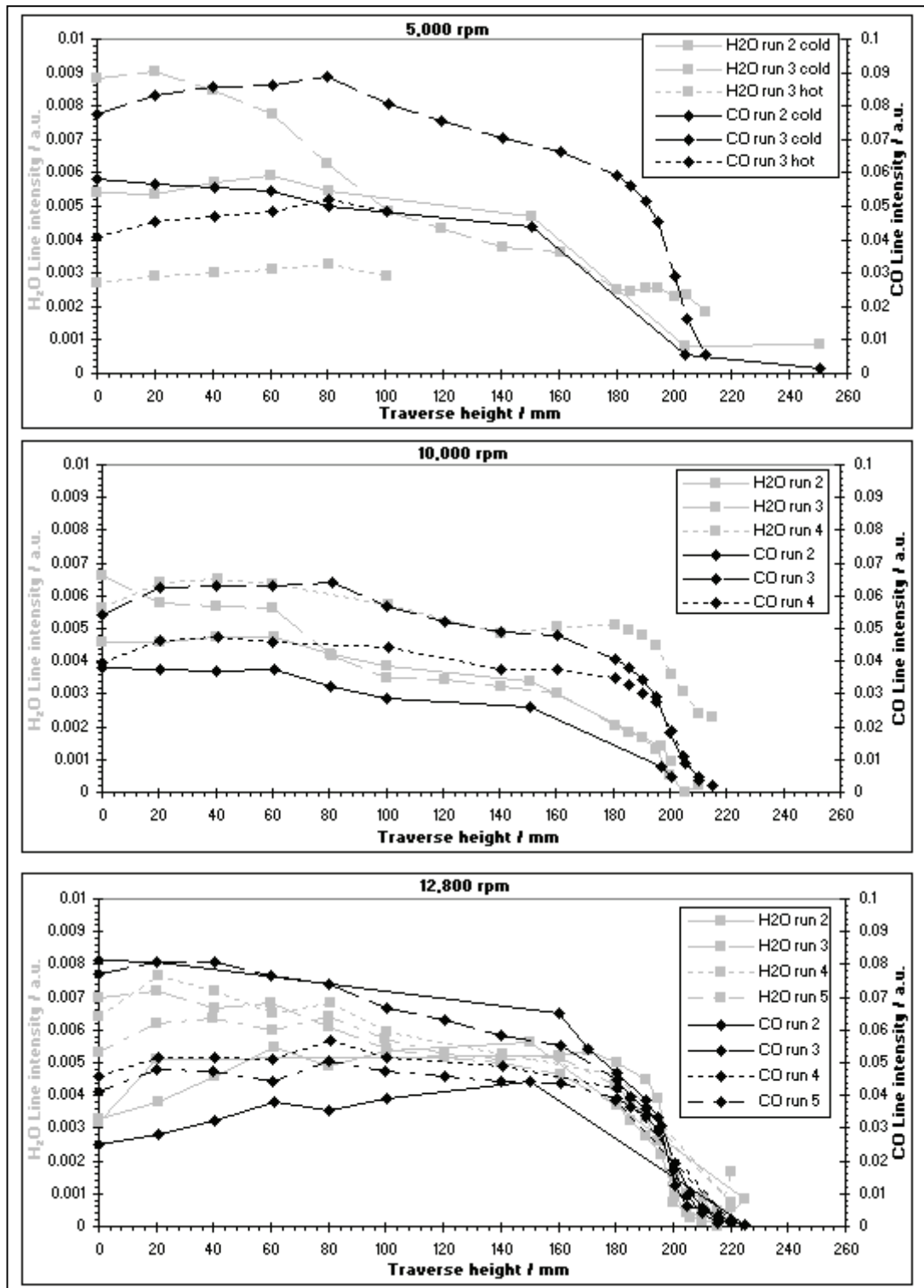


Figure 4.5.3: Water and Carbon Monoxide cross sections through the exhaust plume.

Traverse height 0 mm corresponds to the laser beam passing through the centre of the plume.

The average intensity of the 50 spectra recorded at each traverse location was used to build up a profile of line intensity as a function of position at each engine speed. This is shown in Figure 4.5.3.

At idle speed (5,000 rpm), the overall profile of the plume is fairly predictable, with most gas in the middle, and a gradual decrease towards the edge where there is a more rapid decrease. The large variation in gas line strengths between runs may be related to engine temperature, varying with whether the engine has just been started, or is idling after a period of running.

At cruising speed (10,000 rpm), the pattern is fairly similar, although there is not the same gradual decrease, only the steeper drop at the edge of the plume. This leads to a more squared off profile.

At maximum speed (12,800 rpm), the pattern is fairly similar to that at cruising speed, however the edge of the plume is more clearly defined, with all observations seemingly agreeing on where the decrease is.

At all speeds, there is a notable difference in gas levels on different runs of the engine. It is unlikely that this is a measurement artefact since during the each traverse across the plume, the readings are consistent with each other which would not be the case if there were fluctuations in either the laser, the received signal, or the line fitting process.

Further, more detailed analysis of the recorded spectra should be able to produce more accurate cross-sections at different engine speeds, but these preliminary observations demonstrate that the QC laser is an effective tool for probing exhaust plumes. Schäfer *et al* [110] have performed similar measurements using infrared Fourier Transform spectroscopy. Their measurements of beam cross-section show the exhaust plume to have a generally similar shape to the plume described in this chapter.

The stability of the beam, despite plume turbulence was remarkable, and it seems likely that the work could be repeated with the laser and detector further from the edge of the plume without adversely affecting instrument sensitivity.

#### 4.6: Bus Exhaust Fumes

Vehicle exhaust emissions are a major cause of airborne pollution. In Glasgow, the pollution levels are so high that consideration is being given to introducing a Low Emission Zone, similar to that in London [112]. Within Glasgow city centre, buses are a major contributor to the pollution level.

Although buses are a major polluter, in the past, efforts to reduce their emissions have backfired, most notably when an effort to fit most London buses with particulate matter (PM10) filters led to an increase in nitrogen dioxide emissions [113]. Nitrogen dioxide is one of a number of gases which cause acid rain, so an increase in this is a highly undesirable side effect.

Vehicular emissions have been measured previously by various methods and under various circumstances.

A roadside sensor to measure emissions of CO, NO, hydrocarbons and CO<sub>2</sub> has been operated for many years, and shows definite decreases in pollution from newer vehicles [114]. This sensor uses infrared and ultraviolet absorption spectroscopy to determine the emissions from passing vehicles.

Emissions of nitrous acid and NO<sub>x</sub> have been carried out in the Caldecott Tunnel, San Francisco [115] using sodium carbonate coated glass annular denuders to collect nitrous acid, and chemiluminescent analysers to measure NO<sub>x</sub> concentrations.

Indoor pollution in houses with built in garages has been investigated, to determine the extent to which fumes from a vehicle parking in the garage enter the house [116]. CO<sub>2</sub>, CO, NO<sub>x</sub>, and hydrocarbons were measured using dedicated sensors used for vehicle emission testing. CO and CO<sub>2</sub> were measured using nondispersive infrared instruments, NO<sub>x</sub> by chemiluminescence and hydrocarbons by a flame-ionisation detector.

The first field test of the Cascade 4-laser system following the modifications discussed in Chapter 3.7 was carried out on the 24th of September 2009. Following on from previous work in the group studying car exhaust emissions [117], we carried out an investigation of the exhaust fumes emitted by buses from various decades across the 20th century [118]. The buses measured were chosen to be as typical of their era as possible, and are detailed below in Table 4.6.1.

Year new	Chassis type	Engine type	Original operator
1938	AEC Regent O661	AEC	Glasgow Corporation
1949	Albion Venturer CX37S	Albion	Glasgow Corporation
1959	Leyland Titan PD3	Leyland O.600	Western S.M.T.
1967	Leyland Titan PD3A	Leyland O.600	Blackpool Transport
1977	Leyland Atlantean AN68A/1R	Leyland O.680	Greater Glasgow P.T.E.
1985	MCW Metrobus DR132/6	Cummins L10	Midland Scottish
1993	Leyland Olympian ON2R50C13V3	Cummins L10	Strathclyde's Buses

Table 4.6.1: Buses used for exhaust fume measurements.

The inlet used a length of pipe, the end of which was held 69 cm away from the exhaust pipe, in line with the where the exhaust plume was expected to be. Some buses had unexpected plume directions and required the pipe to be moved once the bus had been started. The sampling pipe is shown in position by the 1967 Leyland Titan as the bus started in Figure 4.6.1. The measurements were carried out at a cell pressure of 108 Torr.



Figure 4.6.1: Sampling pipe in the exhaust plume from the 1967 Leyland Titan.

Once the pipe was positioned and the system was recording, each bus was started, allowed to idle for around 10 minutes, then switched off. Data recording continued

until the gas levels had dropped back to equilibrium.

Each laser in the system had at least two spectral lines visible, as discussed:

Laser 0 (NO<sub>2</sub>): Around 12 NO<sub>2</sub> absorption lines were visible between 1630.4 cm<sup>-1</sup> and 1632.0 cm<sup>-1</sup>. The line at 1631.02 cm<sup>-1</sup> was free from overlaps with other lines and was used to calculate the NO<sub>2</sub> mixing ratio in post-processing.

Laser 1 (CO<sub>2</sub>): In addition to the CO<sub>2</sub> line at 2050.57 cm<sup>-1</sup>, this laser detected a CO line at 2050.85 cm<sup>-1</sup> and a weak H<sub>2</sub>O line at 2051.56 cm<sup>-1</sup>, all of which were used for mixing ratio retrieval, although the water line was so weak that there was no measurable difference between background levels and exhaust emission gases.

Laser 2 (N<sub>2</sub>O): While the N<sub>2</sub>O line at 1274.62 cm<sup>-1</sup> was detectable, the buses did not emit noticeably more than atmospheric background levels of N<sub>2</sub>O. Data retrieval from this laser was challenging as 6 strong formaldehyde (H<sub>2</sub>CO) lines and several weaker lines forming quasicontinua spread across the spectrum made it hard to find lines clear of overlaps. Ultimately, one H<sub>2</sub>CO line at 1274.29 cm<sup>-1</sup>, and two CH<sub>4</sub> lines at 1275.39 cm<sup>-1</sup> and 1275.04 cm<sup>-1</sup> were used to calculate mixing ratios.

Laser 3 (NO): Two NO lines at 1903.13 cm<sup>-1</sup> and 1903.64 cm<sup>-1</sup> were used for mixing ratio retrieval, although only the weaker one is plotted as the strong line reached saturation while measuring several of the buses. Also visible were a very strong H<sub>2</sub>O line at 1904.35 cm<sup>-1</sup>, which was saturated and could not give any useful data, and a weak line at 1903.55 cm<sup>-1</sup>, which has not been identified.

Sample spectra are shown from each laser in Figure 4.6.2. These all were recorded while measuring the exhaust of the 1967 Leyland Titan. Lines are labelled with the gas which absorbs at that frequency. Those which were used for measuring the mixing ratios shown in subsequent figures are also labelled with the line centre, taken from HITRAN [49], or in the case of formaldehyde, Nadler *et al* [119].

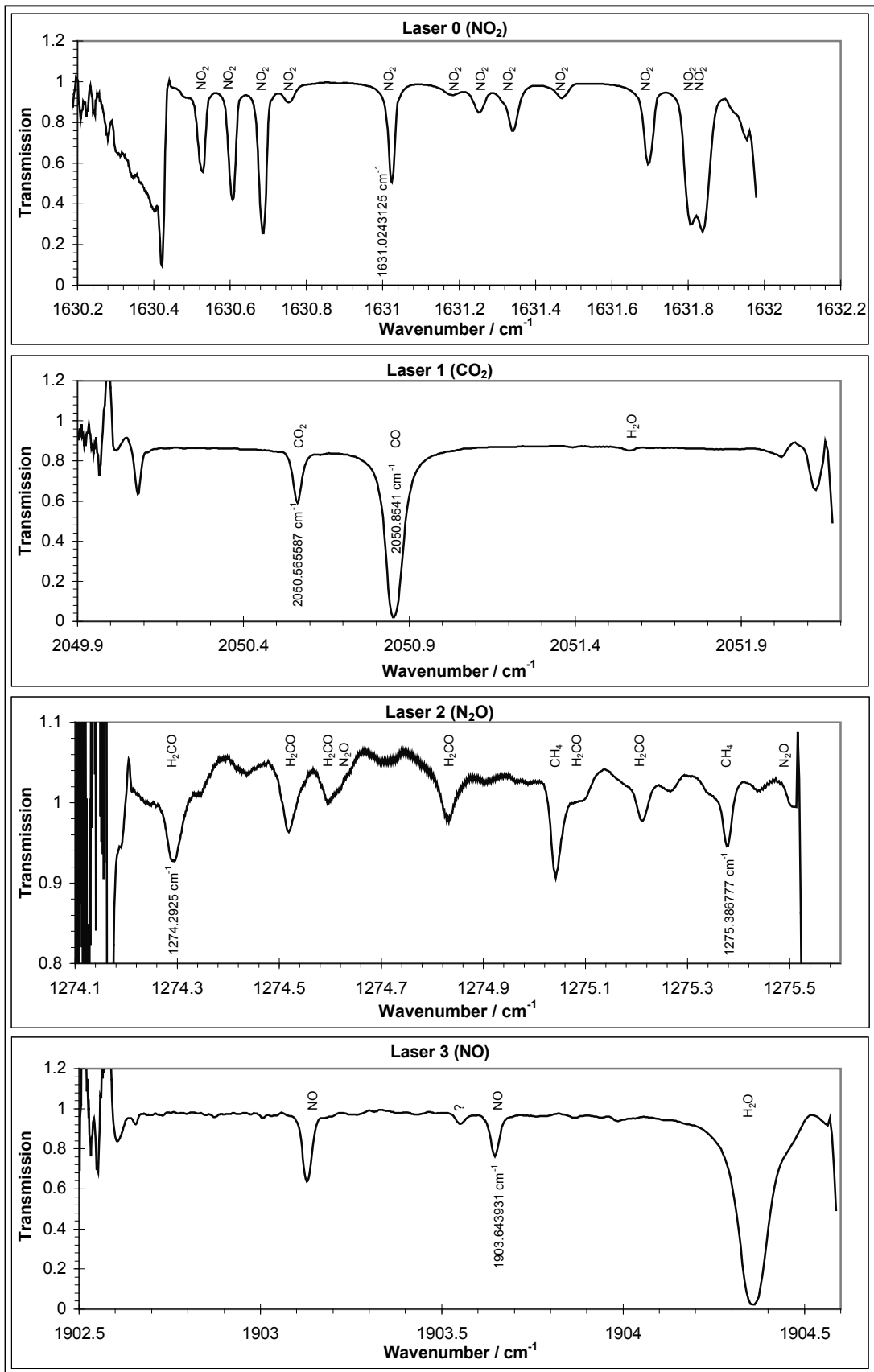


Figure 4.6.2: Sample exhaust spectra. The laser 3 line labelled ? is currently unidentified.

Background spectra were recorded in the laboratory by flowing zero air through the cell for 5 minutes to flush any contaminants out the cell, then spectra were recorded as normal. These zero air spectra were later analysed to give the standard deviation of the zero reading. The results are shown below in Table 4.6.2.

Gas	Standard deviation of zero reading / ppb	Maximum reading during measurements / ppb	Standard deviation as percentage of maximum
CO	32	68,000	0.05
CO <sub>2</sub>	9500	3,100,000	0.30
CH <sub>4</sub>	32	13,000	0.25
H <sub>2</sub> CO	700	44,000	0.91
NO	1.0	14,000	0.01
NO <sub>2</sub>	0.62	4,500	1.37

Table 4.6.2: Zero reading standard deviation for each gas mixing ratio calculated.

As can be seen, for nearly all gases, the standard deviation is less than one percent of the maximum reading. The worst readings are obtained from the H<sub>2</sub>CO lines, which as discussed later were challenging to accurately fit, and the NO<sub>2</sub> lines, although here the high percentage standard deviation is caused by the relatively low levels of NO<sub>2</sub> measured. The absolute value of the standard deviation is lower than all the other gases.

Figures 4.6.3 to 4.6.6 shows the time evolution of CH<sub>4</sub>, CO, CO<sub>2</sub>, H<sub>2</sub>CO, NO and NO<sub>2</sub> for each bus. All are plotted on the same scales for comparison.

The main trend is that the old buses in general give off more pollutant gases than the new ones, but other details are also seen. All buses showed a CO level which dropped as the engine began to warm up. In the case of the 1967 Leyland Titan, as the CO level was above the saturation limit it is impossible to see if this occurred.

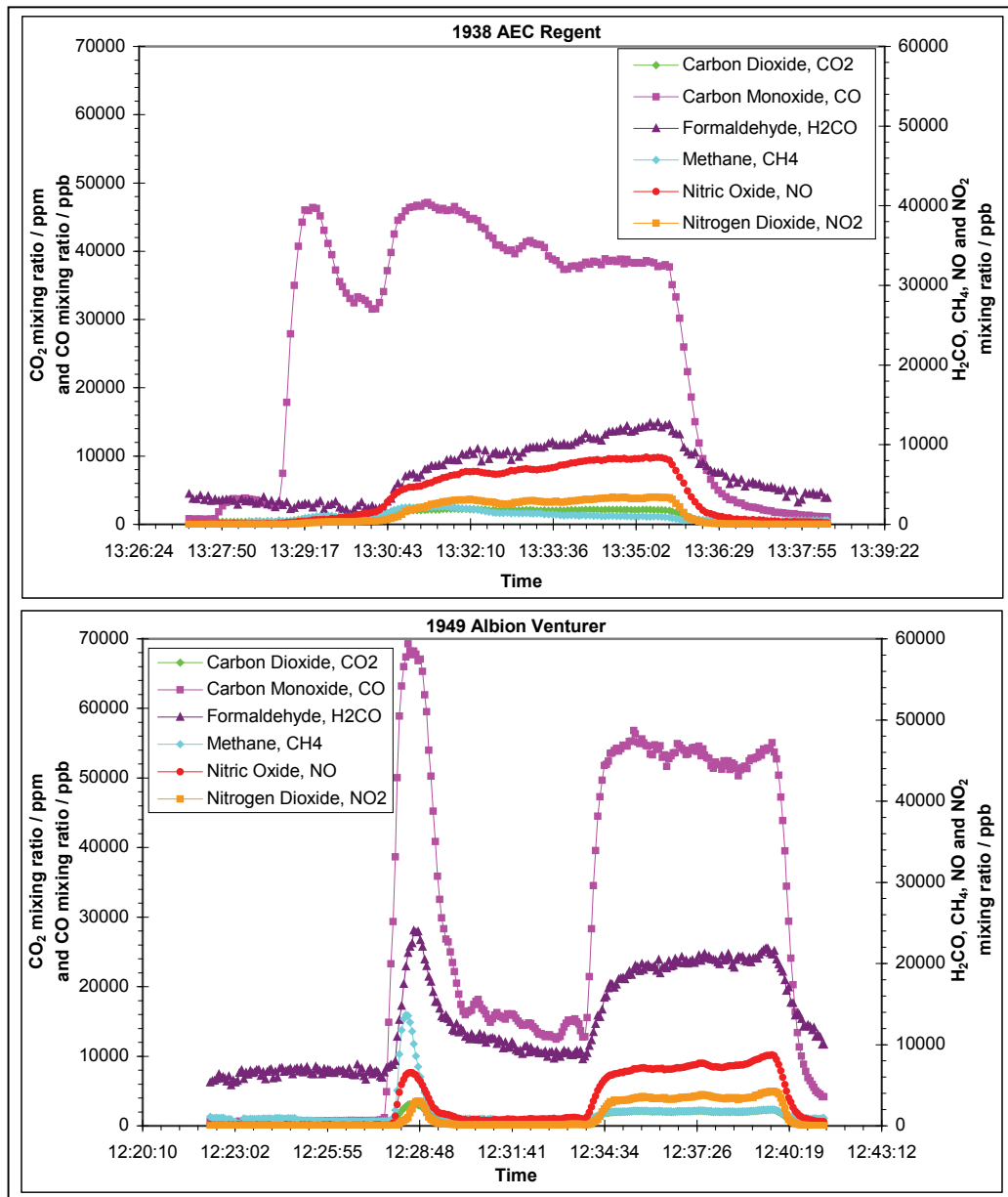


Figure 4.6.3: Exhaust emissions from the 1938 and 1949 buses.

While the 1938 AEC Regent and the 1949 Albion Venturer were pretty similar, the latter put out more carbon monoxide. Both were so smoky at first that the pipe was moved clear until the worst of the smoke died away. This is visible in both plots as an initial peak, followed by a lower spell. Both showed a drop in carbon monoxide as they warmed up, compared to when they had just started. A possible explanation for the similarity in emissions is that owing to the Second World War, there was very little development of civilian vehicles during the 1940s so although the 1949 Albion was a postwar model, there would be very little to distinguish it from a prewar bus.



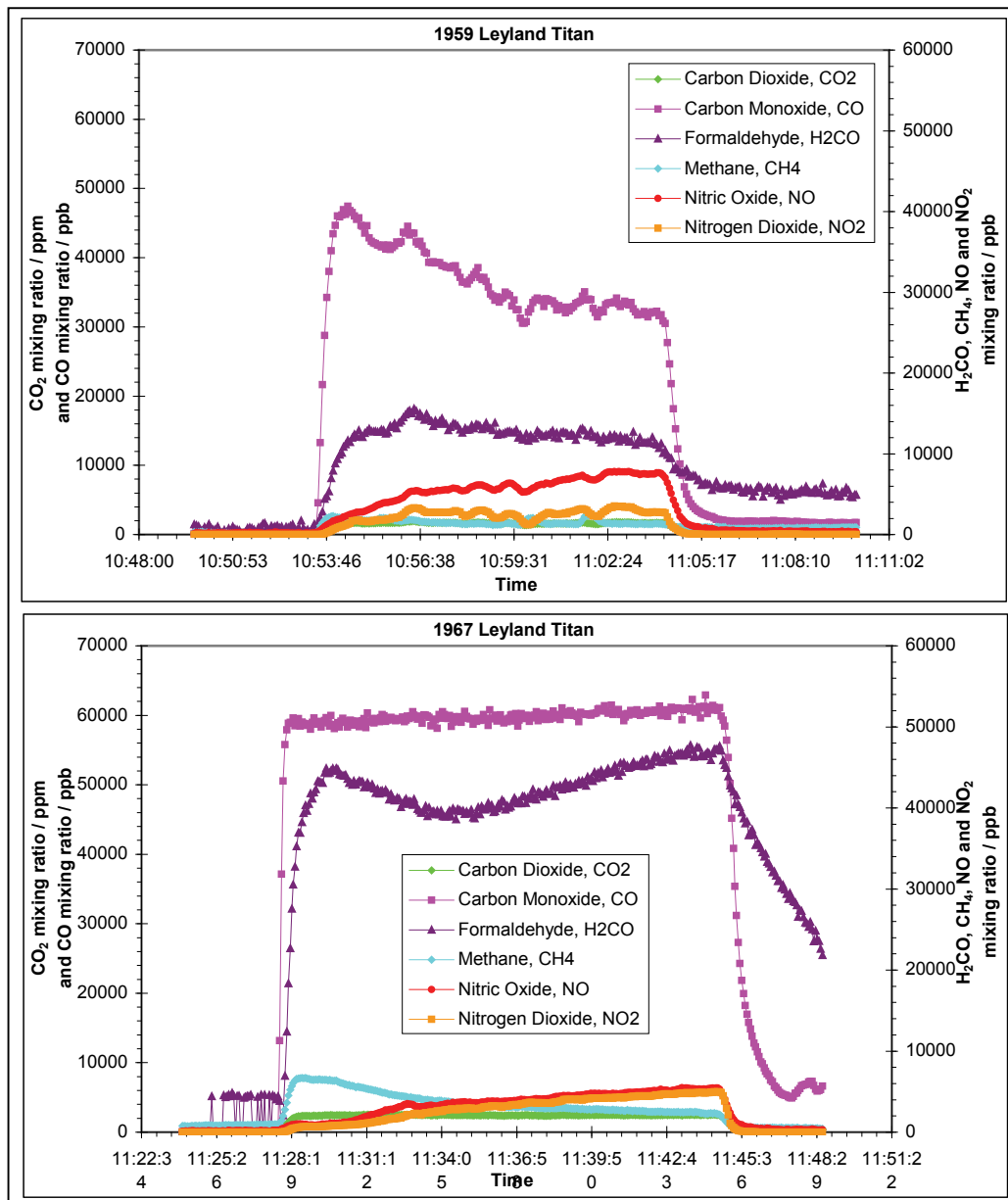


Figure 4.6.4: Exhaust emissions from the 1959 and 1967 buses.

The 1959 Leyland Titan was an interesting bus as the engine idle speed was oscillating between too high and too low. The peaks and troughs in every gas correspond to these oscillations in engine speed. There is a particularly good match between the increase in methane and the drop in all other gases when the bus unexpectedly stalled at 10:59. It had to be restarted to complete the test. Later mechanical investigations revealed the bus had a broken piston ring, explaining its erratic running.

The 1967 Leyland Titan was remarkable different from the 1959 one. Its emissions contained so much carbon monoxide that the absorption line was saturated. There was also a much higher level of formaldehyde. Based on the emissions of another engine when cold compared to those after it had been warmed up thoroughly by a short drive, it is expected that this bus would give out considerably less pollution once it had warmed up properly.

The fumes from this bus collected in the space between parked buses which highlighted a drawback of the measurement method – the instrument effectively ended up measuring an ever increasing level of NO<sub>2</sub>, NO and H<sub>2</sub>CO as the gases accumulated. This was avoided for subsequent buses which were parked further apart.

The emissions from the 1977 and 1985 buses are shown in Figure 4.6.5.

The 1977 Leyland Atlantean saturated the absorption by nitric oxide, leading to a reading which was at the upper limit of the scale. It also had an unexpectedly high nitrogen dioxide reading. With the exceptions of these gases, it did follow the general trend of dropping exhaust pollution levels with decreasing age of bus. This bus was also used to compare the emissions of a cold engine with those of a hot one as described later.

The 1985 MCW Metrobus also had a high nitric oxide level, although not high enough to saturate the instrument. For the other gases, the levels were generally low as emissions from a relatively modern bus should be.

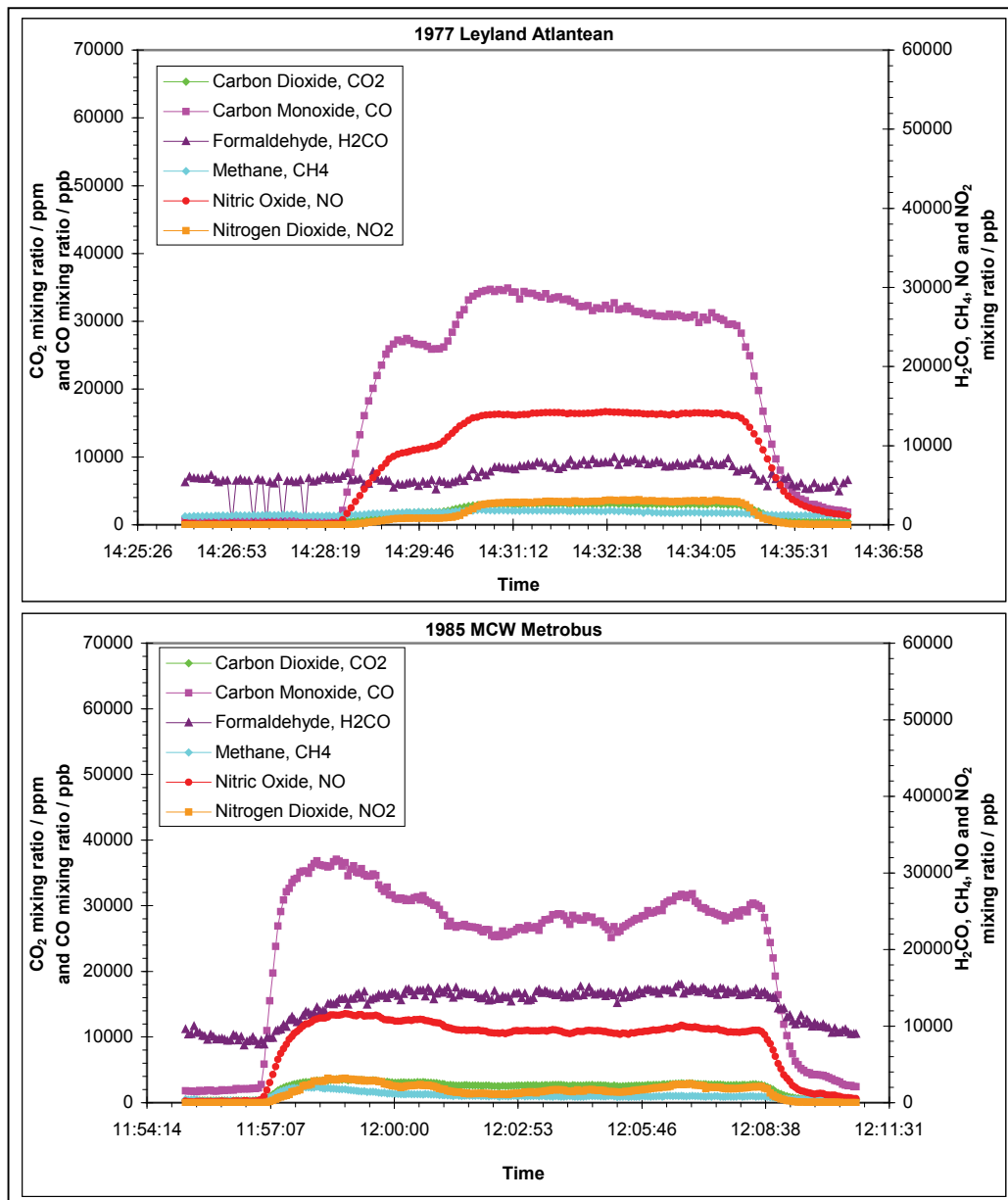


Figure 4.6.5: Exhaust emissions from the 1977 and 1985 buses.

The 1993 Leyland Olympian emissions are shown in Figure 4.6.6. It had very low levels of all gases measured. It seems unlikely that this level of reduction in pollution is entirely due to design improvements between 1985 and 1993. It is possible that the exhaust was bent oddly, resulting in the plume hitting the garage floor and bouncing up in an unexpected direction. Theoretically, as a modern bus, it should have lower emissions than the others, but as stated, it seems unlikely this is the only cause of its low readings.

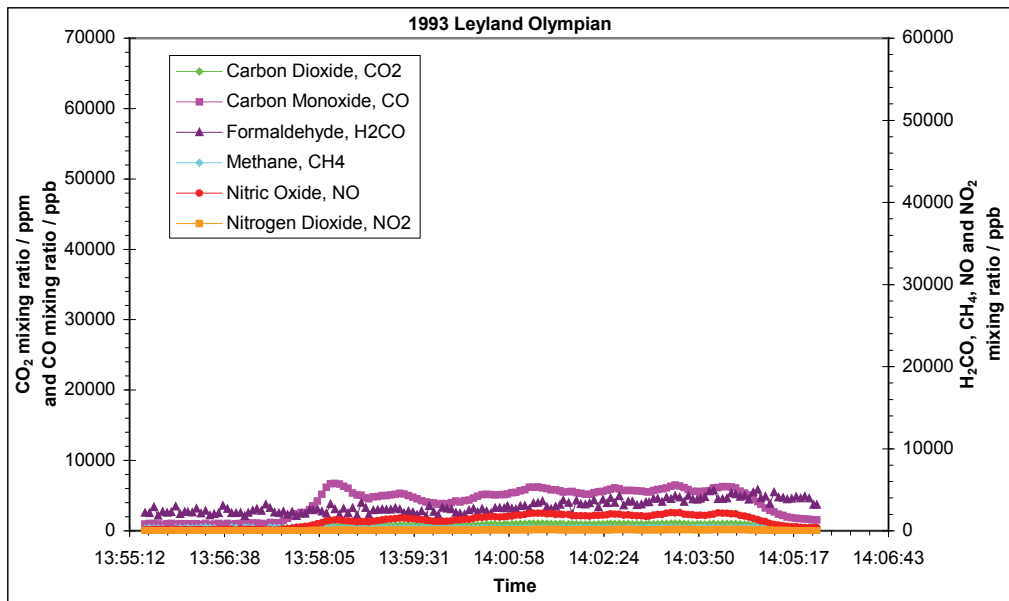


Figure 4.6.6: Exhaust emissions from the 1993 bus.

The 1993 Leyland Olympian was also used to investigate the difference between running at idle, and revving at a moderate rate. For this second experiment, the bus was started, then, once its air pressure had built up enough to allow the accelerator to work, revved gently at as near to a constant rate as possible for two minutes. It was then allowed to idle again for 1 minute before switching off. The time evolution of each gas which was measurable during this test is shown in Figure 4.6.7.

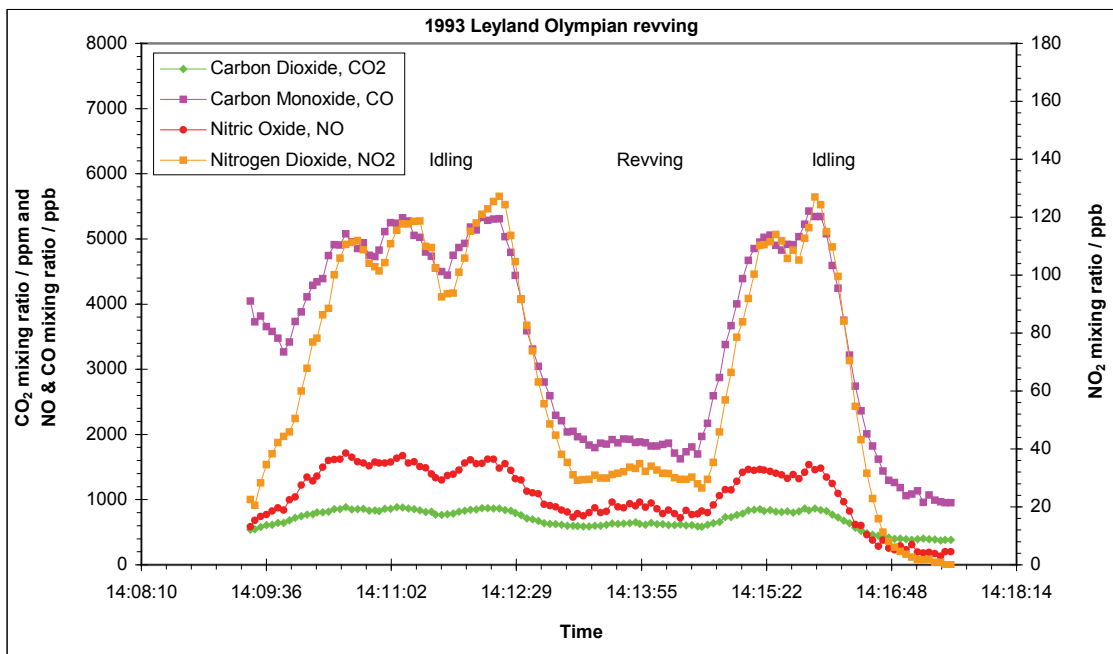


Figure 4.6.7: The difference in emissions between an idling engine, and a revving engine, demonstrated by the 1993 Leyland Olympian.

At a higher rate of revs, there is far less carbon monoxide, nitric oxide and nitrogen dioxide, and only a little less carbon dioxide. Some of the reduction is likely to be caused by the fumes being blown past the pipe, but the differences between CO and CO<sub>2</sub> suggest that the combustion process is more efficient when the engine is revving.

The final experiment was to compare the emissions from the 1977 Leyland Atlantean when cold to those after the bus had been warmed up by being taken for a drive. These are shown in Figure 4.6.8.

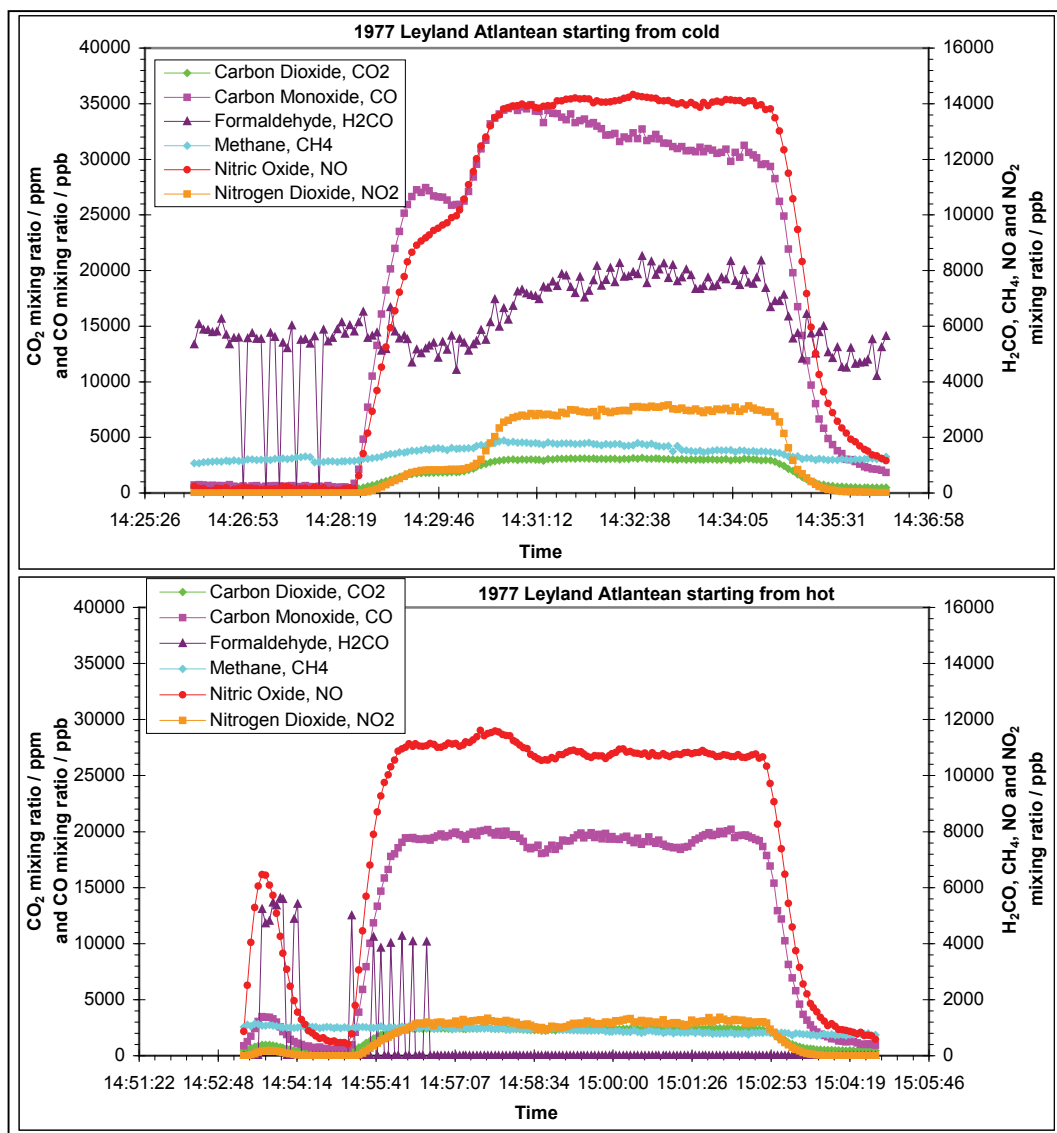


Figure 4.6.8: The 1977 Leyland Atlantean's fumes before and after a trip round the block.

The methane and carbon dioxide levels remain about the same, but there is far less of the other gases, especially the nitrogen compounds. It is likely that the lower pollution levels are therefore due to the increased operating efficiency of the engine as it warms up.

This work demonstrates that the QC laser spectrometer makes an effective gas analyser for vehicular exhaust fumes from heavy diesel engines, in addition to fumes from car engines as previously studied [117]. With automotive pollution being a serious problem and vehicles already subject to annual emissions checks, the QC laser spectrometer could be an effective tool to carry out such tests. Calibration of the instrument would need carried out. An effective method of calibration would be to measure emissions in tandem with the existing analysers used by MOT stations. Current analysers use nondispersive infrared absorption at specific wavelengths to measure hydrocarbons, carbon monoxide and carbon dioxide.

#### 4.7: Rapid Passage

Rapid passage signals have been observed [120] in which a delayed switch from absorption to emission is observed as the optical density of acetylene in a long path length cell is increased. The delayed switch results in the generation of a large, narrow, transient gain signal. Using numerical solutions of the Maxwell-Bloch equations it has been demonstrated that this effect is due to constructive interference between the incident laser field and the field generated by the response of the gaseous medium. This occurs as a consequence of minimal collisional damping at the low gas pressures within the gas cell, so that the chirp rate of the laser is faster than the collisional reorientation time of the molecules.

One of the main advantages of the present experiments, which use the frequency chirped 30 mW peak power output from an electrically pulsed 8  $\mu\text{m}$  QC laser, is the very long absorbing path length due to the alignment of an astigmatic Herriott cell [60]. For a 50 cm cell, accurate rotation and spacing of the mirrors can lead to path lengths of over 100 m [62, 121]. This allows us to achieve strong absorption with very low pressures, and hence with a very low molecular collision frequency, while minimising dephasing collisions with the cell walls. In other words, this is an optically thick minimally damped molecular gas.

This section discusses measurements of the effects of propagation of chirped QC laser pulses, at 8  $\mu\text{m}$ , through gaseous acetylene, with a path length of 60 m, as the optical density is varied from optically thin to optically thick.

For this work, the laser was excited by a rectangular current pulse of about 1.5 A with duration between 0.5  $\mu\text{s}$  and 2  $\mu\text{s}$ . The temperature tuning from the QC laser was  $-0.093 \text{ cm}^{-1}\text{K}^{-1}$ . The pulse repetition frequency ranged from 5 to 20 kHz, and the laser drive voltage from 10.5 to 11.5 V. The rate of the frequency down-chirp of the laser output frequency decreases across the temporal profile of the pulse. In the time windows used for the current experiments, the P23 acetylene line can be placed in a 110 MHz/ns chirp by using a base temperature of 8  $^{\circ}\text{C}$ , or in a 24 MHz/ns chirp by

using a temperature of  $-6\text{ }^{\circ}\text{C}$ . This gives effective resolutions, FWHM, of 220 MHz and 103 MHz respectively [43].

The rapid passage experiments were carried out using the P23 line of the  $\nu_4 + \nu_5$  overtone band of acetylene at  $1275.5122\text{ cm}^{-1}$ . This is a parallel component of the combination band of the two degenerate bending vibrations  $\nu_4$  and  $\nu_5$ . The spectrum of the P23 line, using low pressures of acetylene is shown in Figure 4.7.1. In addition to the main lines of interest, the large number of weak absorption lines which are also observed on account of the long absorbing path length are due to hot band transitions (see Figure 4.7.2).

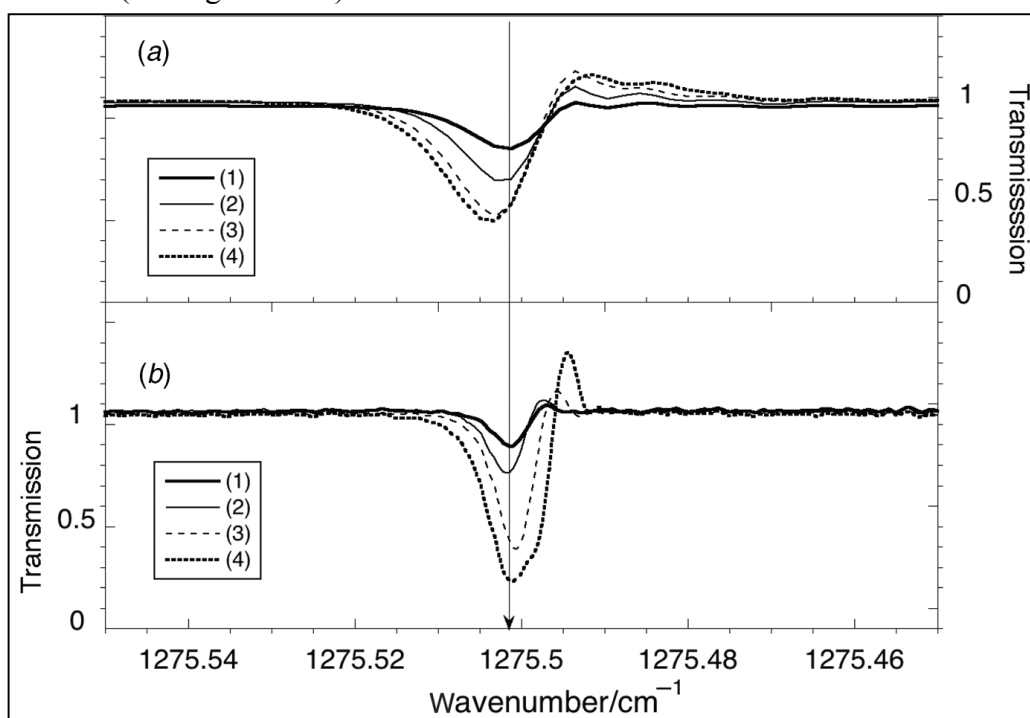


Figure 4.7.1: Rapid passage structure of the P23 line of the  $\nu_4 + \nu_5$  band of acetylene as a function of increasing gas pressure and laser frequency chirp rate. The line centre is indicated by the arrowed line. (a) Substrate temperature  $8\text{ }^{\circ}\text{C}$ , chirp rate 110 MHz/ns; (b) substrate temperature  $-6\text{ }^{\circ}\text{C}$ , chirp rate 24 MHz/ns. Acetylene pressures: (1) 0.006 Torr, (2) 0.009 Torr, (3) 0.015 Torr and (4) 0.033 Torr.

The lineshape of the normalised transmission spectra appear to have absorption followed by an emission spike, which is characteristic of the 'wiggles' reported in nuclear magnetic resonance experiments [122, 123, 124] and also of the rapid passage behaviour observed by Pietiläinen *et al* [55].



As the laser field is not sufficiently strong for adiabatic rapid passage to be fulfilled at resonance, a transverse component of the polarisation remains. Consequently, the electric dipole radiation field emitted by the molecules continues to beat with the frequency of the rapidly scanning driving laser. The effect of the change from a fast scan rate to a slow scan rate is clearly seen in Figure 4.7.1.

As the normalised resonance transmission becomes less than 10%, the form of the rapid passage signal is very different. As shown in Figure 4.7.2, a strong, narrow emission spike is observed following the absorption.

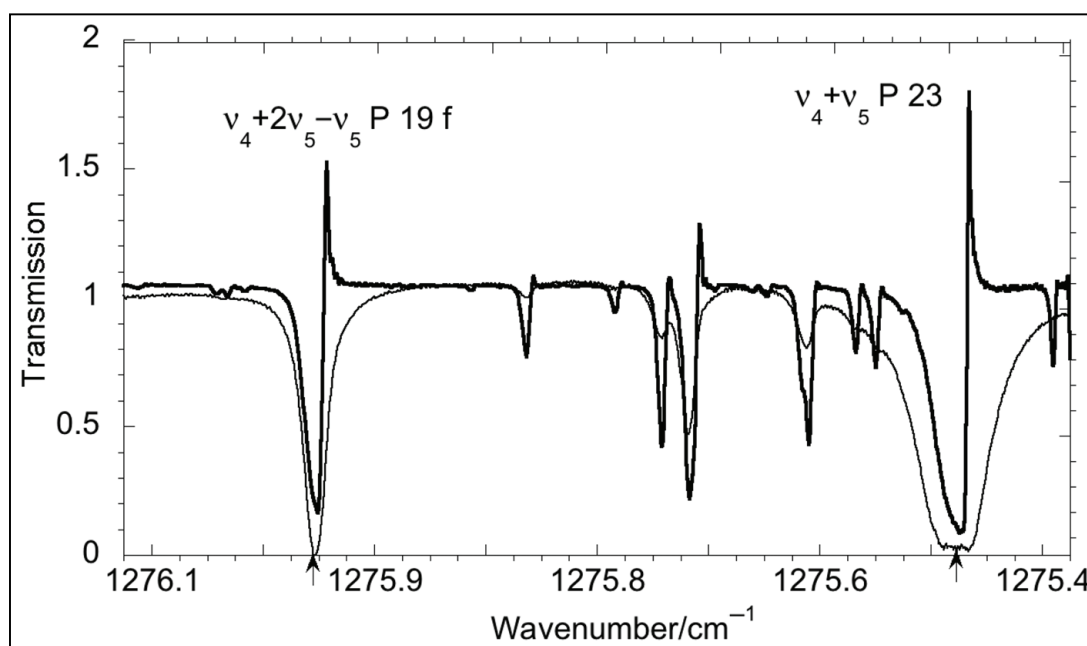


Figure 4.7.2: Rapid passage structure of the spectrum of acetylene from  $1276.1 \text{ cm}^{-1}$  to  $1275.4 \text{ cm}^{-1}$  recorded using an acetylene pressure of 1.2 Torr (heavy line) and after the addition of 39.9 Torr of nitrogen (narrow line). The positions of the line centres of the strongest absorbing lines are indicated by arrows. The weaker P19 f hot band line develops a Lorentzian line shape on addition of the nitrogen, and becomes completely absorbing at line centre. The main P23 absorption line becomes optically thick after the addition of nitrogen. The apparent flat peak is an effect of the absorption saturating when transmission is 0.

If nitrogen gas is added as a non-absorbing collision partner, a typical pressure-broadened line shape may be recovered. If the collisional damping provided by the nitrogen is faster than the chirp rate, normal collisional equilibrium is obtained and complete absorption of the laser radiation is observed at the line centre. A symmetric

pressure-broadened line shape is not observed if high pressures of acetylene alone are used, as shown in Figure 4.7.3.

At the highest pressure of acetylene admitted to the cell (6.9 Torr), it was possible to obtain complete absorption at the centre of the lines with the largest absorption coefficients, but the lines remained very asymmetric. As the acetylene behaves both as a chromophore and as a collision partner, the effects of the additional number of collisions between the acetylene molecules is partly offset by the additional driving provided by the enhanced coupling to the radiation field of the laser.

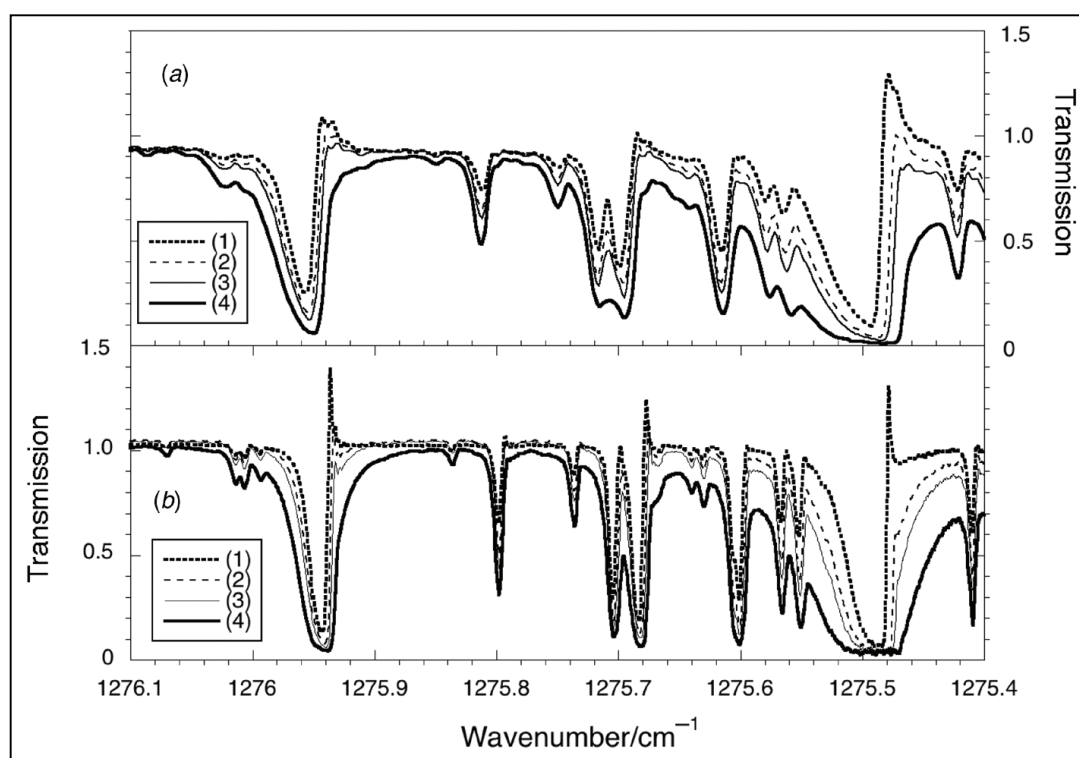


Figure 4.7.3: Rapid passage structure of the spectrum of acetylene from  $1276.1 \text{ cm}^{-1}$  to  $1275.4 \text{ cm}^{-1}$ , recorded at higher gas pressures. (a) Substrate temperature  $8 \text{ }^\circ\text{C}$  (b) Substrate temperature  $-6 \text{ }^\circ\text{C}$ . The acetylene pressures are (1) 2.1 Torr, (2) 3.1 Torr, (3) 4.5 Torr and (4) 6.9 Torr.

When nitrogen is introduced into the gas cell it acts as a non-absorbing collision partner. As shown in Figure 4.7.2, complete absorption at line centre can then occur. The unusual line shapes shown in Figure 4.7.3 demonstrate that when a rapidly chirped laser is used to record an absorption spectrum, pure acetylene gas does not behave as a normal absorber, but as a chromophore being strongly driven by the laser

under conditions of minimal transverse damping [124, 125, 126]. Under these conditions it has become an optically thick, minimally damped gas.

When pure acetylene is used, as the acetylene pressure is increased both absorption and emission increase in magnitude. The spectra shown in Figure 4.7.1 demonstrate that up to an absorption maximum of around 70%, the switch from absorption to emission occurs at the same time delay from the start of the laser current sweep. The spectra shown in Figure 4.7.4 illustrate that at higher acetylene pressures, the shape of the absorption by the P23 line becomes increasingly asymmetric, and the switch from absorption to emission is delayed relative to that at lower pressure.

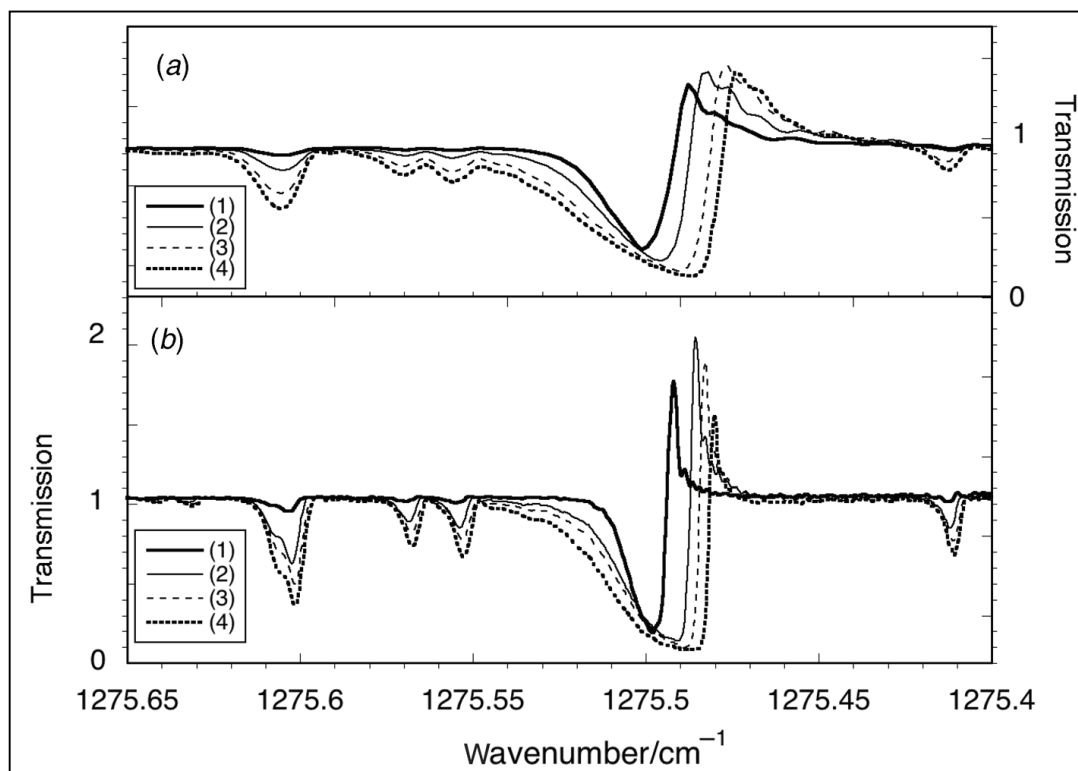


Figure 4.7.4: Rapid passage structure as a function of increasing gas pressure and laser frequency chirp rate, at gas pressures where delayed emission occurs. (a) Substrate temperature 8 °C (b) Substrate temperature -6 °C. Acetylene pressures used are (1) 0.13 Torr, (2) 0.38 Torr, (3) 0.98 Torr and (4) 1.8 Torr.

At the highest pressures used (1.8 Torr), complete absorption is observed when a slow chirp rate is used, or when nitrogen is added to provide collisional damping. However, in the fast scan spectrum there is residual transmission at this pressure. In both Figures 4.7.1 and 4.7.4 spectra are shown at both fast (110 MHz/ns) and slow

(24 MHz/ns) scan rates. At the higher rate the spectra are appreciably broadened as the rate of passage is too rapid for the two-level molecular systems to follow the rapidly changing field.

In Figure 4.7.4 the size of the emission spike increases with pressure to give a maximum effective transmission value at a pressure of 0.38 Torr. The maximum transmission is 1.7 in the fast scan spectrum, and 2 in the slow scan spectrum, an increase of 100% of the directional emission compared with the signal from the laser alone at that time. Increasing the pressure of the acetylene to 1.8 Torr decreased the maximum transmission to 1.5 in the slow chirp spectrum. The generation of this large emission spike and the increasing delay of the switch from absorption to emission is believed to be due to propagation effects of the laser radiation within the gas beginning to play an important role.

These results can be compared to the theoretical lineshapes obtained from previously described [62] numerical solutions to the coupled Maxwell-Bloch equations [127]. In these experiments the absorption lines are inhomogeneously broadened due to the Doppler effect. During the frequency sweep of the laser, each homogeneously broadened velocity component of the Doppler-broadened line is interrogated sequentially (see Chapter 2.4), so that the velocity packets are excited as a phased array [62, 121]. Optical pumping effects have been included by projecting the molecule-fixed transition dipole on to the space-fixed direction of the laser field [62]. As the  $J''$  value of the transition is quite large (23) calculations have been carried out using a  $J''$  value of 10, but a number density appropriate to  $J = 23$ . This is equivalent to the 'bundled' M approach used previously [62] for high  $J$  transitions.

In the calculations of the variation of the polarisation of a set of two-level systems, as the radiation propagates through the absorption cell, a step length of 1 m, and a total path length of up to 60 m were used. At each step in the propagation of the laser radiation the cumulative polarisation is evaluated by incoherent addition of the contributions of the  $M_J$  components.

We believe that the mechanism for the generation of amplification of the incident intensity of the QC laser beam by a single strongly absorbing line of acetylene at resonance is related to that proposed by Brickman, Genack and Schenzle [128, 129] to explain the travelling wave amplification of short pulses from a carbon dioxide laser in a cell containing hot carbon dioxide, following a shift in the phase of the laser radiation imposed using a CdTe phase shifter. Their explanation of the amplification was based upon the classical theory of absorption.

Absorption is the result of interference between the incident laser field,  $E_{in}$ , and the field generated by the response of the medium,  $E_s$ . The  $E_s$  field grows in intensity as the absorption depth increases. It is the interference between  $E_{in}$  and  $E_s$  which can lead to either loss or gain. If the molecules can follow the changes in the incident field the interference is destructive and enhanced absorption can occur. However, if the incident field is changed faster than the reorientation time of the polarisation of the gas, constructive interference effects can occur and gain will be observed.

In order to calculate the formation and propagation of this transient, Brickman, Genack and Schenzle [128, 129] solved the coupled Maxwell-Bloch equations for the case of a  $\pi$  phase shift and a Lorentzian line shape. They then calculated the values of the output field, given by Equation 4.7.1, at increasing propagation distances,  $X$ , in the absorbing gas.

$$E_o = E_{in} + E_s \quad (4.7.1)$$

Brickman *et al* [128] show exponentially decaying plots which represent the steady state values of  $E_o$  for times long before, or long after, the phase shift which they used to initiate the gain (see Figure 3 in [128]). Their transient response connects their pair of steady state curves. Experimentally they were able to measure large gain signals following transmission through a 2.8 m hot cell at pressures of 6 Torr [127], with steady state transmission approx. 13%, and of 20 Torr [128], with transmission less than 3%.

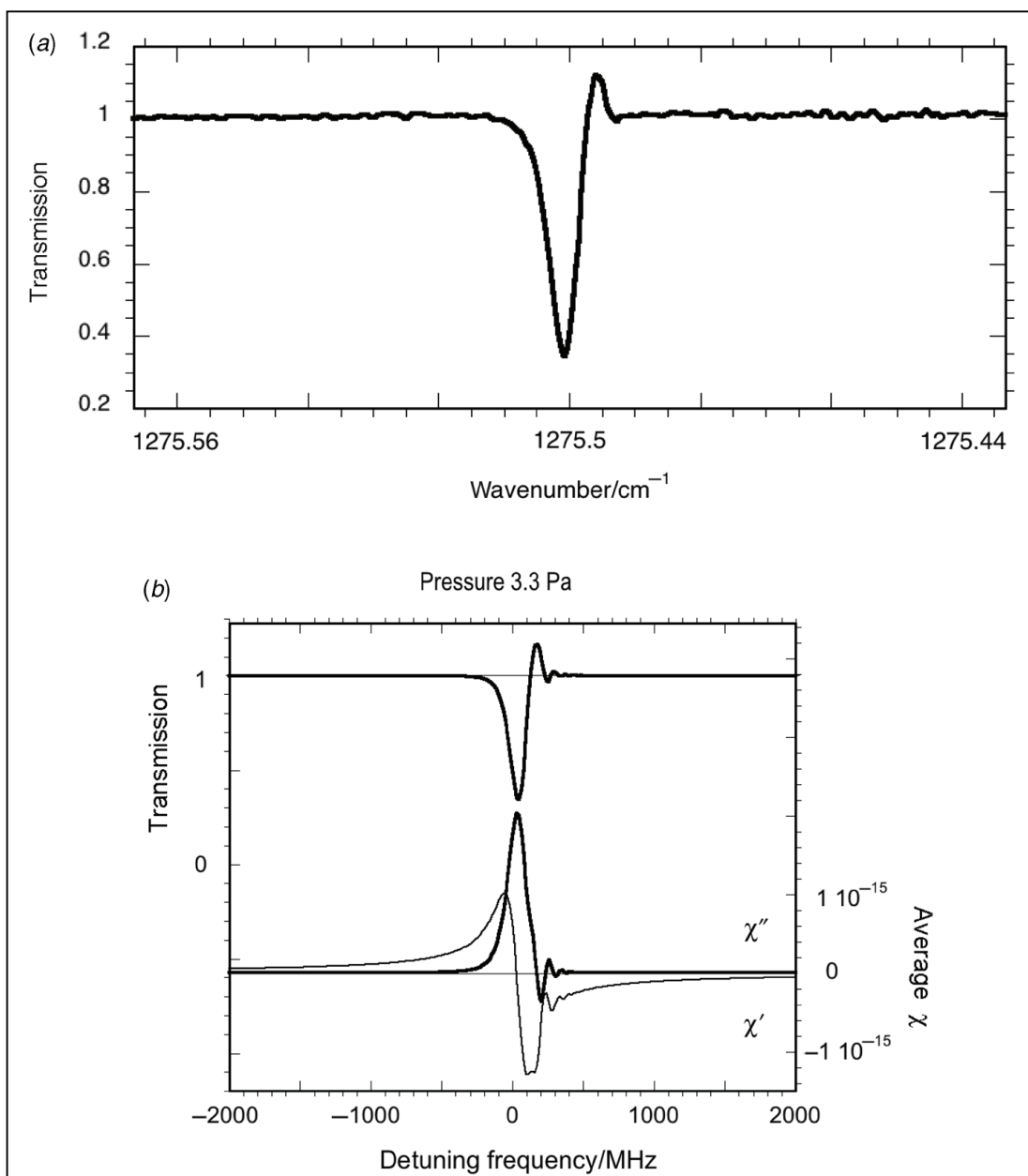


Figure 4.7.5: Observed and calculated rapid passage structure of the P23 line of the  $v_4 + v_5$  band of acetylene at low pressure with a slow chirp rate. (a) Observed spectrum, substrate temperature  $-6^\circ\text{C}$ , chirp rate 24 MHz/ns. Acetylene pressure 0.015 Torr. (b) Calculated rapid passage structure (bold, black), and real ( $\chi''$  - grey) and imaginary ( $\chi'$  - black) of the cumulative complex refractive index, of the P23 line with a linear chirp rate of 20 MHz/ns at a gas pressure of 0.025 Torr.

The other parameters used in the calculation were: transition dipole moment,  $\mu_{ij} = 0.078$  D; laser power = 10 mW; effective beam waist = 0.1 mm;  $T_1 = T_2 = 0.113$  MHz/Pa; number of time steps = 105; number of points in the velocity grid = 400; total path length = 60 m and propagation length = 1 m.

In these experiments there is no active control of the phase of the laser, however phase shifts can develop during the propagation of the chirped 1.5  $\mu\text{s}$  duration QC laser pulse through the gas within the long path length Herriott cell.

Some effects analogous to those described by Brickman *et al* [128, 129] may be recognised in these calculations of the behaviour of the rapid passage signals and of the real and imaginary components of the complex refractive index as a function of pressure. These calculations have concentrated on slow chirp behaviour, since the rapid passage effects are most marked when the chirp rate is minimised.

Figure 4.7.5 shows both an experimental transmission signal recorded at low gas pressure of 0.015 Torr using a path length of 60 m, and also the calculated cumulative behaviour of the transmission, and of the real and imaginary parts of the complex refractive index, at low gas pressure of 0.023 Torr, after propagating over path length of 60 m, using a propagation step length of 1 m. Under these conditions a normal rapid passage lineshape is observed in both the experimental and calculated spectra, and the real and imaginary components of the calculated refractive index resemble those of a slightly perturbed absorption line.

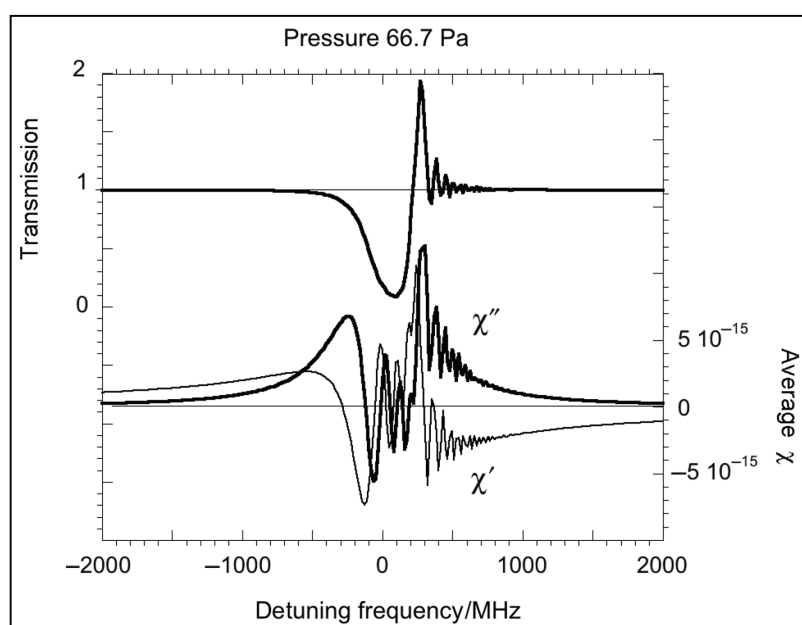


Figure 4.7.6: Calculated transmission, and cumulative complex refractive index, of the P23 line of the  $\nu_4 + \nu_5$  band of acetylene with linear chirp rate 20 MHz/ns at gas pressure 0.025 Torr, just above the threshold for delayed emission. Other parameters given in Figure 4.7.5.

However, at higher gas pressure, a delayed emission spike following the absorption is calculated, as shown in Figures 4.7.6 and 4.7.7. The calculated transmission spectra are very similar to the experimental spectra shown in Figure 4.7.4(b). The behaviour of the real and imaginary components of the complex refractive index,  $\chi'$  and  $\chi''$ , derived from the solution of the Maxwell-Bloch equations, provides evidence of very strong coupling between the real and imaginary parts of the complex refractive index driven by the rapidly changing field of the laser.

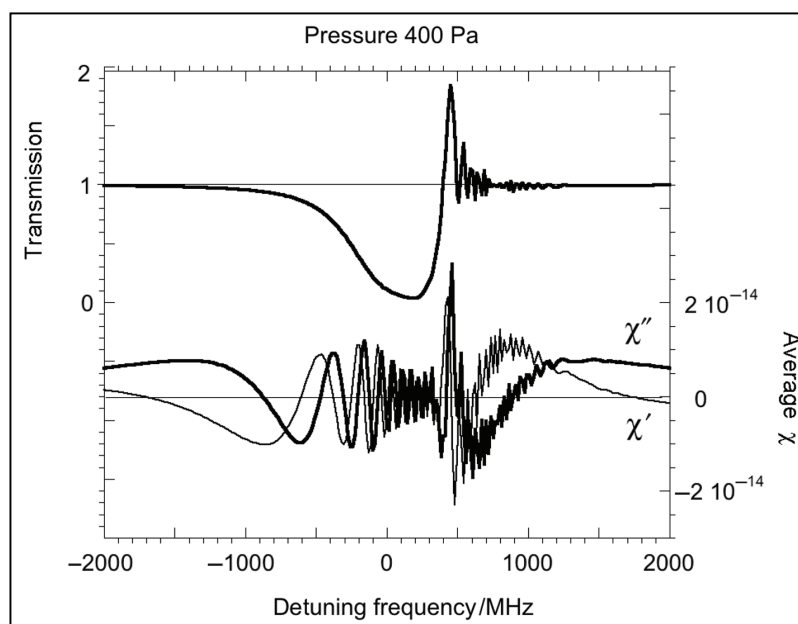


Figure 4.7.7: Calculated transmission, and cumulative complex refractive index, of the P23 line of the  $\nu_4 + \nu_5$  band of acetylene with linear chirp rate 20 MHz/ns at gas pressure 3 Torr, well above the threshold for delayed emission. Other parameters given in Figure 4.7.5.

In the calculated behaviour of the complex refractive index, a damped oscillatory structure is followed by the generation of an emission spike. At the highest gas pressure used for the calculation of the behaviour shown in Figure 4.7.7, the period of these Rabi nutations varies from around 80 MHz at the beginning of the strong absorption to 40 MHz at the onset of the emission spike. This structure is not observable at the minimum chirp rates of 24 MHz/ns available with the current spectrometer. The emission spike is in turn followed by emission of a damped free precession signal. The calculated free precession frequency is between 40 MHz and 90 MHz; this is smaller than the maximum experimental resolution of approx. 150 MHz at the slowest experimental chirp rate used, thus this structure is also



unable to be resolved in the experimental spectrum.

The fact that as the gas pressure is increased, the residual transmission decreases, the time delay of the emitted pulse is increased and the length of the damped oscillatory structure increases suggests that the oscillations of the field in the gaseous medium occur between the steady state values of the decaying field. This form of damping of the pulse train in the optically thick region is similar to that calculated by Brickman *et al* [128]. It may also be noted that the frequency period of this oscillation increases as it becomes more strongly damped.

To summarize, it has been observed that when rapid passage effects occur in a strongly absorbing gas the absorption is followed by a delayed pulse of amplified emission. By solving coupled Maxwell-Bloch equations numerically, it has been demonstrated that this is due to constructive interference of the laser field and the field generated within the gas. The reason for this amplification is associated with the long absorbing path length and low collision frequency within the gas cell. This prevents reorientation of the gas molecules on the time scale of the rapidly down-chirped laser field.

#### 4.8: 2-Laser Spectroscopy

In an effort to investigate more of the spectrum, a pellicle beamsplitter was used as a polariser to combine the beams from 7.5  $\mu\text{m}$  laser no.64 with 8  $\mu\text{m}$  laser no.51, which was mounted sideways to shift its polarisation through 90  $^\circ$ .

The optical setup is illustrated in Figure 4.8.1.

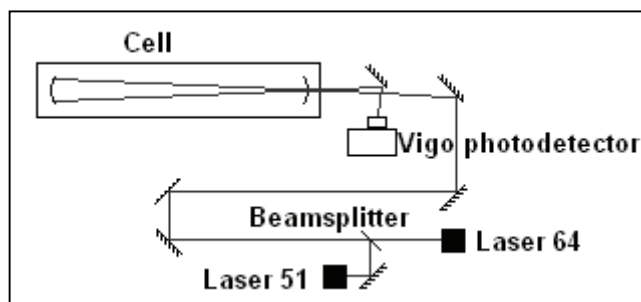


Figure 4.8.1: Optical setup for 2-laser spectroscopy.

The operation of the two lasers required one to be driven from an external trigger source, specifically the other laser drive box. This necessitated the use of an older version of the laser drive software. External triggering is not an available option in the newer versions. The necessary electronic setup is illustrated in Figure 4.8.2. The Stanford signal generator was used to introduce a time delay of 1500 ns. This prevents the two laser pulses overlapping.

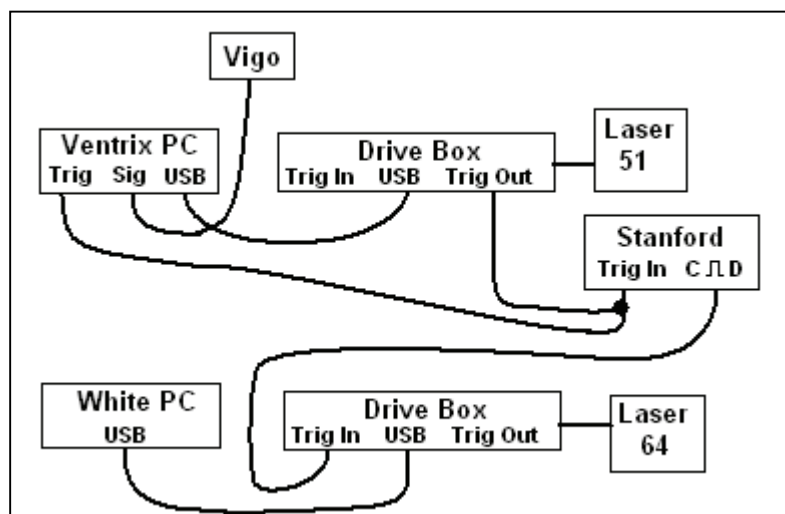


Figure 4.8.2: Electrical connections to allow for external triggering.

In order to avoid saturating the detector, laser 64 had a coarse grid attenuator placed between the laser head and the beamsplitter. Laser 51 had a partially shut iris in order to keep the two laser beams at similar intensities.

Laser 64 has a faster chirp than laser 51. It chirps at 362 MHz/ns at the start of the pulse and 54 MHz/ns at the end of the pulse. This compares to laser 51's chirp rates of 145 MHz/ns and 38 MHz/ns respectively.

The cell was initially filled with 0.163 Torr of methane, which has spectral lines in both lasers' wavelength ranges. The raw signal showing the two pulses is shown in Figure 4.8.3.

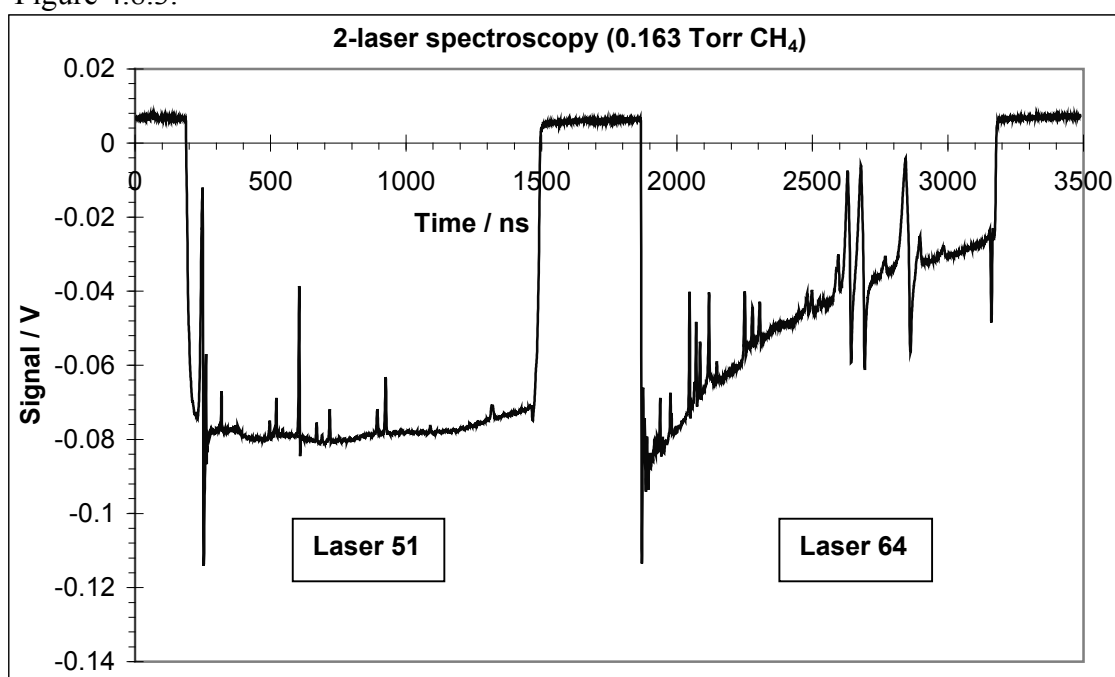


Figure 4.8.3: One "spectrum" consisting of two pulses. The processed spectra corresponding to these pulses are shown in red in Figures 4.8.4 and 4.8.5.

Each recorded spectrum was then split into two separate spectra, one for each laser. For this work, background spectra were recorded with the cell evacuated as the use of zero air is unnecessary at such low pressures. These files were similarly split in order to allow the calculation of transmission spectra using our existing routines.

Etalon fringe spectra recorded individually for each laser were used for the

calibration. Calibrated spectra from each laser are shown in Figures 4.8.4 and 4.8.5 illustrating the effect on the line shapes of gradually adding nitrogen gas to a pressure of 21.5 Torr.

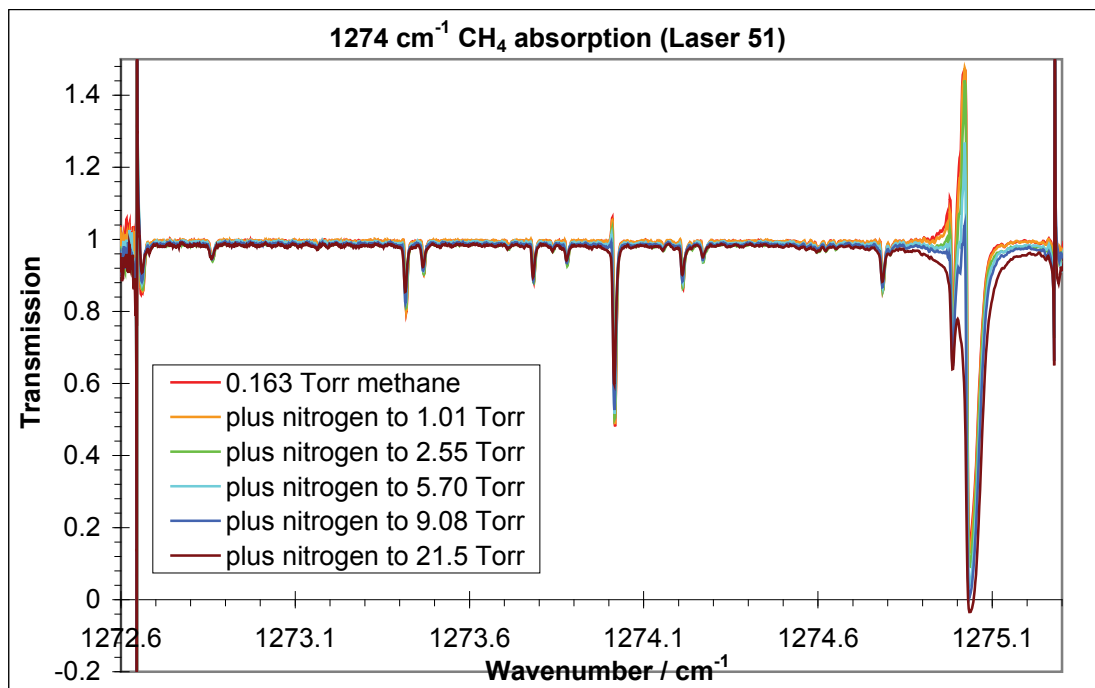


Figure 4.8.4: Methane spectra recorded during 2-laser spectroscopy using Laser 51.

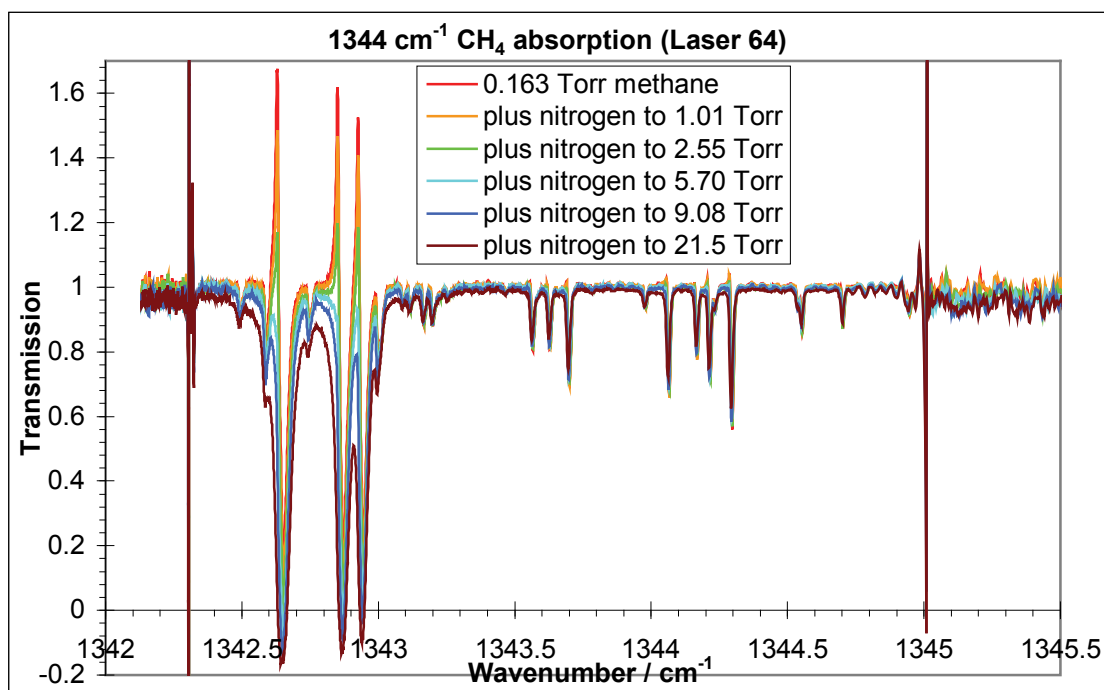


Figure 4.8.5: Methane spectra recorded during 2-laser spectroscopy using Laser 64.

At the fast chirp (high wavenumber) end of both spectra, it takes 9.08 Torr of nitrogen to quench the rapid passage emission spike. At the slower chirp end, even the strong absorption lines seen by laser 64 lose their emission spike with only 5 Torr of nitrogen.

By choosing the two lasers carefully, using this 2-laser method should give us the ability to measure gases with absorption lines in different regions of the spectrum. It would be impossible to measure absorption lines separated by more than  $6\text{ cm}^{-1}$  simultaneously using only one laser.

#### **4.9: Conclusion**

We have used a QC laser spectrometer in a wide variety of different situations, many of them to obtain difficult measurements, and have consistently demonstrated that absorption spectroscopy by a QC laser is a useful method of probing gas mixtures.

In the laboratory, the frequency downchirp of the laser running in inter-pulse tuning mode allows us to investigate nonlinear processes such as rapid passage in great detail, while under field conditions the instrument has proved very robust. Regardless of whether fieldwork is challenging for the instrument, as in the flight based work, or merely measuring challenging conditions such as the aero engine exhaust work and plasma reactor work, the spectrometer has always succeeded in recording absorption spectra. Under some conditions, notably during the flights from Gloucester Airport (See Chapter 4.3), the resultant spectra have not been reliably converted to mixing ratios. With improved analysis methods, it should be possible to resolve this and obtain more consistent results, regardless of operating conditions.

## Chapter 5: Conclusion

My work has involved improving the performance of a portable QC laser spectrometer system by increasing the path length of the multipass cell, replacing the detector and characterising additional lasers operating at different wavelengths.

This improved system was used for a wide variety of field and laboratory measurements, and has shown itself to be a useful tool for recording gas mixing ratios, or absorption spectra under many circumstances. With suitable calibration and testing, the intra-pulse QC laser spectrometer has the potential to become a powerful measurement method under most conditions.

Flight based atmospheric measurements have shown the instrument to be virtually immune to vibration owing to the fast spectrum recording. Proper calibration, ideally under flight conditions, would verify the results obtained. If this were done, the spectrometer could potentially replace numerous instruments within the FAAM aircraft, many of its instruments measuring one gas each, compared to the multiple simultaneous gas measurements which the QC spectrometer is capable of.

With a simple version of the system without the multipass cell, measurements of hot methane and acetylene in a CVD plasma reactor have been carried out. The QC laser spectrometer has shown itself to be a useful tool for probing the outer, cooler layer of the plasma. Although the temperature distribution within the plasma means that no information on the central hot core of the plasma can be obtained from this instrument, the measurements of the outer layer have proved useful and informative. By measuring the relative levels of different gases in different regions of the plasma, it is possible to improve a model [100] of the reaction process, and thus improve the quality of the deposited diamonds through improvements to the plasma.

Free space measurements of carbon monoxide, carbon dioxide and water in a turbojet engine exhaust plume have also been carried out with the simple version of the system without the multipass cell. More detailed analysis of the recorded spectra should produce more accurate plume cross-sections, but preliminary observations

show that the QC laser is an effective tool for probing exhaust plumes. In addition to the ability to measure multiple species, the QC spectrometer requires no modifications to the engine, and does not disturb the exhaust plume. The stability of the beam, despite plume turbulence was remarkable, and it is likely that the work could be repeated with the laser and detector further from the edge of the plume without adversely affecting instrument sensitivity. In principle the exhaust plume could be mapped out by comparing horizontal and vertical cross sections through the plume, a task to which the QC laser spectrometer is ideally suited.

A commercially available 4-laser version of the spectrometer has also been used for a study on the differences in diesel engine pollution from buses of various ages from the 1930s to the 1990s. This work demonstrated that the QC laser spectrometer makes an effective gas analyser for exhaust fumes from heavy diesel engines. For MOT testing vehicles, the instrument would need to be very accurately calibrated. An effective method of calibration would be to measure emissions in tandem with existing analysers used by MOT stations to verify instrument performance.

In the laboratory, the frequency downchirp of the laser running in inter-pulse tuning mode allows us to investigate nonlinear processes such as rapid passage in great detail. To summarize, it has been observed that when rapid passage effects occur in a strongly absorbing gas the absorption is followed by a delayed pulse of amplified emission. The reason for this amplification is associated with the long absorbing path length and low collision frequency within the gas cell. This prevents reorientation of the gas molecules on the time scale of the rapidly down-chirped laser field.

Under field conditions the instrument has proved very mechanically robust. Regardless of operating conditions, the spectrometer has always succeeded in recording spectra. Under some conditions, notably the flight from Gloucester Airport (See Chapter 4.3), the resultant spectra were not converted to reliable mixing ratios. There is a possibility that the rescaling of the transmission spectra is distorting the results. It should be possible to resolve this by improving the analysis to obtain consistent results under any operating conditions.



## Chapter 6: Future Work

We have a number of different pieces of fieldwork planned for the future, as discussed below. In addition to the fieldwork, studies on rapid passage based in the laboratory are likely to continue, possibly using the 2-laser method to probe spectral lines in widely separated regions of the spectrum (see Chapter 4.8).

Further airborne measurements using the Cascade 4-laser system are planned. These would use the FAAM aircraft [80] to measure high altitude atmospheric gas mixing ratios.

Many of the improvements to the system (see Chapter 3.8) were carried out to ensure the spectrometer will function successfully under the in-flight conditions. The additional cooling and ventilation grille are required as the aircraft gets very warm during flights. A typical external atmospheric pressure during flight is 200 Torr, which is considerably lower than ground level pressure. In order to confirm that the pressure control worked under such conditions, the program modification to add a pressure readout was essential. To increase the pressure differential, the cell operating pressure was reduced to 108 Torr. To mimic the low external pressure, tests were then carried out with the spectrometer inlet pipe connected to another larger cell which was kept at a pressure of 200 Torr. Even pumping the system quite hard with an external pump, the cell pressure remained steady, suggesting that the low pressure conditions will not adversely affect the system.

The only remaining flight preparation for the system is to have the box bolted into a rack mount and approved as flightworthy, which should take place soon.

Other work is to be carried out using a simpler setup with a laser and photodetector only:

We are currently planning flame measurements in conjunction with the Department of Chemical Engineering here at Strathclyde University. This work would use either a single-pass or a few repeat passes of a laser beam to probe through a linear flame

from a burner, investigating the gas distribution within the flame. This would be similar to previous work carried out by our group in collaboration with Physikalische Chemie I at the University of Bielefeld, Germany [130, 131].

Further aero engine measurements in collaboration with Rolls-Royce, similar to these already carried out (see Chapter 4.5), are also planned. Having investigated CO and CO<sub>2</sub>, other gases may also be present, and if a different laser, or more than one laser are used, it may be possible to investigate a wider variety of gases.

Using a similar setup to that used for aero engine measurements, another possibility is the measurement of rocket exhausts in collaboration with Reaction Engines, a company based in Oxfordshire.

## References

- [1] *Cascade Technologies Test Plan* by R. Lindley and P. Miller, Cascade Technologies, Stirling, 2009.
- [2] *A compact quantum-cascade laser based spectrometer for monitoring the concentrations of methane and nitrous oxide in the troposphere* by S. Wright, G. Duxbury and N. Langford; *Applied Physics B*, November 2006, vol.85 no.2-3, p.243-249.
- [3] *Folded Optical Delay Lines* by Donald R. Herriott and Harry J. Schulte; *Applied Optics*, August 1965, vol.4 no.8, p.883-889.
- [4] *Climate Change 2007: The Physical Science Basis* by the Intergovernmental Panel on Climate Change, Cambridge University Press, Cambridge, 2007.
- [5] *Recent Greenhouse Gas Concentrations* by T.J. Blasing, Carbon Dioxide Information Analysis Center (CDIAC), Oak Ridge National Laboratory, USA, December 2009.
- [6] *Mace Head Atmospheric Research Station – characterization of aerosol radiative parameters* by S. Gerard Jennings, Christoph Kleefeld, Colin D. O'Dowd, Carsten Junker, T. Gerard Spain, Phillip O'Brien, Aodhaghan F. Roddy and Thomas C. O'Connor; *Boreal Environment Research*, 10 December 2003, vol.8, p.303-314.
- [7] NERC Dornier 228 aircraft, NERC-ARSF Operations Centre, Firfax House, Meteor Business Park, Cheltenham Road East, Gloucester, GL2 9QL.
- [8] *Sensitive detection of ammonia and ethylene with a pulsed quantum cascade laser using intra and interpulse spectroscopic techniques* by J. Manne, W. Jäger and J. Tulip; *Applied Physics B*, 15 November 2008, vol.94, p.337-344.

- [9] *Nitric oxide breath testing by tunable-diode laser spectroscopy: application in monitoring respiratory inflammation* by Chad Roller, Khosrow Namjou, James D. Jeffers, Mark Camp, Adam Mock, Patrick J. McCann and Joe Grego; *Applied Optics*, 1 October 2002, vol.41 no.28, p.6018-6029.
- [10] *Breath-methane in patients with cancer of the large bowel.* by A. Haines, G. Metz, J. Dilawari, L. Blendis and H. Wiggins; *The Lancet*, 3 September 1977, vol.310 no.8036, p.481-483.
- [11] *Measurement of nitrous oxide emission from agricultural land using micrometeorological methods* by K.J. Hargreaves, F.G. Wienhold, L. Klemedtsson, J.R.M. Arah, I.J. Beverland, D. Fowler, B. Galle, D.W.T. Griffith, U. Skiba, K.A. Smith, M. Welling and G.W. Harris; *Atmospheric Environment*, 1996, vol.30 nos.10-11, p.1563-1571.
- [12] *Measuring Eddy Covariance Fluxes of Ammonia using Tunable Diode Laser Spectroscopy* by D. Famulari, D. Fowler, K. Hargreaves, C. Milford, E. Nemitz, M. A. Sutton and K. Weston; *Water, Air and Soil Pollution: Focus*, 2004, vol.4, p.151-158.
- [13] *Evaluation of Laser Absorption Spectroscopic Techniques for Eddy Covariance Flux Measurements of Ammonia* by James D. Whitehead, Marsailidh Twigg, Daniela Famulari, Eiko Nemitz, Mark A. Sutton, Martin W. Gallagher and David Fowler; *Environmental Science & Technology*, 2008, vol.42 no.6, p.2041-2046.
- [14] *Nitrous oxide emissions from a beech forest floor measured by eddy covariance and soil enclosure techniques* by M. Pihlatie, J. Rinne, P. Ambus, K. Pilegaard, J.R. Dorsey, Ü. Rannik, T. Markkanen, S. Launiain and T. Vesala; *Biogeosciences Discussions*, 2005, vol.2, p.581-607.

- [15] *Aircraft observations of aerosol composition and ageing in New England and Mid-Atlantic States during the summer 2002 New England Air Quality Study field campaign* by Lawrence I. Kleinman, Peter H. Daum, Yin-Nan Lee, Gunnar I. Senum, Stephen R. Springston, Jian Wang, Carl Berkowitz, John Hubbe, Rahul A. Zaveri, Fred J. Brechtel, John Jayne, Timothy B. Onasch and Douglas Worsnop; *Journal of Geophysical Research*, 11 May 2007, vol.112 no.D09310, p1-18.
- [16] *A high precision pulsed quantum cascade laser spectrometer for measurements of stable isotopes of carbon dioxide* by J.B. McManus, D.D. Nelson, J.H. Shorter, R. Jiminez, S. Herndon, S. Saleska and M. Zahniser; *Journal of Modern Optics*, 10 November 2005, vol.52 no.16, p.2309-2321.
- [17] *Airborne measurements of HCHO and HCOOH during the New England Air Quality Study 2004 using a pulsed quantum cascade laser spectrometer* by Scott C. Hendon, Mark S. Zahniser, David D. Nelson Jr., Joanne Shorter, J. Barry McManus, Rodrigo Jiménez, Carstene Warneke and Joost A. de Gouw; *Journal of Geophysical Research*, 10 February 2007, vol.112 no.D10S03, p.1-15.
- [18] *Quantum cascade laser based spectrometer for in situ stable carbon dioxide isotope measurements* by B. Tuzson, M.J. Zeeman, M.S. Zahniser and L. Emenegger; *Infrared Physics & Technology*, 29 June 2007, vol.51, p.198-206.
- [19] *High precision measurements of atmospheric nitrous oxide and methane using thermoelectrically cooled mid-infrared quantum cascade lasers and detectors* by David D. Nelson, Barry McManus, Shawn Urbanski, Scott Herndon and Mark S. Zahniser; *Spectrochimica Acta Part A*, 2004, vol.60 no.14, p.3325-3335.
- [20] *Quad quantum cascade laser spectrometer with dual gas cells for the simultaneous analysis of mainstream and sidestream cigarette smoke* by Randall E. Baren, Milton E. Parrish, Kenneth H. Shafer, Charles N. Harward, Quan Shi, David D. Nelson, J. Barry McManus and Mark S. Zahniser; *Spectrochimica Acta Part A*, 2004, vol.60, p.3437-3447.

- [21] *Development of a spectrometer using a continuous wave distributed feedback quantum cascade laser operating at room temperature for the simultaneous analysis of N<sub>2</sub>O and CH<sub>4</sub> in the Earth's atmosphere* by Lilian Joly, Claude Robert, Bertrand Parvitte, Valery Catoire, Georges Durry, Guy Richard, Bernard Nicollaud and Virginie Zéninari; *Applied Optics*, 14 March 2008, vol.47 no.9, p.1206-1214.
- [22] *Potentials and limits of mid-infrared laser spectroscopy for the detection of explosives* by C. Bauer, A.K. Sharma, U. Willer, J. Burgmeier, B. Braunschweig, W. Schade, S. Blaser, L. Hvozdar, A. Müller and G. Holl; *Applied Physics B*, 2008, vol.92, p.327-333.
- [23] *Detection of carbon dioxide emissions from a diesel engine using a mid-infrared optical fibre based sensor* by Jim Mulrooney, John Clifford, Colin Fitzpatrick and Elfed Lewis; *Sensors and Actuators A*, 2007, vol.136, p.104-110.
- [24] *Cavity-enhanced absorption spectroscopy of methane at 1.73  $\mu\text{m}$*  by H.R. Barry, L. Corner, G. Hancock, R. Peverall and G.A.D. Ritchie; *Chemical Physics Letters*, 12 January 2001, vol.333 nos.3-4, p.285-289.
- [25] *Pulsed cavity ring-down spectroscopy of NO and NO<sub>2</sub> in the exhaust of a diesel engine* by R. Everts, A. Staicu, N. Dam, A. Van Vliet and J.J. Ter Meulen; *Applied Physics B*, 2002, vol.74 nos.4-5, p.465-468.
- [26] *Pulsed quantum cascade laser-based cavity ring-down spectroscopy for ammonia detection in breath* by Jagadeeshwari Manne, Oleksandr Sukhorukov, Wolfgang Jäger and John Tulip; *Applied Optics*, 20 December 2006, vol.45 no.36, p.9230-9237.
- [27] *Cavity enhanced absorption spectroscopy of multiple trace gas species using a supercontinuum radiation source* by J.M. Langridge, T. Laurila, R.S. Watt, R.L. Jones, C.F. Kaminski and J. Hult; *Optics Express*, 23 June 2008, vol.16 no.14, p.10178-10188.

[28] *The chemistry of OH and HO<sub>2</sub> radicals in the boundary layer over the tropical Atlantic Ocean* by L.K. Whalley, K.L. Furneaux, A. Goddard, J.D. Lee, A. Mahajan, H. Oetjen, K.A. Read, N. Kaaden, L.J. Carpenter, A.C. Lewis, J.M.C. Plane, E.S. Saltzmann, A. Wiedensohler and D.E. Heard; *Atmospheric Chemistry and Physics*, 2010, vol.10, p.1555-1576.

[29] *Pulsed Laval nozzle study of the kinetics of OH with unsaturated hydrocarbons at very low temperatures* by Sally E. Taylor, Andrew Goddard, Mark A. Blitz, Patricia A. Cleary and Dwayne E. Heard; *Physical Chemistry Chemical Physics*, 7 November 2007, vol.10, p.422-437.

[30] *Microwave remote sensing of stratospheric trace gases using digital Fast Fourier Transform spectrometers* by Stefan C. Müller, Axel Murk, Christian Monstein, Niklaus Kämpfer and Hansueli Meyer; *GeMiC 2006 Conference Proceedings* (German Microwave Conference), 2006.

[31] *A novel spectrometer concept for microwave remote sensing of middle atmospheric trace components* by Stefan C. Müller, Niklaus Kämpfer, Christian Monstein, Hansueli Meyer, Axel Murk and Vladimir Vasic; *Remote Sensing of Clouds and the Atmosphere X*, 2005, vol.5979, p.280-288.

[32] *Amplification of electromagnetic waves in a semiconductor with a superlattice* by R.F. Kazarinov and R.A. Suris; *Soviet Physics: Semiconductors*, 1971, vol.5, p.707-709.

[33] *Quantum Cascade Laser* by Jerome Faist, Federico Capasso, Deborah L. Sivco, Carlo Sirtori, Albert L. Hutchinson and Alfred Y. Cho; *Science*, 22 April 1994, vol.264, p.553-556.

[34] *Molecular beam epitaxy* by A. Y. Cho and J. R. Arthur Jr.; *Progress in Solid State Chemistry*, 1975, vol.10, p.157-192.

- [35] *THz and sub-THz quantum cascade lasers* by Giacomo Scalari, Christoph Walther, Milan Fischer, Romain Terazzi, Harvey Beere, David Ritchie and Jérôme Faist; *Laser & Photonics Reviews*, February 2009, vol.3 nos.1-2, p.45-66.
- [36] *Continuous-wave operation of quantum cascade laser emitting near 5.6  $\mu\text{m}$*  by D.A. Yarekha, M. Beck, S. Blaser, T. Aellen, E. Gini, D. Hofstetter and J. Faist; *Electronics letters*, 24th July 2003, vol.39 no.15, p.1123-1125.
- [37] *High-power continuous-wave operation of a 6  $\mu\text{m}$  quantum-cascade laser at room temperature* by J.S. Yu, S. Slivken, A. Evans, L. Doris and M. Razeghi; *Applied Physics Letters*, 29 September 2003, vol.83 no.13, p.2503-2505.
- [38] *High-resolution (Doppler limited) spectroscopy using quantum-cascade distributed-feedback lasers* by S. W. Sharpe, J. F. Kelly, J. S. Hartmann, C. Gmachl, F. Capasso, D. L. Sivco, J. N. Baillargeon and A. Y. Cho; *Optics Letters*, 1 September 1998, vol.23 no.17, p.1396-1398.
- [39] *Distributed feedback quantum cascade lasers* by Jérôme Faist, Claire Gmachl, Federico Capasso, Carlo Sirtori, Deborah L. Sivco, James N. Baillargeon and Alfred Y. Cho; *Applied Physics Letters*, 19 May 1997, vol.70 no.20, p.2670-2672.
- [40] *Sensitive absorption spectroscopy with a room-temperature distributed-feedback quantum-cascade laser* by K. Namjou, S. Cai, E. A. Whittaker, J. Faist, C. Gmachl, F. Capasso, D. L. Sivco and A. Y. Cho; *Optics Letters*, February 1998, vol.23 no.3, p.219-221.
- [41] *Trace-gas detection in ambient air with a thermoelectrically cooled, pulsed quantum-cascade distributed feedback laser* by A. A. Kosterev, R. F. Curl, F. K. Tittel, C. Gmachl, F. Capasso, D. L. Sivco, J. N. Baillargeon, A. L. Hutchinson and A. Y. Cho; *Applied Optics*, 20 December 2000, vol.39 no.36, p.6866-6872.



- [42] *Fast, real-time spectrometer based on a pulsed quantum-cascade laser* by E. Normand, M. McCulloch, G. Duxbury and N. Langford; *Optics Letters*, 1 January 2003, vol.28 no.1, p.16-18.
- [43] *Highly sensitive detection of trace gases using the time-resolved frequency downchirp from pulsed quantum-cascade lasers* by M. T. McCulloch, E. L. Normand, N. Langford, G. Duxbury and D. A. Newnham; *Journal of the Optical Society of America B*, August 2003, vol.20 no.8, p.1761-1768.
- [44] *Alternative method for gas detection using pulsed quantum-cascade-laser spectrometers* by Bruno Grouiez, Bertrand Parvitte, Lilian Joly and Virginie Zeninari; *Optics Letters*, 15 January 2009, vol.34 no.2, p.181-183.
- [45] *Quantum cascade semiconductor infrared and far infrared lasers: from trace gas sensing to non-linear optics* by Geoffrey Duxbury, Nigel Langford, Michael T. McCulloch and Stephen Wright; *Chemical Society Reviews*, 2005, vol.34, p.921-934.
- [46] *The Fourier Transform and Its Applications* by R. Bracewell; McGraw-Hill, New York, 1965.
- [47] *Über den anschaulichen Inhalt der quantentheoretischen Kinematik und Mechanik* by W. Heisenberg; *Zeitschrift für Physik*, March 1927, vol.43 nos. 3-4, p.172-198.
- [48] *Molecular Spectra and Molecular Structure II. Infrared and Raman Spectra of Polyatomic Molecules* by Gerhard Herzberg FRSC, Van Nostrand Reinhold Company, New York and Canada, 1945.

- [49] *The HITRAN molecular spectroscopic database: edition of 2000 including updates through 2001* by L.S. Rothman, A. Barbe, D. Chris Benner, L.R. Brown, C. Camy-Peyret, M. R. Carleer, K. Chance, C. Clerbaux, V. Dana, V.M. Devy, A. Fayt, J.-M. Flaud, R.R. Gamache, A. Goldman, D. Jacquemart, K.W. Jucks, W.J. Lafferty, J.-Y. Mandin, S.T. Massie, V. Nemtchinov, D.A. Newnham, A. Perrin, C.P. Rinsland, J. Schroeder, K.M. Smith, M.A.H. Smith, K. Tang, R.A. Toth, J. Vander Auwera, P. Varanasi and K. Yoshino; *Journal of Quantitative Spectroscopy & Radiative Transfer*, 15 November – 15 December 2003, vol.82 no.1, p.5-44.
- [50] *Quantum cascade laser spectroscopy: Diagnostics to non-linear optics*. by Geoffrey Duxbury, Nigel Langford, Kenneth Hay and Nicola Tasinato; *Journal of Modern Optics*, 20 October - 10 November 2009, vol.56 no.18-19, p.2034-2048.
- [51] *Sensitivity Enhancement in Magnetic Resonance* by R.R. Ernst; *Advances in Magnetic Resonance*, Academic Press, 1966, vol.2, p.1-135.
- [52] *Observation of Population Inversion by Optical Adiabatic Rapid Passage* by Michael M. Loy; *Physical Review Letters*, 15 April 1974, vol.32 no.15, p.814-817.
- [53] *Coherent Optical Spectroscopy* by R.G. Brewer; *Nonlinear Spectroscopy, Proceedings of the International School for Physics "Enrico Fermi", Course LXIV* edited by N. Bloembergen, 1977, p.87-135.
- [54] *Optical free-induction decay of laser-cooled  $^{85}\text{Rb}$*  by K. Toyoda, Y. Takahashi, K. Ishiwata and T. Yabuzaki; *Physical Review A*, 1 August 1997, vol.56 no.2, p.1564-1568.
- [55] *Investigation of trapped rubidium atoms through frequency-modulation-induced coherent transient effects* by Antti Pietiläinen, Markku Kujala, and Erkki Ikonen; *Journal of the Optical Society of America B*, 1 December 1998, vol.15 no.12, p.2823-2830.

- [56] *Coherent transient amplification in inhomogeneously broadened rubidium atoms by diode-laser frequency switching* by Yong-qing Li, W.H. Burkett, and Min Xiao; *Optics Letters*, 1 July 1996, vol.21 no.13, p.982-984.
- [57] *Free-induction decay in molecular iodine measured with an extended-cavity diode laser* by P. Dubé, M.D. Levenson and J.L. Hall; *Optics Letters*, 1 February 1997, vol.22 no.3, p.184-186.
- [58] *Observation of coherent transients by use of current switching of a semiconductor diode laser* by R.M. Mcfarlane and M. Zhu; *Optics Letters*, 15 February 1997, vol.22 no.4, p.248-250.
- [59] *Coherent Transient Infrared Spectroscopy* by R.L. Shoemaker; *Laser and Coherence Spectroscopy* edited by J.I. Steinfeld, Plenum, New York, 1978, p.197-371.
- [60] *Astigmatic mirror multipass absorption calls for long-path-length spectroscopy* by J. B. McManus, P. L. Kebabian and M. S. Zahniser; *Applied Optics*, 20 June 1995, vol.34 no.18, p.3336-3348.
- [61] *Development of the Strathclyde University QC laser spectrometer for the measurement of methane, nitrous oxide and water on the NERC ARSF Dornier Aircraft* by G. Duxbury, N. Langford, S. Wright and K. Hay; presented at NCAS Annual Staff, Affiliates & Science Conference, Cambridge, 14 December 2006.
- [62] *Rapid passage induced population transfer and coherences in the 8 micron spectrum of nitrous oxide* by G. Duxbury, N. Langford, M. T. McCulloch and S. Wright; *Molecular Physics*, 10 March – 10 April 2007, vol.107 nos.5-7, p.741-754.
- [63] *Quantum Cascade Laser based Absorption Spectrometer for Trace Gas Molecular Detection and Nonlinear Optics* by Michael Telfer McCulloch; PhD Thesis 2005.

- [64] *Development of a portable, mid infrared, Quantum Cascade laser based spectrometer for the detection of trace gases in the atmosphere and a reactive plasma* by Stephen Wright; PhD Thesis 2007.
- [65] *Smoothing & Differentiation of Data by Simplified Least Squares Procedures* by Abraham Savitzky and Marcel J. E. Golay; *Analytical Chemistry*, July 1964, vol.36 no.8, p.1627-1639.
- [66] *User Manual CT2400 High Sensitivity Multi-Gas Sensor*, Cascade Technologies, Stirling, 2008 (Revision 6).
- [67] *Field scale N<sub>2</sub>O flux measurements from grassland using eddy covariance* by C. Di Marco, U. Skiba, K. Weston, K. Hargreaves and D. Fowler; *Water, Air and Soil Pollution: Focus*, 2004, vol.4, p.143-149.
- [68] *Measurements of CH<sub>4</sub> and N<sub>2</sub>O fluxes at the landscape scale using micrometeorological methods* by D. Fowler, K.J. Hargreaves, U. Skiba, R. Milne, M.S. Zahniser, J.B. Moncrieff, I.J. Beverland and M.W. Gallagher; *Philosophical Transactions of the Royal Society of London A*, 1995, vol.351, p.339-356.
- [69] *Measurement of trace gas fluxes using tunable diode laser spectroscopy* by Mark S. Zahniser, David D. Nelson, J. Barry McManus and Paul L. Kebabian; *Philosophical Transactions of the Royal Society of London A*, 1995, vol.351, p.371-382.
- [70] *Principles of Environmental Physics* by J.L. Monteith and M.H. Unsworth, University of Chicago Press, Chicago, 1989 (second edition).
- [71] *Nitrous oxide release from arable soil: Importance of N-fertilization, crops and temporal variation* by E.-A. Kaiser, K. Kohrs, M. Kücke, E. Schnug, O. Heinemeyer and J.C. Munch; *Soil Biology & Biochemistry*, 1998, vol.30 no.12, p.1553-1563.

- [72] *Automated gas injector system for gas chromatography: Atmospheric nitrous oxide analysis* by O. Heinemeyer and E.-A. Kaiser; *Soil Science Society of America Journal*, May 1996, vol.60 no.3, p.808-811.
- [73] *Fertiliser induced nitrous oxide emissions during energy crop cultivation on loamy sand soils* by Hans J. Hellebrand, Volkhard Scholz and Jürgen Kern; *Atmospheric Environment*, 2008, vol.42, p.8403-8411.
- [74] *Current Greenhouse Gas Concentrations* by T.J. Blasing and S. Jones, Carbon Dioxide Information Analysis Center (CDIAC), Oak Ridge National Laboratory, USA, October 2002.
- [75] *Soil processes and global change* by A.R. Mosier; *Biology and fertility of soils*, July 1998, vol.27 no.3, p.221-229.
- [76] *Quantum Cascade Laser Spectrometer Measurements of Atmospheric Water, Nitrous Oxide and Methane Levels* by Kenneth Hay, Geoffrey Duxbury and Nigel Langford; presented at the International Workshop on Infrared Plasma Spectroscopy, Greifswald, Germany, 26 July 2007.
- [77] *Lightening-produced NO<sub>x</sub> during the Northern Australian monsoon; results from the ACTIVE campaign* by L. Labrador, G. Vaughan, W. Heyes, D. Waddicor, A. Volz-Thomas, H.-W. Pätz and H. Höller; *Atmospheric Chemistry and Physics*, 5 October 2009, vol.9, p.7419-7429.
- [78] *Measurements of total odd nitrogen (NO<sub>y</sub>) aboard MOZAIC in-service aircraft: instrument design, operation and performance* by A. Volz-Thomas, M. Berg, T. Heil, N. Houben, A. Lerner, W. Petrick, D. Raak and H.-W. Pätz; *Atmospheric Chemistry and Physics*, 25 February 2005, vol.5, p.583-595.

- [79] *An improved fast-response Vacuum-UV resonance fluorescence CO instrument* by C. Gerbing, S. Schmitgen, D. Kley and A. Volz-Thomas; *Journal of Geophysical Research*, 1999, vol.104 no.D1, p.1699-1704.
- [80] FAAM BAE146-301 aircraft, Cranfield Airport, College Road, Cranfield, Bedfordshire, MK43 0AL.
- [81] *Direct estimates of emissions from the megacity of Lagos* by J.R. Hopkins, M.J. Evans, J.D. Lee, A.C. Lewis, J.H. Marsham, J.B. McQuaid, D.J. Parker, D.J. Stewart, C.E. Reeves and R.M. Purvis; *Atmospheric Chemistry and Physics*, 6 November 2009, vol.9, p.8471-8477.
- [82] *Quantum-cascade laser measurements of stratospheric methane and nitrous oxide* by Christopher R. Webster, Gregory J. Flesch, David C. Scott, James E. Swanson, Randy D. May, W. Stephen Woodward, Claire Gmachl, Federico Capasso, Deborah L. Sivco, James N. Baillargeon, Albert L. Hutchinson and Alfred Y. Cho; *Applied Optics*, 20 January 2001, vol.40 no.3, p.321-326.
- [83] *Observations of an atmospheric chemical equator and its implications for the tropical warm pool region* by Jacqueline F. Hamilton, Grant Allen, Nicola M. Watson, James D. Lee, Julie E. Saxton, Alastair C. Lewis, Geraint Vaughan, Keith N. Bower, Michael J. Flynn, Jonathan Crosier, Glenn D. Carver, Neil R.P. Harris, Robert J. Parker, John J. Remedios and Nigel A.D. Richards; *Journal of Geophysical Research*, 31 October 2008, vol.113 no.D20313, p.1-12.
- [84] *In-flight measurements of ambient methane, nitrous oxide and water using a quantum cascade laser based spectrometer* by K. G. Hay, S. Wright, G. Duxbury and N. Langford; *Applied Physics B*, February 2008, vol.90, p.329-337.

- [85] *In-flight QC laser spectrometer measurement of ambient methane, nitrous oxide and water using the NERC ARSF DORNIER aircraft* by G. Duxbury, N. Langford, S. Wright and K. Hay; presented at 6th International Conference on Tunable Diode Laser Spectroscopy, Reims, France, 9-13 June 2007.
- [86] *The Effect of Collisions upon the Doppler Width of Spectral Lines* by R. H. Dicke; *Physical Review*, 15 January 1953, vol.89 no.2, p.472-473.
- [87] *Methane emission of the Amsterdam urban area* by D. Veenhuysen, A.T. Vermeulen, P. Hofschreuder and W.C.M. Van Den Bulk; *Water, Air and Soil Pollution: Focus*, 1998, vol.107, p.321-333.
- [88] *Development and Application of a Mobile Laboratory for Measuring Emissions from Diesel Engines. 1. Regulated Gaseous Emissions* by David R. Cocker III, Sandip D. Shah, Kent Johnson, J. Wayne Miller and Joseph M. Norbreck; *Environmental Science & Technology*, 5 March 2004, vol.38 no.7, p.2182-2189.
- [89] *Regulated and speciated hydrocarbon emissions from a catalyst equipped internal combustion engine* by S.G. Pouloupoulos, D.P. Samaras and C.J. Philippopoulos; *Atmospheric Environment*, 2001, vol.35, p.4443-4450.
- [90] *Methane Emissions from Vehicles* by E.K. Nam, T.E. Jensen and T.J. Wallington; *Environmental Science & Technology*, 26 February 2004, vol.38 no.7, p.2005-2010.
- [91] *Low Relative Humidity in the Atmosphere* by Dorathy A. Stewart; *U.S. Army Missile Command Technical Report RD-RE-89-3*, U.S. Army Missile Command, Alabama, 1 August 1985.
- [92] *Observational study of ozone and carbon monoxide at the summit of mount Tai (1534 a.s.l.) in central-eastern China* by Jian Gaom Tao Wang, Aijun Ding and Chunbo Liu; *Atmospheric Environment*, 2005, vol.39, p.4779-4791.

- [93] *Diamond deposition and plasma diagnostics in a 27 MHz inductive coupled reactor (ICP)* by Peter Awakowicz, Roland Schwefel, Manfred Werder and Wolfgang Kasper; *Diamond and Related Materials*, 1997, vol.6, p.1816-1823.
- [94] *Plasma diagnostics of a direct current arcjet diamond reactor. I. Electrostatic probe analysis* by S.W. Reeve and W.A. Weimer; *Journal of Vacuum Science and Technology A*, November/December 1994, vol.12 no.6, p.3131-3136.
- [95] *Plasma diagnostics of a direct-current arcjet diamond reactor. II. Optical emission spectroscopy* by S.W. Reeve and W.A. Weimer; *Journal of Vacuum Science and Technology A*, March/April 1995, vol.13 no.2, p.359-367.
- [96] *Plasma channels produced by a laser-triggered high-voltage discharge* by N.C. Lopes, G. Figueira, L.O. Silva, J.M. Dias, R. Fonseca, L. Cardoso, C. Russo, C. Carias, G. Mendes, J. Vieira and J.T. Mendonça; *Physical Review E*, 26 September 2003, vol.68 no.035402, p.1-4.
- [97] *Optical diagnostics of an atmospheric pressure diamond-depositing DC plasma reactor* by Maosheng Zhao, Thomas G. Owano and Charles H. Kruger; *Diamond and Related Materials*, 2001, vol.10, p.1565-1568.
- [98] *Detection of CH in an expanding argon/acetylene plasma using cavity ring down absorption spectroscopy* by R. Engeln, K.G.Y. Letourneur, M.G.H. Boogaarts, M.C.M. van de Sanden and D.C. Schram; *Chemical Physics Letters*, 1999, vol.310, p.405-410.
- [99] *Exploration of the gas phase chemistry in microwave-activated diamond deposition plasmas using an intra-pulse quantum cascade laser spectrometer* by Jie Ma, Andy Cheesman, Mike N.R. Ashfold, Geoffrey Duxbury, Nigel Langford and Kenneth G. Hay; presented at Photon 08, Heriot Watt University, Edinburgh, Scotland, 27 August 2008.



[100] *Plasma-chemical processes in microwave plasma-enhanced chemical vapor deposition reactors operating with C/H/Ar gas mixtures* by Yuri A. Mankelevich, Michael N.R. Ashfold and Jie Ma; *Journal of Applied Physics*, 1 December 2008, vol.104 no.11, p.113304-1 to 113304-11.

[101] *Application of a Quantum Cascade Laser for Time-Resolved, in Situ Probing of CH<sub>4</sub>/H<sub>2</sub> and C<sub>2</sub>H<sub>2</sub>/H<sub>2</sub> Gas Mixtures during Microwave Plasma Enhanced Chemical Vapor Deposition of Diamond* by A. Cheesman, J. A. Smith, M. N. R. Ashfold, N. Langford, S. Wright and G. Duxbury; *The Journal of Physical Chemistry A*, 10 January 2006, vol.110, p.2821-2828.

[102] *QCL Study of the gas phase chemistry in Ar/H<sub>2</sub>/hydrocarbon plasmas in a microwave reactor used for diamond CVD* by Jie Ma, PhD Thesis Chapter 4, 2007.

[103] *Quantum cascade laser investigations of CH<sub>4</sub> and C<sub>2</sub>H<sub>2</sub> interconversion in hydrocarbon/H<sub>2</sub> gas mixtures during microwave plasma enhanced chemical vapor deposition of diamond.* by Jie Ma, Andrew Cheesman, Michael N. R. Ashfold, Kenneth G. Hay, Stephen Wright, Nigel Langford, Geoffrey Duxbury and Yuri A. Mankelevich; *Journal of Applied Physics*, 1 August 2009, vol.106 no.3, p.03305-1 to 03305-15.

[104] *The bending energy levels of C<sub>2</sub>H<sub>2</sub>* by Y. Kabbadj, M. Herman, G. Di Lonardo, L. Fusina and J.W.C. Johns; *Journal of Molecular Spectroscopy*, December 1991, vol.150 no.2, p.535-565.

[105] *l-type resonances in C<sub>2</sub>H<sub>2</sub>* by M. Herman, T.R. Huet, Y. Kabbadj and J. Vander Auwera; *Molecular Physics*, January 1991, vol.72 no.1, p.75-88.

[106] *Exploration of the combustion products in the exhaust of a small gas turbine using an intra-pulse quantum cascade laser spectrometer* by Mark P. Johnson, John Black, K.G. Hay, G. Duxbury and N. Langford; presented at FLAIR 2009 – Field Laser Applications in Industry and Research, Grainau, Germany, 6-11 September 2009.

[107] *On the effect of emissions from aircraft engines on the state of the atmosphere* by U. Schumann; *Annales Geophysicae*, 1994, vol.12, p.365-384.

[108] *Rapid measurement of emissions from military aircraft turbine engines by downstream extractive sampling of aircraft on the ground: Results for C-130 and F-15 aircraft* by Chester W. Spicer, Michael W. Holdren, Kenneth A. Cowen, Darrell W. Joseph, Jan Satola, Bradley Goodwin, Howard Mayfield, Alexander Laskin, M. Elizabeth Alexander, John V. Ortega, Matthew Newburn, Robert Kagann and Ram Hashmonay; *Atmospheric Environment*, 2009, vol.43, p.2612-2622.

[109] *Characterization of chemical and particulate emissions from aircraft engines* by Harshit Agrawal, Aniket A. Sawant, Karel Jansen, J. Wayne Miller and David R. Cocker III; *Atmospheric Environment*, 2008, vol.42, p.4380-4392.

[110] *Nonintrusive optical measurements of aircraft engine exhaust emissions and comparison with standard intrusive techniques* by Klaus Schäfer, Jörg Heland, Dave H. Lister, Chris W. Wilson, Roger J. Howes, Robert S. Falk, Erwin Lindermeir, Manfred Birk, Georg Wagner, Peter Haschberger, Marc Bernard, Olivier Legras, Peter Wiesen, Ralf Kurtenbach, Klaus J. Brockmann, Volker Kriesche, Moira Hilton, Gary Bishop, Roy Clarke, John Workman, Michael Caola, Rachel Geatches, Roger Burrows, John D. Black, Philippe Hervé and Johanna Vally; *Applied Optics*, 20 January 2000, vol.39 no.3, p.441-455.

[111] *Hydrocarbon emissions from jet engines operated at simulated high-altitude supersonic flight conditions* by H. Katzman and W.F. Libby; *Atmospheric Environment*, 1975, vol.9, p.839-842.

- [112] *Public consultation on air quality action plan draft proposals* by Glasgow City Council, 2008.
- [113] *Evidence of an increasing NO<sub>2</sub>/NO<sub>x</sub> emissions ratio from road traffic emissions* by David C. Carslaw; *Atmospheric Environment*, 2005, vol.39, p.4793-4802.
- [114] *Measuring the Emissions of Passing Cars* by G.A. Bishop and D.H. Stedman; *Accounts of Chemical Research*, 1996, vol.29, p.489-495.
- [115] *Measurement of Nitrous Acid in Motor Vehicle Exhaust* by Thomas W. Kirchstetter and Robert A. Harley, 1996, vol.30 no.9, p.2843-2849.
- [116] *Contribution of Vehicle Emissions from an Attached Garage to Residential Indoor Air Pollution Levels* by Lisa A. Graham, Lianne Noseworthy, Don Fugler, Kevin O'Leary, Deniz Karman and Carmela Grande; *Journal of the Air & Waste Management Association*, May 2004, vol.54, p.563-584.
- [117] *Real-time trace-level detection of carbon dioxide and ethylene in car exhaust gases* by M. T. McCulloch, N. Langford and G. Duxbury; *Applied Optics*, 10 May 2005, vol.44 no.14, p.2887-2894.
- [118] *Bus Exhaust Fumes Through the Ages* by Kenneth Hay; *Fare Stage: The magazine of the Glasgow Vintage Vehicle Trust*, Winter 2009, p.20-23.
- [119] *The  $\nu_3$ ,  $\nu_4$ , and  $\nu_6$  Bands of Formaldehyde: A Spectral Catalog From 900  $\text{cm}^{-1}$  to 1580  $\text{cm}^{-1}$*  by Shachar Nadler, D.C. Reuter, S.J. Daunt and J.W.C. Johns; *NASA Technical Memorandum 100709*, National Aeronautics and Space Administration, Maryland, September 1988.

[120] *Delayed rapid passage and transient gain signals generated using a chirped 8  $\mu\text{m}$  quantum cascade laser* by Geoffrey Duxbury, Nigel Langford and Kenneth Hay; *Journal of Modern Optics*, November 2008, vol.55 nos.19-20, p.3293-3303.

[121] *Observation of saturation and rapid passage signals in the 10.25 micron spectrum of ethylene using a frequency chirped quantum cascade laser* by M. T. McCulloch, G. Duxbury and N. Langford; *Molecular Physics*, 20 August - 10 September 2006, vol.104 nos.16-17, p.2767-2779.

[122] *Relaxation Effects in Nuclear Magnetic Resonance Absorption* by N. Bloembergen, E.M. Purcell and R.V. Pound; *Physical Review*, 1 April 1948, vol.73 no.7, p.679-712.

[123] *Nuclear Induction Due to Free Larmor Precession* by E.L. Hahn; *Physical Review*, 15 January 1950, vol.77 no.2, p.297-298.

[124] *The Principles of Nuclear Magnetism* by A. Abragam, Oxford University Press, Oxford, 1961.

[125] *Photo Echo and Optical Nutation in Molecules* by Richard G. Brewer and R.L. Shoemaker; *Physical Review Letters*, 6 September 1971, vol.27 no.10, p.631-634.

[126] *Optical Free Induction Decay* by Richard G. Brewer and R.L. Shoemaker; *Physical Review A*, 1 December 1972, vol.6 no.6, p.2001-2007.

[127] *Optical Resonance and Two Level Atoms* by L. Allen and J.H. Eberly, Dover, New York, 1975.

- [128] *Pulse Formation and Amplification by Optical Phase Switching* by R.O. Brickman, A.Z. Genack and A. Schenzle; *Proceedings of the International Conference on Lasers* edited by C.B. Collins, Society for Optical and Quantum Electronics p.822-826.
- [129] *Pulse Formation and Amplification in an Absorbing Medium by Optical Phase Switching* by A.Z. Genack, R.O. Brickman and A. Schenzle; *Applied Physics B*, June 1982, vol.28 nos.2-3, p.276-277.
- [130] *Quantenkaskadenlaser für Untersuchungen im IR in der Flammendiagnostik* by M. Köhler, P. Nau, K. Kohse-Höinghaus, A. Brockhinke, G. Duxbury and P. Black; presented at Hauptversammlung der Deutschen Bunsen-Gesellschaft für Physikalische Chemie, Graz, Austria, 17-19 May 2007.
- [131] *Improved absorption measurements in flames using a novel 8  $\mu\text{m}$  quantum cascade laser* by M. Köhler, P. Nau, K. Kohse-Höinghaus and A. Brockhinke; presented at the Gordon Research Conference on Laser Diagnostics in Combustion, Oxford, England, 12-17 August 2007.

## Publications

### Papers

*In-flight measurements of ambient methane, nitrous oxide and water using a quantum cascade laser based spectrometer* by K. G. Hay, S. Wright, G. Duxbury and N. Langford; *Applied Physics B*, February 2008, vol.90, p.329-337.

*Delayed rapid passage and transient gain signals generated using a chirped 8  $\mu\text{m}$  quantum cascade laser* by Geoffrey Duxbury, Nigel Langford and Kenneth Hay; *Journal of Modern Optics*, November 2008, vol.55 nos.19-20, p.3293-3303.

*Quantum cascade laser investigations of  $\text{CH}_4$  and  $\text{C}_2\text{H}_2$  interconversion in hydrocarbon/ $\text{H}_2$  gas mixtures during microwave plasma enhanced chemical vapor deposition of diamond* by Jie Ma, Andrew Cheesman, Michael N.R. Ashfold, Kenneth G. Hay, Stephen Wright, Nigel Langford, Geoffrey Duxbury and Yuri A. Mankelevich; *Journal of Applied Physics*, 1 August 2009, vol.106 no.3, p.03305-1 to 03305-15.

*Bus Exhaust Fumes Through the Ages* by Kenneth Hay; *Fare Stage: The magazine of the Glasgow Vintage Vehicle Trust*, Winter 2009, p.20-23.

*Quantum cascade laser spectroscopy: Diagnostics to non-linear optics.* by Geoffrey Duxbury, Nigel Langford, Kenneth Hay and Nicola Tassinato; *Journal of Modern Optics*, 20 October - 10 November 2009, vol.56 no.18-19, p.2034-2048.

*An investigation of collisional processes in a Dicke narrowed transition of water vapor in the 7.8  $\mu\text{m}$  spectral region by frequency down-chirped quantum cascade laser spectroscopy* by Nicola Tassinato, Geoffrey Duxbury, Nigel Langford and Kenneth G. Hay; *The Journal of Chemical Physics*, 29 January 2010, vol.132 no.4, p044316-1 to 044316-8.

*Time dependent measurements of nitrous oxide and carbon dioxide collisional relaxation processes by a frequency down-chirped quantum cascade laser: Rapid passage signals and the time dependence of collisional processes* by Nicola Tassinato, Kenneth G. Hay, Nigel Langford, Geoffrey Duxbury and David Wilson; *The Journal of Chemical Physics*, 28 April 2010, vol.132 no.16, p.164301-1 to 164301-11.

## Talks

*Exploration of the gas phase chemistry in microwave-activated diamond deposition plasmas using an intra-pulse quantum cascade laser spectrometer* by Jie Ma, Andy Cheesman, Mike N.R. Ashfold, Geoffrey Duxbury, Nigel Langford and Kenneth G. Hay; presented at Photon 08, Heriot Watt University, Edinburgh, 27 August 2008.

*Development of the Strathclyde University QC laser spectrometer for the measurement of methane, nitrous oxide and water on the NERC ARSF Dornier Aircraft* by G. Duxbury, N. Langford, S. Wright and K. Hay; presented at NCAS Annual Staff, Affiliates & Science Conference, Cambridge, 14 December 2006.



## Posters

*Quantum Cascade Laser Spectrometer Measurements of Atmospheric Water, Nitrous Oxide and Methane Levels* by Kenneth Hay, Geoffrey Duxbury and Nigel Langford; presented at the International Workshop on Infrared Plasma Spectroscopy, Greifswald, Germany, 26 July 2007.

*In-flight QC laser spectrometer measurement of ambient methane, nitrous oxide and water using the NERC ARSF DORNIER aircraft* by G. Duxbury, N. Langford, S. Wright and K. Hay; presented at 6th International Conference on Tunable Diode Laser Spectroscopy, Reims, France, 9-13 June 2007.

*Time Dependent Measurements of Molecular Collisional Processes in a Dicke Narrowed Absorption Line in the 8 Micron Spectrum of Water by a Frequency Downchirped QCL* by Nicola Tassinato, Geoffrey Duxbury, Nigel Langford and Kenneth G. Hay; presented at PRAHA 2008 - The 20th International Conference on High Resolution Molecular Spectroscopy, Prague, Czech Republic, 2-6 September 2008.

*Exploration of the combustion products in the exhaust of a small gas turbine using an intra-pulse quantum cascade laser spectrometer* by Mark P. Johnson, John Black, K.G. Hay, G. Duxbury and N. Langford; presented at FLAIR 2009 - Field Laser Applications in Industry and Research, Grainau, Germany, 6-11 September 2009.

# Appendix: LabVIEW Program Diagrams

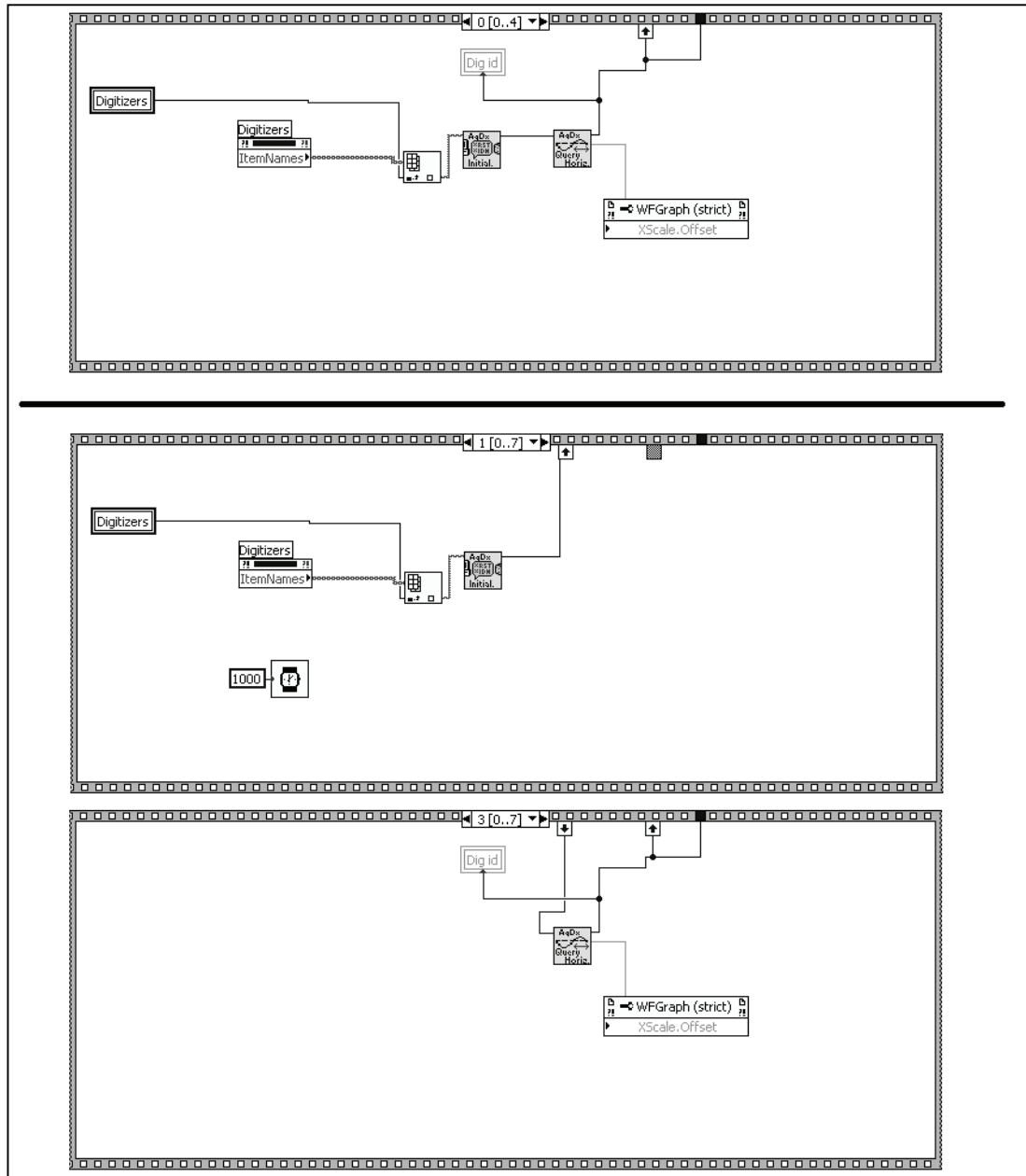


Figure A.1.1: Acqiris initialisation frame in Flight Program 5.1.vi (top) split into two separate frames in Flight Program 6.vi (bottom).

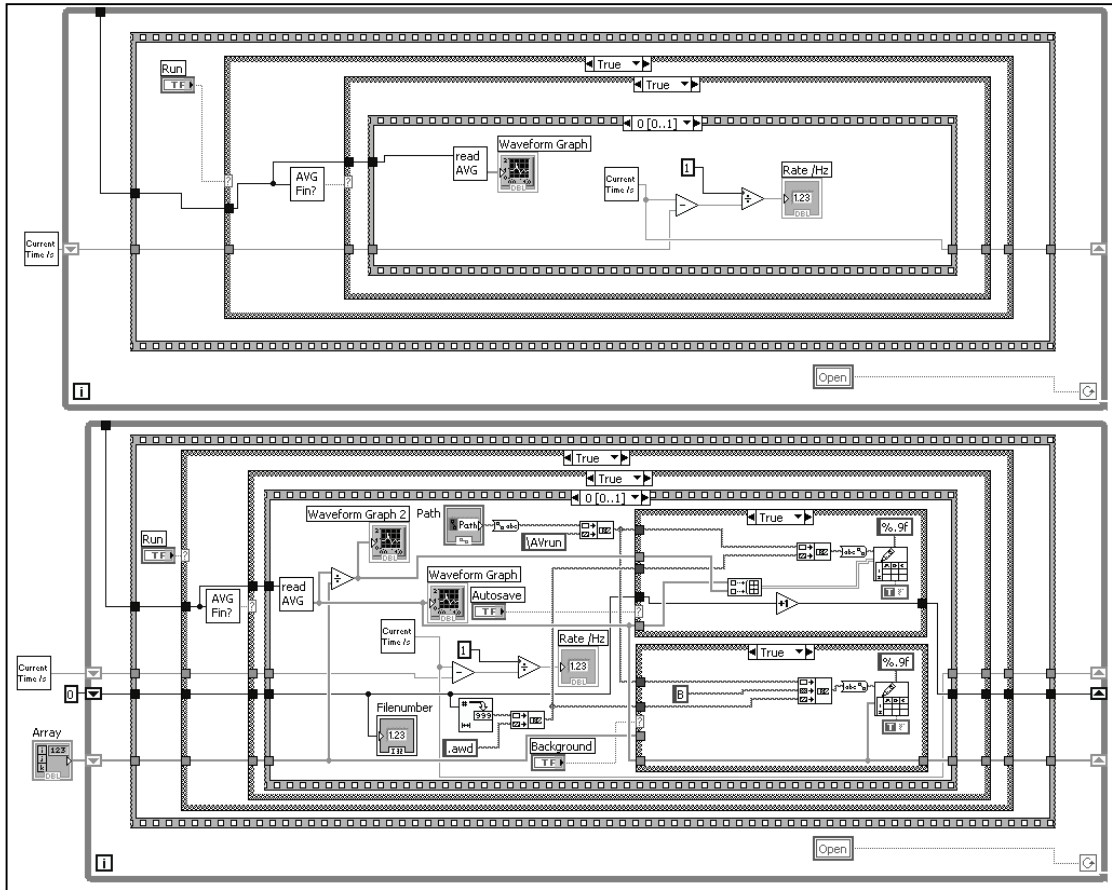


Figure A.1.2: The data plotting frame of Averager.vi (top) compared to Acquisition Only for New Digitisers.vi (bottom).

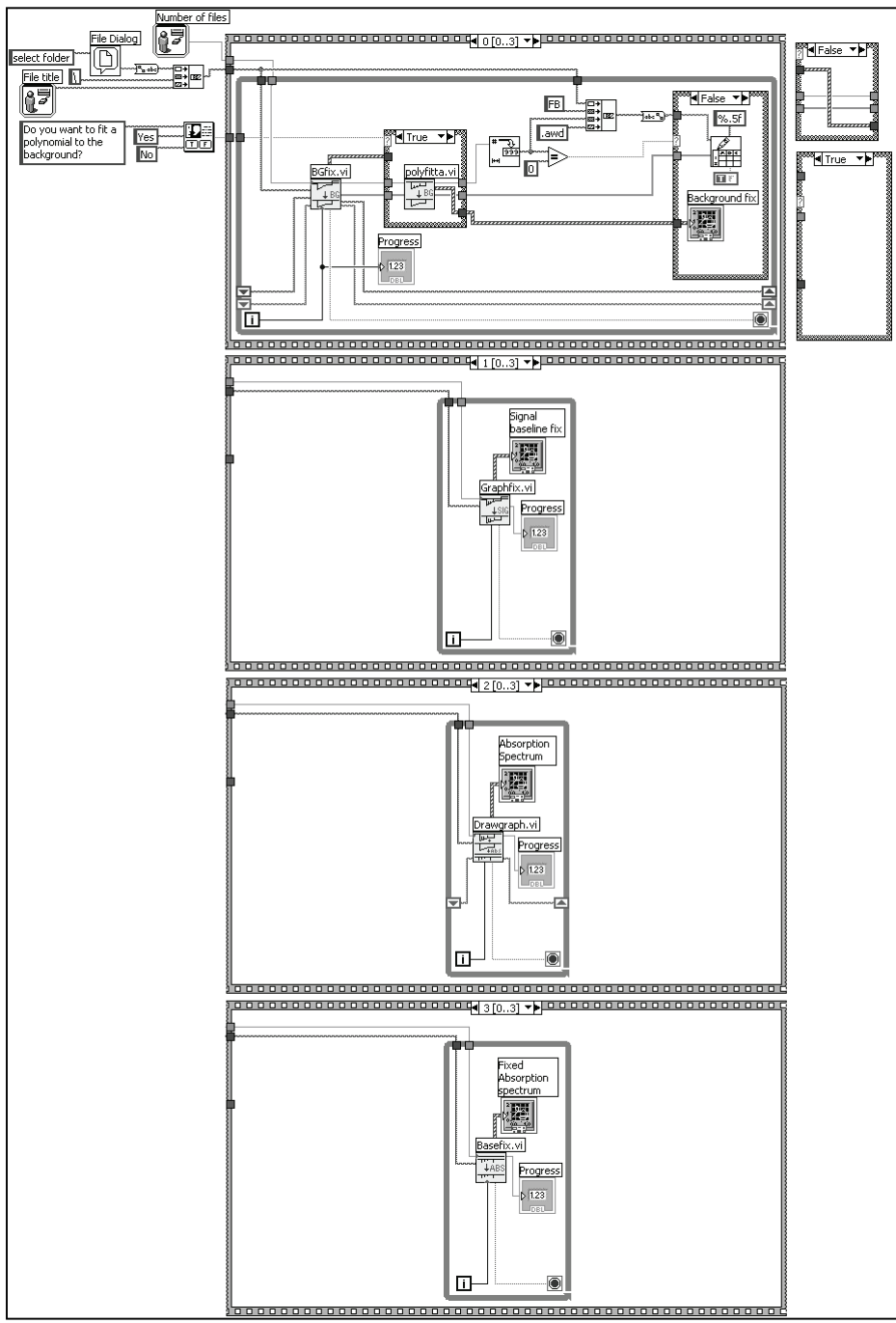


Figure A.1.3: Datafix.vi block diagram.

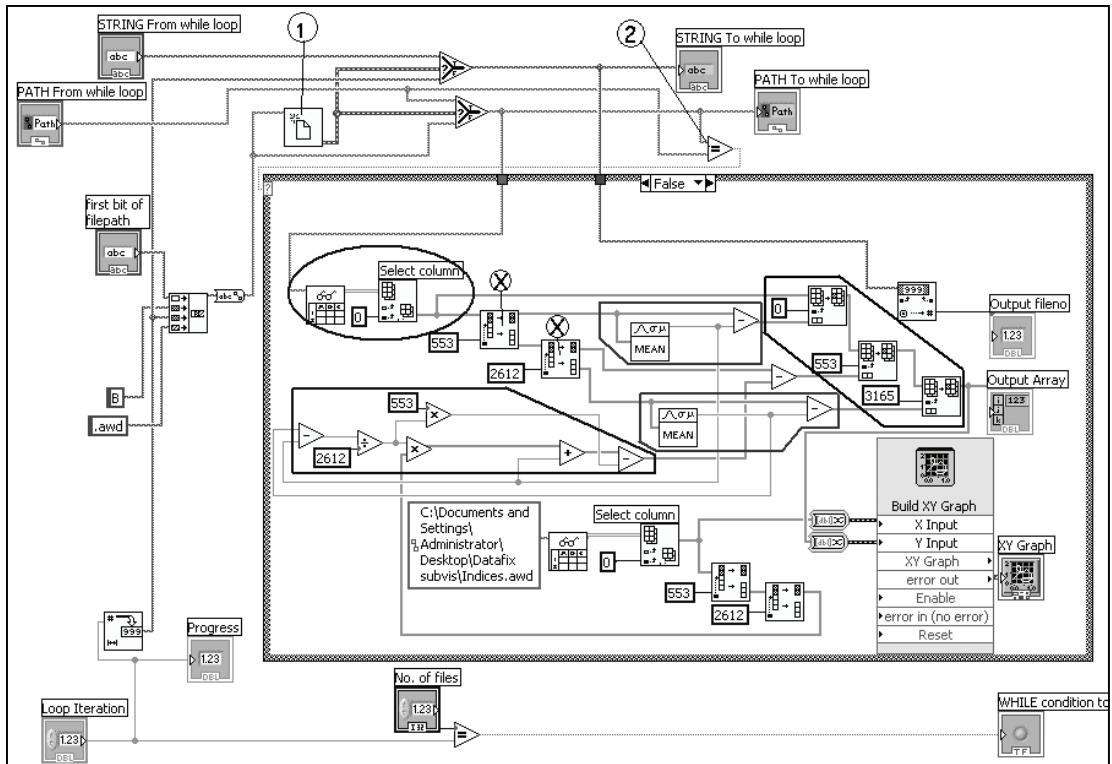


Figure A.1.4: BGfix.vi subVI block diagram.

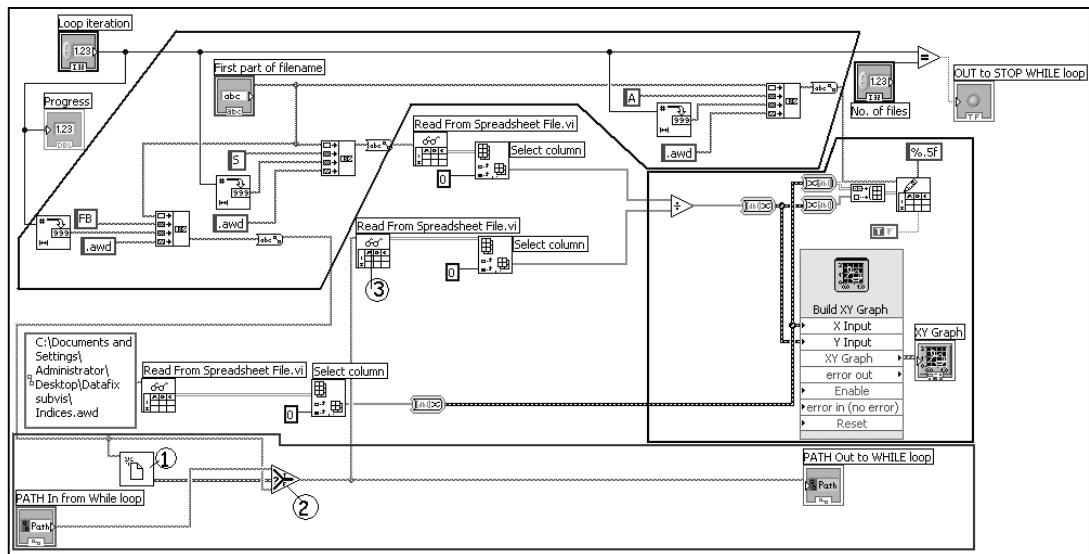


Figure A.1.5: Drawgraph.vi subVI block diagram.

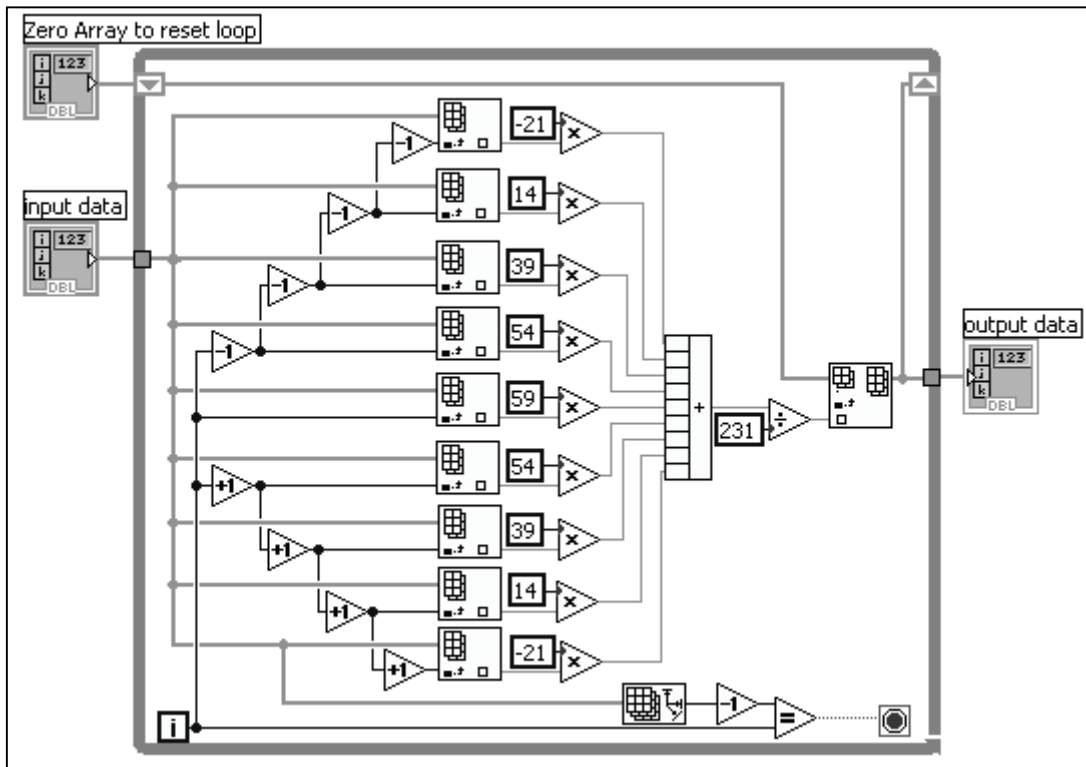


Figure A.1.6: 9-Point Savitzky-Golay.vi subVI block diagram.

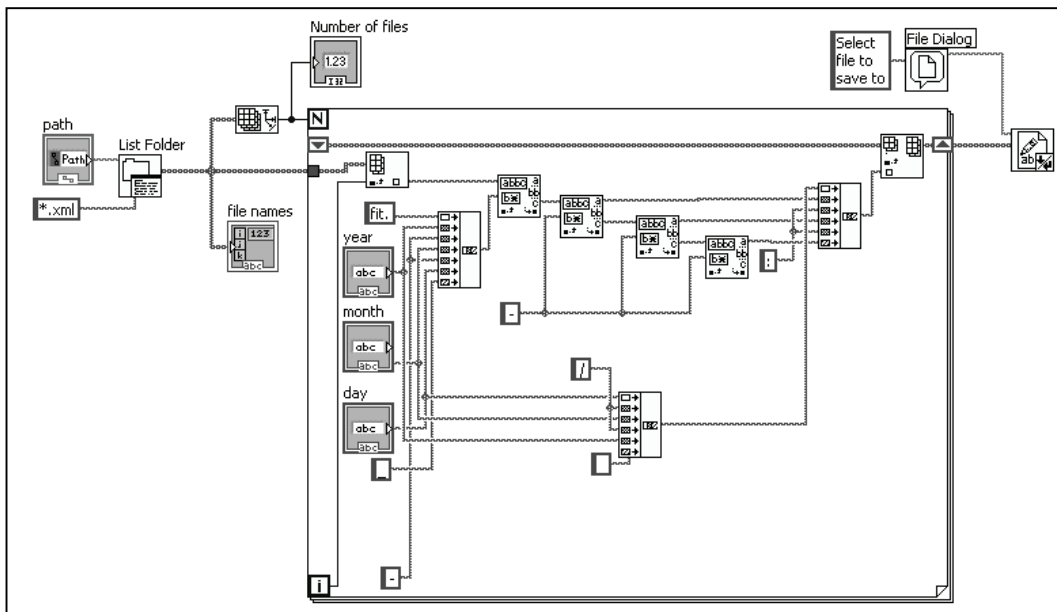


Figure A.1.7: Datestamp retrieval using ExtractXML Datestamps.vi.